

WAVE ATTENUATION BY COASTAL FORESTS

A Dissertation

Presented to the Faculty of the Graduate School
of Cornell University

in Partial Fulfillment of the Requirements for the Degree of
Doctor of Philosophy

by

Che-Wei Chang

August 2017

© 2017 Che-Wei Chang
ALL RIGHTS RESERVED

WAVE ATTENUATION BY COASTAL FORESTS

Che-Wei Chang, Ph.D.

Cornell University 2017

Extreme weather events and rising sea level have largely raised attention to shore protection. As a natural means against ocean waves, coastal vegetation on dissipating incoming wave energy has been extensively studied via mathematical/numerical modeling and laboratory/field observations. The hydrodynamics and sediment transport within vegetated areas have also received an increasing interest. However, the vegetation effects on damping waves have not been fully understood and are awaiting further investigation. In addition, the model forests in most of the existing literature are impractical and still far from real situations. Most importantly, a reliable approach to predict wave attenuation by coastal vegetation is still demanded.

In this dissertation, accordingly, the theoretical development in [Mei et al. \(2011, 2014\)](#) is extended to study water waves propagating through a heterogeneous coastal forest of arbitrary shape. Arrays of rigid and surface-piercing cylinders are used to model the trees. Assuming that the incident wavelength is much longer than the characteristic cylinder spacing (and cylinder diameter), the multi-scale perturbation theory of homogenization ([Mei and Vernescu 2010](#)) is applied to separate the micro-scale flow problem within a unit cell from the macro-scale wave dynamics throughout the entire vegetated area. Driven by the macro-scale (wavelength-scale) pressure gradients, the flow motion within a unit cell, which can have one or a few cylinders inside, is obtained by solving the micro-scale boundary-value-problem. The cell-averaged equations gov-

erning the macro-scale wave dynamics are derived with consideration of the cell effects, which would be parameterized into the complex coefficients. Employing the boundary integral equation method, the macro-scale wave dynamics is solved numerically in which a coastal forest can be composed of multiple patches of arbitrary shape. Each patch can be further divided into several subzones based on different properties, e.g. vegetation sizes, planting arrangements and porosity. Each subzone is then considered as a homogeneous region where a constant bulk value of eddy viscosity can be yielded. The integral formulations for a forest subzone and the open water region are both provided. The matching conditions along the boundaries are also presented.

Two types of small-amplitude waves are first considered. To model wind waves, the theoretical model for periodic waves of relatively short wavelength in [Mei et al. \(2014\)](#) is extended from two-dimensional to three-dimensional applications. The constant bulk value of eddy viscosity for each homogenous forest subzone is determined by invoking the balance of time-averaged energy dissipation rate and the averaged rate of work done by wave forces on cylinders within the specific subzone. Morison-type formula ([Morison et al. 1950](#)) is used to model the wave forces, in which the drag coefficient formula is constructed based on the experimental data in [Hu et al. \(2014\)](#). A computing program is established based on the present approach and can be used for solving wave dynamics with proper inputs. In the interest of understanding the capability of coastal vegetation to dissipate long waves, a transient wave of small amplitude is studied by extending the theoretical model in [Mei et al. \(2011\)](#). Fourier transform is employed to solve the transient problem. The constant bulk value of eddy viscosity for each homogenous forest subzone is determined by modifying the empirical formula in [Mei et al. \(2011\)](#). A similar computing program is

also developed for solving the wave amplitude spectrum. Once the wave amplitude spectrum is obtained, the wave solution can be found by inverse Fourier transform. For simplicity, only the incident waves with a soliton-like shape are considered.

Three special forest configurations with experimental data are used to check the present models for both types of waves. An infinitely long forest belt with a finite width, where the semi-analytical solutions are provided, is first used to study the wave damping inside the forest. For periodic waves, the model results of normal incidences are compared with [Hu et al. \(2014\)](#)'s experimental measurements. Obliquely incident waves are also discussed. For transient long waves, the experiments reported in [Mei et al. \(2011\)](#) are re-examined. Very good agreements with experimental data are found in both conditions. A single circular patch is then used as a special configuration to study a forest region with finite extent. The semi-analytical solutions for periodic and transient problems are respectively presented, in which negligible differences are found in comparison with the numerical results. A set of experiments was conducted at the University of Cantabria for model validation. Good agreements are found in the data-model comparisons. For transient waves, the effects of wave parameters and different arrangements of cylinders on wave damping are also discussed. The numerical model is then further explored by using a forest region consisting of multiple circular patches as used in [Maza \(2015\)](#). Good agreements are also observed between the simulated free surface elevations and the experimental measurements. The effectiveness of different forest configurations on wave attenuation is discussed as well.

The capability of the linear models to predict wave attenuation by coastal forests has been presented for both types of waves. However, the limitation of

the nonlinearity of incident waves is also confirmed by comparison with experimental data. The last part of this dissertation aims to study the possible nonlinear effects by including the convection terms in the momentum equations. Considering shallow-water incident waves of simple harmonic, higher harmonic components are expected to grow within the vegetated area and be radiated out to the open water region. Applying multi-scale perturbation technique, the micro- and macro-scale equations for each harmonic are derived. The cell problem for micro-scale flow motion, driven by the macro-scale pressure gradient, becomes a nonlinear boundary-value-problem while the macro-scale problem for wave dynamics remains linear. A modified pressure correction method is employed to solve the nonlinear cell problem. Using a forest belt as a special case, the comparisons of numerical results obtained by linear and nonlinear models are presented. The numerical results are also compared with the experimental data reported in [Mei et al. \(2011\)](#). Varying nonlinearity is further tested and the effects of different parameters on wave solutions are discussed as well.

BIOGRAPHICAL SKETCH

Che-Wei Chang was born and raised in Taiwan. Before coming to the United States, he obtained his Bachelor of Science degree from National Chung Hsing University in 2006 and Master of Science degree from National Taiwan University in 2008. After graduation, he worked as a full-time research assistant at Hydrotech Research Institute, National Taiwan University and Institute of Physics, Academia Sinica in Taipei until 2010. He was a doctoral student at Virginia Tech for one year before joining the School of Civil and Environmental Engineering at Cornell University in August 2012. With an interest in natural disasters of coastal regions, Che-Wei focused on wave-vegetation interactions and developed a theoretical/numerical model for his doctoral research, which aims to investigate wave attenuation by coastal forests. Most of his works have been published in Coastal Engineering. In addition to wave-vegetation-structure interactions, his research interests include coastal hydrodynamics and sediment transport, nearshore/estuarine processes, coastal hazards (e.g. Tsunami, storm surges/waves) reduction, numerical modelings and experimental fluid mechanics. Upon graduation, Che-Wei will start working as a postdoctoral researcher. He plans to seek a faculty/researcher position and to expand his research interests in the long term.

To my family
for all their love and support

ACKNOWLEDGEMENTS

First and foremost, I would like express my sincerest gratitude to my advisor, Dr. Philip L.-F. Liu, for his continuous guidance, immense patience and support throughout my study at Cornell University. His insights into the research problems and technical advice have been of vital importance to the completion of this dissertation and our published journal papers. I would also like to thank my committee members, Dr. Peter Diamessis and Dr. James Jenkins, for their valuable comments and suggestions on my dissertation. Thanks also need to go to Dr. Maria Maza and Dr. Zhan Hu for providing the experimental data, which was used for parts of the model validation in this work. Besides, special appreciation must be given to Dr. Todd Cowen for the opportunities he provided me to work with him as a Teaching Assistant from 2013 to 2015. I learned so much from him about how to guide and communicate with students in their learning paths, which have been and will always be valuable in my future career. With his support, I earned the John E. Perry Teaching Assistant Prize in 2015. Furthermore, I would like to thank my professors in Taiwan, especially Dr. Ko-Fei Liu and Dr. Liang-Hsiung Huang, for their recommendation on my pursue of this Ph.D. degree. I am also grateful to all my friends and my colleagues in the EFMH community for being supportive during the last five years. Finally and most importantly, my deepest gratitude must be given to my parents, my sister and my dear Joy for their endless love and support in my life. I dedicate this work to them.

TABLE OF CONTENTS

Biographical Sketch	iii
Dedication	iv
Acknowledgements	v
Table of Contents	vi
List of Tables	ix
List of Figures	x
1 Introduction	1
2 Theoretical formulation and test conditions	12
2.1 Governing equations and boundary conditions	12
2.2 Conditions and simplifications	14
3 Small-amplitude periodic waves through coastal forests	16
3.1 Governing equations and boundary conditions	17
3.2 Homogenization method	20
3.2.1 Micro-scale (cell) problem	22
3.2.2 Macro-scale (wavelength-scale) problem	25
3.3 Boundary integral equation method	28
3.3.1 Integral formulation for a forest subzone	28
3.3.2 Integral formulation for open water	30
3.3.3 Matching conditions along the boundaries	31
3.3.4 Numerical implementation	33
3.4 Eddy viscosity	39
3.5 Cornell HomogEnization model for WAVE-VEgetation interac- tion – Periodic waves	48
3.6 Model validation and numerical results	49
3.6.1 Water waves propagating through a forest belt	50
3.6.2 Water waves scattered by a circular forest	60
3.6.3 Water waves scattered by multiple circular forest patches	74
3.6.4 Model demonstration	84
3.7 Concluding remarks and discussions	95
4 Small-amplitude transient long waves through coastal forests	101
4.1 Governing equations and boundary conditions	102
4.2 Homogenization method	105
4.2.1 Micro-scale (cell) problem	106
4.2.2 Macro-scale (wavelength-scale) problem	108
4.3 Boundary integral equation method	108
4.3.1 Integral formulation for a forest subzone	109
4.3.2 Integral formulation for open water	110

4.3.3	Matching conditions along the boundaries	111
4.3.4	Numerical implementation	112
4.4	Cornell HomogEnization model for WAVE-VEgetation interaction – Transient waves	115
4.5	Model validation and numerical results	116
4.5.1	Solitary wave through a forest belt	117
4.5.2	Solitary wave through a circular forest	121
4.5.3	Solitary wave through multiple circular forest patches	129
4.6	Concluding remarks and discussions	135
5	Harmonics generation by a coastal forest	142
5.1	Governing equations and boundary conditions	143
5.2	Homogenization method	145
5.2.1	Micro-scale (cell) problem	147
5.2.2	Macro-scale (wavelength scale) problem	153
5.3	Shallow-water waves through a forest belt	155
5.3.1	Linear results	159
5.3.2	Nonlinear results	161
5.4	Concluding remarks and discussions	170
6	Summary and suggested future works	174
A	Detailed derivations of integral formulation	180
A.1	Derivation of Helmholtz equation	180
A.2	Boundary integral formulation	182
A.2.1	Forest region (bounded domain)	182
A.2.2	Open water (unbounded domain)	185
B	Further information for the numerical model	187
B.1	Small-amplitude periodic waves	187
B.1.1	Inputs/outputs for the numerical model	188
B.1.2	Cell problem solver	191
B.2	Small-amplitude transient long waves	191
B.2.1	Inputs/outputs for the numerical model	191
C	Derivations of matching conditions for two special forest configurations	195
C.1	Water waves propagating through a forest belt	195
C.2	Water waves scattered by a circular forest	197
D	More data-model comparisons for solitary wave through a circular forest	199
D.1	Cases in Table 4.1	199

D.2	Cases in Table 4.2	204
E	More numerical results for harmonics generation problem	207
E.1	Micro-scale velocity fields	207
E.2	Macro-scale wave amplitude variations through the forest belt .	218
	Bibliography	222

LIST OF TABLES

3.1	Test conditions and dimensionless parameters – normally incident waves through a forest belt (Hu et al. 2014)	53
3.2	Dimensionless parameters – obliquely incident waves through a forest belt	58
3.3	Test conditions and dimensionless parameters – wave scattered by a circular forest (Frequency Test I)	64
3.4	Test conditions and dimensionless parameters – wave scattered by a circular forest (Frequency Test II)	64
3.5	Test conditions and dimensionless parameters – wave scattered by a circular forest (Amplitude Test I)	64
3.6	Test conditions and dimensionless parameters – wave scattered by a circular forest (Amplitude Test II)	65
3.7	Test conditions and dimensionless parameters – wave scattered by multiple circular forest patches	75
4.1	Test conditions and dimensionless parameters – solitary wave through a circular forest (Test I)	122
4.2	Test conditions and dimensionless parameters – solitary wave through a circular forest (Test II)	122
4.3	Test conditions and dimensionless parameters – solitary wave through multiple circular forest patches	129
5.1	Test conditions and dimensionless parameters – normal incident waves through a forest belt (Mei et al. 2011)	158
B.1	Size of each input file – P	190
B.2	Size of each input file – T	194

LIST OF FIGURES

1.1	Sketch of a typical coastal forest	11
3.1	Typical cylinder arrangements in laboratory experiments	24
3.2	Finite element discretization for two types of cell problem	25
3.3	Discretization and assignment of boundary elements – forest re- gion	37
3.4	Discretization and assignment of boundary elements – open water	38
3.5	Drag coefficient formula curve	44
3.6	Convergence histories of iteration tests on eddy viscosity	47
3.7	Flowchart for running the numerical model (CHEWAVE-P)	49
3.8	Comparison of model results and experimental data – normally incident waves through a forest belt – I	54
3.9	Comparison of model results and experimental data – normally incident waves through a forest belt – II	54
3.10	Horizontal velocity fields at mean water level – normally inci- dent waves through a forest belt – I	56
3.11	Horizontal velocity fields at mean water level – normally inci- dent waves through a forest belt – II	56
3.12	Horizontal velocity fields at mean water level – normally inci- dent waves through a forest belt – III	57
3.13	Model results – obliquely incident waves through a forest belt – I	58
3.14	Model results – obliquely incident waves through a forest belt – II	59
3.15	Instantaneous dimensionless free surface elevation – normally & obliquely incident waves through a forest belt	59
3.16	Experimental layout – circular forest	63
3.17	Photos during experiments – circular forest	63
3.18	Boundary element discretization of a single circular patch	67
3.19	Convergence tests for numerical model – circular forest	68
3.20	Instantaneous dimensionless free surface elevation – waves scat- tered by a circular forest	69
3.21	Comparison of model results and experimental data – waves scattered by a circular forest – I	70
3.22	Comparison of model results and experimental data – waves scattered by a circular forest – II	71
3.23	Horizontal velocity fields at mean water level – waves scattered by a circular forest – I	72
3.24	Horizontal velocity fields at mean water level – waves scattered by a circular forest – II	73
3.25	Horizontal velocity fields at mean water level – waves scattered by a circular forest – III	73
3.26	Experimental layout – multiple circular forest patches	75

3.27	Comparison of model results and experimental data – waves scattered by multiple circular patches – I	80
3.28	Comparison of model results and experimental data – waves scattered by multiple circular patches – II	81
3.29	Comparison of model results and experimental data – waves scattered by multiple circular patches – III	82
3.30	Comparison of model results and experimental data – waves scattered by multiple circular patches – IV	83
3.31	Instantaneous dimensionless free surface elevation – waves scattered by multiple circular patches	84
3.32	Instantaneous dimensionless free surface elevation – waves scattered by a single rectangular patch	85
3.33	Instantaneous dimensionless free surface elevation – waves scattered by two rectangular patches	86
3.34	Sketch of a single circular patch with two subzones	89
3.35	Instantaneous dimensionless free surface elevation – waves scattered by a circular forest with two subzones – I	91
3.36	Wave amplitude variation – waves scattered by a circular forest with two subzones – I	92
3.37	Instantaneous dimensionless free surface elevation – waves scattered by a circular forest with two subzones – II	93
3.38	Wave amplitude variation – waves scattered by a circular forest with two subzones – II	94
3.39	Comparison of spatial-varying and spatial-averaged eddy viscosity – normally incident waves through a forest belt – I	99
3.40	Comparison of spatial-varying and spatial-averaged eddy viscosity – normally incident waves through a forest belt – II	99
3.41	Comparison of model results based on spatial-varying and spatial-averaged eddy viscosity – normally incident waves through a forest belt – I	100
3.42	Comparison of model results based on spatial-varying and spatial-averaged eddy viscosity – normally incident waves through a forest belt – II	100
4.1	Comparison of model results and experimental data – solitary wave through a forest belt	120
4.2	Comparison of normalized damping height – solitary wave through a forest belt	121
4.3	Comparison of model results and experimental data – solitary wave through a circular forest (4S1)	126
4.4	Comparison of model results and experimental data – solitary wave through a circular forest (4S2)	126

4.5	Comparison of model results and experimental data – solitary wave through a circular forest (4S7)	127
4.6	Comparison of model results and experimental data – solitary wave through a circular forest (4S8)	127
4.7	Comparison of simulated and measured wave height profiles along the centerline – solitary wave through a circular forest (4S)	128
4.8	Comparison of normalized damping height along the centerline – solitary wave through a circular forest	128
4.9	Comparison of model results and experimental data – solitary wave through multiple circular patches (Case 1)	132
4.10	Comparison of model results and experimental data – solitary wave through multiple circular patches (Case 2)	133
4.11	Comparison of model results and experimental data – solitary wave through multiple circular patches (Case 3)	134
4.12	Comparison of simulated wave heights through the centerline of the single circular forest and multiple circular forest patches	135
4.13	Comparison of simulated wave heights between aligned and staggered cylinder arrangements – solitary wave through a forest belt (Case 3 & 4)	139
4.14	Comparison of simulated wave heights along the centerline between aligned and staggered cylinder arrangements – solitary wave through a circular forest (4S7)	140
4.15	Comparison of simulated wave height profiles along the centerline between aligned and staggered cylinder arrangements – solitary wave through a circular forest (4S)	141
4.16	Comparison of normalized damping height along the centerline between aligned and staggered cylinder arrangements – solitary wave through a circular forest (4S)	141
5.1	Staggered grid discretization	150
5.2	Iteration steps in the modified pressure correction method – nonlinear cell problem	152
5.3	Iteration steps for solving coupled micro- and macro-problem	157
5.4	Comparison of macro-scale linear model results	159
5.5	Micro-scale flow velocity profiles along $x_1 = 0$	160
5.6	Comparison of nonlinear wave amplitude variation – Case 7 & 8	162
5.7	Comparison of nonlinear wave amplitude variation – Case 4 & 5	162
5.8	Wave amplitude variation for each mode – Case 7 & 8	163
5.9	Wave amplitude variation for each mode – Case 4 & 5	164
5.10	Convergence histories of micro-scale iteration	166
5.11	Comparisons of reflection and transmission coefficients by linear & nonlinear models and data	167

5.12	Comparisons of reflection and transmission coefficients with different values of α_n	169
5.13	Convergence histories of macro-scale iterations	170
D.1	Comparison of model results and experimental data – solitary wave through a circular forest (3S1)	199
D.2	Comparison of model results and experimental data – solitary wave through a circular forest (3S2)	200
D.3	Comparison of model results and experimental data – solitary wave through a circular forest (3S3)	200
D.4	Comparison of model results and experimental data – solitary wave through a circular forest (3S4)	201
D.5	Comparison of model results and experimental data – solitary wave through a circular forest (3S5)	201
D.6	Comparison of model results and experimental data – solitary wave through a circular forest (3S6)	202
D.7	Comparison of model results and experimental data – solitary wave through a circular forest (3S7)	202
D.8	Comparison of model results and experimental data – solitary wave through a circular forest (3S8)	203
D.9	Comparison of model results and experimental data – solitary wave through a circular forest (4S3)	204
D.10	Comparison of model results and experimental data – solitary wave through a circular forest (4S4)	205
D.11	Comparison of model results and experimental data – solitary wave through a circular forest (4S5)	205
D.12	Comparison of model results and experimental data – solitary wave through a circular forest (4S6)	206
E.1	Horizontal velocity fields of 0 th mode – waves through a forest belt (Case 5 & 7)	207
E.2	Horizontal velocity fields of 1 st mode – waves through a forest belt (Case7)	208
E.3	Horizontal velocity fields of 2 nd mode – waves through a forest belt (Case7)	209
E.4	Horizontal velocity fields of 3 rd mode – waves through a forest belt (Case7)	210
E.5	Horizontal velocity fields of 4 th mode – waves through a forest belt (Case7)	211
E.6	Horizontal velocity fields of 5 th mode – waves through a forest belt (Case7)	212
E.7	Horizontal velocity fields of 1 st mode – waves through a forest belt (Case5)	213

E.8	Horizontal velocity fields of 2 _{nd} mode – waves through a forest belt (Case5)	214
E.9	Horizontal velocity fields of 3 _{rd} mode – waves through a forest belt (Case5)	215
E.10	Horizontal velocity fields of 4 _{th} mode – waves through a forest belt (Case5)	216
E.11	Horizontal velocity fields of 5 _{th} mode – waves through a forest belt (Case5)	217
E.12	Wave amplitude variation of different harmonic components – $\alpha_n = 0.3$	218
E.13	Wave amplitude variation of different harmonic components – $\alpha_n = 0.6$	219
E.14	Wave amplitude variation of different harmonic components – $\alpha_n = 0.9$	220
E.15	Wave amplitude variation of different harmonic components – $\alpha_n = 1.2$	221

CHAPTER 1

INTRODUCTION

Coastal forest, as a natural barrier of shore regions, has been considered as an effective means against ocean waves. Its capability as a shore protection from both long waves (e.g. tsunami waves, storm surges) and short waves (e.g. wind waves) has been proved by field studies, e.g. [Danielsen et al. \(2005\)](#) indicates the essential role of coastal trees on reducing damage from Indian Ocean tsunami in 2004. Similar conclusions were also proposed by [Tanaka et al. \(2007\)](#), showing the effective protection by mangroves from the 2004 tsunami damage. Plantation of mangrove vegetation was suggested by [Kathiresan and Rajendran \(2005\)](#) based on their study in several coastal hamlets after the 2004 tsunami. [Das and Vincent \(2009\)](#) also evidently presented a connection between mangrove shields and death reduction during the attacks from storm waves in 1999. In [Massel et al. \(1999\)](#)'s field tests, relatively short waves were observed, showing only a few parts of incident wave energy were transmitted through mangrove areas. Wave attenuation by mangroves and the related effects on sedimentation were also studied in fields, e.g. [Quartel et al. \(2007\)](#) and [Horstman et al. \(2014\)](#). Knowing the vital role of coastal vegetation on shore protection, the desire of understanding the hydrodynamics and related physical processes within coastal forests has motivated numerous studies by laboratory experiments and mathematical/numerical modelings. A comprehensive review of the existing literature has been given in [Mei et al. \(2011, 2014\)](#). However, some of the most relevant works are still worthy of mentioning here. Also, the most recent studies deserve to be reviewed in this dissertation.

Providing direct observations and measurements, laboratory experiments

have been widely used to study wave-flow-vegetation interactions and relevant topics. In most of the experimental studies, an array of cylinders is usually used to mimic coastal trees or mangroves due to their rigidity. On the other hand, flexible tubes or even real vegetation are used to model wetlands/marshes. For modeling relatively shorter waves, [Augustin \(2007\)](#) and [Augustin et al. \(2009\)](#) conducted flume tests by using both rigid wooden dowels and flexible polyethylene foam tubing to model different kinds of vegetation. Different arrangements of cylinders with different stem densities were tested. The effectiveness of both types of cylinders on damping incoming waves was discussed. [Wu et al. \(2011, 2012\)](#) and [Ozeren et al. \(2014\)](#) also used similar rigid and flexible elements to model coastal vegetation in their flume experiments. Additionally, two species of live grasses, commonly existing in wetlands – *Spartina alterniflora* and *Juncus roemerianus*, were used in their tests. For these three different materials, both emergent and submerged conditions were tested. The decaying wave amplitudes inside the model forest were collected by wave gauges and video images. Similar experiments were also reported in [Hu et al. \(2014\)](#) by adding steady current in their flume tests.

For modeling longer waves (e.g. tsunami waves, storm surges), [Huang et al. \(2011\)](#) conducted laboratory experiments on solitary waves through an array of emergent rigid cylinders. Different arrangements of cylinders were tested. Different sizes of cylinder arrays were also included. By measuring the free surface elevation, the wave evolution across the targeted array was reported and the wave attenuation was evident. In addition, [Irtem et al. \(2009\)](#)'s experiments, using both artificial trees and cylindrical timber sticks, demonstrated the effectiveness of a coastal forest on reducing the maximum run-up of tsunami waves.

[Ismail et al. \(2012\)](#) also examined the influences of vegetation density on wave dissipation and tsunami run-up in their experiments. Different parameterized models of mangroves were adopted in tsunami damping tests as well (e.g. [Husrin et al. 2012](#) and [Strusinska-Correia et al. 2013](#)). A coastal forest with an open gap is another common type of configuration especially existing in some areas with urban developments. According to the field studies of Sumatra Tsunami in 2004, the open gaps within coastal forests significantly enhanced the damage to those areas behind gaps. Some experimental studies have shown the same conclusion, e.g. [Fernando et al. \(2008\)](#) and [Thuy et al. \(2009\)](#), who used cylinder arrays with an open gap in their flume tests and compared the measurements with the field studies of Sumatra Tsunami.

Among the aforementioned references, the physical modelings were mostly conducted in wave flumes, which can reduce experimental difficulties and complexities. However, vegetation patches with finite areas are more commonly observed in fields. An increasing number of studies on relevant topics has been found and shall be reviewed here. Most recently, [Truong et al. \(2015\)](#) used three circular patches in their laboratory experiments to model coastal wetlands. The cylinder patches were built on the tops of artificial marsh mounds, which led to breaking waves and swash currents occurring on the slopes of mounds and passing through the patches. The same type of cylinder patches was further studied numerically by [Yang et al. \(2015\)](#). Rip currents were observed within the channels between patches. Effects of bathymetry, vegetation and the spacing between patches were investigated. Wave dissipation by vegetation was also discussed. Similar laboratory experiments were conducted by [Irish et al. \(2014\)](#) and [Yang et al. \(2017\)](#), placing multiple smaller cylinder patches with

different porosities along a steep slope to study the run-up of a tsunami. In addition to discontinuous patches, a single patch with a finite area has been used in several numerical studies to investigate wave dissipation by vegetation. [Ma et al. \(2013\)](#) developed a numerical model to study surface wave attenuation through a rectangular patch on a slope and the nearshore circulation in the surf zone. Similar vegetation patch was used in [Zhang et al. \(2016\)](#) to simulate wave propagation and wave-induced current. [Anderson and Smith \(2015\)](#) used different numerical models to study the effects of a finite rectangular cylinder patch on wave dissipation. Furthermore, [Lara et al. \(2016\)](#) proposed a guideline for large-scale physical modeling on the interactions of waves and currents with a real salt marsh vegetation patch, where the analysis was reported in [Maza et al. \(2015a\)](#). Apart from water waves, the interactions between water flows and vegetation patches were also investigated both numerically (e.g. [Yüksel-Ozan et al. 2016](#); [de Lima et al. 2015](#)) and experimentally (e.g. [Meire et al. 2014](#); [Zong and Nepf 2011](#)). By conducting laboratory experiments, the first-hand observations on wave evolution/propagation through the model forest can be provided. The direct measurements, e.g. wave amplitude and wave forces on cylinder arrays, further enhance the understanding of physical problems. However, deeper physical insights and related prediction tools on wave attenuation are still demanded and shall rely on mathematical/numerical modeling.

Regarding mathematical/numerical modeling on wave-vegetation interactions, mainly three types of modeling have been proposed and investigated. The first approach directly solves flow problem with applications of appropriate numerical methods, in which each cylinder within the model forest has to be resolved in the numerical discretization. The spatial and temporal variation

of free surface profiles needs to be accurately computed. In addition, a turbulence closure scheme at the sub-grid scale is required, which usually contains a number of empirical coefficients. Several numerical models on water waves (or water flows) have been developed in recent studies. For example, water waves of short periods through cylinder arrays have been simulated based on Reynolds-averaged Navier-Stokes (RANS) equations in [Li and Yan \(2007\)](#) and [Wu et al. \(2012\)](#). [Maza et al. \(2013\)](#) solved similar equations but focused on submerged vegetation in their model. The plant deformation was also simulated and discussed. For longer waves, [Maza et al. \(2015b\)](#) proposed a three-dimensional numerical scheme, simulating the interactions between solitary waves and emergent rigid cylinders, where the flow field around each cylinder was computed. In addition to RANS models, large eddy simulation (LES) is another popular way to model the turbulence between cylinders. In [Stoesser et al. \(2010\)](#), LES was applied to model an open-channel flow through a periodic cylinder array. The results were compared with experimental data in [Liu et al. \(2008\)](#). [Cui and Neary \(2008\)](#) and [Stoesser et al. \(2009\)](#) also applied LES to investigate the interactions between flows and submerged cylinders. Most recently, [Chakrabarti et al. \(2016\)](#) conducted large eddy simulation for periodic waves through emergent cylinders and provided more detailed interpretations of wave forces on cylinder arrays. The flow fields in the vicinity of cylinders were also presented. Although detailed flow fields and physical processes can be provided, both RANS and LES models demand considerable computational resources for a large forest region.

Another approach focuses only on solving the macro-scale (wavelength-scale) equations (e.g. [Dalrymple et al. 1984](#), [Mendez and Losada 1999](#), [Massel](#)

et al. 1999 and Mazda et al. 2005). The effects of vegetation on wave propagation are considered as an additional drag force term in the macro-scale momentum equations. To compute the drag force, the corresponding drag coefficient has to be prescribed and can only be determined by fitting the model results with experimental data. A well-known wave height damping formulation was presented by Dalrymple et al. (1984) and has been used in several studies, e.g. Ozeren et al. (2014), Anderson and Smith (2014), Hu et al. (2014) and Maza (2015). The formulation was further extended to irregular waves by Mendez and Losada (2004). Usually, the macro-scale wave profiles need to be prescribed and can only rely on fitting the model results with measurements. Detailed resolutions of flow fields and wave profiles are not available.

The third approach applies the multi-scale perturbation technique (homogenization theory), which requires a strong contrast between wavelength and tree spacing. Using this approach, macro-scale wave dynamics is solved from a set of cell-averaged effective equations, which include complex coefficients being computed based on micro-scale flows within unit cells. Driven by the macro-scale pressure gradient, the boundary-value-problem for micro-scale flows is derived essentially from the RANS equations with the use of constant eddy viscosity model for turbulence. Among the above three approaches, using multi-scale perturbation method is much more computational-efficient than the numerical approach. It also provides deeper physical insights than the macro-scale scheme. Accordingly, in this dissertation we shall apply the homogenization technique to study wave-vegetation interactions of different cases as follows.

We first focus on small-amplitude waves propagating through a coastal forest in a constant water depth. The theoretical model on wave-vegetation interac-

tions developed in [Mei et al. \(2011, 2014\)](#) is extended to a heterogeneous coastal forest of arbitrary shape. As sketched in [Fig.1.1](#), a heterogeneous forest region can consist of multiple vegetated patches, which is more commonly observed in fields as mentioned. Each patch has an arbitrary shape and can be further divided into subzones due to different properties, e.g. vegetation sizes, planting patterns, and porosity. Each subzone is then considered as a homogeneous region such that a corresponding bulk value of constant eddy viscosity can be yielded. Here the eddy viscosity model is adopted to describe the turbulence generated within the forest. Vertical, rigid and surface-piercing cylinders in a periodic array are used to model the trees, where the effects of roots, branches, and leaves are neglected for simplicity. Assuming a strong contrast between the incident wavelength and the cylinder spacing, the multiple-scale perturbation theory of homogenization is applied. The micro-scale flow fields in a unit cell, with one or a few cylinders inside, can be obtained by numerically solving the boundary-value cell problem. The equations governing macro-scale wave dynamics over the entire forest region are derived with consideration of micro-scale effects. As shown in [Fig.1.1](#), a forest subzone can be surrounded by other subzones and/or open water. To deal with the possible arbitrary shape of a forest subzone, the boundary integral equation method is employed to solve the macro-scale problem numerically.

Boundary integral equation methods have been widely applied to porous media flow problems (e.g. [Liggett and Liu 1983](#)), wave propagation and scattering problems (e.g. [Lee and Ayer 1981](#), [Williams 1990](#) and [Williams and Vazquez 1991](#)). The boundary integral equation method was also used to study the wave oscillations and resonance behaviors in harbors with an arbitrary geometry (e.g.

Lee 1971). One of the advantages of using this numerical method is that it reduces the dimension of boundary-value-problem (BVP) by one. Solutions to the BVP are first provided along the boundaries of flow domain. The solutions inside the domain can then be obtained by boundary integral formulas. The boundary integral formulations for macro-scale wave solutions within a forest subzone and open water will be introduced in this dissertation. The matching conditions along the interface between adjacent subzones and along the exterior boundary between each patch and open water will be presented as well.

Two types of small-amplitude waves are considered in this study. To model short waves (e.g. wind waves), periodic waves are first investigated. Focusing on simple-harmonic (monochromatic) incident waves, the theoretical model developed in Mei et al. (2014) is extended both analytically and numerically. As mentioned above, a forest subzone is considered as a homogeneous region, where a constant bulk value of eddy viscosity can be issued. Using the energy concept, the eddy viscosity is determined by equating the time-averaged dissipation rate and the averaged rate of work done by wave forces acting on cylinders within the certain subzone. The wave forces are modeled by the Morison-type formula, in which the inertia force does not contribute to the rate of work done when taking the wave-period average. Different from Mei et al. (2014), a new drag coefficient formula is introduced by using Hu et al. (2014)'s experimental work. To the best knowledge of the author, this shall be the first attempt to propose a drag coefficient formula based on direct laboratory measurements of wave forces on cylinder arrays in recent years. With the prescribed drag coefficient, the corresponding eddy viscosity can be obtained. A computing program is established based on the present approach for solving both micro-

and macro-scale problem numerically. Three different types of forest configurations are used to check the present model. An infinitely long forest belt with a finite width, where the semi-analytical solutions are also presented, is first used to study the wave decay within the vegetated area. The flume test in [Hu et al. \(2014\)](#) is adopted for the data-model comparisons. In addition to normal incidences, obliquely incident waves are included with discussions on the effects of incident angles. A single circular forest is then used as a special case to check the present model for a forest region with a finite area. The corresponding semi-analytical solutions are provided as a preliminary validation of the numerical model. A series of laboratory experiments conducted at the University of Cantabria is used to make a comparison with the numerical results. Another special forest, containing multiple circular patches in [Maza \(2015\)](#)'s experiments, is then tested. Other types of forest configurations, e.g. multiple subzones and non-circular patches, are also presented as a model demonstration.

To study the interactions between longer waves (e.g. storm surge, tsunami) and coastal vegetation, a transient wave with small amplitude is then considered. Starting with linearized shallow-water wave equations, the wave dispersion is assumed negligible. Fourier transform is employed such that the unknowns are solved in the frequency domain. Once the wave amplitude spectrum is obtained, the free surface elevation through the forest region and open water can be computed by the inverse Fourier transform. Only the incident wave with a soliton-like shape is considered in this study. Different from the previous case (short periodic waves), now we have so-called polychromatic incident waves. The constant bulk value of eddy viscosity for each subzone is

determined by modifying the empirical formula in [Mei et al. \(2011\)](#). Three different forest configurations, as used for testing short waves, are investigated. The forest belt studied in [Mei et al. \(2011\)](#) is first re-examined with new analytical solutions being provided. A homogeneous circular forest is then employed to check the numerical model. The corresponding semi-analytical solutions are also provided to validate the numerical results. Using the same facility, the experiments for a solitary wave propagating through the circular forest were conducted at the University of Cantabria as well. The comparisons between model results and experimental data are presented. The relationship between normalized damping height and nonlinearity of incident waves is discussed. For further investigation of the numerical model, the experiments on multiple circular patches in [Maza \(2015\)](#) are simulated. The effectiveness of a circular forest and multiple patches on damping the incident waves is compared. Different arrangements of cylinders and the related impacts on normalized damping height are also discussed.

In the first two parts, the capability of the linear model on predicting the dissipation of incoming waves has been presented. However, the limitation on the nonlinearity of incident waves has also been confirmed for both types of waves, i.e. periodic and transient waves. Accordingly, the last part of this dissertation starts taking the nonlinear effects into account without ignoring the convective terms in the momentum equations. Only shallow-water waves with weakly nonlinearity are considered. Assuming incident waves as simple harmonic, higher harmonic waves are anticipated to be generated within cylinder arrays and shall propagate to open water. Expressing the wave solution as a summation of different harmonic components, the micro- and macro-scale

equations for each mode are both derived. As a result, the cell problem equations become nonlinear while the macro-scale equations still remain linear with cell effects being reflected in the complex coefficients. A modified pressure correction method along with finite difference approach is employed for solving the nonlinear cell problem. The macro-scale wave dynamics is then obtained numerically. An iterative scheme is introduced to solve this coupled system. Using an infinitely long forest belt with a finite width as a special case to check the approach, the numerical results are compared with those obtained by the linear model. The reflection and transmission coefficients are compared by using the data reported in [Mei et al. \(2011\)](#). Unfortunately, it is not allowed to further check the wave profiles without available gauge measurements inside the model forest. Varying nonlinearity and the corresponding higher harmonic components are presented. The effects of different parameters on wave solutions are discussed. Future model improvement is also pointed out.

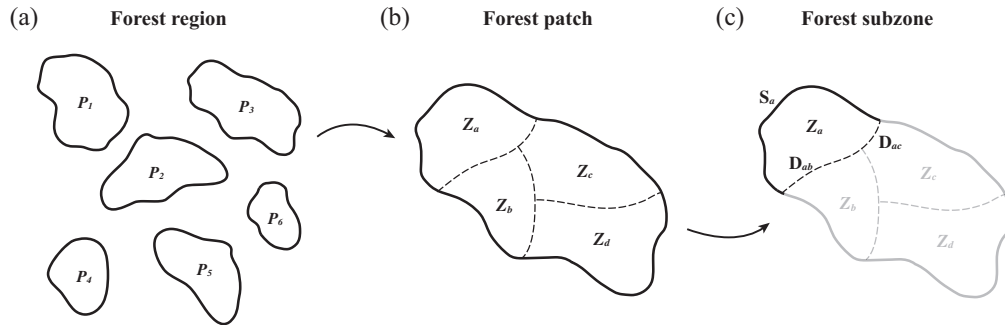


Figure 1.1: Sketch of a typical coastal forest configuration: (a) a forest region – consists of multiple patches with arbitrary shape; (b) one of the forest patches (e.g. Patch 3) – can be composed of several subzones; (c) one of the subzones (e.g. Subzone a) within Patch 3 – S denotes the boundary between the subzone and open water, while D shows the interface with adjacent subzone.

CHAPTER 2

THEORETICAL FORMULATION AND TEST CONDITIONS

In the following, we first show the Reynolds-averaged Navier-Stokes equations which will be used in this study. The corresponding boundary conditions are also specified. For long-wave cases, the depth-averaged equations are presented. The simplifications made in this dissertation are also described.

2.1 Governing equations and boundary conditions

■ RANS equations

Defining $\vec{x} = (x_1, x_2)$ and z as the horizontal and vertical Cartesian coordinates, respectively, with origin at the mean sea level, the three-dimensional flow motion is governed by the Reynolds-averaged Navier-Stokes equations:

$$\frac{\partial u_i}{\partial x_i} + \frac{\partial w}{\partial z} = 0, \quad i = 1, 2 \quad (2.1)$$

$$\frac{\partial u_i}{\partial t} + u_j \frac{\partial u_i}{\partial x_j} + w \frac{\partial u_i}{\partial z} = -\frac{1}{\rho} \frac{\partial p}{\partial x_i} + \nu_e \left(\frac{\partial^2 u_i}{\partial x_j \partial x_j} + \frac{\partial^2 u_i}{\partial z^2} \right), \quad i \& j = 1, 2 \quad (2.2)$$

and

$$\frac{\partial w}{\partial t} + u_j \frac{\partial w}{\partial x_j} + w \frac{\partial w}{\partial z} = -\frac{1}{\rho} \frac{\partial p}{\partial z} + \nu_e \left(\frac{\partial^2 w}{\partial x_j \partial x_j} + \frac{\partial^2 w}{\partial z^2} \right), \quad j = 1, 2 \quad (2.3)$$

in which the constant eddy viscosity model is used to describe the turbulence generated between vegetation. In the above equations, ρ is the density of water and p denotes the dynamic pressure, which is defined as

$$p = P + \rho g z, \quad P : \text{total pressure} \quad (2.4)$$

The horizontal velocities u_i and vertical velocity w are separated. The eddy viscosity ν_e is assumed as a bulk quantity, which remains constant over a certain homogeneous area.

Along the mean free surface, the kinematic boundary condition requires

$$\frac{\partial \eta}{\partial t} + u_i \frac{\partial \eta}{\partial x_i} = w \quad \text{at } z = 0 \quad (2.5)$$

while the dynamic boundary conditions in normal and tangential directions are respectively

$$g\eta - \frac{p}{\rho} + 2\nu_e \frac{\partial w}{\partial z} = 0 \quad \text{at } z = 0 \quad (2.6)$$

and

$$\frac{\partial u_i}{\partial z} + \frac{\partial w}{\partial x_i} = 0 \quad \text{at } z = 0 \quad (2.7)$$

in which η denotes the free surface displacement. In the above, the air is assumed to be stress-free and zero atmospheric (gage) pressure is used. In addition to the free surface conditions, the no-slip boundary condition along the sea bed states

$$u_i = w = 0 \quad \text{at } z = -h_0 \quad (2.8)$$

and also along the surface of cylinders (S_c):

$$u_i = w = 0 \quad \text{when } (\vec{x}, z) \in S_c \quad (2.9)$$

where h_0 denotes the constant water depth.

■ Depth-averaged equations

For long-wave condition, the water depth is assumed much smaller than the wavelength, i.e. $h_0/L < 0.05$. The vertical variation of flow fields and the vertical

velocity component w are assume relatively weak. Accordingly, the free surface elevation can be expressed as $z = \eta(\vec{x}, t)$. Defining the depth-averaged quantity as

$$\bar{f} = \left(\frac{1}{h_0 + \eta} \right) \int_{-h_0}^{\eta} f dz \quad (2.10)$$

, then the depth-averaged continuity equation can be derived as

$$\frac{\partial \eta}{\partial t} + \frac{\partial}{\partial x_i} [\bar{u}_i (h + \eta)] = 0, \quad i = 1, 2 \quad (2.11)$$

in which (2.5) and (2.8) are both applied. Similarly, the depth-averaged momentum equations can be deduced from (2.2):

$$\frac{\partial \bar{u}_i}{\partial t} + \bar{u}_j \frac{\partial \bar{u}_i}{\partial x_j} = -g \frac{\partial \eta}{\partial x_i} + \nu_e \frac{\partial^2 \bar{u}_i}{\partial x_j \partial x_j}, \quad i \& j = 1, 2 \quad (2.12)$$

where the hydrostatic pressure for the shallow-water condition has been used. The kinematic boundary conditions along the free surface (2.5) and along the sea bed (2.8) are both applied as well.

2.2 Conditions and simplifications

As we know, the size of coastal trees in fields can range from 10 to 100 cm while the typical wavelength of wind waves is around 10 – 100 m. Therefore, a strong contrast can be found between tree sizes and wavelength of wind waves, let alone longer waves, e.g. tsunamis and storm surges. Therefore, the flow motion around coastal trees can be considered as a micro-scale problem, being subject to a macro-scale forcing from incoming waves. With this condition, it is reasonable to apply the multi-scale perturbation technique and build up a model to study the macro-scale wave dynamics with consideration of the effects from micro-scale flow fields.

Before starting the analysis, we should point out several simplifications which need to be made in this dissertation. As we know, coastal vegetation could have branches, leaves, and roots. The complicated root system, especially of mangroves (Massel et al. 1999), may introduce different effects on the estimation of wave forces and the resulting wave evolutions. However, applying simplified conditions can help isolate each dynamic factor and understand the detailed physics, providing a preliminary study and model development. Thus, in this dissertation, coastal trees will be modeled by vertical, rigid and surface piercing cylinders, where the effects of branches and roots are neglected. A periodic arrangement of cylinder array is also required (e.g. Fig.3.1). A constant eddy viscosity model, as shown in Sec.2.1, is used to describe the turbulence generated between cylinders. For each homogeneous forest subzone, a constant bulk value of eddy viscosity can be issued.

In the following, with these simplifications, we first study small-amplitude waves through a heterogeneous coastal forest of arbitrary shape. Short periodic waves are used to model wind waves while transient waves are applied to study long waves-vegetation interactions. Afterwards, focusing on shallow-water waves through a forest belt as a special case, the nonlinear effects are included and harmonics generation within a vegetated water are discussed.

CHAPTER 3

SMALL-AMPLITUDE PERIODIC WAVES THROUGH COASTAL FORESTS

In this chapter, we first consider small-amplitude water waves propagating through a heterogeneous coastal forest of arbitrary shape. Due to the infinitesimal amplitude, the governing equations and boundary conditions are both linearized. Assuming a strong contrast between incident wavelength and cylinder spacing, the multi-scale perturbation theory of homogenization is applied to separate the micro-scale flow problem and the macro-scale wave dynamics. The complex coefficients in the derived macro-scale governing equations are computed from the solutions of micro-scale problem, in which the macro-scale pressure gradient are the driven force.

In order to handle the arbitrary shape of any forest patch, the boundary integral equation method is employed to establish a numerical model for solving the macro-scale wave dynamics. As described in Chap.1, each patch can be divided into subzones according to different properties, such as porosity, cylinder size, and planting pattern. Each subzone is then considered as a homogeneous forest region where a constant bulk eddy viscosity can be issued. The eddy viscosity is determined by equating the time-averaged dissipation rate and the averaged rate of work done by wave forces over the certain subzone. Wave forces are modeled by the Morison-type equation (Morison et al. 1950), in which the drag coefficient formula is constructed based on Hu et al. (2014)'s experimental data. A computing program is established based on the present approach.

To validate the numerical model, three different forest configurations with

existing laboratory experiments are investigated. An infinitely long forest belt with a finite width as adopted in [Hu et al. \(2014\)](#)'s experiment is first used to check the present approach. Instead of using the boundary integral equation method, the semi-analytical solutions are provided due to the infinite length. In addition to normally incident condition, obliquely incident waves are also included with a discussion on the effects of incident angles. A single circular forest is another special case where the corresponding semi-analytical solutions are also derived. The numerical results are shown to compare almost perfectly with the semi-analytical solutions, which provides a preliminary validation of the numerical model. A series of laboratory experiments was conducted at the University of Cantabria, which provides a comprehensive data-model comparison with different wave conditions. The numerical model is further applied to cases where the forest region is made of multiple circular patches. Experimental works in [Maza \(2015\)](#) is then used to check the numerical results. For both special forest configurations, the comparisons between model predictions and experimental data shows reasonable agreements. The effectiveness of different forest configurations on wave attenuation is discussed. Numerical results for other types of forest (e.g. multiple subzones, non-circular patches) are also presented for demonstration.

3.1 Governing equations and boundary conditions

Considering small-amplitude water waves propagating through a coastal forest in a constant water depth h_0 , the momentum equations in [\(2.2\)](#) and [\(2.3\)](#) are

linearized as:

$$\frac{\partial u_i}{\partial t} = -\frac{1}{\rho} \frac{\partial p}{\partial x_i} + \nu_e \left(\frac{\partial^2 u_i}{\partial x_j \partial x_j} + \frac{\partial^2 u_i}{\partial z^2} \right), \quad i \& j = 1, 2 \quad (3.1)$$

and

$$\frac{\partial w}{\partial t} = -\frac{1}{\rho} \frac{\partial p}{\partial z} + \nu_e \left(\frac{\partial^2 w}{\partial x_j \partial x_j} + \frac{\partial^2 w}{\partial z^2} \right), \quad j = 1, 2 \quad (3.2)$$

The kinematic free-surface boundary condition is also linearized as

$$\frac{\partial \eta}{\partial t} = w, \quad z = 0 \quad (3.3)$$

while the continuity equation (2.1) and other boundary conditions, (2.6) – (2.9), stay the same.

As stated above, the trees are idealized by rigid vertical cylinders with characteristic spacing ℓ . With the characteristic frequency ω and amplitude A_{inc} , the infinitesimal incident waves have the typical wavelength $1/k_{\text{inc}}$ where k_{inc} denotes the characteristic wavenumber. Based on the above scales, the following normalization can be introduced:

$$x_i^* = \frac{x_i}{\ell}, \quad z^* = k_{\text{inc}} z, \quad h^* = k_{\text{inc}} h_0, \quad t^* = t\omega, \quad \eta^* = \frac{\eta}{A_{\text{inc}}} \quad (3.4)$$

and

$$p^* = \frac{p}{\rho g A_{\text{inc}}}, \quad u_i^* = \frac{u_i}{\omega A_{\text{inc}}}, \quad w^* = \frac{w}{\omega A_{\text{inc}}} \quad (3.5)$$

in which the horizontal coordinates are scaled by the micro-length ℓ while the vertical coordinate by the macro-length $1/k_{\text{inc}}$. The water depth h_0 is assumed to be in the same order of magnitude as the typical wavelength $1/k_{\text{inc}}$, which is much greater than the tree spacing ℓ . Thus,

$$k_{\text{inc}} h_0 = \mathcal{O}(1) \quad (3.6)$$

and the small parameter ε is defined as

$$\varepsilon = k_{\text{inc}}\ell \equiv \omega^2\ell/g \ll O(1) \quad (3.7)$$

, representing the ratio of micro-to-macro length scales in which the wavenumber for waves of intermediate length are used, i.e. $k_{\text{inc}} \equiv \omega^2/g$. It is also noted that the free surface displacement η is scaled by the incident wave amplitude A_{inc} . The horizontal and vertical velocity components are normalized by ωA_{inc} . Based on the above scales, the normalized governing equations are carried out as

$$\frac{\partial u_i^*}{\partial x_i^*} + \varepsilon \frac{\partial w^*}{\partial z^*} = 0, \quad i = 1, 2 \quad (3.8)$$

$$\varepsilon \frac{\partial u_i^*}{\partial t^*} = -\frac{\partial p^*}{\partial x_i^*} + \sigma \varepsilon \left(\frac{\partial^2 u_i^*}{\partial x_j^* \partial x_j^*} + \varepsilon^2 \frac{\partial^2 u_i^*}{\partial z^* \partial z^*} \right), \quad i \& j = 1, 2 \quad (3.9)$$

and

$$\frac{\partial w^*}{\partial t^*} = -\frac{\partial p^*}{\partial z^*} + \sigma \left(\frac{\partial^2 w^*}{\partial x_j^* \partial x_j^*} + \varepsilon^2 \frac{\partial^2 w^*}{\partial z^* \partial z^*} \right), \quad j = 1, 2 \quad (3.10)$$

where the dimensionless eddy viscosity is defined as

$$\sigma = \frac{\nu_e}{\omega\ell^2} \quad (3.11)$$

We assume $\sigma \approx O(1)$ due to its importance and impact on the energy dissipation.

The kinematic boundary condition along the free surface is also normalized:

$$\frac{\partial \eta^*}{\partial t^*} = w^* \quad \text{at} \quad z^* = 0 \quad (3.12)$$

and the normalized dynamic boundary conditions are

$$\eta^* - p^* + 2\varepsilon^2 \sigma \frac{\partial w^*}{\partial z^*} = 0 \quad \text{at} \quad z^* = 0 \quad (3.13)$$

and

$$\varepsilon \frac{\partial u_i^*}{\partial z^*} + \frac{\partial w^*}{\partial x_i^*} = 0, \quad \text{at} \quad z^* = 0 \quad (3.14)$$

The normalized no-slip boundary conditions along seabed and cylinder surfaces become

$$u_i^* = w^* = 0 \quad \text{at} \quad z^* = -h^* \quad (3.15)$$

and

$$u_i^* = w^* = 0 \quad \text{when} \quad (\vec{x}^*, z^*) \in S_c \quad (3.16)$$

3.2 Homogenization method

Due to the sharply contrasting scales between tree spacing ℓ and typical wavelength $1/k_{\text{inc}}$, we introduce two horizontal coordinates to capture the flow motion surrounding cylinders as well as the wave dynamics over the entire forest area:

$$X_i^* \equiv \varepsilon x_i^* = k_{\text{inc}} x_i \quad (3.17)$$

in which the micro-scale x_i^* is used to describe the flow motion in the vicinity of cylinders while the macro-scale X_i^* is for the wave dynamics. Note that the vertical (i.e. water depth) direction only depends on the macro scale:

$$Z^* \equiv z^* = k_{\text{inc}} z \quad (3.18)$$

By using two-scale perturbation method, all the dimensionless variables can be expanded as

$$u_i^* = u_i^{*(0)} + \varepsilon u_i^{*(1)} + \varepsilon^2 u_i^{*(2)} + \dots, \quad w^* = w^{*(0)} + \varepsilon w^{*(1)} + \varepsilon^2 w^{*(2)} + \dots \quad (3.19)$$

and

$$\eta^* = \eta^{*(0)} + \varepsilon \eta^{*(1)} + \varepsilon^2 \eta^{*(2)} + \dots, \quad p^* = p^{*(0)} + \varepsilon p^{*(1)} + \varepsilon^2 p^{*(2)} + \dots \quad (3.20)$$

in which u_i^* , w^* , p^* and η^* are all functions of (x_i^*, X_i^*, Z^*, t^*) . From here on, only dimensionless variables are used with the asterisks $(\cdot)^*$ dropped for brevity. With (3.19) and (3.20), the governing equations and boundary conditions are separated by different orders as follows.

• $\boxed{\mathcal{O}(\varepsilon^0)}$:

$$\frac{\partial u_i^{(0)}}{\partial x_i} = 0, \quad i = 1, 2 \quad (3.21)$$

$$\frac{\partial p^{(0)}}{\partial x_i} = 0, \quad i = 1, 2 \quad (3.22)$$

and

$$\frac{\partial w^{(0)}}{\partial t} = -\frac{\partial p^{(0)}}{\partial Z} + \sigma \left(\frac{\partial^2 w^{(0)}}{\partial x_j \partial x_j} \right), \quad j = 1, 2 \quad (3.23)$$

with the kinematic boundary condition along the mean water level:

$$\frac{\partial \eta^{(0)}}{\partial t} = w^{(0)} \quad \text{at} \quad Z = 0 \quad (3.24)$$

and the dynamic boundary conditions in normal & tangential directions:

$$\eta^{(0)} = p^{(0)} \quad \& \quad \frac{\partial w^{(0)}}{\partial x_i} = 0 \quad \text{at} \quad Z = 0 \quad (3.25)$$

In (3.22), the leading-order pressure $p^{(0)}$ is shown to be independent of the micro-scale coordinates, i.e. $p^{(0)} = p^{(0)}(X_i, Z, t)$. The leading-order free surface elevation can then be obtained from the pressure field at the mean water level by (3.25):

$$\eta^{(0)} = p^{(0)}(X_i, Z = 0, t) \quad (3.26)$$

It is also shown in (3.25) that the leading-order vertical velocity at the mean water level is independent of the micro-scale coordinates, i.e. $w^{(0)}|_{Z=0} = w^{(0)}(X_i, Z = 0, t)$. On the other hand, $w^{(0)}$ beneath the mean water level can depend on the micro-scale coordinate, i.e. $w^{(0)}|_{Z<0} = w^{(0)}(x_i, X_i, Z, t)$.

• $O(\varepsilon^1)$:

$$\frac{\partial u_i^{(0)}}{\partial X_i} + \frac{\partial u_i^{(1)}}{\partial x_i} + \frac{\partial w^{(0)}}{\partial Z} = 0, \quad i = 1, 2 \quad (3.27)$$

$$\frac{\partial u_i^{(0)}}{\partial t} = -\frac{\partial p^{(0)}}{\partial X_i} - \frac{\partial p^{(1)}}{\partial x_i} + \sigma \left(\frac{\partial^2 \tilde{u}_i^{(0)}}{\partial x_j \partial x_j} \right), \quad i \& j = 1, 2 \quad (3.28)$$

and

$$\frac{\partial w^{(1)}}{\partial t} = -\frac{\partial p^{(1)}}{\partial Z} + 2\sigma \left(\frac{\partial^2 w^{(0)}}{\partial x_j \partial X_j} \right), \quad j = 1, 2 \quad (3.29)$$

with the kinematic boundary conditions along the mean water level:

$$\frac{\partial \eta^{(1)}}{\partial t} = w^{(1)} \quad \text{at} \quad Z = 0 \quad (3.30)$$

and the dynamic boundary conditions:

$$\eta^{(1)} = p^{(1)} \quad \& \quad \frac{\partial u_i^{(0)}}{\partial Z} + \frac{\partial w^{(0)}}{\partial X_i} + \frac{\partial w^{(1)}}{\partial x_i} = 0 \quad \text{at} \quad Z = 0 \quad (3.31)$$

For periodic waves, all the variables can be expressed as

$$F(x_i, X_i, Z, t) = \Re \left\{ \tilde{F}(x_i, X_i, Z) e^{-it} \right\} \quad (3.32)$$

where the time dependency is separated with \tilde{F} being the spatially-dependent variables and the operator $\Re \{ \cdot \}$ denoting that only the real part is considered.

3.2.1 Micro-scale (cell) problem

Focusing on the flow motion in a micro-scale cell with one or more cylinders inside, the leading-order velocity and the pressure fluctuation can be expressed in terms of the leading-order pressure gradient as follows,

$$\tilde{u}_i^{(0)} = -\tilde{K}_{ij}(\vec{x}) \frac{\partial \tilde{p}^{(0)}}{\partial X_j}, \quad \tilde{w}^{(0)} = -\tilde{W}(\vec{x}) \frac{\partial \tilde{p}^{(0)}}{\partial Z}, \quad \tilde{p}^{(1)} = -\tilde{A}_j(\vec{x}) \frac{\partial \tilde{p}^{(0)}}{\partial X_j}, \quad \vec{x} \in \Omega_f \quad (3.33)$$

where Ω_f represents the fluid part within a unit cell Ω . The governing equations for the cell problem can then be derived from the mass conservation of $O(1)$ and the momentum equations of $O(\varepsilon)$ as presented in (3.21), (3.28) and (3.29):

$$\frac{\partial \tilde{K}_{ij}}{\partial x_i} = 0, \quad -i\tilde{K}_{ij} = \delta_{ij} - \frac{\partial \tilde{A}_j}{\partial x_i} + \frac{\partial \tilde{\tau}_{ik}^{(j)}}{\partial x_k}, \quad \vec{x} \in \Omega_f \quad (3.34)$$

and

$$-i\tilde{W} = 1 + \sigma \frac{\partial^2 \tilde{W}}{\partial x_j \partial x_j}, \quad \vec{x} \in \Omega_f \quad (3.35)$$

in which the stress tensor is

$$\tilde{\tau}_{ik}^{(j)} = \sigma \left(\frac{\partial \tilde{K}_{ij}}{\partial x_k} + \frac{\partial \tilde{K}_{kj}}{\partial x_i} \right) \quad \text{with} \quad \sigma = \frac{\nu_e}{\omega \ell^2} \quad (3.36)$$

due to the forcing by the unit pressure gradient in the direction j . In (3.36), ν_e and σ respectively denote the dimensional and dimensionless eddy viscosity. Here we propose that each subzone of the forest region can be considered as a homogeneous area where a bulk eddy viscosity is assumed. Note that \tilde{K}_{ij} and \tilde{A}_j vary only horizontally.

Along the solid surface of cylinders, the no-slip boundary conditions yields

$$\tilde{K}_{ij} = \tilde{W} = 0 \quad \text{when} \quad (\vec{x}, Z) \in S_c \quad (3.37)$$

For unique solution, we also require

$$\langle \tilde{A}_j \rangle = 0 \quad (3.38)$$

where $\langle \cdot \rangle$ represents the cell-averaged quantity over the horizontal cross-section and is defined as

$$\langle f \rangle = \frac{1}{\Omega} \iint_{\Omega_f} f dx_1 dx_2 \quad (3.39)$$

In the above, Ω is the total cross-sectional area projected on the horizontal plane and Ω_f represents the area occupied by the fluid inside Ω . Note that \tilde{K}_{ij} , \tilde{A}_j and

\tilde{W} are all subject to cell-periodicity. The no-flux condition along the seabed is satisfied by requiring $\partial \tilde{p}^{(0)} / \partial Z = 0$.

Following Mei et al. (2014), we use the Galerkin finite element method to solve the micro-scale boundary-value problem. Fig.3.1 sketches two typical types of cylinder arrangements. The corresponding finite element discretization for cell problem is presented in Fig.3.2. An example of the velocity fields for these two types of cell configurations will be presented in Fig.3.10–3.12 and Fig.3.23–3.25. Similar flow patterns can be found in Mei et al. (2014). The cell problem solutions \tilde{K}_{ij} and \tilde{W} have been presented in Mei et al. (2014)'s Fig.2 and shall not be repeated here.

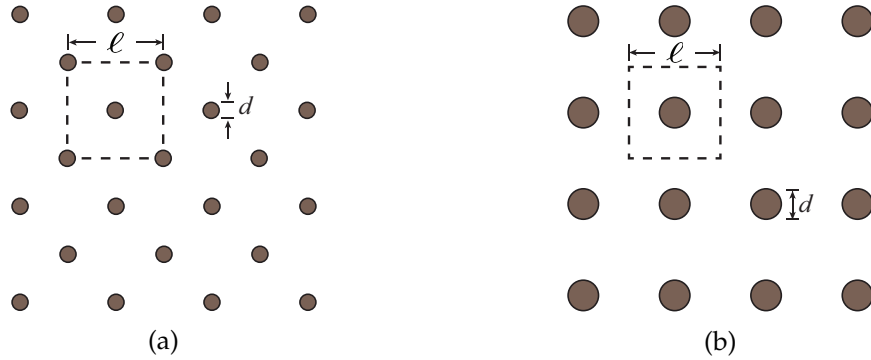


Figure 3.1: Cylinder arrangements in the experiments – (a) Hu et al. (2014): each circular cylinder has 1 cm in diameter ($d=1$ cm). Three array densities were adopted in their works, i.e. VD1: $\ell = 18$ cm, $n= 99.51$ %; VD2: $\ell=12$ cm, $n= 98.91$ %; and VD3: $\ell= 6$ cm, $n= 95.63$ %. (b) Circular forest experiment: each cylinder has 3 cm in diameter ($d=3$ cm) and the cell size $\ell = 9$ cm. The dashed square represents a unit cell Ω .

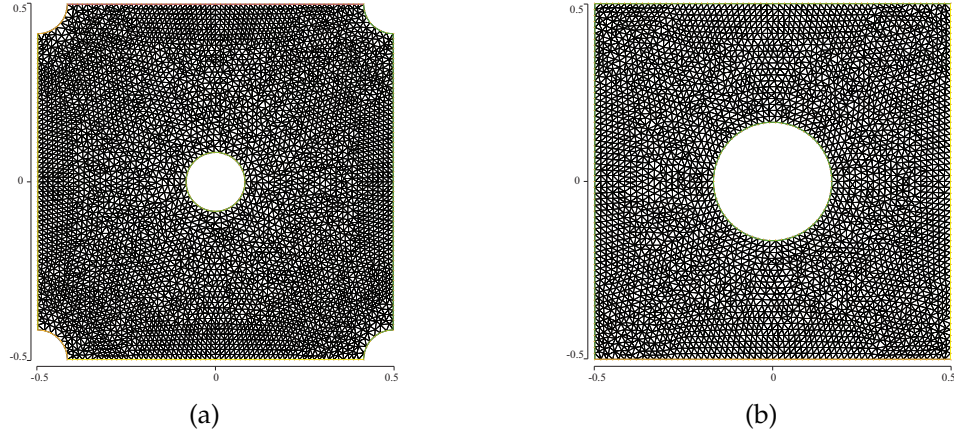


Figure 3.2: Finite element discretization corresponding to experiments by (a) [Hu et al. \(2014\)](#) with porosity $n=95.63\%$ and (b) circular forest experiments with porosity $n=91.27\%$.

3.2.2 Macro-scale (wavelength-scale) problem

With the cell problem solutions, now we turn to the macro-scale problem for wave dynamics. Taking cell average, as shown in (3.39), over the mass conservation of $\mathcal{O}(\varepsilon)$, then (3.27) becomes:

$$\frac{\partial \langle \tilde{u}_i^{(0)} \rangle}{\partial X_i} + \frac{\partial \langle \tilde{w}^{(0)} \rangle}{\partial Z} = 0, \quad i = 1, 2 \quad (3.40)$$

where the Gauss's theorem is applied along with the cell-periodicity and no-slip boundary conditions on the surface of cylinders. Defining a complex potential $\phi \equiv -i\tilde{p}^{(0)}$, the cell-averaged velocity components can be obtained from (3.28) and (3.23), i.e.

$$\langle \tilde{u}_i^{(0)} \rangle = n \frac{\partial \phi}{\partial X_i} + M_{ik} \frac{\partial \phi}{\partial X_k} \quad \text{and} \quad \langle \tilde{w}^{(0)} \rangle = (n + N) \frac{\partial \phi}{\partial Z} \quad (3.41)$$

where the porosity n is defined as

$$n = \frac{\Omega_f}{\Omega} \quad (3.42)$$

while the complex coefficients M_{ik} and N are determined from the cell problem solutions:

$$M_{ik} = \frac{1}{\Omega} \oint_{S_c} \left[-\tilde{A}_k \delta_{ij} + \sigma \left(\frac{\partial \tilde{K}_{ik}}{\partial x_j} + \frac{\partial \tilde{K}_{jk}}{\partial x_i} \right) \right] n_j^{S_c} ds, \quad N = \frac{1}{\Omega} \sigma \oint_{S_c} \left(\frac{\partial \tilde{W}}{\partial x_j} n_j^{S_c} \right) ds \quad (3.43)$$

in which $n_j^{S_c}$ denotes the unit normal vector to the cylinder surface S_c . Combining (3.41) with (3.40), the leading-order cell-averaged governing equation for the macro-scale problem is derived:

$$\frac{\partial}{\partial X_i} \left[n \frac{\partial \phi}{\partial X_i} + M_{ik} \frac{\partial \phi}{\partial X_k} \right] + (n + N) \frac{\partial^2 \phi}{\partial Z^2} = 0, \quad i \& k = 1, 2 \quad (3.44)$$

where the relationships between macro-scale and micro-scale coefficients can also be derived as

$$M_{ik} = -n \delta_{ik} - i \langle \tilde{K}_{ik} \rangle, \quad N = -n - i \langle \tilde{W} \rangle \quad (3.45)$$

When the cell geometry is symmetric, the cell problem is isotropic and homogeneous. The cell-averaged hydraulic conductivity can then be expressed as $\langle \tilde{K}_{ik} \rangle = \mathcal{K} \delta_{ik}$. According to the cell problem solutions (Mei et al. 2014), it has been shown that $\langle \tilde{K}_{11} \rangle = \langle \tilde{K}_{22} \rangle \equiv \mathcal{K}$ such that $M_{11} = M_{22} \equiv M$. On the other hand, $\langle \tilde{K}_{12} \rangle = \langle \tilde{K}_{21} \rangle \approx 0$ results in $M_{12} = M_{21} \approx 0$. As stated previously, the eddy viscosity σ is assumed as a constant bulk value within a homogeneous subzone such that the cell properties, i.e. $\langle \tilde{K}_{ij} \rangle$, $\langle \tilde{A}_j \rangle$ and $\langle \tilde{W} \rangle$, along with the complex coefficients M and N also remain constant over a specific subzone. This is different from Mei et al. (2014), who treated the cell properties as functions of the macro-scale coordinates. This simplification has been justified by making a comparison between two schemes, which will be given in Sec.3.7. Therefore, the cell-averaged equation (3.44) for any subzone can be rewritten as

$$(n + M) \frac{\partial^2 \phi}{\partial X_i \partial X_i} + (n + N) \frac{\partial^2 \phi}{\partial Z^2} = 0, \quad i = 1, 2 \quad (3.46)$$

The cell-averaged kinematic boundary condition along the free surface can be derived from (3.24):

$$\langle \tilde{w}^{(0)} \rangle = -in\tilde{\eta}^{(0)} = -in\tilde{p}^{(0)} \quad \text{at } Z = 0 \quad (3.47)$$

which can also be expressed in terms of complex potential ϕ :

$$n\phi - (n + N)\frac{\partial\phi}{\partial Z} = 0 \quad \text{at } Z = 0 \quad (3.48)$$

in which $\langle \tilde{w}^{(0)} \rangle$ in (3.41) is used. The dynamic boundary condition as stated in (3.26) gives

$$\tilde{\eta}^{(0)} = \tilde{p}^{(0)}(X_i, Z = 0) \equiv i\phi(X_i, Z = 0) \quad (3.49)$$

Along the sea bed, the no-slip boundary requires

$$\langle \tilde{w}^{(0)} \rangle = \frac{\partial\phi}{\partial z} = 0 \quad \text{at } Z = -h \quad (3.50)$$

In open water, the complex coefficients vanish (i.e. $M = N = 0$) and the porosity $n = 1$. Then (3.46) reduces to the Laplace's equation governing the complex potential as

$$\frac{\partial^2\phi}{\partial X_i\partial X_i} + \frac{\partial^2\phi}{\partial Z^2} = 0, \quad i = 1, 2 \quad (3.51)$$

with the boundary conditions along the free surface:

$$\phi - \frac{\partial\phi}{\partial Z} = 0, \quad \tilde{\eta}^{(0)} = i\phi(X_i, Z = 0) \quad \text{at } Z = 0 \quad (3.52)$$

and along the sea bed:

$$\frac{\partial\phi}{\partial Z} = 0 \quad \text{at } Z = -h \quad (3.53)$$

3.3 Boundary integral equation method

To deal with the arbitrary shape of a forest area, we employ the boundary integral equation method to solve the macro-scale problem numerically. In the following, the integral formulation for a forest subzone (e.g. Fig.1.1c) and for the open water region are introduced, respectively. The matching conditions along the interfaces between adjacent subzones and along the boundary between forest and open water are presented as well.

3.3.1 Integral formulation for a forest subzone

First, we consider any forest subzone ξ with an arbitrary shape, e.g. Fig.1.1c. We note that a subzone could be surrounded by other subzones and/or the open water region. As shown in (3.46), the governing equation for the complex potential ϕ_ξ has

$$\frac{\partial^2 \phi_\xi}{\partial X_1 \partial X_1} + \frac{\partial^2 \phi_\xi}{\partial X_2 \partial X_2} + \left[\frac{n_\xi + N_\xi}{n_\xi + M_\xi} \right] \frac{\partial^2 \phi_\xi}{\partial Z^2} = 0 \quad (3.54)$$

in which the complex coefficients M_ξ and N_ξ are obtained for each subzone ξ respectively. Due to the arbitrary shape of subzone ξ , the solution to (3.54) can be expressed as

$$\phi_\xi = \sum_{q=0}^{\infty} \mathcal{A}_{\xi_q}(\vec{X}_i) \frac{\cosh \hat{k}_{\xi_q}(Z + h)}{\cosh \hat{k}_{\xi_q} h} \quad (3.55)$$

which separates the horizontal variables from the vertical variable with the corresponding wavenumber \hat{k}_{ξ_q} being the complex roots of the dispersion relationship:

$$1 = \left(\frac{n_\xi + N_\xi}{n_\xi} \right) \hat{k}_{\xi_q} \tanh \hat{k}_{\xi_q} h \quad (3.56)$$

The horizontal function \mathcal{A}_{ξ_q} in (3.55) satisfies the two-dimensional Helmholtz equation:

$$\left(\frac{\partial^2 \mathcal{A}_{\xi_q}}{\partial X_1 \partial X_1} + \frac{\partial^2 \mathcal{A}_{\xi_q}}{\partial X_2 \partial X_2} \right) + (\gamma_\xi \hat{k}_{\xi_q})^2 \mathcal{A}_{\xi_q} = 0 \quad \text{with} \quad \gamma_\xi = \left(\frac{n_\xi + N_\xi}{n_\xi + M_\xi} \right)^{1/2} \quad (3.57)$$

which can be converted into the following integral equation (Liggett and Liu 1983):

$$\mathcal{A}_{\xi_q}(\vec{X}_i) = \frac{-i\pi}{2\alpha} \int_{S_\xi + D_{\xi\psi}} \left\{ \mathcal{A}_{\xi_q}(\vec{X}_j) \frac{\partial [H_0^{(1)}(\gamma_\xi \hat{k}_{\xi_q} r)]}{\partial \hat{n}_\xi} - H_0^{(1)}(\gamma_\xi \hat{k}_{\xi_q} r) \frac{\partial \mathcal{A}_{\xi_q}(\vec{X}_j)}{\partial \hat{n}_\xi} \right\} dS \quad (3.58)$$

The boundary of subzone ξ can include the boundary S_ξ to open water and/or the interfaces $D_{\xi\psi}$ with adjacent subzones ψ . In the integral equation, \vec{X}_i denotes the coordinate of a point located on the boundary of subzone ξ (i.e. $\vec{X}_i \in S_\xi$ or $D_{\xi\psi}$) where its interior angle α (Fig.3.3) has to be taken into account. \vec{X}_j denotes another boundary point of the subzone with $r = |\vec{X}_i - \vec{X}_j|$ giving the distance between these two boundary points. $H_0^{(1)}$ denotes the Hankel function of the first kind and \hat{n}_ξ represents the outward normal direction to the boundary of subzone ξ . Therefore, the integral equation (3.58) can be used to solve unknown \mathcal{A}_{ξ_q} and its normal derivative along the boundary. Once the solutions along the forest boundary are obtained, the wave solutions inside the forest subzone can be found by assigning \vec{X}_i as an interior point with its interior angle = 2π :

$$\mathcal{A}_{\xi_q}(\vec{X}_i) = \frac{-i}{4} \int_{S_\xi + D_{\xi\psi}} \left\{ \mathcal{A}_{\xi_q}(\vec{X}_j) \frac{\partial [H_0^{(1)}(\gamma_\xi \hat{k}_{\xi_q} r)]}{\partial \hat{n}_\xi} - H_0^{(1)}(\gamma_\xi \hat{k}_{\xi_q} r) \frac{\partial \mathcal{A}_{\xi_q}(\vec{X}_j)}{\partial \hat{n}_\xi} \right\} dS \quad (3.59)$$

in which the point \vec{X}_i is an interior point in subzone ξ while \vec{X}_j are on the boundary of subzone ξ .

3.3.2 Integral formulation for open water

In the open water region (with subscript S), the equation governing the complex potential ϕ_S is shown in (3.51):

$$\frac{\partial^2 \phi_S}{\partial X_1 \partial X_1} + \frac{\partial^2 \phi_S}{\partial X_2 \partial X_2} + \frac{\partial^2 \phi_S}{\partial Z^2} = 0 \quad (3.60)$$

and its solution, including both incident and scattered waves, can be expressed as

$$\phi_S = A_0 \frac{\cosh k_0(Z+h)}{\cosh k_0 h} e^{ik_0 X_{1i}} + \sum_{p=0}^{\infty} \mathcal{B}_p(\vec{X}_i) \frac{\cosh k_p(Z+h)}{\cosh k_p h} \quad (3.61)$$

where $A_0 = -i$ and k_p satisfies the dispersion relationship:

$$1 = k_p \tanh k_p h \quad (3.62)$$

with one real root k_0 and infinite number of imaginary roots $k_p = ik_p$ (when $p \geq 1$). Assuming the incident waves in X_1 direction, X_{1i} in (3.61) denotes the X_1 coordinate of point i . The corresponding Helmholtz equation for \mathcal{B}_p is

$$\left(\frac{\partial^2 \mathcal{B}_p}{\partial X_1 \partial X_1} + \frac{\partial^2 \mathcal{B}_p}{\partial X_2 \partial X_2} \right) + k_p^2 \mathcal{B}_p = 0 \quad (3.63)$$

which can also be converted into the following integral equation:

$$\mathcal{B}_p(\vec{X}_i) = \frac{-i\pi}{2(2\pi - \alpha)} \int_{\mathbf{S}} \left\{ \mathcal{B}_p(\vec{X}_j) \frac{\partial [H_0^{(1)}(k_p r)]}{\partial \hat{n}_S} - H_0^{(1)}(k_p r) \frac{\partial \mathcal{B}_p(\vec{X}_j)}{\partial \hat{n}_S} \right\} dS \quad (3.64)$$

where \vec{X}_i and \vec{X}_j are both on the boundary between open water and all the forest patches and \mathbf{S} in (3.64) represents the combination of the boundaries of all the forest patches, i.e. the boundary between open water and forest region. Likewise, once \mathcal{B}_p along the boundary of all the forest patches is found, the wave solutions can be obtained from (3.61) with (3.64) being modified as

$$\mathcal{B}_p(\vec{X}_i) = \frac{-i}{4} \int_{\mathbf{S}} \left\{ \mathcal{B}_p(\vec{X}_j) \frac{\partial [H_0^{(1)}(k_p r)]}{\partial \hat{n}_S} - H_0^{(1)}(k_p r) \frac{\partial \mathcal{B}_p(\vec{X}_j)}{\partial \hat{n}_S} \right\} dS \quad (3.65)$$

in which \vec{X}_i is assigned at any location within the open water region (i.e. an interior point of an unbounded area) while \vec{X}_j are on the boundary between open water and forest region. Note again that the outward normal directions of the boundary with respect to the forest region and open water are opposite. The detailed derivations of Helmholtz equations and integral formulation for both forest region and open water can be found in Appendix [A.1](#) and [A.2](#).

3.3.3 Matching conditions along the boundaries

The wave solutions along the boundaries between two subzones and those between subzones and the open water region can be found from (3.58) and (3.64) if matching conditions along the boundaries are prescribed. As noted, a forest subzone can have its boundary in contact with open water and/or adjacent subzones. Hereafter the former will be referred as the exterior boundary of a forest subzone while the latter as the interface with other zones. In both situations, the continuity of pressure and normal mass fluxes are imposed.

3.3.3.1 Boundary between a forest subzone and open water

We first consider the exterior boundary. The pressure continuity provides

$$\phi_\xi = \phi_S, \quad -h < Z < 0 \quad (3.66)$$

i.e.

$$\sum_{q=0}^{\infty} \mathcal{A}_{\xi_q} \frac{\cosh \hat{k}_{\xi_q}(Z+h)}{\cosh \hat{k}_{\xi_q} h} = A_0 \frac{\cosh k_0(Z+h)}{\cosh k_0 h} e^{ik_0 X_{1i}} + \sum_{p=0}^{\infty} \mathcal{B}_p \frac{\cosh k_p(Z+h)}{\cosh k_p h} \quad (3.67)$$

The normal fluxes must also be continuous along the forest boundary:

$$(n_\xi + M_\xi) \frac{\partial \phi_\xi}{\partial \hat{n}_\xi} = \frac{\partial \phi_S}{\partial \hat{n}_\xi}, \quad -h < Z < 0 \quad (3.68)$$

i.e.

$$\begin{aligned} (n_\xi + M_\xi) \sum_{q=0}^{\infty} \frac{\partial \mathcal{A}_{\xi q}}{\partial \hat{n}_\xi} \frac{\cosh \hat{k}_{\xi q}(Z+h)}{\cosh \hat{k}_{\xi q} h} \\ = A_0 \frac{\cosh k_0(Z+h)}{\cosh k_0 h} \frac{\partial e^{ik_0 X_{1i}}}{\partial \hat{n}_\xi} + \sum_{p=0}^{\infty} \frac{\partial \mathcal{B}_p}{\partial \hat{n}_\xi} \frac{\cosh k_p(Z+h)}{\cosh k_p h} \end{aligned} \quad (3.69)$$

where (3.55) and (3.61) have been used. It is known that the orthogonality condition applies to both k_p and \hat{k}_q ($p, q \geq 0$):

$$\int_{-h}^0 \cosh k_m(Z+h) \cosh k_n(Z+h) dZ = \begin{cases} 0 & , m \neq n \\ \frac{h}{2} \left(1 + \frac{\sinh 2k_m h}{2k_m h} \right) & , m = n \end{cases} \quad (3.70)$$

Applying the above orthogonality of hyperbolic cosine function to (3.67) and (3.69) yields

$$\mathcal{A}_{\xi q} \frac{\Pi(\hat{k}_{\xi q})}{\cosh \hat{k}_{\xi q} h} = A_0 \frac{\Gamma_{0\xi q}}{\cosh k_0 h} e^{ik_0 X_{1i}} + \sum_{p=0}^{\infty} \mathcal{B}_p \frac{\Gamma_{p\xi q}}{\cosh k_p h} \quad (3.71)$$

and

$$(n_\xi + M_\xi) \sum_{q=0}^{\infty} \frac{\partial \mathcal{A}_{\xi q}}{\partial \hat{n}_\xi} \frac{\Gamma_{\xi q p}}{\cosh \hat{k}_{\xi q} h} = A_0 \delta_{0p} \frac{\Pi(k_0)}{\cosh k_0 h} \frac{\partial e^{ik_0 X_{1i}}}{\partial \hat{n}_\xi} + \frac{\partial \mathcal{B}_p}{\partial \hat{n}_\xi} \frac{\Pi(k_p)}{\cosh k_p h} \quad (3.72)$$

in which δ_{0p} denotes the Kronecker delta with nonzero value only when $p = 0$ (i.e. $\delta_{0p} = 1$ when $p = 0$), while $\Pi(\hat{k}_{\xi q})$ and $\Gamma_{p\xi q}$ are defined as

$$\Pi(\mathbf{k}) = \frac{h}{2} \left(1 + \frac{\sinh 2\mathbf{k}h}{2\mathbf{k}h} \right) \quad \text{where } \mathbf{k} = \hat{k}_{\xi q}, k_p \quad (3.73)$$

and

$$\Gamma_{p\xi q} = \frac{k_p \sinh(k_p h) \cosh(\hat{k}_{\xi q} h) - \hat{k}_{\xi q} \cosh(k_p h) \sinh(\hat{k}_{\xi q} h)}{k_p^2 - \hat{k}_{\xi q}^2} \quad (3.74)$$

3.3.3.2 Interface between forest subzones

Likewise, along the interface between two subzones (i.e. $D_{\xi\psi}$ with ξ and ψ denoting two adjacent zones), the pressure continuity yields

$$\phi_\xi = \phi_\psi, \quad -h < Z < 0 \quad (3.75)$$

Substituting (3.55) into the above condition gives

$$\sum_{q=0}^{\infty} \mathcal{A}_{\xi_q}(\vec{X}_i) \frac{\cosh \hat{k}_{\xi_q}(Z+h)}{\cosh \hat{k}_{\xi_q}h} = \sum_{r=0}^{\infty} \mathcal{A}_{\psi_r}(\vec{X}_i) \frac{\cosh \hat{k}_{\psi_r}(Z+h)}{\cosh \hat{k}_{\psi_r}h} \quad (3.76)$$

Also, the continuity of normal fluxes is required:

$$(n_\xi + M_\xi) \frac{\partial \phi_\xi}{\partial \hat{n}_\xi} = -(n_\psi + M_\psi) \frac{\partial \phi_\psi}{\partial \hat{n}_\psi}, \quad -h < Z < 0 \quad (3.77)$$

i.e.

$$(n_\xi + M_\xi) \sum_{q=0}^{\infty} \frac{\partial \mathcal{A}_{\xi_q}}{\partial \hat{n}_\xi} \frac{\cosh \hat{k}_{\xi_q}(Z+h)}{\cosh \hat{k}_{\xi_q}h} = -(n_\psi + M_\psi) \sum_{r=0}^{\infty} \frac{\partial \mathcal{A}_{\psi_r}}{\partial \hat{n}_\psi} \frac{\cosh \hat{k}_{\psi_r}(Z+h)}{\cosh \hat{k}_{\psi_r}h} \quad (3.78)$$

Again, applying the orthogonality of $\cosh(\cdot)$ in (3.70) to (3.76) and (3.78) yields

$$\mathcal{A}_{\xi_q} \frac{\Pi(\hat{k}_{\xi_q})}{\cosh \hat{k}_{\xi_q}h} = \sum_{r=0}^{\infty} \mathcal{A}_{\psi_r} \frac{\Gamma_{\psi_r \xi_q}}{\cosh \hat{k}_{\psi_r}h} \quad (3.79)$$

and

$$(n_\xi + M_\xi) \sum_{q=0}^{\infty} \frac{\partial \mathcal{A}_{\xi_q}}{\partial \hat{n}_\xi} \frac{\Gamma_{\xi_q \psi_r}}{\cosh \hat{k}_{\xi_q}h} = -(n_\psi + M_\psi) \frac{\partial \mathcal{A}_{\psi_r}}{\partial \hat{n}_\psi} \frac{\Pi(\hat{k}_{\psi_r})}{\cosh \hat{k}_{\psi_r}h} \quad (3.80)$$

Equations (3.71), (3.72) along with (3.79), (3.80) are to be used for solving unknown \mathcal{A}_{ξ_q} , \mathcal{A}_{ψ_r} and \mathcal{B}_p as well as their normal derivatives on the exterior boundary of each forest patch and the interfaces between subzones.

3.3.4 Numerical implementation

In numerical computations, the boundary of a forest subzone ξ is discretized into elements. Assuming uniform-distributed solution along each element of

length ΔS with \vec{X}_j denoting its middle point, we express (3.58) in the discrete form as:

$$\mathcal{A}_{\xi_q}(\vec{X}_i) = \frac{-i\pi}{2\alpha} \sum_{j=1}^{\mathbb{N}_\xi} \left\{ \mathcal{A}_{\xi_q}(\vec{X}_j) \frac{\partial [H_0^{(1)}(\gamma_\xi \hat{k}_{\xi_q} r)]}{\partial \hat{n}_\xi} - H_0^{(1)}(\gamma_\xi \hat{k}_{\xi_q} r) \frac{\partial \mathcal{A}_{\xi_q}(\vec{X}_j)}{\partial \hat{n}_\xi} \right\} \Delta S \quad (3.81)$$

in which \mathbb{N}_ξ denotes the total number of elements along the boundary of subzone ξ , which can include its exterior boundary (S_ξ) to open water and/or interfaces ($D_{\xi\psi}$) with other subzones. Equation (3.81) can be written by index notation as:

$$\left(\mathcal{A}_{\xi_q}\right)_i + \left(\bar{\mathcal{C}}_{\xi_q}\right)_{ij} \left(\mathcal{A}_{\xi_q}\right)_j = \left(\bar{\mathcal{D}}_{\xi_q}\right)_{ij} \left(\frac{\partial \mathcal{A}_{\xi_q}}{\partial \hat{n}_\xi}\right)_j \quad \text{with } i \ \& \ j = 1 \cdots \mathbb{N}_\xi \quad (3.82)$$

where

$$\left(\bar{\mathcal{C}}_{\xi_q}\right)_{ij} = \frac{i\pi}{2\alpha} \left[(-\gamma_\xi \hat{k}_{\xi_q}) H_1^{(1)}(\gamma_\xi \hat{k}_{\xi_q} r_{ij}) \right] \frac{\partial r_{ij}}{\partial \hat{n}_\xi} \Delta S, \quad \left(\bar{\mathcal{D}}_{\xi_q}\right)_{ij} = \frac{i\pi}{2\alpha} H_0^{(1)}(\gamma_\xi \hat{k}_{\xi_q} r_{ij}) \Delta S \quad (3.83)$$

We can also rearrange (3.82) and express the unknown \mathcal{A}_{ξ_q} at the boundary point \vec{X}_i in terms of the normal derivatives of \mathcal{A}_{ξ_q} along the entire boundary of the subzone ξ :

$$\left(\mathcal{A}_{\xi_q}\right)_i = \left(\bar{\mathcal{G}}_{\xi_q}\right)_{ij} \left(\frac{\partial \mathcal{A}_{\xi_q}}{\partial \hat{n}_\xi}\right)_j \quad \text{with } i \ \& \ j = 1 \cdots \mathbb{N}_\xi \quad (3.84)$$

in which the coefficient matrix is obtained by $\left[\bar{\mathcal{G}}_{\xi_q}\right] = \left[\mathcal{I} + \bar{\mathcal{C}}_{\xi_q}\right]^{-1} \left[\bar{\mathcal{D}}_{\xi_q}\right]$ with \mathcal{I} being the identity matrix.

For open water, on the other hand, (3.64) in the discrete form is

$$\mathcal{B}_p(\vec{X}_i) = \frac{-i\pi}{2(2\pi - \alpha)} \sum_{j=1}^{\mathbb{N}_S} \left\{ \mathcal{B}_p(\vec{X}_j) \frac{\partial [H_0^{(1)}(k_p r)]}{\partial \hat{n}_S} - H_0^{(1)}(k_p r) \frac{\partial \mathcal{B}_p(\vec{X}_j)}{\partial \hat{n}_S} \right\} \Delta S \quad (3.85)$$

where \mathbb{N}_S gives the total number of elements along the boundary that separates all the forest patches from the open water region, i.e. the exterior boundaries of

all the forest subzones ($\mathbf{S} = \sum S_\xi$). Again, we rearrange the above equation and express it by index notation:

$$(\mathcal{B}_p)_i + (\bar{\mathcal{E}}_p)_{ij} (\mathcal{B}_p)_j = (\bar{\mathcal{F}}_p)_{ij} \left(\frac{\partial \mathcal{B}_p}{\partial \hat{n}_S} \right)_j \quad \text{with } i \& j = 1 \cdots \mathbb{N}_S \quad (3.86)$$

where

$$(\bar{\mathcal{E}}_p)_{ij} = \frac{i\pi}{2(2\pi - \alpha)} \left[-k_p H_1^{(1)}(k_p r_{ij}) \right] \frac{\partial r_{ij}}{\partial \hat{n}_S} \Delta S, \quad (\bar{\mathcal{F}}_p)_{ij} = \frac{i\pi}{2(2\pi - \alpha)} H_0^{(1)}(k_p r_{ij}) \Delta S \quad (3.87)$$

We can also express the unknown function \mathcal{B}_p in terms of its normal derivative along the boundaries:

$$(\mathcal{B}_p)_i = (\bar{\mathcal{Q}}_p)_{ij} \left(\frac{\partial \mathcal{B}_p}{\partial \hat{n}_S} \right)_j \quad \text{with } i \& j = 1 \cdots \mathbb{N}_S \quad (3.88)$$

where $[\bar{\mathcal{Q}}_p] = [\mathcal{I} + \bar{\mathcal{E}}_p]^{-1} [\bar{\mathcal{F}}_p]$ denotes the coefficient matrix.

To solve the unknown functions \mathcal{A}_{ξ_q} and \mathcal{B}_p and their normal derivatives, the matching conditions introduced in Sec.3.3.3 must be applied. As specified in (3.71) and (3.72), along the exterior boundary of a forest subzone in contact with open water (i.e. $\vec{X}_i \in S_\xi$), the continuity of pressure and normal fluxes yields

$$\frac{\Pi(\hat{k}_{\xi_q})}{\cosh \hat{k}_{\xi_q} h} (\bar{\mathcal{G}}_{\xi_q})_{ij} \left(\frac{\partial \mathcal{A}_{\xi_q}}{\partial \hat{n}_\xi} \right)_j = A_0 \frac{\Gamma_{0\xi_q}}{\cosh k_0 h} (e^{ik_0 X_1})_i + \sum_{p=0}^{\infty} \frac{\Gamma_{p\xi_q}}{\cosh k_p h} (\bar{\mathcal{Q}}_p)_{im} \left(\frac{\partial \mathcal{B}_p}{\partial \hat{n}_S} \right)_m \quad (3.89)$$

in which the substitution of (3.84) and (3.88) has been made, and

$$(n_\xi + M_\xi) \sum_{q=0}^{\infty} \frac{\Gamma_{\xi_q p}}{\cosh \hat{k}_{\xi_q} h} \left(\frac{\partial \mathcal{A}_{\xi_q}}{\partial \hat{n}_\xi} \right)_i = A_0 \delta_{0p} \frac{\Pi(k_0)}{\cosh k_0 h} \left(\frac{\partial e^{ik_0 X_1}}{\partial \hat{n}_\xi} \right)_i + \frac{\Pi(k_p)}{\cosh k_p h} \left(\frac{\partial \mathcal{B}_p}{\partial \hat{n}_\xi} \right)_i \quad (3.90)$$

In (3.89) and (3.90), ξ can be any subzones that are exposed to the open water region. Accordingly, \vec{X}_i is on the exterior boundary of subzone ξ . In (3.89), \vec{X}_j ($j = 1 \cdots \mathbb{N}_\xi$) denotes the boundary points of subzone ξ while \vec{X}_m ($m = 1 \cdots \mathbb{N}_S$)

are on the boundary of open water (i.e. \mathbf{S}), which includes the boundaries of all the forest patches. We should note that the outward normal direction along the boundary from the forest region is opposite to that from open water, i.e. $\hat{n}_\xi = -\hat{n}_\mathbf{S}$.

On the other hand, when \vec{X}_i is along the interface between two subzones (i.e. $\vec{X}_i \in D_{\xi\psi}$), combining (3.84) with (3.79) and (3.80) provides

$$\frac{\Pi(\hat{k}_{\xi q})}{\cosh \hat{k}_{\xi q} h} (\bar{\mathcal{G}}_{\xi q})_{ij} \left(\frac{\partial \mathcal{A}_{\xi q}}{\partial \hat{n}_\xi} \right)_j = \sum_{r=0}^{\infty} \frac{\Gamma_{\psi_r \xi q}}{\cosh \hat{k}_{\psi_r} h} (\bar{\mathcal{G}}_{\psi_r})_{ik} \left(\frac{\partial \mathcal{A}_{\psi_r}}{\partial \hat{n}_\psi} \right)_k \quad (3.91)$$

and

$$(n_\xi + M_\xi) \sum_{q=0}^{\infty} \frac{\Gamma_{\xi q \psi_r}}{\cosh \hat{k}_{\xi q} h} \left(\frac{\partial \mathcal{A}_{\xi q}}{\partial \hat{n}_\xi} \right)_i = - (n_\psi + M_\psi) \frac{\Pi(\hat{k}_{\psi_r})}{\cosh \hat{k}_{\psi_r} h} \left(\frac{\partial \mathcal{A}_{\psi_r}}{\partial \hat{n}_\psi} \right)_i \quad (3.92)$$

in which \vec{X}_j ($j = 1 \cdots N_\xi$) and \vec{X}_k ($k = 1 \cdots N_\psi$) represent the boundary points of subzones ξ and ψ , respectively. Likewise, the outward normal directions along the interface with respect to these two adjacent subzones (ξ and ψ) are opposite, i.e. $\hat{n}_\xi = -\hat{n}_\psi$.

Equations (3.89), (3.90), (3.91) and (3.92) formulate a system of equations for solving the unknown $\mathcal{A}_{\xi q}$, \mathcal{A}_{ψ_r} and \mathcal{B}_p as well as their normal derivatives along all the exterior boundaries and interfaces between subzones simultaneously. The wave solutions within each subzone and open water can then be obtained by (3.55), (3.59), (3.61) and (3.65). It may be noted that the infinite p , q and r have to be truncated to finite numbers based on convergence tests.

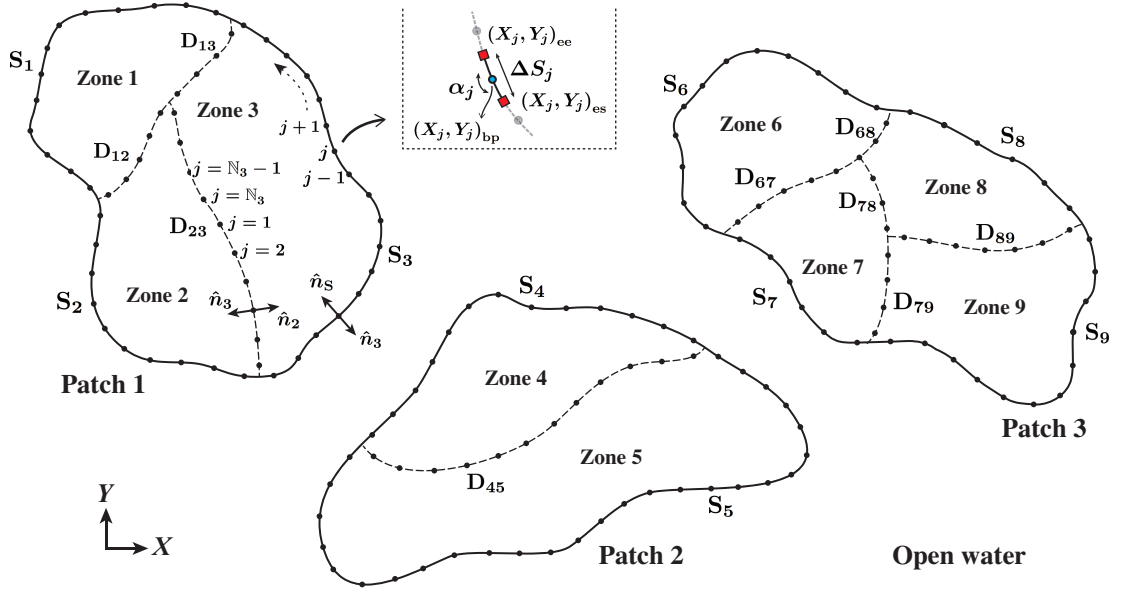


Figure 3.3: Discretization of boundary elements for a general forest region. For each subzone ξ ($= 1 \cdots 9$), the exterior boundary (S_ξ) as well as the interfaces ($D_{\xi\psi}$) are divided into elements where N_ξ gives the total number of its elements. (X_j, Y_j) denotes the boundary points with subscripts bp, es and ee indicating the middle, starting and end point of j th element, respectively. The dotted line with arrow indicates the direction of numbering system for each subzone (e.g. Zone 3). α_j is the interior angle and ΔS_j represents the element length. \hat{n} shows the outward normal directions to the boundaries of subzones and open water. Note that the number of dots in this figure only serves the purpose of illustration. A convergence test will be needed in the numerical computations to determine the resolution of boundary elements.

Fig.3.3 is an example of a general forest configuration, showing the sketch of discretization on both the exterior boundaries (S_ξ) and the interfaces ($D_{\xi\psi}$) of each subzone ξ . Totally 3 patches ($N_{\text{patch}} = 3$) with 9 subzones ($N_{\text{zone}} = 9$) are included. The indices of patches ($\mathbb{P} = 1 - 3$) and of subzones ($\xi = 1, 2, \cdots, 9$) are both indicated. For each subzone, the total number of boundary points are given as N_ξ , e.g. Zone 3 has N_3 elements along both the exterior boundary S_3 and two interfaces D_{13} & D_{23} . The total number of boundary points for the entire forest region is then given by $N_{\text{bp|fs}} = \sum N_\xi$ (i.e. $N_1 + \cdots + N_9$). Note that for each subzone, the direction of integration along its boundary has to be

counterclockwise as shown by dotted line with arrow in Fig.3.3. The interior angle α and the element length ΔS are both indicated. The outward normal directions along the boundaries of subzones and of open water are presented as well.

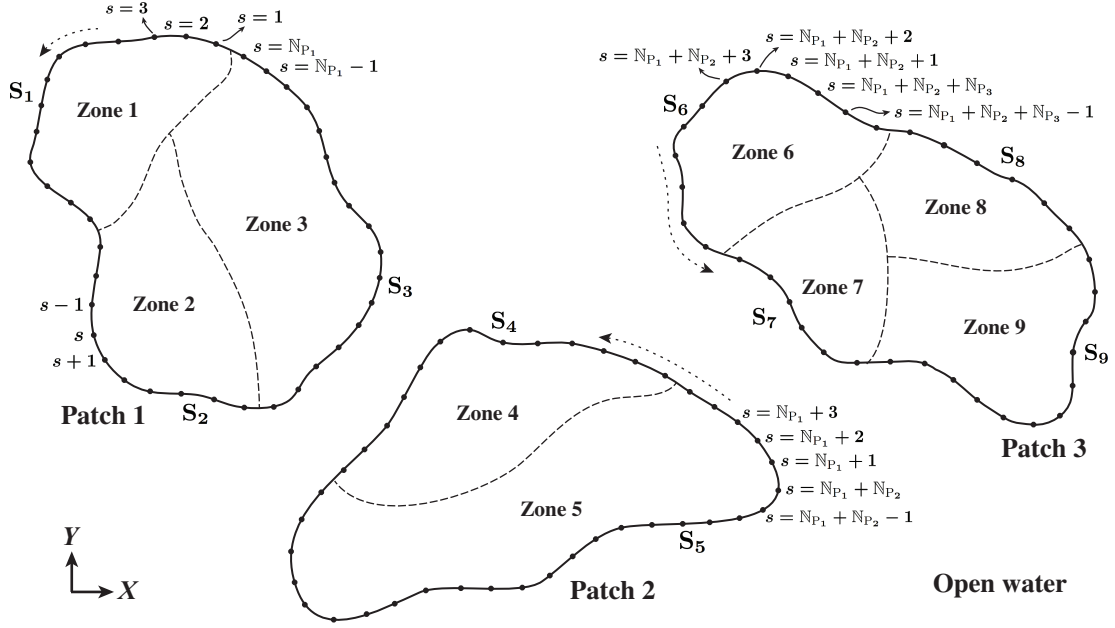


Figure 3.4: Discretization of the exterior boundaries of forest patches (i.e. the boundary of open water): s denotes the index of boundary point; N_{P_1} , N_{P_2} and N_{P_3} give the number of boundary points for Patch 1, 2 and 3, respectively. Dashed lines show the interfaces of subzones. Dotted lines with arrows present the directions for assigning boundary points. Note that the number of dots in this figure only serves the purpose of illustration. A convergence test will be needed in the numerical computation to determine the resolution of boundary elements.

For open water, on the other hand, the boundary has $\mathbf{S} = \sum S_\xi = S_1 + S_2 + \dots + S_9$. Fig.3.4 shows the corresponding assignment of discrete points along boundary \mathbf{S} with arrows indicating the directions. N_{P_κ} denotes the number of discrete elements along the exterior boundary of κ th patch (e.g. N_{P_1} for Patch 1). Thus, the total number of boundary elements for open water can be obtained by $N_{\text{bp|low}} = \sum_\kappa N_{P_\kappa}$ (e.g. $N_{P_1} + N_{P_2} + N_{P_3}$). It must be noted that the order of boundary

points cannot jump from one patch to another.

3.4 Eddy viscosity

For modeling turbulence by RANS, the eddy viscosity is calculated in general as a function of position. It is known in uniform flows that the turbulent wake behind an isolated object is affected by the turbulent intensity of the free stream. Specifically, [Wu and Faeth \(1994a\)](#) have reported experiments for a sphere in a steady pipe flow with $0 < Re_d < 300$ and $600 < Re_d < 1560$, and 4% ambient turbulence intensity, that the turbulent wake has mean streamwise velocities scaled like self-preserving laminar wakes, with enhanced eddy viscosities roughly independent of position. Moreover, the eddy viscosity increases roughly linearly with the particle Reynolds number. Within the transitional range, vortex shedding is evident. These observations have been numerically confirmed by [Bagchi and Balachandar \(2004\)](#) for the range of $Re_d \leq 610$ using DNS simulation. [Wu and Faeth \(1994b\)](#) later extended the range of free stream turbulence intensity to 2% – 9.5% for $125 < Re_d < 1560$ and found that vortex shedding was suppressed when the turbulence intensity in the free stream exceeded 7%. Wakes were again similar to those seen in laminar flows. Since every cylinder in the forest is in the turbulent environment due to neighboring cylinders, it is reasonable to adopt the simple assumption of constant eddy viscosity while confirmation of course must await detailed experiments for cylinder arrays similar to [Wu and Faeth \(1994a,b\)](#).

As stated previously, the eddy viscosity ν_e is assumed as a constant bulk

value over a homogeneous subzone and can be determined by using the concept of energy balance (Mei et al. 2014). Namely, the time-averaged energy dissipation rate in a subzone ξ is required to be balanced by the total time-averaged rate of work done by wave forces on the cylinders inside that specific subzone:

$$\begin{aligned} & \rho v_e \iint_{\xi} \left\{ \int_{-h}^0 \left[\iint_{\Omega_f} \overline{\frac{1}{2} \left(\frac{\partial u_i}{\partial x_j} + \frac{\partial u_j}{\partial x_i} \right)^2 + \left(\frac{\partial u_i}{\partial z} + \frac{\partial w}{\partial x_i} \right)^2 + \left(\frac{\partial w}{\partial z} \right)^2 dx_1 dx_2} \right] dZ \right\} dA_{\xi} \\ &= \frac{1}{2} \rho d C_D \iint_{\xi} \left\{ \int_{-h}^0 \overline{[U(U|U)]} dZ \right\} dA_{\xi} + \rho \ell^2 C_M \iint_{\xi} \left[\int_{-h}^0 \overline{U \left(\frac{\partial U}{\partial t} \right)} dZ \right] dA_{\xi} \end{aligned} \quad (3.93)$$

where $\overline{(\cdot)}$ represents the time-averaged quantity over one wave period. Using the leading-order approximation for the velocity components, the approximated energy balance equation becomes

$$\begin{aligned} & \rho v_e \iint_{\xi} \left\{ \int_{-h}^0 \left[\iint_{\Omega_f} \overline{\frac{1}{2} \left(\frac{\partial u_i^{(0)}}{\partial x_j} + \frac{\partial u_j^{(0)}}{\partial x_i} \right)^2 + \left(\frac{\partial w^{(0)}}{\partial x_i} \right)^2} dx_1 dx_2 \right] dZ \right\} dA_{\xi} \\ &= \frac{1}{2} \rho d C_D \iint_{\xi} \left\{ \int_{-h}^0 \overline{[U^{(0)}(U^{(0)}|U^{(0)})]} dZ \right\} dA_{\xi} + \rho \ell^2 C_M \iint_{\xi} \left[\int_{-h}^0 \overline{U^{(0)} \left(\frac{\partial U^{(0)}}{\partial t} \right)} dZ \right] dA_{\xi} \end{aligned} \quad (3.94)$$

Note that the time-averaged rate of work done by the inertia force would vanish for periodic waves. Applying (3.32) and (3.33), the above equation can be written as

$$\begin{aligned} & \rho v_e \iint_{\xi} \left\{ \mathcal{F}_{K_i} \left[\int_{-h}^0 \left| \frac{\partial \tilde{p}^{(0)}}{\partial X_i} \right|^2 dZ \right] + \mathcal{F}_W \left[\int_{-h}^0 \left| \frac{\partial \tilde{p}^{(0)}}{\partial Z} \right|^2 dZ \right] \right\} dA_{\xi} \\ &= \frac{1}{2} \rho d C_D \iint_{\xi} \left\{ \int_{-h}^0 \overline{U^{(0)}(U^{(0)}|U^{(0)})} dZ \right\} dA_{\xi} \end{aligned} \quad (3.95)$$

where

$$\begin{aligned}
\mathcal{F}_{K_1} &= \iint_{\Omega_f} \left\{ \left| \frac{\partial \tilde{K}_{11}}{\partial x_1} \right|^2 + \left| \frac{\partial \tilde{K}_{21}}{\partial x_2} \right|^2 + \frac{1}{2} \left(\left| \frac{\partial \tilde{K}_{11}}{\partial x_2} \right|^2 + \left| \frac{\partial \tilde{K}_{21}}{\partial x_1} \right|^2 \right) + \Re \left[\left(\frac{\partial \tilde{K}_{11}}{\partial x_2} \right)' \frac{\partial \tilde{K}_{21}}{\partial x_1} \right] \right\} dx_1 dx_2 \\
\mathcal{F}_{K_2} &= \iint_{\Omega_f} \left\{ \left| \frac{\partial \tilde{K}_{12}}{\partial x_1} \right|^2 + \left| \frac{\partial \tilde{K}_{22}}{\partial x_2} \right|^2 + \frac{1}{2} \left(\left| \frac{\partial \tilde{K}_{12}}{\partial x_2} \right|^2 + \left| \frac{\partial \tilde{K}_{22}}{\partial x_1} \right|^2 \right) + \Re \left[\left(\frac{\partial \tilde{K}_{12}}{\partial x_2} \right)' \frac{\partial \tilde{K}_{22}}{\partial x_1} \right] \right\} dx_1 dx_2 \\
\mathcal{F}_W &= \iint_{\Omega_f} \frac{1}{2} \left(\left| \frac{\partial \tilde{W}}{\partial x_1} \right|^2 + \left| \frac{\partial \tilde{W}}{\partial x_2} \right|^2 \right) dx_1 dx_2
\end{aligned} \tag{3.96}$$

The cell-averaged velocity $U^{(0)}$ can be obtained from (3.32) and (3.33):

$$\begin{aligned}
U^{(0)} &\equiv \sqrt{\langle u_1^{(0)} \rangle^2 + \langle u_2^{(0)} \rangle^2} \\
&= \left\{ \left[\Re \left(-\langle \tilde{K}_{11} \rangle \frac{\partial \tilde{P}^{(0)}}{\partial X_1} e^{-i\omega t} \right) \right]^2 + \left[\Re \left(-\langle \tilde{K}_{22} \rangle \frac{\partial \tilde{P}^{(0)}}{\partial X_2} e^{-i\omega t} \right) \right]^2 \right\}^{1/2}
\end{aligned} \tag{3.97}$$

Note that $(\cdot)'$ denotes the complex conjugate operator. To determine the bulk eddy viscosity, the drag coefficient C_D needs to be prescribed. As we know, turbulence can be generated due to the existence of cylinders. Ignoring smaller-scale eddies, the eddy viscosity model is used to calculate large-scale flow motions. The eddy viscosity is to characterize the transport and dissipation of energy in smaller-scale flows. Accordingly, it is reasonable to use the present energy model, which links the eddy viscosity to the work done by wave forces on cylinders. As expected, the form drag shall be the main contribution of the dissipation of wave energy. The wall friction or skin friction effects can then be considered as being lumped into the drag coefficient in (3.95).

In Mei et al. (2014), the spatial variation of eddy viscosity inside the forest area was considered. Namely, both ν_e and C_D varied spatially and the energy balance equation in (3.95) was used for each cell without the area integrals over the subzone. The empirical drag coefficient formula for steady unidirectional

flows (Cheng and Nguyen 2011) was employed for estimating the eddy viscosity within each cell. However, since the drag coefficient formula did not adequately represent the oscillatory flow condition, a fitting coefficient was introduced when comparing the model results with experimental data for each wave condition. To overcome this shortcoming, a new drag coefficient formula is introduced in the present approach based on direct measurements of wave forces by Hu et al. (2014).

In Hu et al. (2014)'s flume experiments, both emergent and submerged cylinders were used. A series of different wave conditions was conducted, including regular waves and combined wave-current cases. Wave forces acting on four individual cylinders within the model forest and the mid-depth velocities in the vicinity of these cylinders were measured directly. Using the Morison-type formula, time-averaged bulk drag coefficients C_D over the entire model forest were calculated. A drag coefficient formula in terms of Reynolds number was proposed for all the experimental cases (see Fig.6 in Hu et al. 2014). In the present study, only the cases of emergent cylinders are considered. The data of pure wave conditions are then replotted in Fig.3.5 by re-defining the Reynolds number based on the tree-related hydraulic radius r_v :

$$\text{Re}_v = \frac{U_{\text{mid}} r_v}{\nu_w} \quad \text{with} \quad r_v = \frac{\pi d}{4} \left(\frac{n}{1-n} \right) \quad (3.98)$$

where ν_w is the kinematic viscosity of water and the hydraulic radius r_v is expressed in terms of the porosity n and the cylinder diameter d (Mei et al. 2014). The dimensional characteristic velocity U_{mid} denotes the spatial-averaged velocity at middle depth (i.e. $Z = -h/2$) over the specified forest subzone and can be

determined by

$$\begin{aligned}
U_{\text{mid}} &= \omega A_{\text{inc}} \frac{2}{\pi} \frac{1}{A_{\xi}} \iint_{\xi} \left(|\langle \tilde{u}_1^{(0)} \rangle|^2 + |\langle \tilde{u}_2^{(0)} \rangle|^2 \right)_{Z=-h/2}^{1/2} dX_1 dX_2 \\
&= \omega A_{\text{inc}} \frac{2}{\pi} \frac{1}{A_{\xi}} \iint_{\xi} \left(\left| -\langle \tilde{K}_{11} \rangle \frac{\partial \tilde{P}^{(0)}}{\partial X_1} \right|^2 + \left| -\langle \tilde{K}_{22} \rangle \frac{\partial \tilde{P}^{(0)}}{\partial X_2} \right|^2 \right)_{Z=-h/2}^{1/2} dX_1 dX_2 \quad (3.99)
\end{aligned}$$

where A_{ξ} denotes the area of subzone ξ and (3.33) is used for the amplitude of cell-averaged velocity.

As indicated in Fig.3.5, a best-fitting curve for the available data over a range of Reynolds number ($7.5 \times 10^3 < \text{Re}_v < 2.5 \times 10^5$) is obtained as

$$C_D = \frac{50}{\text{Re}_v^{0.43}} + 2.13 \left[1 - \exp\left(-\frac{\text{Re}_v}{120.74}\right) \right] \quad (3.100)$$

with the root-mean-square error of 0.606. Adopting the new Reynolds number based on hydraulic radius, the drag formula can be generalized for different cell configurations and cylinder shapes. Note that three vegetation densities, referred as VD1, VD2 and VD3, were used in Hu et al. (2014). The cell configuration and the associated porosity n in their experiments can be found in Fig.3.1a. It should also be pointed out that (3.100) has the same form as the formula proposed by Cheng and Nguyen (2011). For a fixed incident wave amplitude, longer waves lead to smaller Reynolds numbers and (3.100) is approximately equal to the formula in Cheng and Nguyen (2011), which is for steady unidirectional flow. It is remarked here that the drag coefficient under oscillatory waves can also depend on the Keulegan-Carpenter (KC) number, which is defined as

$$\text{KC} = 2\pi A_{\text{inc}}/d \quad (3.101)$$

However, Sumer and Fredsøe (2006) suggested that for a single vertical cylinder the drag coefficient becomes less sensitive to the Keulegan-Carpenter (KC)

number when it is greater than 13 for a relatively large Reynolds number. In [Hu et al. \(2014\)](#), the KC number is between 10.47 and 27.80, which falls in the regime that the drag coefficient is less dependent on the KC number.

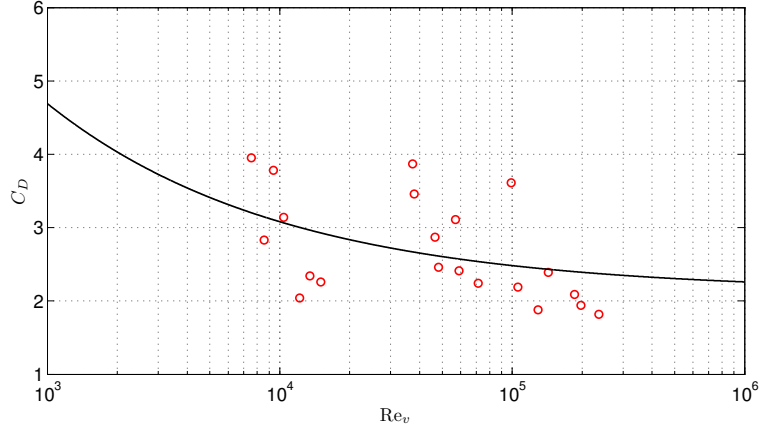


Figure 3.5: Drag coefficient formula – circles show the pure wave data in [Hu et al. \(2014\)](#) and the solid line denotes the best-fitting formula (3.100).

Similar to [Mei et al. \(2014\)](#), an alternative definition of the Reynolds number is by using the depth-averaged velocity rather than that at middle depth:

$$\text{Re}_v^{\text{ave}} = \frac{U_{\text{ave}} r_v}{\nu_w} \quad \text{with} \quad r_v = \frac{\pi}{4} d \left(\frac{n}{1-n} \right) \quad (3.102)$$

in which

$$\begin{aligned} U_{\text{ave}} &= \omega A_{\text{inc}} \frac{2}{\pi} \frac{1}{A_\xi} \iint_\xi \left[\frac{1}{h} \int_{-h}^0 \left(\left| \langle \tilde{u}_1^{(0)} \rangle \right|^2 + \left| \langle \tilde{u}_2^{(0)} \rangle \right|^2 \right)^{1/2} dZ \right] dX_1 dX_2 \\ &= \omega A_{\text{inc}} \frac{2}{\pi} \frac{1}{A_\xi} \iint_\xi \left[\frac{1}{h} \int_{-h}^0 \left(\left| -\langle \tilde{K}_{11} \rangle \frac{\partial \tilde{P}^{(0)}}{\partial X_1} \right|^2 + \left| -\langle \tilde{K}_{22} \rangle \frac{\partial \tilde{P}^{(0)}}{\partial X_2} \right|^2 \right)^{1/2} dZ \right] dX_1 dX_2 \end{aligned} \quad (3.103)$$

It appears that the above two formulas (3.98) and (3.102) lead to very close values of drag coefficient within the range of available Reynolds numbers. Therefore, in this study (3.98) along with (3.100) are used in order to be consistent

with the experimental data by [Hu et al. \(2014\)](#). Once the drag coefficient is determined, the bulk eddy viscosity for subzone ξ can then be obtained by

$$\nu_e = \frac{1}{2} \omega A_{\text{inc}} d C_D \left\{ \frac{\iint_{\xi} \left(\int_{-h}^0 \left(\langle u_1^{(0)} \rangle^2 + \langle u_2^{(0)} \rangle^2 \right) \left| \left(\langle u_1^{(0)} \rangle^2 + \langle u_2^{(0)} \rangle^2 \right)^{1/2} \right| dZ \right) dA_{\xi}}{\iint_{\xi} \left\{ \mathcal{F}_{K_i} \left[\int_{-h}^0 \left| \frac{\partial \bar{p}^{(0)}}{\partial X_i} \right|^2 dZ \right] + \mathcal{F}_W \left[\int_{-h}^0 \left| \frac{\partial \bar{p}^{(0)}}{\partial Z} \right|^2 dZ \right] \right\} dA_{\xi}} \right\}^*, \quad i = 1, 2 \quad (3.104)$$

Note that all the variables inside the braces at the RHS of (3.104) are dimensionless (with an asterisk as a reminder) and the definitions of \mathcal{F}_{K_i} and \mathcal{F}_W can be found in (3.96).

An iterative scheme is established to determine the bulk eddy viscosity. Within each iteration, the cell problem (i.e. \tilde{K}_{ij} , \tilde{W} and \tilde{A}_j) is first solved with the eddy viscosity obtained from the previous iteration. Based on the cell problem solutions, the complex coefficients M_{ξ} and N_{ξ} for each subzone ξ , as defined in (3.43) and (3.45), can be readily calculated and the macro-scale wave dynamics can then be solved. Using the macro-scale solutions, the Reynolds number and bulk drag coefficient for each subzone are computed by (3.98) and (3.100). The corresponding bulk eddy viscosity is then updated by (3.104). Here the convergence criterion is to require the relative error of the dimensionless bulk eddy viscosity for each subzone ξ obtained from two successive iterations to be less than 10^{-5} :

$$\frac{|\sigma^{(n_t+1)} - \sigma^{(n_t)}|}{\sigma^{(n_t)}} < 10^{-5}, \quad \sigma = \frac{\nu_e}{\omega \ell^2} \quad (3.105)$$

where the superscript (n_t) and $(n_t + 1)$ respectively denote the $(n_t)_{\text{th}}$ and $(n_t + 1)_{\text{th}}$ iteration.

■ Initial guess for the iteration process

To initiate the iteration, an appropriate initial guess of eddy viscosity is needed. Two formulas based on [Mei et al. \(2011\)](#) and [Tanino and Nepf \(2008a,b\)](#) are tested. First, the empirical formula suggested by [Mei et al. \(2011\)](#) is used as an initial guess:

$$v_e = 1.86(1 - n)^{2.06} U_0 \ell \quad (3.106)$$

in which U_0 represents the depth-averaged horizontal water particle velocity for long-wave condition (i.e. $U_0 = \sqrt{gh_0} A_{\text{inc}} / h_0 = \omega A_{\text{inc}} / k_{\text{inc}} h_0$). To extend the formula to waves of intermediate length, U_0 in (3.106) is replaced by the following characteristic velocity scale:

$$U_0 = \left(\frac{\omega A_{\text{inc}}}{k_{\text{inc}} h_0} \right) \frac{\tanh(k_{\text{inc}} h_0)}{k_{\text{inc}} h_0} \quad (3.107)$$

In addition, [Tanino and Nepf \(2008a\)](#) conducted experiments on steady flows through random cylinder arrays and proposed

$$\frac{\sqrt{k_t}}{U_p} = 1.1 \left(\frac{2}{\pi} C_D \frac{1 - n}{n} \right)^{1/3} \quad (3.108)$$

where k_t and U_p represent the mean turbulent kinetic energy and the mean flow velocity across the cylinders, respectively. By using (3.107) as U_p and calculate the drag coefficient by (3.100), the eddy viscosity can also be estimated by

$$v_e = c_e d \sqrt{\frac{2}{3} k_t} = 0.071 \left(C_D \frac{1 - n}{n} \right)^{1/3} \left(\frac{\omega A_{\text{inc}}}{k_{\text{inc}} h_0} \right) \frac{\tanh(k_{\text{inc}} h_0)}{k_{\text{inc}} h_0} d \quad (3.109)$$

where the coefficient $c_e=0.092$ is used. The dimensionless eddy viscosity can then be derived from $\sigma = v_e / \omega \ell^2$.

The above two initial guesses yield the same converged result within a few iteration. For both formulas, the ratios of initial guesses to converged values

roughly range from 2 to 6. The relative difference between the resulting values of the dimensionless eddy viscosity is less than 1%. For all the tests, it has been shown that the convergence is satisfied within 10-20 iterations. The convergence histories for two representative cases in Table 3.1 are provided in Fig.3.6. Another two extreme initial guesses (i.e., 10^{-9} and 100) are also tested to check the sensitivity of converged eddy viscosity to the proposed iterative scheme.

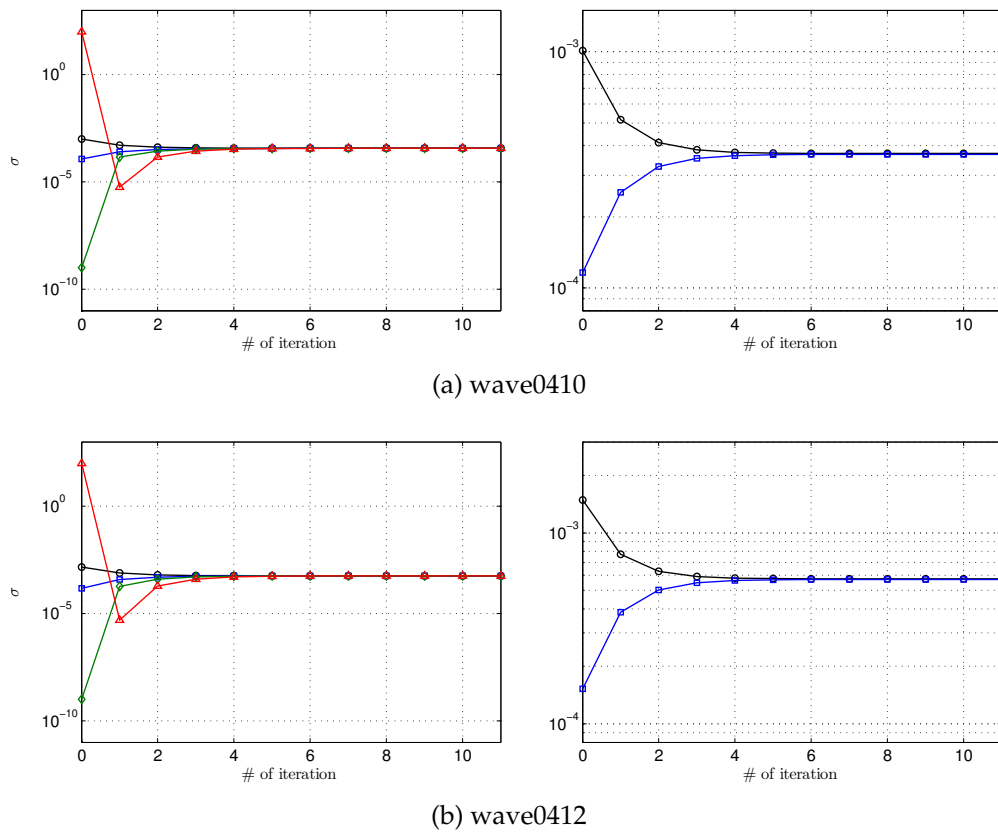


Figure 3.6: Convergence histories of the iterative scheme with different initial guesses for two cases in Table 3.1: squares – (3.106), circles – (3.109). The right figure shows more detailed convergence history. Another two extreme initial guesses were also tested and shown in the left figure, i.e. $\sigma_{ini} = 10^{-9}$ (diamonds) and 100 (triangles).

3.5 Cornell Homogenization model for Wave-Vegetation interaction – Periodic waves

Based on the present approach, a computing program named CHEWAVE-P (Cornell Homogenization model on Wave-Vegetation interaction – Periodic waves) has been developed. The model has the capability of solving the macro-scale wave propagations through a general forest region. The connection between micro- and macro-scale problems is also made. The iterative scheme for determining the bulk eddy viscosity for each subzone is included as well. To conduct the numerical computation with the present model, several inputs are required, such as incident wave conditions, forest properties, discretization of forest boundary and the desired computational domain. The outputs of this model include the corresponding drag coefficient, Reynolds number and eddy viscosity for each subzone. In addition, the dimensionless free surface elevation over the entire computational domain would be provided. A flow chart for running the numerical computation is shown in Fig.3.7 and the details can be found in Appendix B.1.

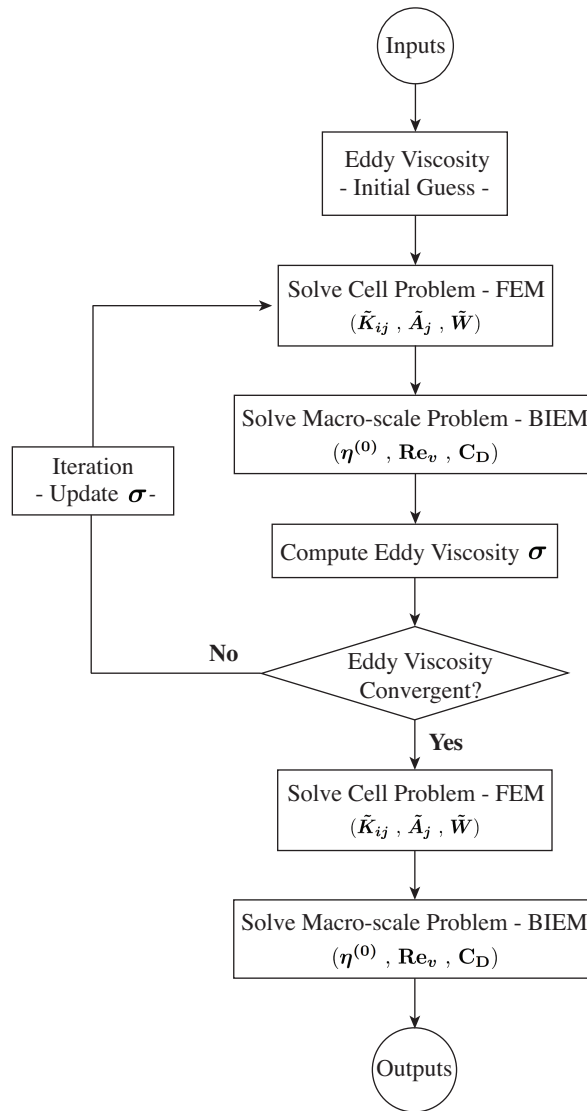


Figure 3.7: Flowchart of the present numerical model

3.6 Model validation and numerical results

In this section, the model results are compared with theoretical solutions and laboratory experiments. Three special forest configurations are considered. The flume test in [Hu et al. \(2014\)](#) is first used to study the wave decay within a model

forest belt, where the semi-analytical solutions are also provided. Since only the normally incident conditions were considered in [Hu et al. \(2014\)](#)'s tests, the semi-analytical solutions with zero incident angle are first compared with their experimental measurements. Using the same test conditions, model results are then extended to obliquely incidences and the discussion on different incident angles are provided. A circular forest is selected as a special configuration with finite extent. The corresponding semi-analytical solutions are provided, which are used as a preliminary validation of the present numerical model based on boundary integral equation method. With the homogeneous configuration, a bulk eddy viscosity throughout the entire region is assumed. A series of laboratory experiments conducted at the University of Cantabria is used for data-model comparisons. To explore the present model further, the experiments on multiple circular forest patches ([Maza 2015](#)) are used as another special configuration. Numerical results and the comparisons with experimental data are presented herein.

3.6.1 Water waves propagating through a forest belt

3.6.1.1 Semi-analytical solutions

We first consider a homogeneous forest belt with an infinite length (i.e. $-\infty < Y < \infty$) but a finite width (i.e. $0 \leq X \leq L_F$). Due to the infinite length, we here present the theoretical solutions instead of using the boundary integral method. Assuming the direction of incident waves has an angle θ with the X -axis, the total solution in the incident region (with subscript I) can be readily obtained by

solving the Laplace's equation in (3.51):

$$\begin{aligned} \phi_I(X, Y, Z) = & A_0 \frac{\cosh k_0(Z+h)}{\cosh k_0 h} e^{i(\alpha_0 X + \beta_0 Y)} + A_0 R \frac{\cosh k_0(Z+h)}{\cosh k_0 h} e^{-i(\alpha_0 X - \beta_0 Y)} \\ & + \sum_{p=1}^{\infty} A_p \frac{\cos \kappa_p(Z+h)}{\cos \kappa_p h} e^{\lambda_p X} e^{i\beta_0 Y}, \quad X < 0 \end{aligned} \quad (3.110)$$

in which the solutions include incident and reflected waves (i.e. the 1st and 2nd term on the RHS), as well as the evanescent waves (i.e. the 3rd term on the RHS), which decay exponentially away from the forest. Likewise, in the transmission region (with subscript T), the transmitted and evanescent waves are both included:

$$\begin{aligned} \phi_T(X, Y, Z) = & A_0 T \frac{\cosh k_0(Z+h)}{\cosh k_0 h} e^{i(\alpha_0 X + \beta_0 Y)} \\ & + \sum_{p=1}^{\infty} B_p \frac{\cos \kappa_p(Z+h)}{\cos \kappa_p h} e^{-\lambda_p X} e^{i\beta_0 Y}, \quad X > L_F \end{aligned} \quad (3.111)$$

where

$$\alpha_0 = k_0 \cos \theta, \quad \beta_0 = k_0 \sin \theta \quad \text{and} \quad \lambda_p = (\kappa_p^2 + \beta_0^2)^{1/2} \quad (3.112)$$

Note that in both (3.110) and (3.111) the scattered waves are restricted to be outgoing at infinity. $A_0 = -i$ is determined by (3.49), while $|R|$ and $|T|$ respectively denote the reflection and transmission coefficients. The dispersion relationship for open water (both incidence and transmission regions) is shown in (3.62). It can also be expressed as

$$1 = k_0 \tanh k_0 h \quad \text{and} \quad 1 = -\kappa_p \tan \kappa_p h \quad (p \geq 1) \quad (3.113)$$

where k_0 and κ_p are both real roots.

Inside the forest (with subscript F), on the other hand, the solutions can be found by solving (3.46):

$$\phi_F(X, Y, Z) = \sum_{q=0}^{\infty} \frac{\cosh \hat{k}_q(Z+h)}{\cosh \hat{k}_q h} [C_q e^{i\hat{\alpha}_q X} + D_q e^{-i\hat{\alpha}_q X}] e^{i\beta_0 Y}, \quad 0 \leq X \leq L_F \quad (3.114)$$

which can be alternatively expressed as

$$\phi_{\text{F}} = \sum_{q=0}^{\infty} \frac{\cosh \hat{k}_q(Z+h)}{\cosh \hat{k}_q h} \left[E_q \cos(\hat{\alpha}_q X) + F_q \sin(\hat{\alpha}_q X) \right] e^{i\beta_0 Y}, \quad 0 \leq X \leq L_{\text{F}} \quad (3.115)$$

with

$$\hat{\alpha}_q = \left[(\gamma \hat{k}_q)^2 - \beta_0^2 \right]^{1/2} \quad \text{and} \quad \gamma = \left(\frac{n+N}{n+M} \right)^{1/2} \quad (3.116)$$

The dispersion relationship inside the forest is in (3.56):

$$1 = \left(\frac{n+N}{n} \right) \hat{k}_q \tanh \hat{k}_q h \quad (q \geq 0) \quad (3.117)$$

where \hat{k}_q are complex roots.

The unknown coefficients $-R, T, A_p, B_p, C_q$ and D_q – are to be determined from the matching conditions, requiring continuous pressure and normal mass fluxes along the edges of forest (i.e. $X = 0$ and $X = L_{\text{F}}$). As presented in (3.66) and (3.68), along the interface between forest and incidence region (i.e. $X = 0$), it is imposed that

$$\phi_{\text{I}} = \phi_{\text{F}} \quad \text{and} \quad \frac{\partial \phi_{\text{I}}}{\partial X} = (n+M) \frac{\partial \phi_{\text{F}}}{\partial X}, \quad -h < Z < 0 \quad (3.118)$$

and along $X = L_{\text{F}}$ we have

$$\phi_{\text{F}} = \phi_{\text{T}} \quad \text{and} \quad (n+M) \frac{\partial \phi_{\text{F}}}{\partial X} = \frac{\partial \phi_{\text{T}}}{\partial X}, \quad -h < Z < 0 \quad (3.119)$$

Substituting the solutions in (3.110), (3.111), and (3.114) into the above matching conditions and taking advantage of the orthogonality properties of hyperbolic cosine function as shown in (3.70), six linear algebraic equations, i.e. (C.3), (C.4), (C.5), (C.10), (C.11), (C.12), can be obtained for solving the unknown coefficients. Detailed derivations can be found in Appendix C.1. The resulting system of equations shall be solved numerically.

3.6.1.2 Normally incident waves

In the following, we first present the cases of normally incident waves (i.e. $\theta = 0$) and compare with the experimental data by [Hu et al. \(2014\)](#). In [Hu et al. \(2014\)](#)'s laboratory experiments, the model forest has a width of 6 m and is composed of circular wooden cylinders with 1 cm in diameter, which are uniformly installed in space as shown in [Fig.3.1a](#). Three cylinder spacings are tested, i.e. $\ell=18$, 12 and 6 cm. The corresponding porosities are 99.51 %, 98.91 % and 95.63 %, respectively. Since the multi-scale perturbation method requires the wavelength to be much greater than the spacing between cylinders:

$$\ell/L \ll O(1) \quad (3.120)$$

only the cases with $\ell=6$ cm, which have $\ell/L \leq 0.05$, are used for the purpose of checking the present theory. The test conditions can be found in [Table 3.1](#). All the incident waves are within the range of intermediate wavelength. The free surface elevation was measured by five wave gauges equally-spaced inside the forest.

Table 3.1: Experimental conditions and dimensionless parameters in [Hu et al. \(2014\)](#)

Case Name	h_0 (cm)	T (s)	A_{inc} (cm)	L (m)	$k_{\text{inc}}h_0$	$k_{\text{inc}}A_{\text{inc}}$	A_{inc}/h_0	Re_v	C_D	σ
wave0410	25	1.0	1.71	1.3038	1.2048	0.0824	0.0684	6485.52	3.2762	3.7075E-04
wave0412		1.2	1.76	1.6596	0.9465	0.0667	0.0705	7264.74	3.2216	5.7439E-04
wave0610		1.0	2.52	1.3038	1.2048	0.1215	0.1009	8600.61	3.1450	6.0532E-04
wave0612		1.2	2.60	1.6596	0.9465	0.0983	0.1039	9640.77	3.0963	9.3084E-04
wave0812		1.2	3.43	1.6596	0.9465	0.1299	0.1372	11573.83	3.0232	1.3196E-03
wave0815		1.5	3.53	2.1732	0.7228	0.1019	0.1410	12590.86	2.9914	2.1282E-03
wave1015		1.5	4.42	2.1732	0.7228	0.1279	0.1770	14373.43	2.9436	2.8153E-03

The above h_0 , T , A_{inc} and L represent the constant water depth, the incident wave period, wave amplitude and wavelength, respectively. k_{inc} denotes the incident wavenumber. For all the cases, the width of the forest region L_F is 6 m and the porosity n is 95.63% (i.e. $\ell=6$ cm), which is referred as VD3 in [Hu et al. \(2014\)](#).

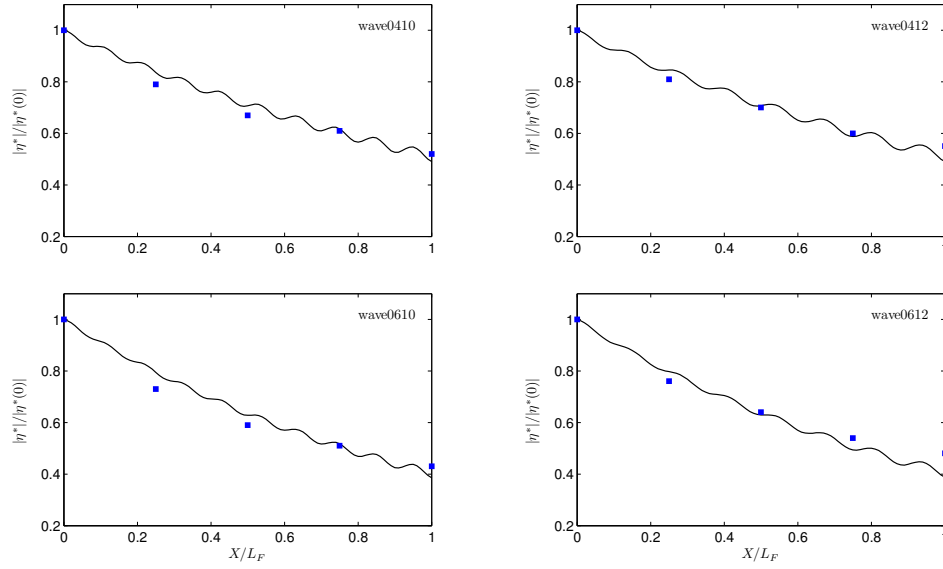


Figure 3.8: Spatial variation of normalized dimensionless wave amplitude inside the model forest (i.e. $|\eta^*|/|\eta^*(0)|$) for normal incidence (i.e. $\theta = 0$). Solid squares represent the laboratory measurements by [Hu et al. \(2014\)](#), while solid lines show the numerical results by present model. The wave conditions can be found in Table 3.1 (wave0410, 0412, 0610, 0612).

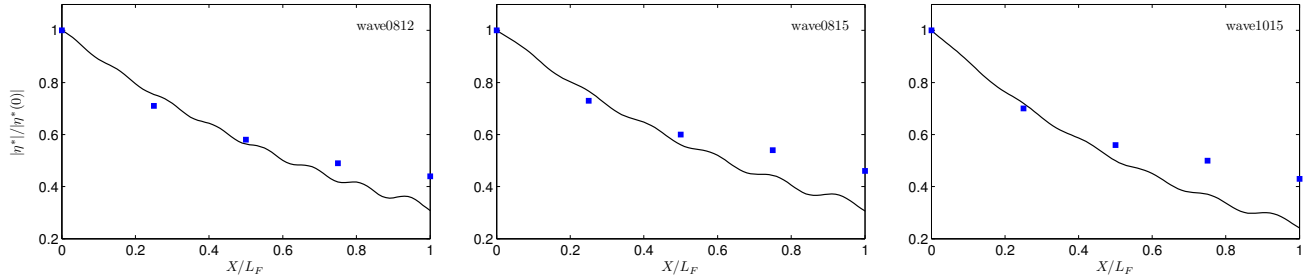


Figure 3.9: Spatial variation of normalized dimensionless wave amplitude inside the model forest (i.e. $|\eta^*|/|\eta^*(0)|$) for normal incidence (i.e. $\theta = 0$). Solid squares represent the laboratory measurements by [Hu et al. \(2014\)](#), while solid lines show the numerical results by present model. The wave conditions can be found in Table 3.1 (wave0812, 0815, 1015).

In Fig.3.8 and 3.9, the spatial variation of normalized dimensionless wave amplitude inside the forest is compared with the experimental data. The agreement between model results and data is good for the first four cases (i.e.

wave0410, 0412, 0610 and 0612 in Fig.3.8). The discrepancy becomes noticeable for the last three cases (i.e. wave0812, 0815 and 1015 in Fig.3.9). As shown in Table 3.1, the nonlinearity, being measured as the ratio of incident wave amplitude to water depth (i.e. A_{inc}/h_0), becomes relatively large for the last three cases, which could be the cause for the increasing discrepancy since the present theory is developed for small-amplitude waves. It is remarked here that some of the laboratory experiments discussed in Mei et al. (2014), e.g. the experiments in Augustin (2007), Augustin et al. (2009) and Wu et al. (2011, 2012), have also been checked with the present theory. The agreement between model results and experimental data is also reasonable for the cases where A_{inc}/h_0 is less than 1/10.

In addition to the macro-scale wave dynamics, the micro-scale flow fields within cells can be obtained by the present model. Using Case wave0410 in Table 3.1 and choosing three locations within the model forest (i.e. $X = 1, 3, 5$ m), the horizontal velocity fields at the mean water level around the cylinders are presented at several instants in Fig.3.10 to 3.12. It can be observed that the symmetric eddies are formed near the central cylinder due to the boundary effects when the flow reversal is right about happening. Small eddies near the cylinders at four corners can also be seen. It should be noted that only Reynolds-averaged velocity is presented by the present theory.

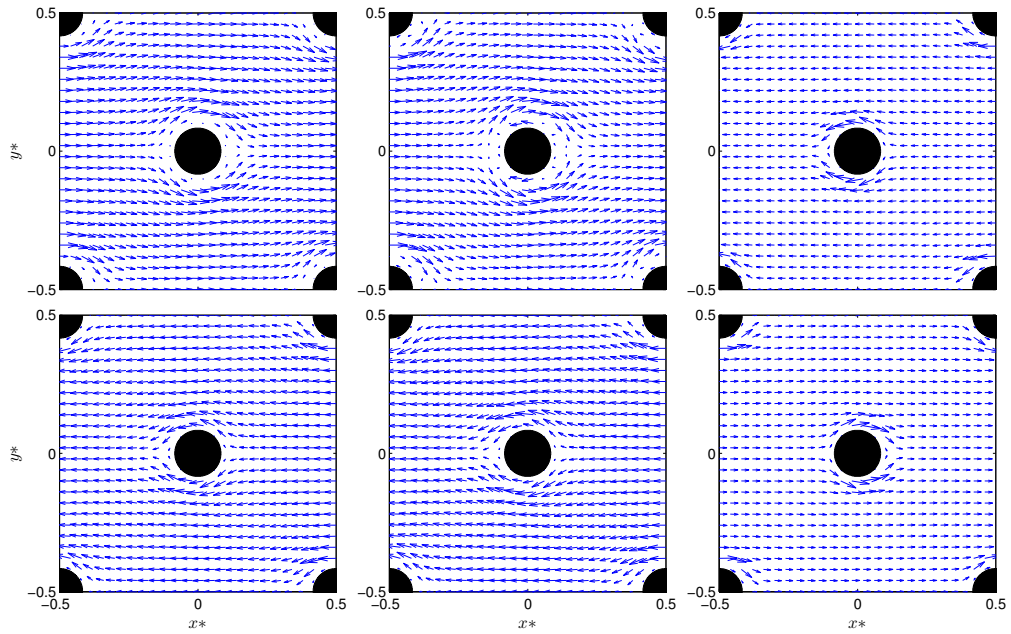


Figure 3.10: Snapshots of horizontal velocity fields $X = 1$ m for wave0410 in Table 3.1. From left to right and top to bottom, the dimensionless time is $t/T = 0, 0.03, 0.13, 0.26, 0.39, 0.63$.

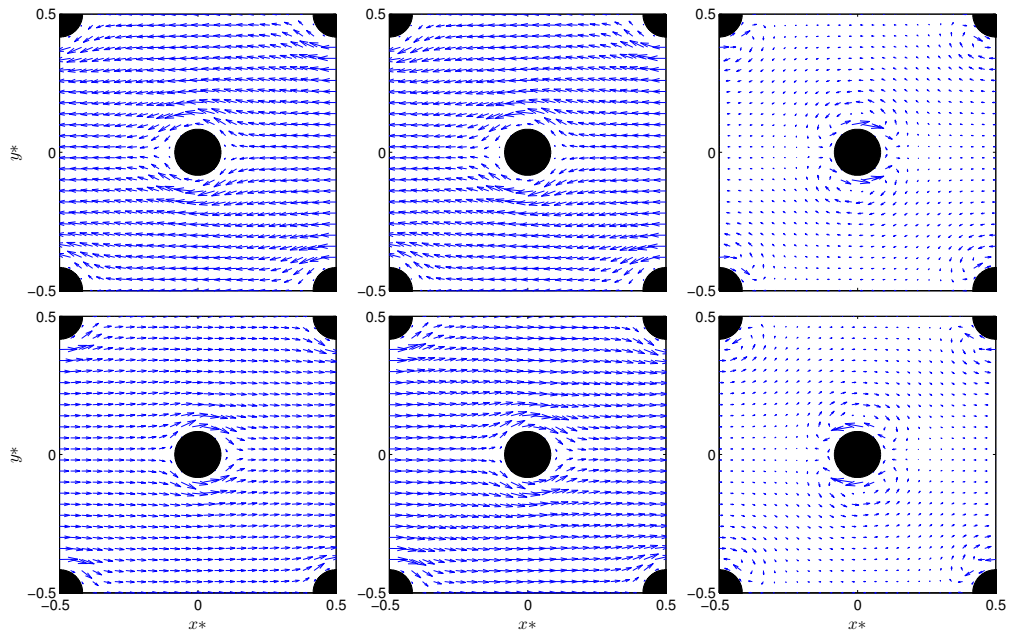


Figure 3.11: Snapshots of horizontal velocity fields at $X = 3$ m for wave0410 in Table 3.1. From left to right and top to bottom, the dimensionless time is $t/T = 0, 0.03, 0.13, 0.26, 0.39, 0.63$.

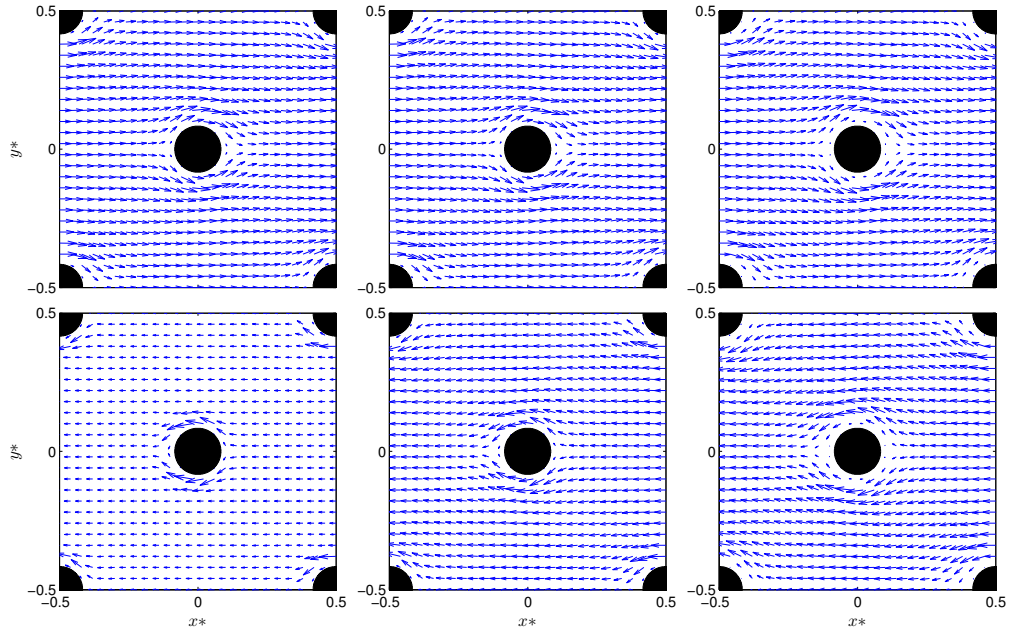


Figure 3.12: Snapshots of velocity fields at $X = 5$ m for wave0410 in Table 3.1. From left to right and top to bottom, the dimensionless time is $t/T = 0, 0.03, 0.13, 0.26, 0.39, 0.63$.

3.6.1.3 Obliquely incident waves

In addition to normal-incident waves, here we extend the model results from [Hu et al. \(2014\)](#)'s experiments by considering three non-zero incident angles (i.e. $\theta = \pi/6, \pi/4$ and $\pi/3$). The same wave conditions in Table 3.1 are used. The corresponding dimensionless parameters are presented in Table 3.2. The normalized dimensionless wave amplitude inside the forest for different incident angles are presented in Fig.3.13. Obviously larger incident angle (e.g. $\theta = \pi/3$) results in smaller Reynolds numbers and consequently greater drag coefficients and more energy dissipation inside the forest. In addition, larger incident waves with the same wave period (e.g. wave0410 and wave0610) lead to more dissipation. Fig.3.15 shows the instantaneous free surface elevation over both outside

and inside the forest region with four different incident angles for wave0410. The wave diffraction pattern can be clearly identified.

Table 3.2: Dimensionless parameters for different incident angles

Case Name	$Re_v^{\theta_1}$	$C_D^{\theta_1}$	σ^{θ_1}	$Re_v^{\theta_2}$	$C_D^{\theta_2}$	σ^{θ_2}	$Re_v^{\theta_3}$	$C_D^{\theta_3}$	σ^{θ_3}
wave0410	6171.29	3.3010	3.5804E-04	5776.42	3.3348	3.4391E-04	5065.97	3.4048	3.1953E-04
wave0412	6917.53	3.2448	5.5416E-04	6477.86	3.2768	5.3155E-04	5692.87	3.3424	4.9161E-04
wave0610	8071.14	3.1732	5.8734E-04	7422.60	3.2115	5.6756E-04	6310.35	3.2898	5.3428E-04
wave0612	9059.44	3.1226	9.0265E-04	8343.40	3.1584	8.7032E-04	7126.48	3.2306	8.1374E-04
wave0812	10744.18	3.0523	1.2884E-03	9749.63	3.0917	1.2511E-03	8137.25	3.1695	1.1822E-03
wave0815	11693.17	3.0193	2.0763E-03	10630.72	3.0565	2.0089E-03	8930.04	3.1287	1.8802E-03
wave1015	13197.65	2.9741	2.7637E-03	11850.96	3.0141	2.6904E-03	9803.02	3.0894	2.5295E-03

Note: The test conditions for the above cases can be found in Table 3.1. The superscripts θ_1 , θ_2 and θ_3 represent the incident angle equal to $\pi/6$, $\pi/4$ and $\pi/3$, respectively.

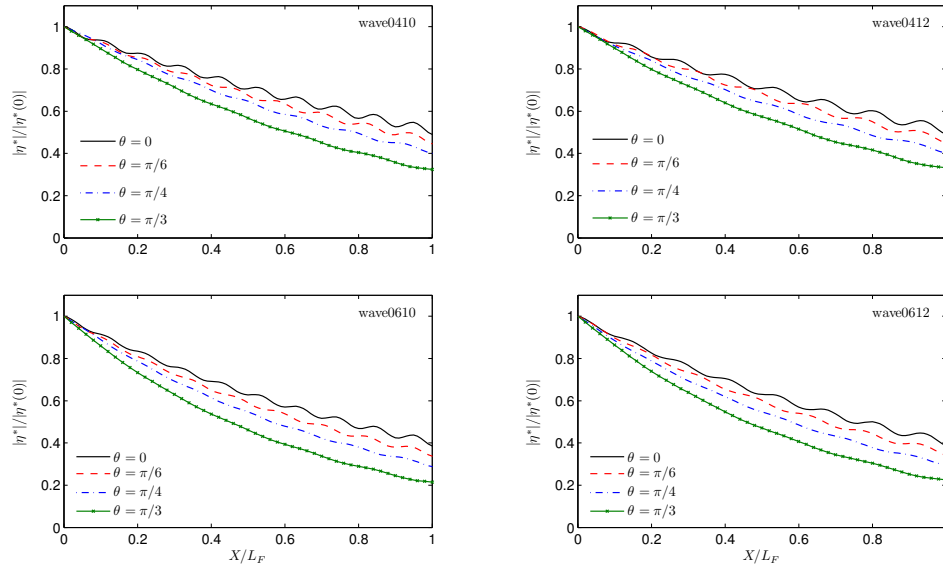


Figure 3.13: Spatial variation of normalized dimensionless wave amplitude inside the model forest (i.e. $|\eta^*|/|\eta^*(0)|$) for different incident angles θ . The wave conditions can be found in Table 3.1 (wave0410, 0412, 0610, 0612).

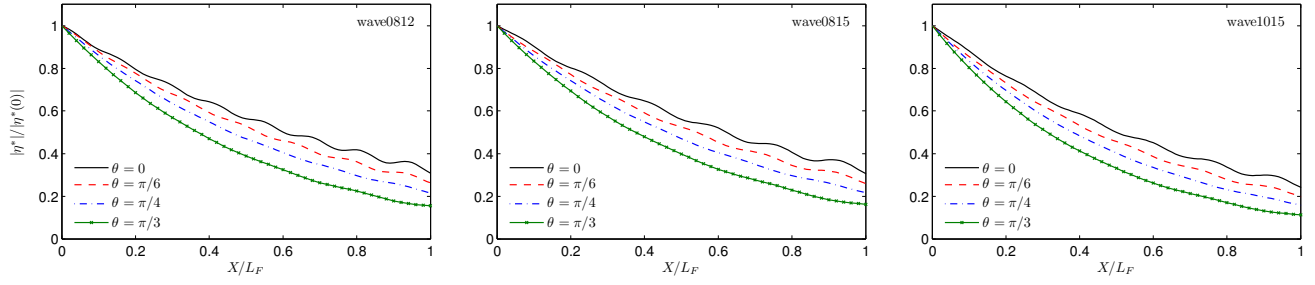


Figure 3.14: Spatial variation of normalized dimensionless wave amplitude inside the model forest (i.e. $|\eta^*|/|\eta^*(0)|$) for different incident angles θ . The wave conditions can be found in Table 3.1 (wave0812, 0815, 1015).

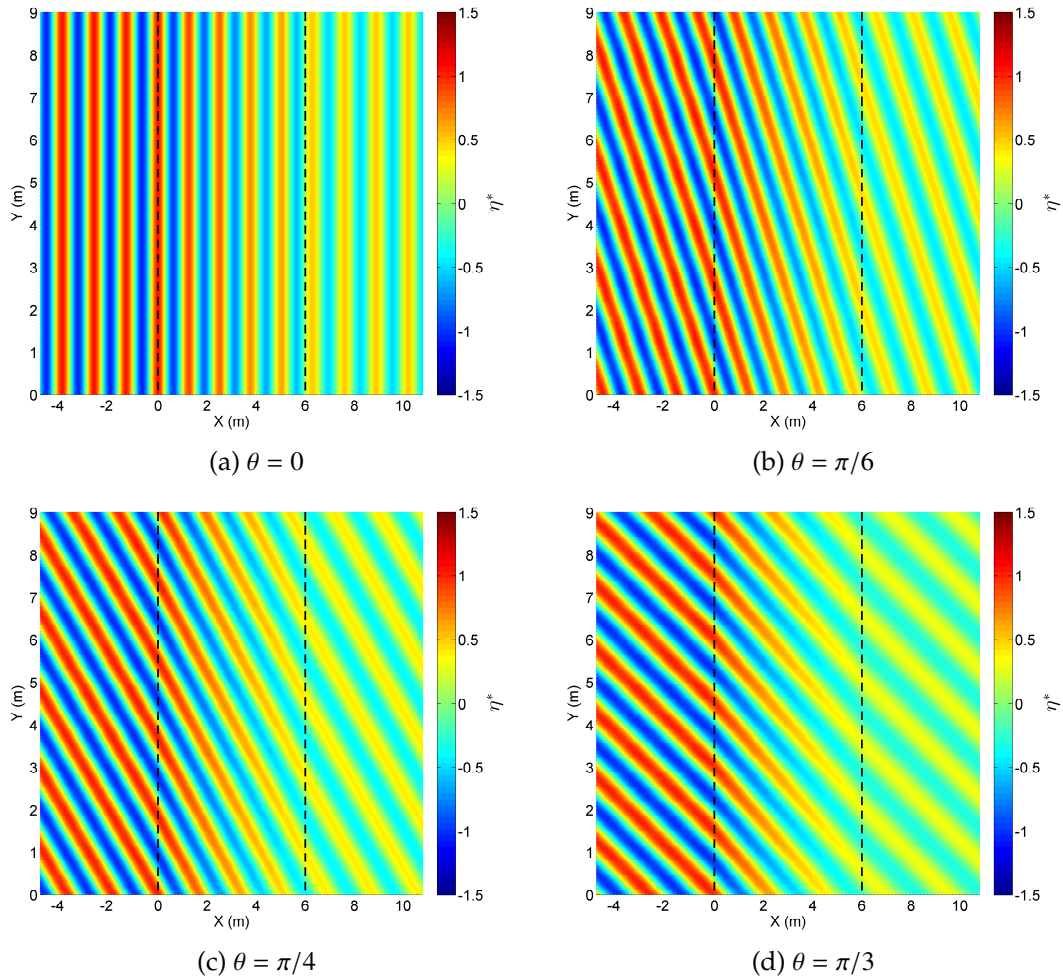


Figure 3.15: Snapshots of the dimensionless free surface elevation over the outside and inside forest region with different incident angles at time $t = k_T T$ for Case wave0410, where k_T can be any arbitrary integer. The forest region is within the dashed lines.

3.6.2 Water waves scattered by a circular forest

In the second example, a homogeneous circular forest with radius R is considered where a constant bulk eddy viscosity is assumed over the entire region. In the following, we first derived the semi-analytical solutions for both inside and outside regions and compare with the numerical results obtained from the boundary integral equation method in Sec.3.3, in which negligible differences are found. Besides, a set of laboratory experiments was conducted at the University of Cantabria in Spain. The comparisons between numerical results and experimental data are also presented.

3.6.2.1 Semi-analytical solutions

Expressing (3.46) in cylindrical coordinates, the governing equations for a circular forest (with subscript F) becomes

$$\frac{1}{r} \frac{\partial}{\partial r} \left(r \frac{\partial \phi_F}{\partial r} \right) + \frac{1}{r^2} \frac{\partial^2 \phi_F}{\partial \theta^2} + \left(\frac{n+N}{n+M} \right) \frac{\partial^2 \phi_F}{\partial Z^2} = 0, \quad r < R \quad (3.121)$$

where the solution can be obtained as

$$\phi_F = A_0 \sum_{m=0}^{\infty} \epsilon_m i^m \cos m \theta \left[\sum_{q=0}^{\infty} B_{mq} J_m(\gamma \hat{k}_q r) \frac{\cosh \hat{k}_q (Z+h)}{\cosh \hat{k}_q h} \right], \quad r < R \quad (3.122)$$

in which J_m denotes the Bessel functions of the first kind and ϵ_m is the Jacobi symbol, defined as

$$\epsilon_0 = 1; \quad \epsilon_m = 2 \quad \text{when} \quad m \geq 1 \quad (3.123)$$

The dispersion relationship is as presented in (3.117):

$$1 = \left(\frac{n+N}{n} \right) \hat{k}_q \tanh \hat{k}_q h \quad (q \geq 0) \quad (3.124)$$

where \hat{k}_q are complex roots. Likewise, for open water (with subscript S), (3.51) in cylindrical coordinates becomes

$$\frac{1}{r} \frac{\partial}{\partial r} \left(r \frac{\partial \phi_S}{\partial r} \right) + \frac{1}{r^2} \frac{\partial^2 \phi_S}{\partial \theta^2} + \frac{\partial^2 \phi_S}{\partial Z^2} = 0, \quad r > R \quad (3.125)$$

and the solution can be readily found as

$$\begin{aligned} \phi_S = A_0 \sum_{m=0}^{\infty} \epsilon_m i^m \cos m\theta & \left\{ \left[J_m(k_0 r) + C_{m0} H_m^{(1)}(k_0 r) \right] \frac{\cosh k_0(Z+h)}{\cosh k_0 h} \right\} \\ & + A_0 \sum_{m=0}^{\infty} \epsilon_m i^m \cos m\theta \left[\sum_{p=1}^{\infty} C_{mp} K_m(\kappa_p r) \frac{\cos \kappa_p(Z+h)}{\cos \kappa_p h} \right], \quad r > R \quad (3.126) \end{aligned}$$

in which $H_m^{(1)}$ and K_m respectively denote the Hankel function of the first kind and the modified Bessel function of the second kind. The open water solution in (3.126) includes both incident waves (i.e. the 1st term on the RHS) and scattered waves. The corresponding dispersion relationship is shown in (3.113):

$$1 = k_0 \tanh k_0 h \quad \text{and} \quad 1 = -\kappa_p \tan \kappa_p h \quad (p \geq 1) \quad (3.127)$$

where k_0 and κ_p ($p \geq 1$) are real roots.

Similar to the forest belt problem, the unknown coefficients C_{m0} , C_{mp} and B_{mp} can be determined by applying the matching conditions along $r = R$:

$$\phi_S = \phi_F, \quad -h < Z < 0 \quad (3.128)$$

and

$$\frac{\partial \phi_S}{\partial r} = (n+M) \frac{\partial \phi_F}{\partial r}, \quad -h < Z < 0 \quad (3.129)$$

The detailed derivations are provided in Appendix C.2. The resulting system of equations (C.17), (C.18) and (C.19) is solved numerically.

3.6.2.2 Laboratory experiments

To check the present theoretical/numerical model on the estimation of wave scattering and attenuation by a finite forest region, a series of experiments was conducted in the Directional Wave Basin at the University of Cantabria (Spain) to establish a benchmark database for data-model comparison. The wave basin is 28 m long, 8.6 m wide and 1.2 m deep and is equipped at one end with 10 paddles of a piston-type wave generation system. A gravel beach with a uniform slope (1:12) is used as passive wave absorber at the other end of the wave basin. A circular forest region with 3 m in diameter is placed approximately 10.70 m from the wave machine and consists of 880 rigid circular cylinders, which are made of wood and have 3 cm in diameter. The cylinders are equally spaced in the forest region, forming a regular series of square cells. The cell configuration can be found in Fig.3.1b. The porosity is estimated as 91.27 %. The test layout is shown in Fig.3.16. Two lateral absorbers are installed to reduce the influence of side walls. Totally 22 wave gauges are used to measure the water surface elevation inside and outside of the forest. Several photos taken during the experiments are shown in Fig.3.17. Two water depths with different wave conditions are tested. Table 3.3, 3.4, 3.5 and 3.6 show all the experimental conditions and dimensionless parameters. Only one set of experiments, i.e. Table 3.4 in which the water depth is 40 cm, is presented and discussed herein. The incident wave condition for each case is determined based on the averaged significant wave height from gauges #1, 2 and 3, which are nearest to the wave maker.

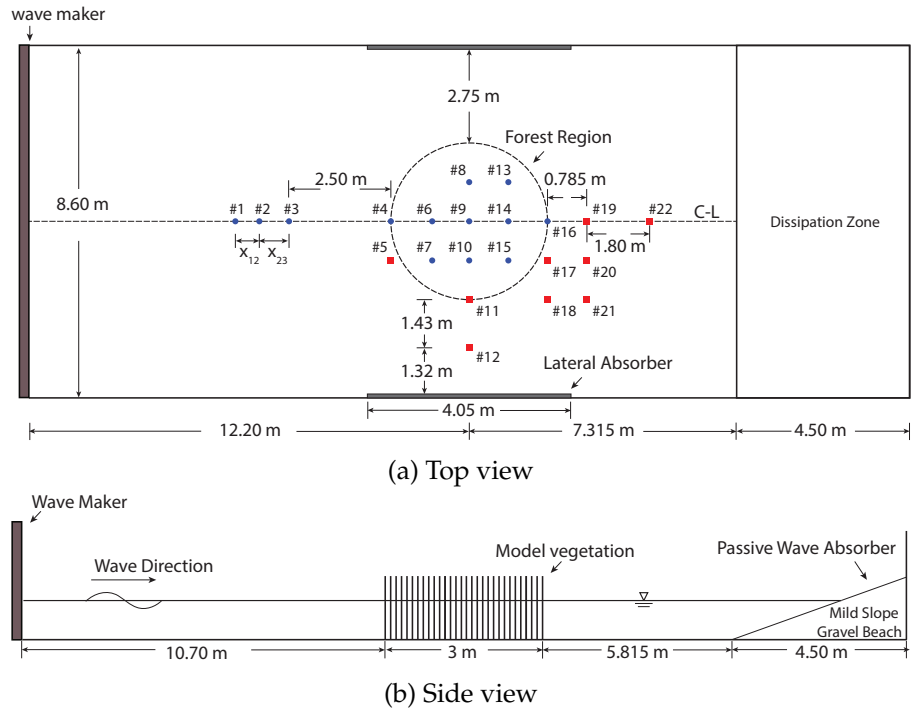


Figure 3.16: Circular forest test layout. In the top view, dots and squares represent the resistive-type and acoustic-type wave gauges, respectively. All the gauges are numbered. C-L denotes the centerline (i.e. $Y = 0$). Note that the distances between wave gauge 1, 2 and 3 (i.e., X_{12} and X_{23}) vary with different wave periods.



Figure 3.17: Photos taken during experiments (provided by University of Cantabria)

Table 3.3: Experimental conditions and dimensionless parameters – Frequency Test I

Case	h_0 (cm)	T (s)	H_{inc} (cm)	L (m)	$k_{inc}h_0$	$k_{inc}A_{inc}$	Re_v	C_D	σ
3F2	30	1.00	4.82	1.3729	1.3729	0.1103	15014.07	2.9408	8.0741E-04
3F3		1.25	5.62	1.8675	1.0094	0.0945	18745.40	2.8931	1.6587E-03
3F4		1.50	5.58	2.3421	0.8048	0.0748	19423.93	2.8866	2.4481E-03
3F5		1.75	5.34	2.8041	0.6722	0.0598	19237.53	2.8883	3.1801E-03
3F6		2.00	5.58	3.2578	0.5786	0.0538	20278.27	2.8790	4.2983E-03
3F7		2.25	5.56	3.7060	0.5086	0.0471	20434.29	2.8776	5.3225E-03
3F8		2.50	5.10	4.1503	0.4542	0.0386	19135.86	2.8893	5.7201E-03
3F9		2.75	5.54	4.5919	0.4105	0.0379	20719.75	2.8753	7.4942E-03

The above h_0 , T and L represent the constant water depth, the incident wave period and wavelength, respectively. The incident wave height H_{inc} is obtained from averaged significant wave height from wave gauges #1, 2 and 3. k_{inc} denotes the incident wavenumber. For all the cases, the diameter of the circular forest is 3 m and the cell porosity is approximately 91.27 %.

Table 3.4: Experimental conditions and dimensionless parameters – Frequency Test II

Case	h_0 (cm)	T (s)	H_{inc} (cm)	L (m)	$k_{inc}h_0$	$k_{inc}A_{inc}$	Re_v	C_D	σ
4F2	40	1.00	4.90	1.4637	1.7170	0.1052	9828.72	3.0883	7.0404E-04
4F3		1.25	5.54	2.0519	1.2249	0.0848	13361.28	2.9696	1.2800E-03
4F4		1.50	5.38	2.6158	0.9608	0.0646	14275.02	2.9460	1.8511E-03
4F5		1.75	5.30	3.1616	0.7949	0.0527	14768.23	2.9342	2.4956E-03
4F6		2.00	5.22	3.6950	0.6802	0.0444	15016.99	2.9284	3.2094E-03
4F7		2.25	5.04	4.2199	0.5956	0.0375	14901.79	2.9311	3.8804E-03
4F8		2.50	5.06	4.7390	0.5303	0.0335	15192.30	2.9244	4.7287E-03
4F9		2.75	5.22	5.2537	0.4784	0.0312	15743.71	2.9123	5.7838E-03

Table 3.5: Experimental conditions and dimensionless parameters – Amplitude Test I

Case	h_0 (cm)	T (s)	H_{inc} (cm)	L (m)	$k_{inc}h_0$	$k_{inc}A_{inc}$	Re_v	C_D	σ
3A2	30	1.00	4.82	1.3729	1.3729	0.1103	15014.07	2.9408	8.0741E-04
3A3		1.00	7.56	1.3729	1.3729	0.1729	21819.78	2.8666	1.4958E-03
3A4		2.50	2.44	4.1503	0.4542	0.0185	9822.17	3.0787	2.2046E-03
3A5		2.50	5.10	4.1503	0.4542	0.0386	19135.86	2.8893	5.7201E-03
3A6		2.50	7.18	4.1503	0.4542	0.0544	25720.44	2.8408	8.7010E-03
3A9		4.00	2.50	6.7757	0.2782	0.0116	10015.90	3.0707	4.9067E-03

Table 3.6: Experimental conditions and dimensionless parameters – Amplitude Test II

Case	h_0 (cm)	T (s)	H_{inc} (cm)	L (m)	$k_{inc}h_0$	$k_{inc}A_{inc}$	Re_v	C_D	σ
4A2	40	1.00	5.54	1.4637	1.7170	0.1189	9828.72	3.0883	7.0404E-04
4A3		1.00	7.22	1.4637	1.7170	0.1550	13673.37	2.9613	1.1784E-03
4A4		2.50	2.26	4.7390	0.5303	0.0150	9822.17	3.0787	2.2046E-03
4A5		2.50	5.06	4.7390	0.5303	0.0335	15192.30	2.9244	4.7287E-03
4A6		2.50	6.94	4.7390	0.5303	0.0460	25720.44	2.8408	8.7010E-03
4A9		4.50	2.66	8.7958	0.2857	0.0095	10015.90	3.0707	4.9067E-03

To check the present model, the measurements on surface elevation within the time record, where only the incident waves are included, shall be used. Namely, the time record in use starts from the first wave until the first reflected wave from the beach arriving at the specific wave gauge. It must be noted that we need to detect the first wave at each gauge with an exclusion of the "ramp-up" or "ramp-down" at the very beginning of wave signals. In the following analysis, the significant wave height is used as the approximate wave height:

$$H_{1/3} = \frac{1}{N_w/3} \sum_{i_w=1}^{N_w/3} H_{i_w} \quad (3.130)$$

where i_w is not the sequence number in the record (i.e. sequence in time). Instead, i_w denotes the rank number of the wave based on the wave height (i.e. $i_w = 1$ represents the highest wave and so on). N_w denotes the number of waves in the time record which only includes incident waves. As mentioned before, averaging the significant wave heights from gauges #1, 2 and 3, which are nearest to the wave maker, gives the incident wave condition for each case:

$$H_{inc} = \frac{1}{3} \sum_{i_{wg}=1}^3 H_{1/3, i_{wg}}, \quad i_{wg} : \text{wave gauge number} \quad (3.131)$$

Accordingly, the incident wave heights for each case in Table 3.3 – 3.6 are determined from (3.131). It is remarked that the relative differences between the

averaged incident wave height, i.e. H_{inc} in (3.131), and the respective significant wave heights from gauges #1, 2, and 3 are within $\pm 5\%$ for all the cases.

3.6.2.3 Numerical results

We first compare the numerical results with the semi-analytical solutions presented in Sec.3.6.2.1 as a preliminary validation of the present model based on the boundary integral equation method. For the circular forest, the outward normal direction of the boundary can be represented by r as shown in Fig.3.18, i.e. $r \equiv \hat{n}_\xi = -\hat{n}_S$. The matching conditions in (3.89) and (3.90) can then be modified as:

$$\frac{\Pi(\hat{k}_q)}{\cosh \hat{k}_q h} (\mathcal{G}_q)_{ij} \left(\frac{\partial \mathcal{A}_q}{\partial r} \right)_j = A_0 \frac{\Gamma_{0q}}{\cosh k_0 h} (e^{ik_0 X_1})_i - \sum_{p=0}^{\infty} \frac{\Gamma_{pq}}{\cosh k_p h} (\mathcal{Q}_p)_{im} \left(\frac{\partial \mathcal{B}_p}{\partial r} \right)_m \quad (3.132)$$

and

$$(n + M) \sum_{q=0}^{\infty} \frac{\Gamma_{qp}}{\cosh \hat{k}_q h} \left(\frac{\partial \mathcal{A}_q}{\partial r} \right)_i = A_0 \delta_{0p} \frac{\Pi(k_0)}{\cosh k_0 h} \left(\frac{\partial e^{ik_0 X_1}}{\partial r} \right)_i + \frac{\Pi(k_p)}{\cosh k_p h} \left(\frac{\partial \mathcal{B}_p}{\partial r} \right)_i \quad (3.133)$$

in which i & $j = 1 \cdots \mathbb{N}_F$ and $m = 1 \cdots \mathbb{N}_S$, where $\mathbb{N}_S = \mathbb{N}_F$ denote the total number of elements along the boundary of the circular forest. A system of equations is then formulated for solving $\partial \mathcal{A}_q / \partial r$ and $\partial \mathcal{B}_p / \partial r$.

To conduct the numerical computations, the discretization of forest boundary has to be done beforehand (e.g. Fig.3.18). Note that for a single homogeneous circular forest, subzone ξ is equivalent to the entire forest region F. Different numbers of boundary elements are examined as a convergence test. Comparing with the semi-analytical solutions in (3.122) and (3.126), the mean relative error (%) of the numerical results over the computational domain for

different discretization resolutions are presented in Fig.3.19a. A part of the dimensionless wave amplitude profiles along the centerline is shown in Fig.3.19b. It can be observed that the numerical results are approaching the semi-analytical solutions when the number of boundary elements is increased, i.e. the central angle is decreased. Therefore, following the convergence test and requiring the mean error lower than 0.1 %, the number of boundary elements for a single circular forest is set as 180 (i.e. $\mathbb{N}_F = 180$) with $\pi/90$ rad as the central angle. Uniform solution along each element is assumed. Once the unknown functions \mathcal{A}_q and \mathcal{B}_p along the boundaries are solved, the wave solutions within the circular forest and open water can be obtained by (3.55), (3.59), (3.61) and (3.65).

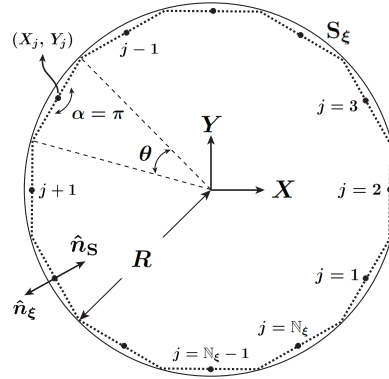


Figure 3.18: Sketch of the discretization of boundary elements (dotted lines) for a homogeneous circular forest patch. A single bulk eddy viscosity and drag coefficient can be yielded. Point (X_j, Y_j) denotes the middle point of j^{th} element with interior angle $\alpha = \pi$ for smooth element. S_ξ denotes the boundary of patch ξ with \hat{n}_ξ and \hat{n}_S showing the outward normal directions from the forest side and the open water region, respectively. In numerical computation, the total number of elements \mathbb{N}_ξ for one single patch is set as 180 with $\theta = 2^\circ$.

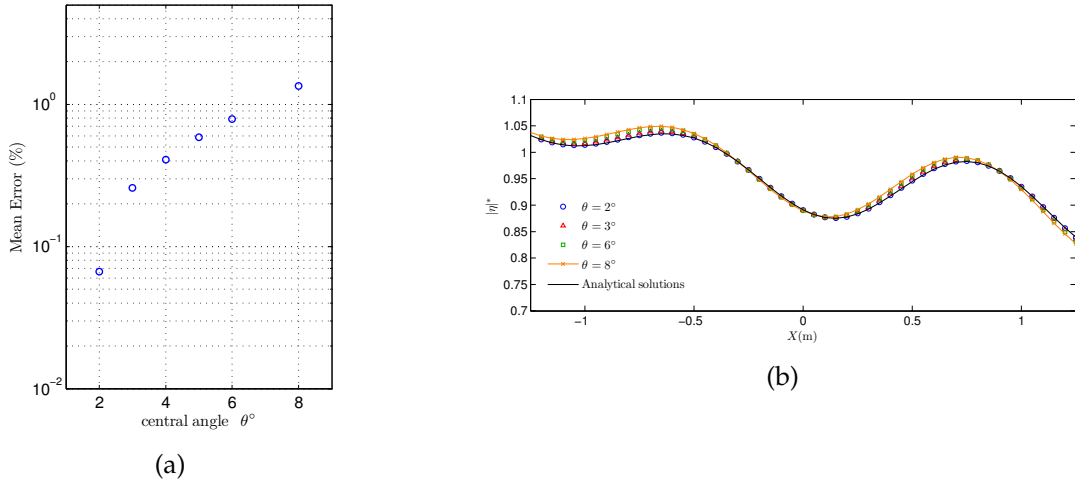


Figure 3.19: Comparison of numerical results for a circular forest by using different resolutions of boundary elements: (a) shows the mean relative error (%) comparing with the semi-analytical solutions in (3.122) and (3.126); (b) shows the dimensionless wave amplitude along the centerline obtained by different discretization.

The instantaneous free surface elevation over both outside and inside the forest region for four different cases are presented in Fig.3.20. Clearly, incident waves are diffracted by the circular forest, while wave amplitudes are reduced because of the energy dissipation inside the forest. The diffracted waves converge behind the circular forest, resulting in a slightly increasing wave amplitude.

We further compare the numerical results with experimental data for those cases given in Table 3.4. As illustrated in Fig.3.21 and 3.22, the comparisons between model results and the laboratory measurements are made along the centerline ($Y = 0$) and the off-centerline ($Y = -R/2$). Note the dimensionless gauge data represents the significant wave height normalized by incident wave height. Overall, the agreement between model results and data is reasonably good. It is also clearly seen in Fig.3.21 and 3.22 that wave scattering and reflection by the forest are not negligible, which cause the oscillatory patterns in

wave amplitude envelopes. It is also not surprising to observe that the forest is a more efficient damper for shorter waves.

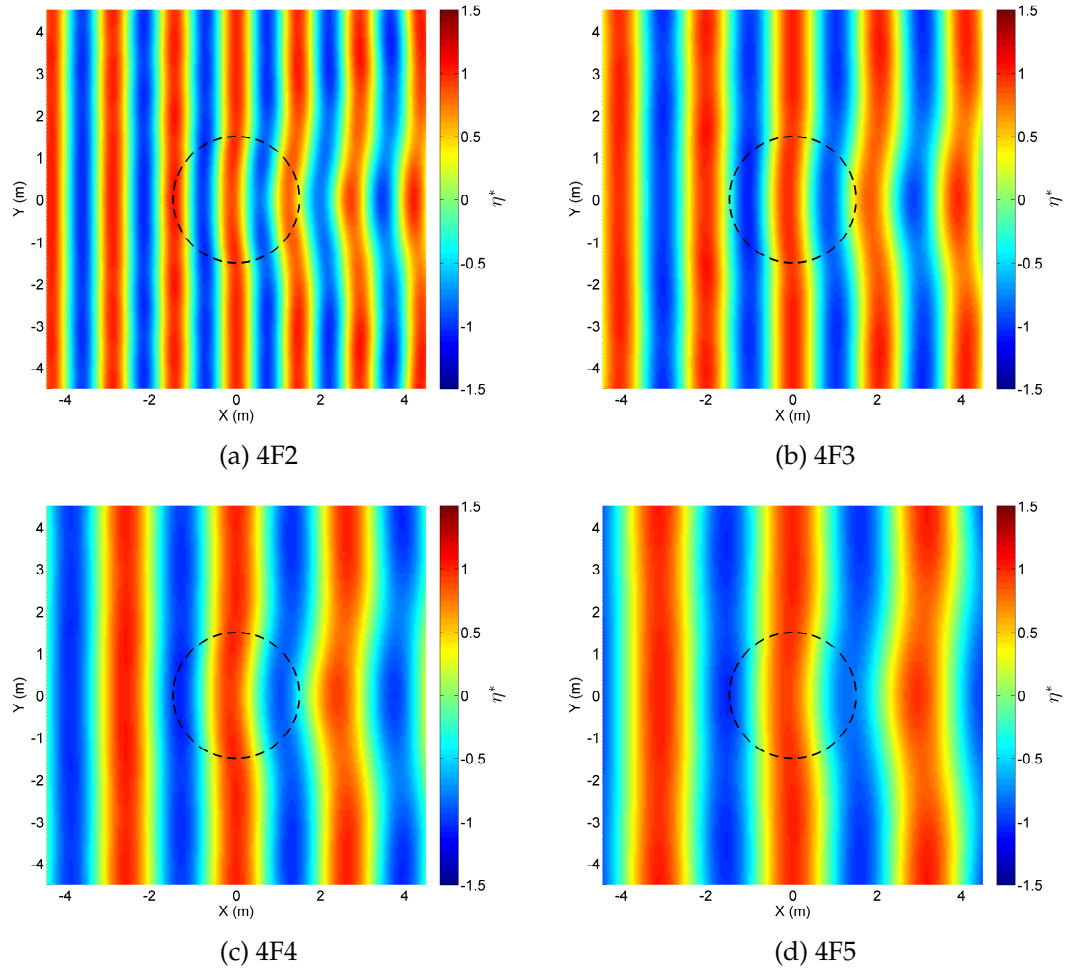
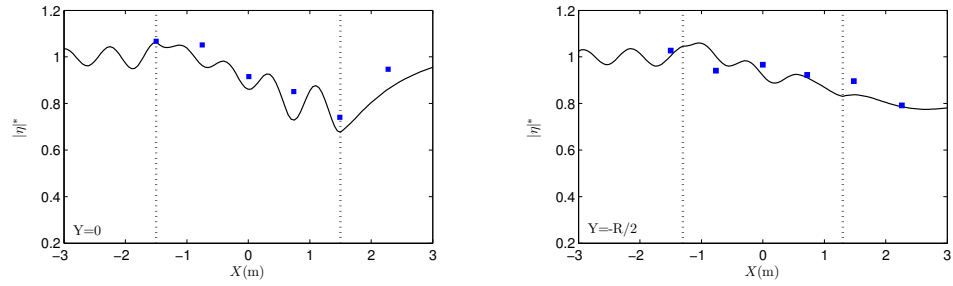
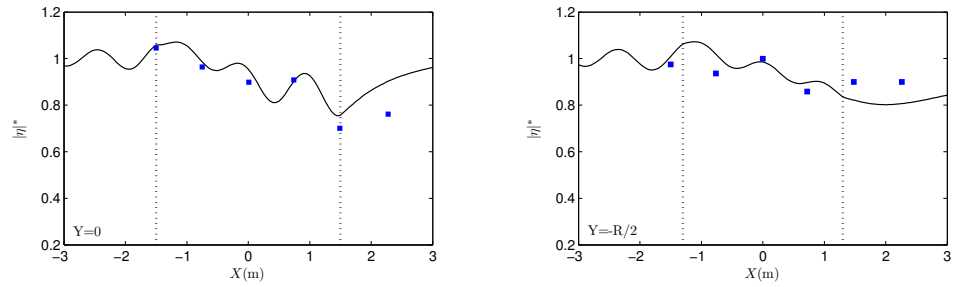


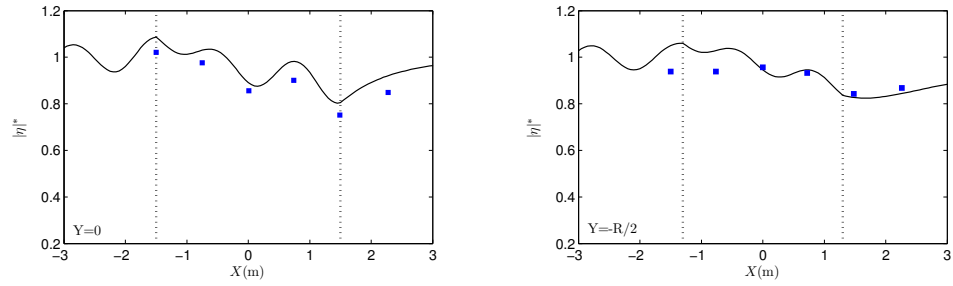
Figure 3.20: Representative snapshots of the dimensionless free surface elevation over the outside and inside forest region at time $t = k_{\Gamma}T$, where k_{Γ} can be any arbitrary integer. The dashed line shows the forest boundary.



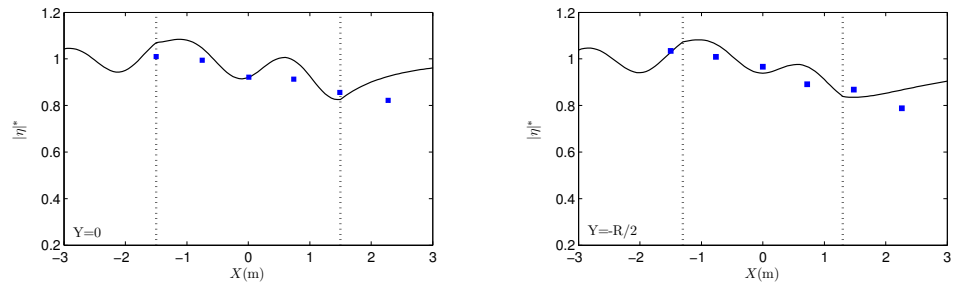
(a) Model results vs. experimental data – Case 4F2



(b) Model results vs. experimental data – Case 4F3

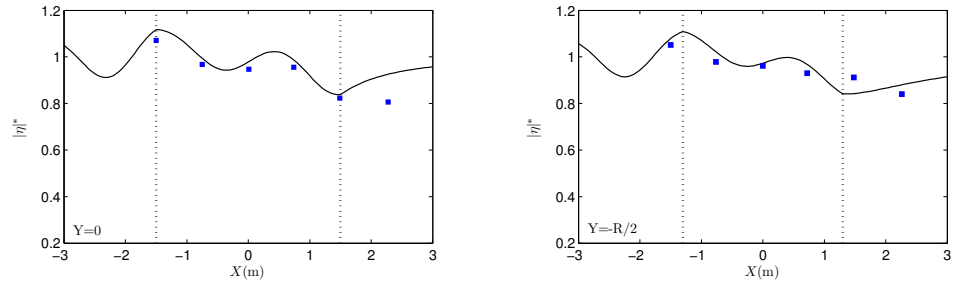


(c) Model results vs. experimental data – Case 4F4

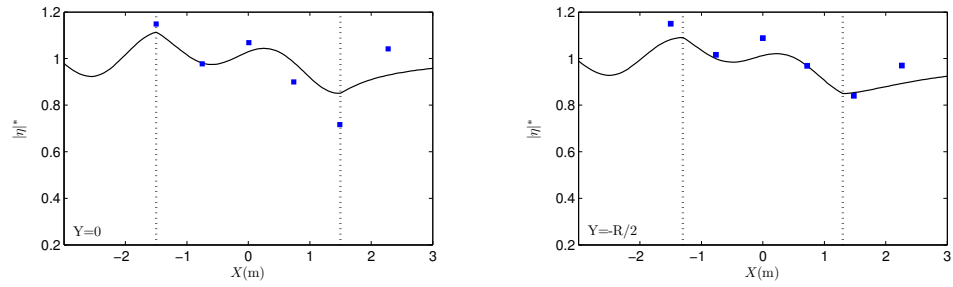


(d) Model results vs. experimental data – Case 4F5

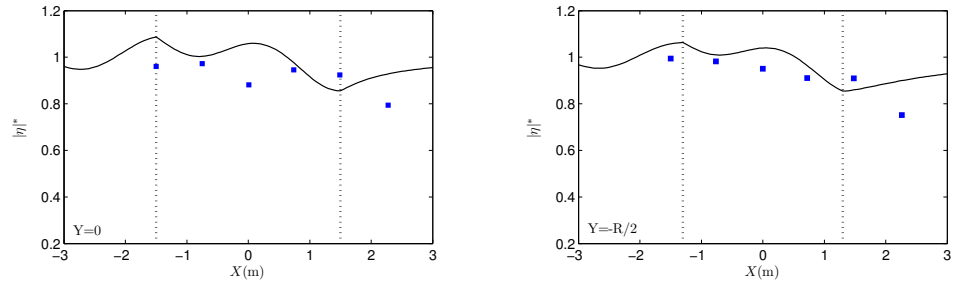
Figure 3.21: Spatial variation of dimensionless wave amplitude inside the circular forest ($|\eta|$) along $Y=0$ and $Y=-R/2$ for cases 4F2 – 4F5. $Y = 0$: WG4, 6, 9, 14, 16, 19; $Y = -R/2$: WG5, 7, 10, 15, 17, 20. Solid squares represent the gauge data; solid lines show the model results; and the dotted lines indicate the forest edges.



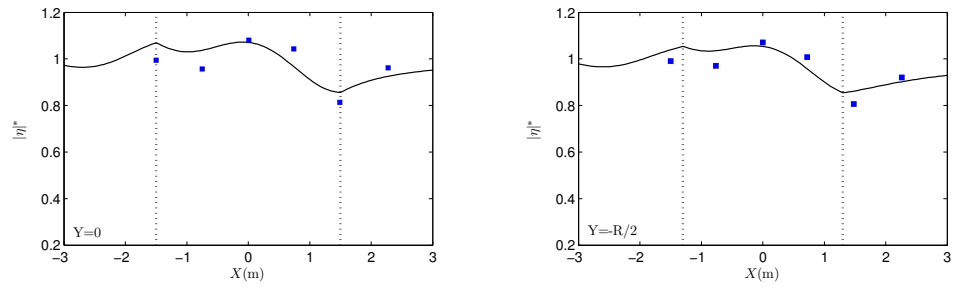
(a) Model results vs. experimental data – Case 4F6



(b) Model results vs. experimental data – Case 4F7



(c) Model results vs. experimental data – Case 4F8



(d) Model results vs. experimental data – Case 4F9

Figure 3.22: Spatial variation of dimensionless wave amplitude inside the circular forest ($|\eta|$) along $Y=0$ and $Y=-R/2$ for cases 4F6 – 4F9. $Y = 0$: WG4, 6, 9, 14, 16, 19; $Y = -R/2$: WG5, 7, 10, 15, 17, 20. Solid squares represent the gauge data; solid lines show the model results; and the dotted lines indicate the forest edges.

As indicated in Table 3.4, the range of Reynolds numbers for this set of experiments is between 9,828 and 15,744, which is within the limits for the drag coefficient formula (3.100). However, the corresponding KC numbers are relatively small, i.e. $KC \leq 5.80$. The discrepancies between experimental data and model results could also be caused by the imperfection of experimental set-up that cannot totally eliminate reflections from the boundaries of wave basin.

Similar to Sec.3.6.1.2, the micro-scale flow fields within cells can be solved by the present model. In Figs.3.23 – 3.25, three different locations along the centerline of the circular forest are selected to present the horizontal velocity fields at the mean water level at different instants. Symmetric eddies are also observed at two sides of the central cylinder when the reversal of wave flows is about to happen. Similar flow patterns can be found in Mei et al. (2014).

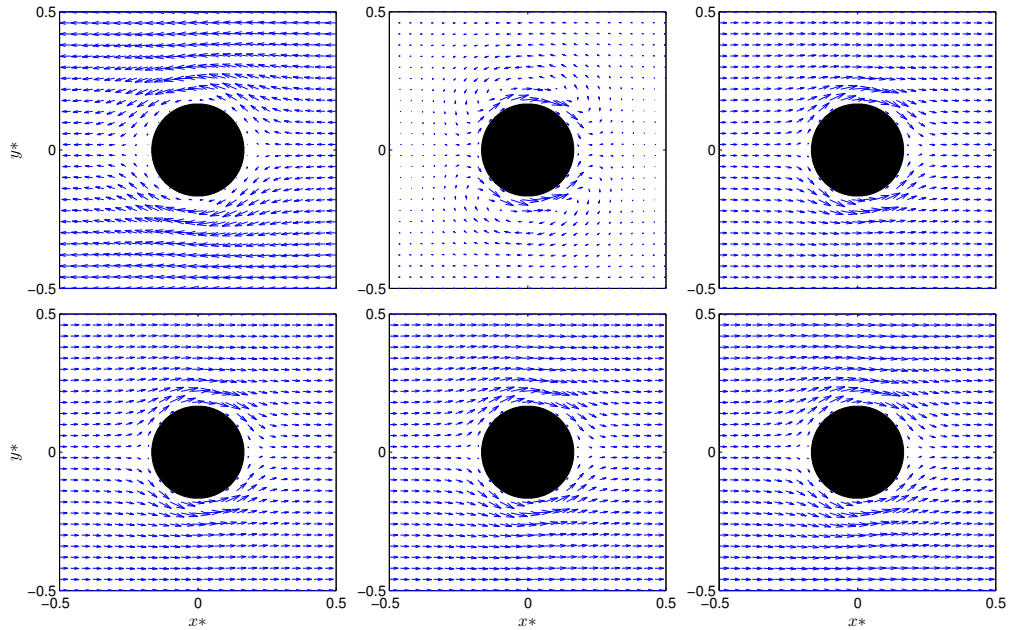


Figure 3.23: Snapshots of horizontal velocity fields at $X = -0.78$ m, $Y = 0.0$ m for Case 4F2 in Table 3.4. From left to right and top to bottom, the dimensionless time is $t/T = 0.13, 0.25, 0.33, 0.35, 0.37, 0.42$.

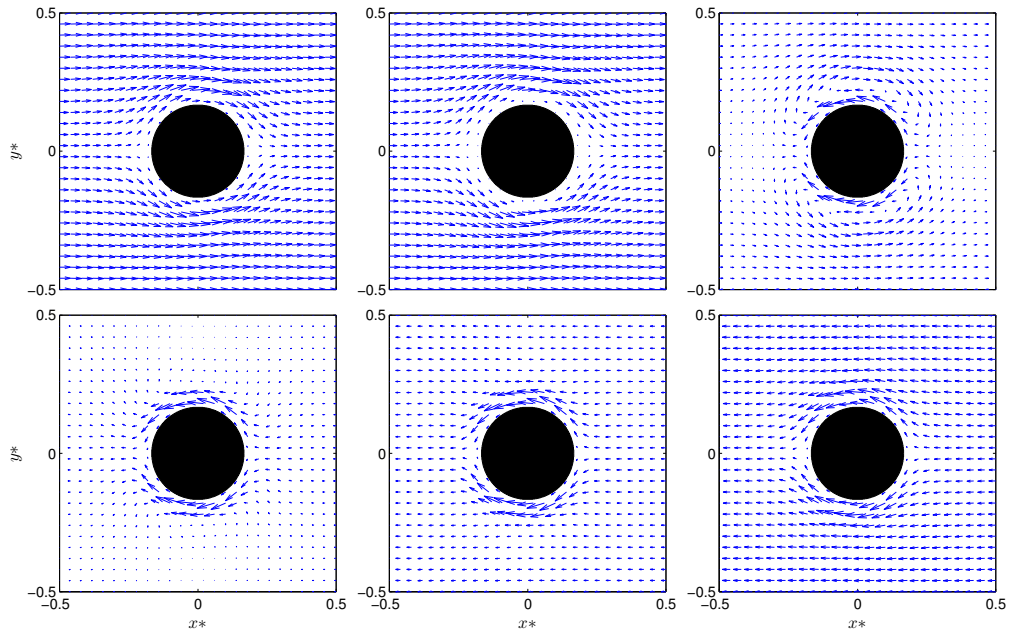


Figure 3.24: Snapshots of horizontal velocity fields at $X = 0.03$ m, $Y = 0.0$ m for Case 4F2 in Table 3.4. From left to right and top to bottom, the dimensionless time is $t/T = 0.13, 0.25, 0.33, 0.35, 0.37, 0.42$.

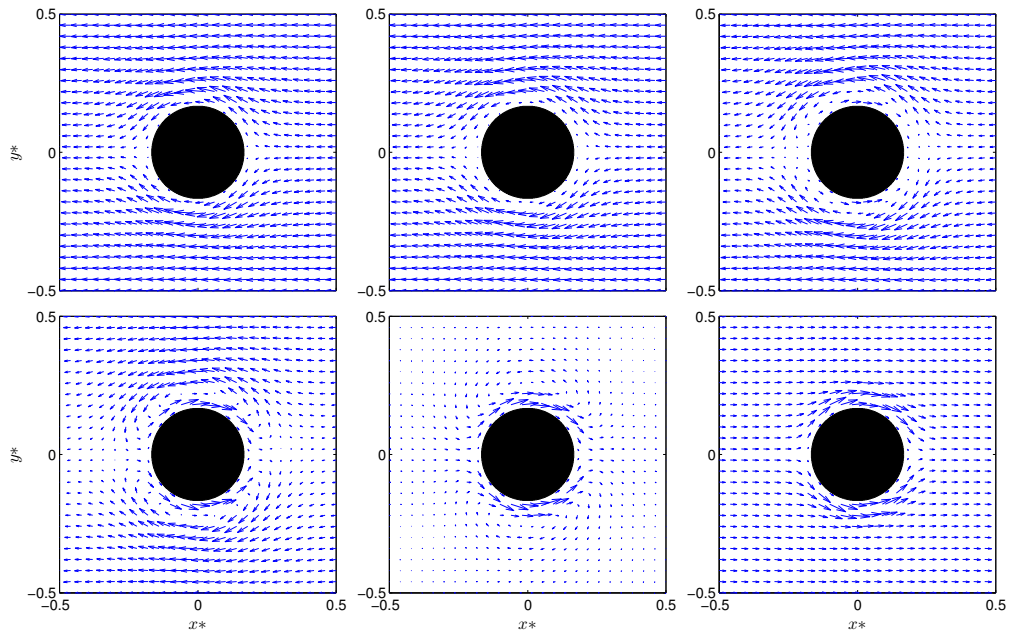


Figure 3.25: Snapshots of horizontal velocity fields at $X = 0.75$ m, $Y = 0.0$ m for Case 4F2 in Table 3.4. From left to right and top to bottom, the dimensionless time is $t/T = 0.13, 0.25, 0.33, 0.35, 0.37, 0.42$.

3.6.3 Water waves scattered by multiple circular forest patches

3.6.3.1 Laboratory experiments

In addition to a single patch, multiple patches is another type of coastal forests commonly existing in fields. To explore the present model further, the experiments on multiple circular patches (Maza 2015) are used as another special configuration. The experiments were also conducted in the Directional Wave Basin at the University of Cantabria in Spain, which is the same facility for the single circular forest experiments in Sec.3.6.2. Different from Fig.3.16, the gravel beach used as a passive wave absorber at the end of wave basin is changed to a uniform slope $\approx 1 : 6.6$. Besides, different arrangements of wave gauges are used in Maza (2015)'s experiments. As shown in Fig.3.26, the forest area, composed of four circular patches, is located around the middle of wave basin. Each patch is 1.0 m in diameter and consists of 112 circular wooden cylinders with 3.0 cm in diameter. The arrangement of cylinders is the same as that applied to the circular forest experiments and can be referred to Fig.3.1b, which provides the porosity as 91.27 %. Totally 29 gauges were used to record the water surface displacement inside and outside of the patches. Only parts of wave gauges are presented in Fig.3.26. The experimental conditions can be found in Table 3.7. The incident wave conditions are estimated based on the time records of wave gauges #1, 2 and 3 (Isaacson 1991).

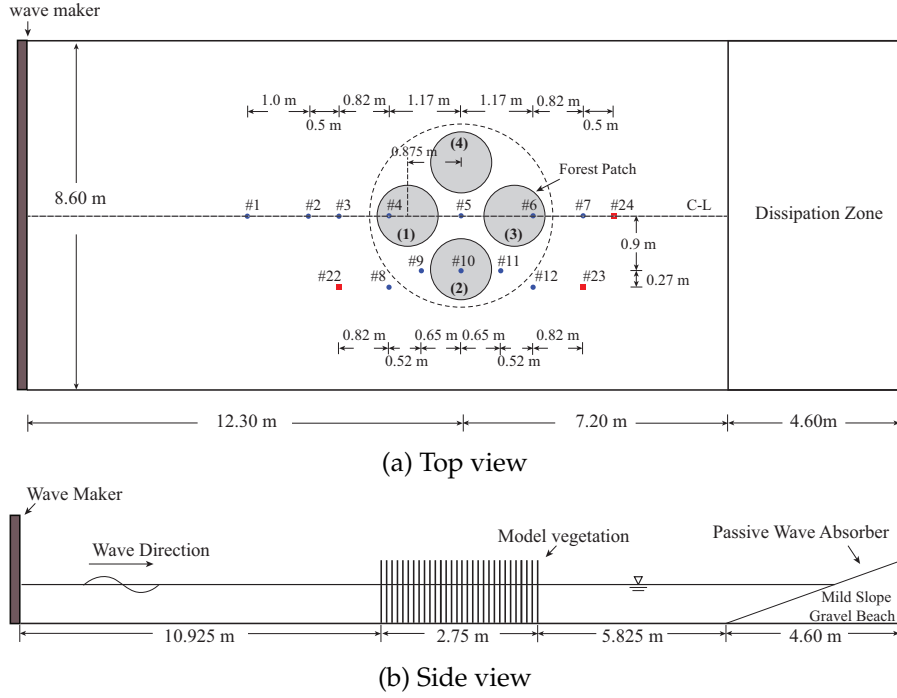


Figure 3.26: Test layout of multiple circular forest patches used in Maza (2015)'s experiments. Each patch is 1.0 m in diameter. The bigger dashed circle indicates the single circular forest in Sec.3.6.2, which has 3.0 m in diameter. Parts of the wave gauges used in the experiments are presented and numbered with dots and squares representing the resistive-type and acoustic-type gauges. The patches are also numbered, i.e. (ξ), $\xi = 1 - 4$. C-L denotes the centerline ($Y = 0$). More details of the experimental setup can be referred to Maza et al. (2015b)'s Fig.8.2 and Table 8.1.

Table 3.7: Experimental conditions and dimensionless parameters for Maza (2015)'s experiments

Case	h_0 (cm)	T (s)	H_{inc} (cm)	L (m)	$k_{inc}h_0$	$k_{inc}A_{inc}$	σ_{cir}
1	30	1.50	5.34	2.3421	0.8048	0.0716	2.4481E-03
2		2.00	4.65	3.2578	0.5786	0.0448	4.2983E-03
3		2.50	4.45	4.1500	0.4542	0.0337	5.7201E-03
4		3.00	5.17	5.0000	0.3770	0.0325	7.4942E-03
5		1.50	11.60	2.3421	0.8048	0.1556	5.9737E-03
6		2.00	9.95	3.2578	0.5786	0.0960	8.5060E-03

The above h_0 , T and L represent the constant water depth, the incident wave period and wavelength, respectively. The incident wave height H_{inc} is obtained from the measurements at wave gauges 1, 2 and 3. k_{inc} denotes the incident wavenumber. The cell porosity is approximately 91.27 %. σ_{cir} is the bulk eddy viscosity given by the numerical results for one single circular forest (Sec.3.6.2).

3.6.3.2 Numerical results

We consider each circular patch as a homogeneous subzone of the entire forest region. Within each patch, the eddy viscosity is assumed as a bulk value but can be different from each other, i.e. σ_ξ with $\xi = 1 \cdots 4$ denoting the indices of patches in Fig.3.26. Thus, the cell problem for each patch has to be solved independently, yielding the corresponding values of the complex coefficients M_ξ , N_ξ and the wavenumber $\hat{k}_{\xi q}$. For each patch (i.e. patch ξ), the outward normal direction of the boundary can be represented by r_ξ as sketched in Fig.3.18 (i.e. $r_\xi \equiv \hat{n}_\xi = -\hat{n}_S$). The matching conditions in (3.89) and (3.90) can then be modified as:

$$\frac{\Pi(\hat{k}_{\xi q})}{\cosh \hat{k}_{\xi q} h} (\mathcal{G}_{\xi q})_{ij} \left(\frac{\partial \mathcal{A}_{\xi q}}{\partial r_\xi} \right)_j = A_0 \frac{\Gamma_{0\xi q}}{\cosh k_0 h} (e^{ik_0 X_1})_i - \sum_{p=0}^{\infty} \frac{\Gamma_{p\xi q}}{\cosh k_p h} (\mathcal{Q}_p)_{im} \left(\frac{\partial \mathcal{B}_p}{\partial r_\xi} \right)_m \quad (3.134)$$

and

$$(n_\xi + M_\xi) \sum_{q=0}^{\infty} \frac{\Gamma_{\xi q p}}{\cosh \hat{k}_{\xi q} h} \left(\frac{\partial \mathcal{A}_{\xi q}}{\partial r_\xi} \right)_i = A_0 \delta_{0p} \frac{\Pi(k_0)}{\cosh k_0 h} \left(\frac{\partial e^{ik_0 X_1}}{\partial r_\xi} \right)_i + \frac{\Pi(k_p)}{\cosh k_p h} \left(\frac{\partial \mathcal{B}_p}{\partial r_\xi} \right)_i \quad (3.135)$$

in which i & $j = 1 \cdots N_\xi$ and $m = 1 \cdots N_S$ with $N_S = \sum_{\xi=1}^4 N_\xi$. A system of equations is formulated for solving $\partial \mathcal{A}_{\xi q} / \partial r_\xi$ and $\partial \mathcal{B}_p / \partial r_\xi$.

Similar to Sec.3.6.2.3, in the numerical computation, the boundary of each forest patch needs to be discretized into elements as shown in Fig.3.18. According to the convergence test in Sec.3.6.2.3, the number of boundary elements for each patch is set as 180 (i.e. $N_\xi = 180$, $\xi = 1 - 4$) with $\pi/90$ rad as the central angle. Totally 720 elements (i.e. $N_S = 720$) are used to discretize the boundary of four circular patches. Uniform solution along each element is assumed. Once the unknown functions $\mathcal{A}_{\xi q}$ and \mathcal{B}_p along the boundaries are solved, the wave

solutions within each patch as well as the open water region can be obtained by (3.55), (3.59), (3.61) and (3.65).

As mentioned above, each patch is considered as a subzone of the entire forest region and should have its own bulk value of eddy viscosity: σ_ξ with $\xi = 1 \dots 4$. Each eddy viscosity can be determined respectively by the energy concept and the iterative scheme introduced in Sec.3.4. Before iterating the eddy viscosity, we first employ the bulk value (shown in Table 3.7) given by the numerical results for one single circular forest (Sec.3.6.2), assigning the value to all the four patches to observe the effects of this special forest configuration on the incoming wave attenuation. Note that the details of estimation on the eddy viscosity and the associated iterative scheme can be found in Sec.3.4.

Totally 6 cases in Maza (2015)'s experiments are tested and the wave conditions are in Table 3.7. For the same wave conditions, Maza (2015) also conducted experiments on one single circular forest as shown in Fig.3.26. The comparisons between model results and experimental data for two forest configurations are presented in Fig.3.27 – 3.30. The corresponding wave gauges can be found in Fig.3.26. In the results, the reduced wave amplitudes due to the energy dissipation inside the forest patches are observed. However, due to the arrangement of wave gauges, it does not allow the detailed comparison. Overall, the agreement over the entire forest region is reasonable. The present model also works well even for the cases with higher nonlinearity (e.g. Case 5 & 6). In Fig.3.27 and 3.28, the effects of incident wave height on wave attenuation are also compared. As presented, larger waves (Case 5 & 6) have higher normalized dissipation rates in comparison with smaller waves (Case 1 & 2). The comparisons of longer waves with reasonable trends are also presented in Fig.3.29 and 3.30. As shown

in Fig.3.26, more cylinders are in use for the single circular forest comparing with four smaller patches in the vegetated area. Thus, it can be observed that the former is more efficient on dissipating the incoming wave energy than the latter. The diffracted waves converged behind the forest region are observed for both configurations, resulting in slightly increasing wave amplitude. While the circular forest is more efficient for damping shorter waves (Sec.3.6.2), it is not clear for multiple patches.

In the present model, a sharp contrast between the wavelength and the tree spacing is required. The leading-order free surface elevation is independent of the micro-scale coordinates and only varies with the macro-scale coordinates. The free surface fluctuation can be captured by the solutions of $O(\varepsilon)$. Ideally, the macro-scale grid size (i.e. $\Delta X_i, i = 1, 2$) in the numerical computations shall be greater than the cylinder spacing (i.e. ℓ) such that a unit cell in the micro-scale computation can be an averaged representative of several real cylinders. However, due to the limitations of laboratory experiments, the current cylinder spacing and the computational grid size are in the same order of magnitude, i.e. $O(\ell) \approx O(\Delta X_i)$. Therefore, a uniform leading-order free surface within a cell in real scale is used to compare with the gauge measurements. In reality, the free surface elevation would vary around cylinders and the wave gauge can only provide instantaneous measurements at a specific location. This might contribute to the discrepancies between numerical results and experimental data. Besides, it could be observed that the wave dissipation becomes lower when the wavelength is larger. This might bring about difficulties in interpreting the accuracy of experimental data. For example, along $Y = -0.9$ m in Fig.3.29 and 3.30, the measured wave amplitude is increasing when propagating through the

forest. Also, the wavelength of case 3 and 4 becomes 4 and 5 times of the smaller patch size. As mentioned above, it is not allowed to compare the wave damping trends in numerical results with measurements due to the lack of available gauges inside each patch.

The snapshots of dimensionless free surface elevation over four forest patches and the open water region for Case 1 are presented in Fig.3.31. Although the incident wavelength is more than twice of the patch size, we can still recognize the diffraction caused by the forest region. Note that the numerical results presented above are based on the bulk eddy viscosity for one single circular forest. However, the eddy viscosity should be different in different patches. To investigate the possible influences of different values of eddy viscosity on the prediction of wave attenuation, Case 1 (in Table 3.7) is used to perform the iterative scheme, which requires that the relative error of the bulk eddy viscosity (σ_ξ) within each patch from two successive iterations has to be sufficiently small (e.g. $\leq 10^{-3}$). The converged values can usually be reached within 10–20 iterations (Sec.3.4). As a result, the iteration yields the dimensionless eddy viscosity for four patches as $[\sigma_1, \sigma_2, \sigma_3, \sigma_4] = [2.4284, 2.3701, 2.2554, 2.3701](\times 10^{-3})$. An insignificant difference (below 0.5%) is observed. It may be noted that the distance between patches and the patch size comparing with the single circular forest may affect the estimation of eddy viscosity and the resultant wave attenuation.

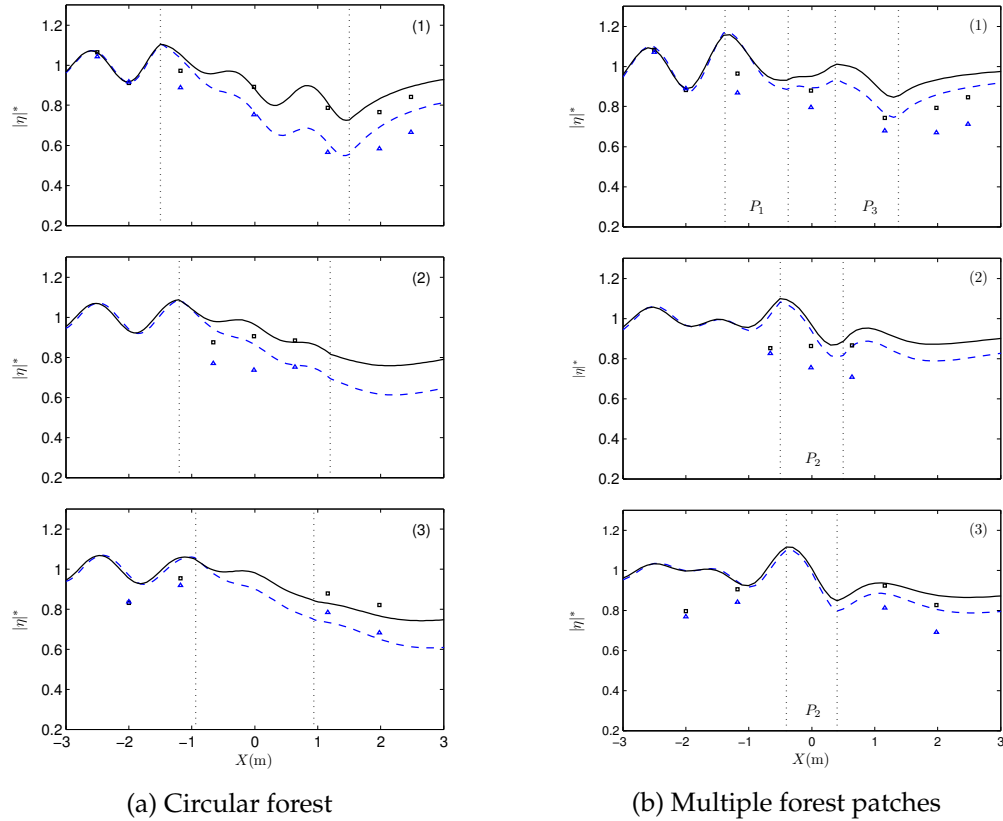


Figure 3.27: Spatial variation of dimensionless wave amplitude I – along (1) $Y = 0$ m (WG2, 3, 4, 5, 6, 7, 24), (2) $Y = -0.9$ m (WG9, 10, 11) and (3) $Y = -1.17$ m (WG22, 8, 12, 23). Two wave heights are compared: Case 1 – solid lines (model predictions) and squares (gauge data); Case 5 – dashed lines (model predictions) and triangles (gauge data). Dotted vertical lines show the forest edges. P_ξ ($\xi = 1 - 4$) denotes the patch index.

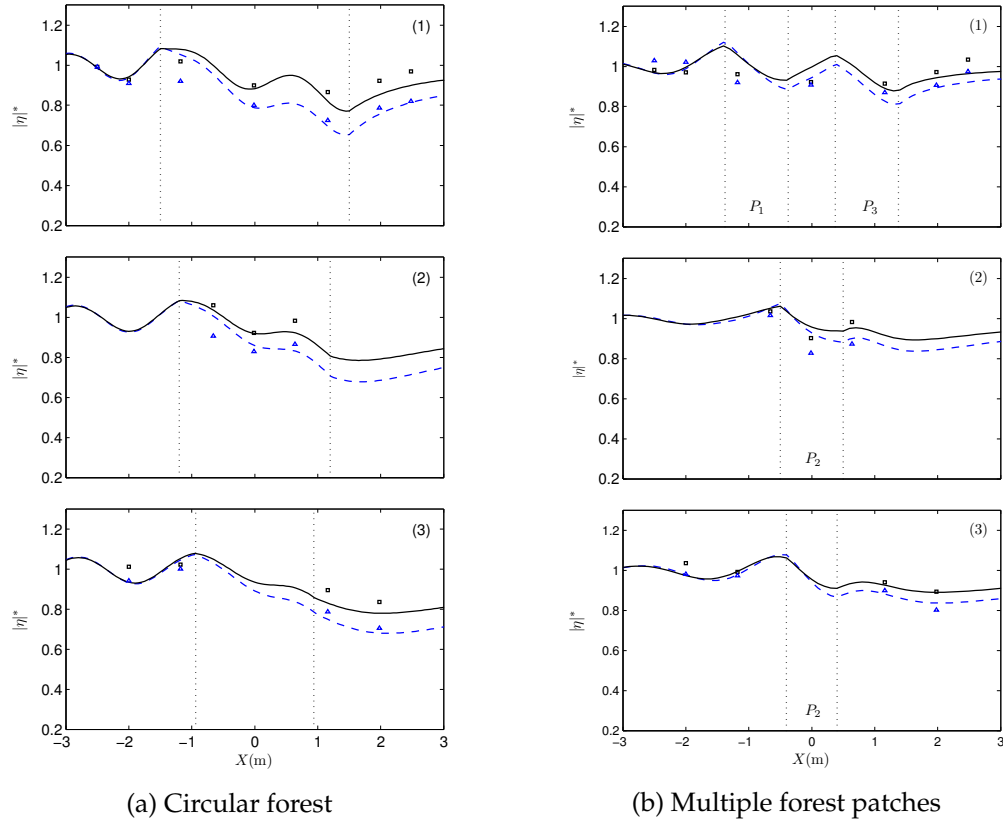


Figure 3.28: Spatial variation of dimensionless wave amplitude II – along (1) $Y = 0$ m (WG2, 3, 4, 5, 6, 7, 24), (2) $Y = -0.9$ m (WG9, 10, 11) and (3) $Y = -1.17$ m (WG22, 8, 12, 23). Two wave heights are compared: Case 2 – solid lines (model predictions) and squares (gauge data); Case 6 – dashed lines (model predictions) and triangles (gauge data). Dotted vertical lines show the forest edges. P_ξ ($\xi = 1 - 4$) denotes the patch index.

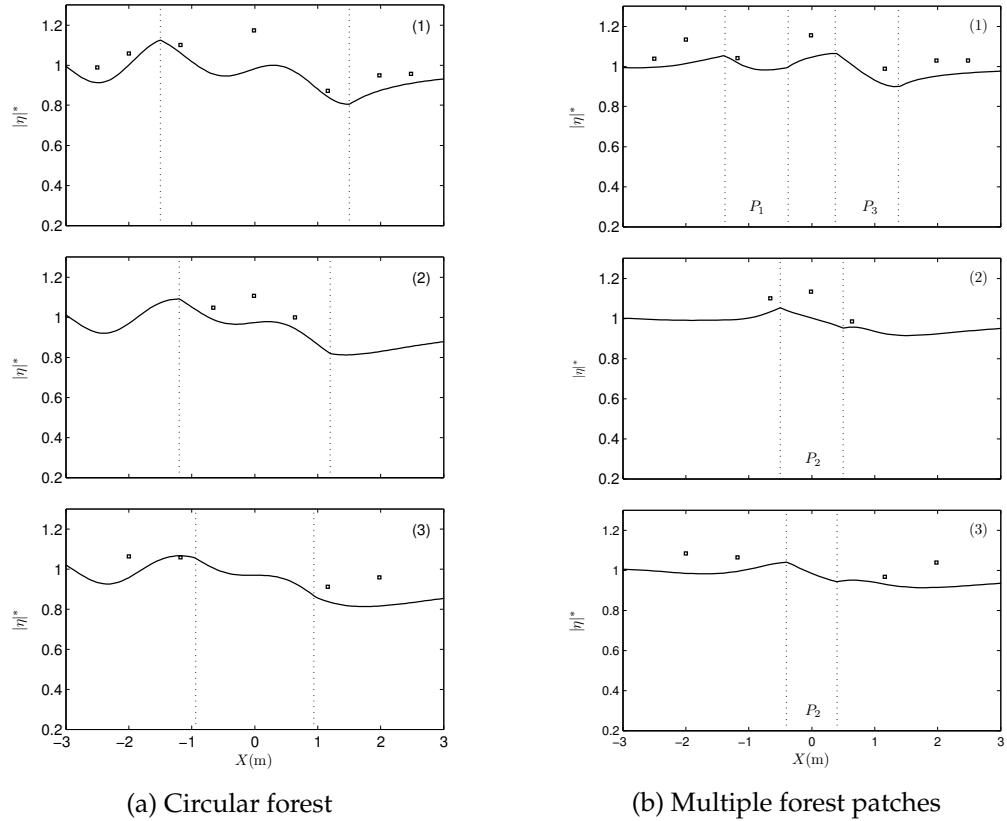


Figure 3.29: Spatial variation of dimensionless wave amplitude III – along (1) $Y = 0$ m (WG2, 3, 4, 5, 6, 7, 24), (2) $Y = -0.9$ m (WG9, 10, 11) and (3) $Y = -1.17$ m (WG22, 8, 12, 23). Case 3 – solid lines (model predictions) and squares (gauge data). Dotted vertical lines show the forest edges. P_ξ ($\xi = 1 - 4$) denotes the patch index.

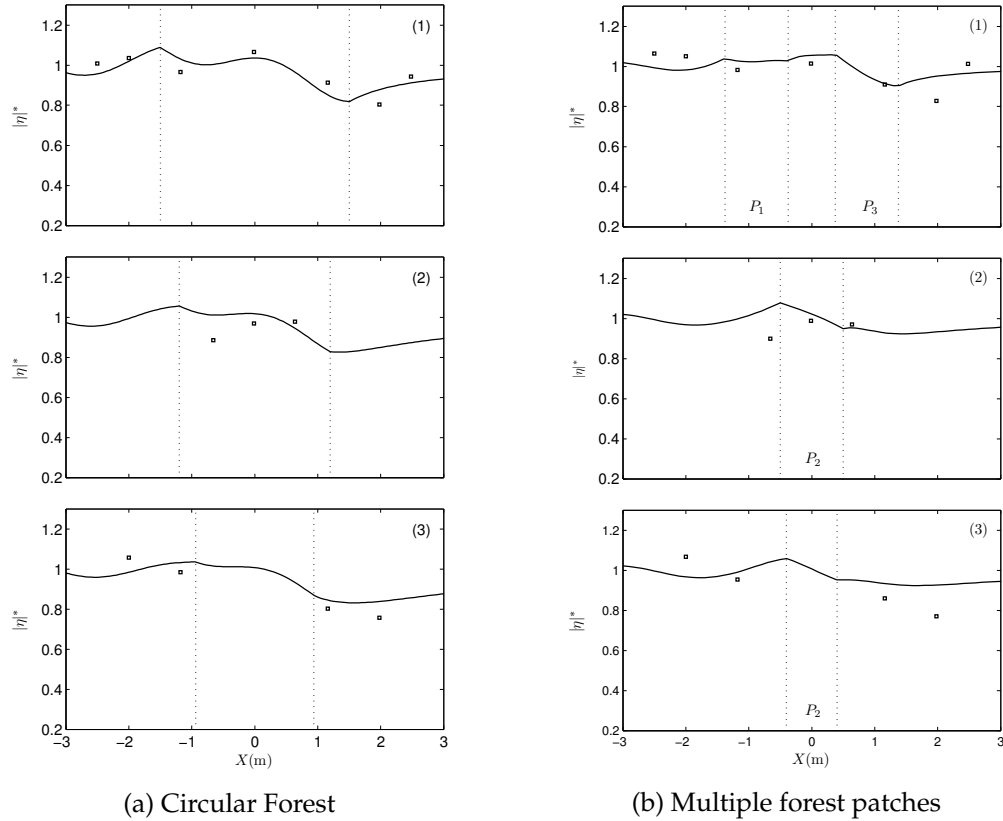


Figure 3.30: Spatial variation of dimensionless wave amplitude III – along (1) $Y = 0$ m (WG2, 3, 4, 5, 6, 7, 24), (2) $Y = -0.9$ m (WG9, 10, 11) and (3) $Y = -1.17$ m (WG22, 8, 12, 23). Case 4 – solid lines (model predictions) and squares (gauge data). Dot-dashed vertical lines show the forest edges. P_ξ ($\xi = 1 - 4$) denotes the patch index.

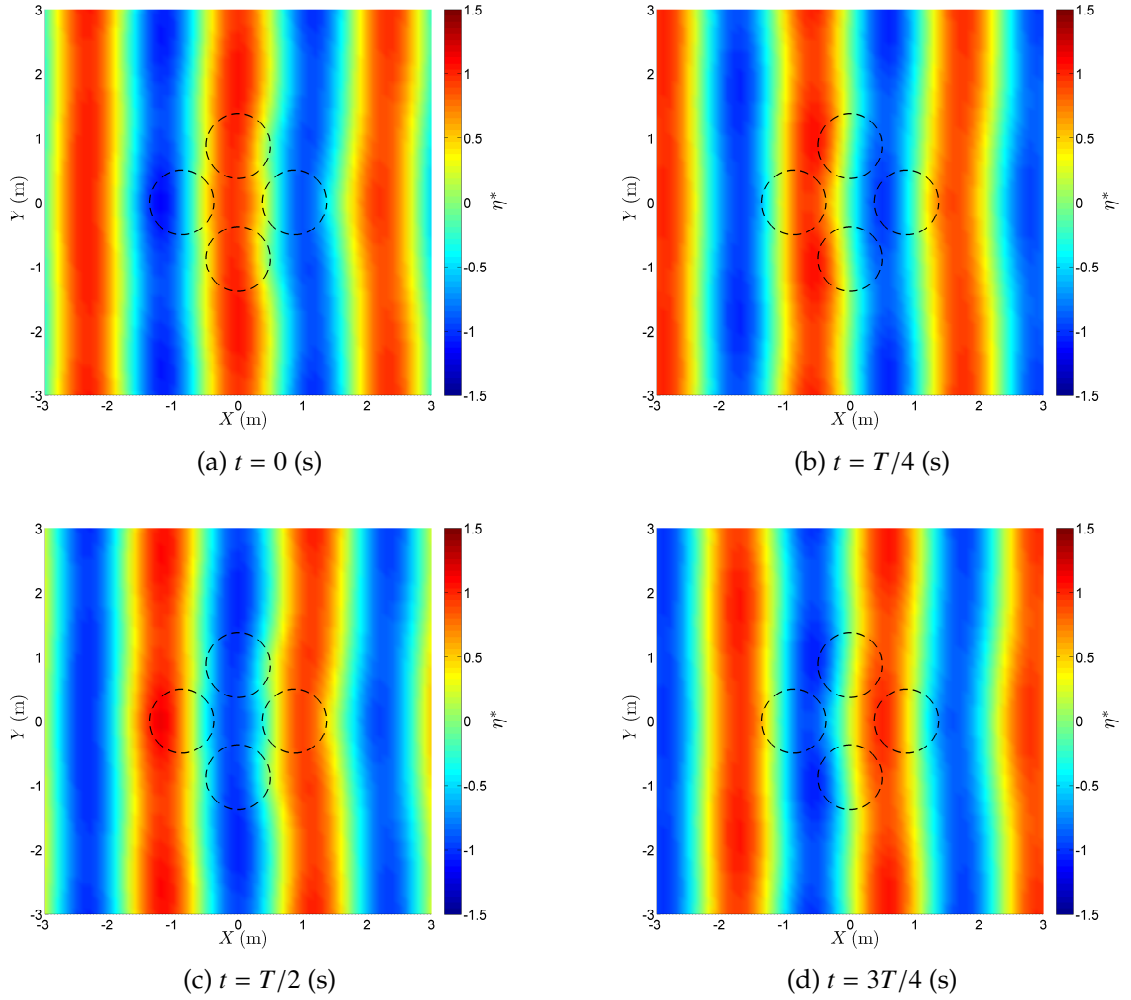


Figure 3.31: Snapshots of the dimensionless free surface elevation over the outside and inside forest region at different times. The incident wave condition has $T = 1.50$ s and $H_{\text{inc}} = 5.34$ cm with constant water depth $h_0 = 30$ cm. The dashed line shows the boundary of the forest patches.

3.6.4 Model demonstration

To demonstrate the capability of the present model, here we select two different non-circular forest configurations. Applying the same cylinder arrangement and cell porosity as used for Sec.3.6.3.1, the dissipation of wave ampli-

tude through a single rectangular patch (Fig.3.32) and two separated rectangular patches (Fig.3.33) can both be observed. In addition, the diffraction of propagating waves for these two forest configurations is being captured by the present model. Note again that the discretization of forest boundary is required to be prepared before performing the computations.

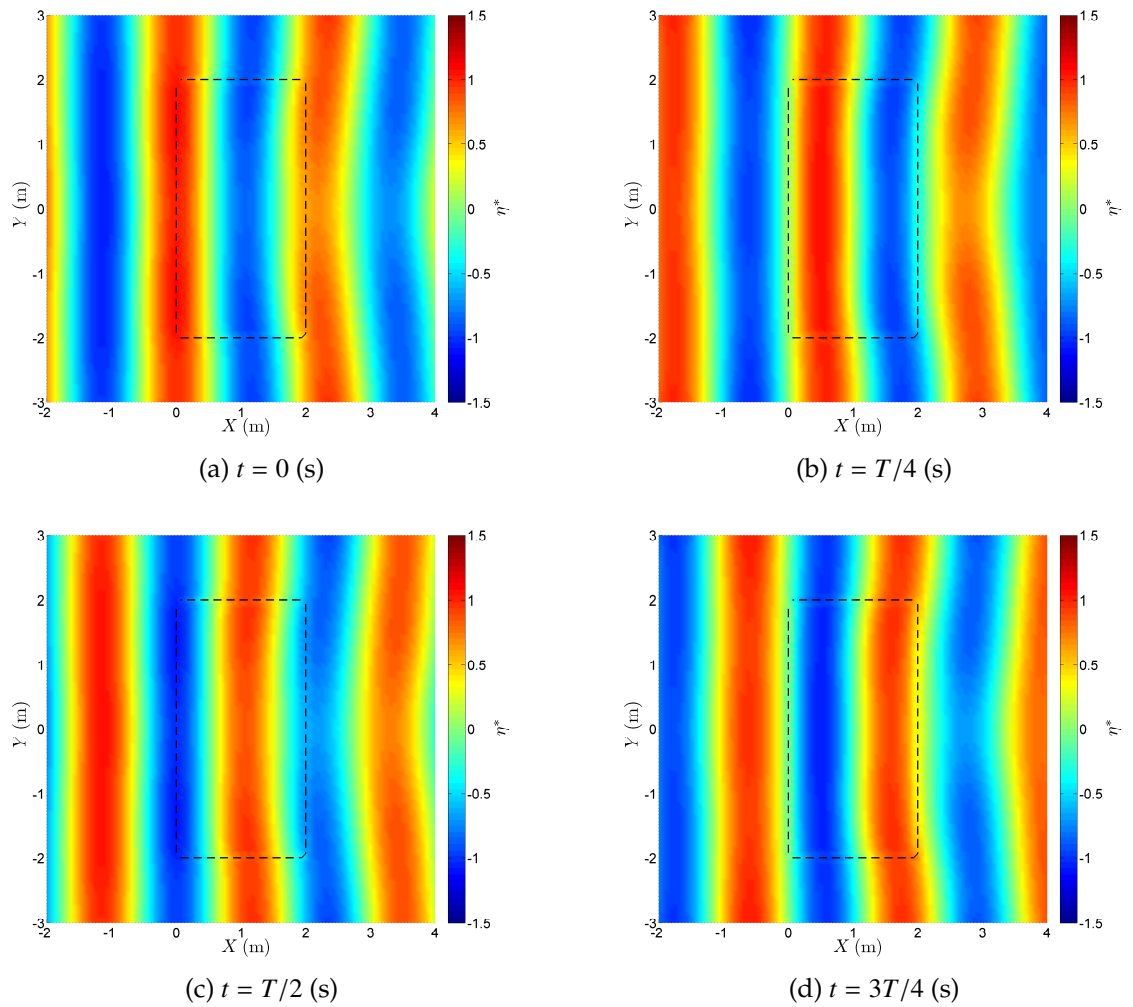


Figure 3.32: Snapshots of dimensionless free surface elevation over one rectangular forest within one wave period. The incident wave condition has $T = 1.50$ s and $H_{\text{inc}} = 5.34$ cm with constant water depth $h_0 = 30$ cm. The dashed line shows forest boundary.

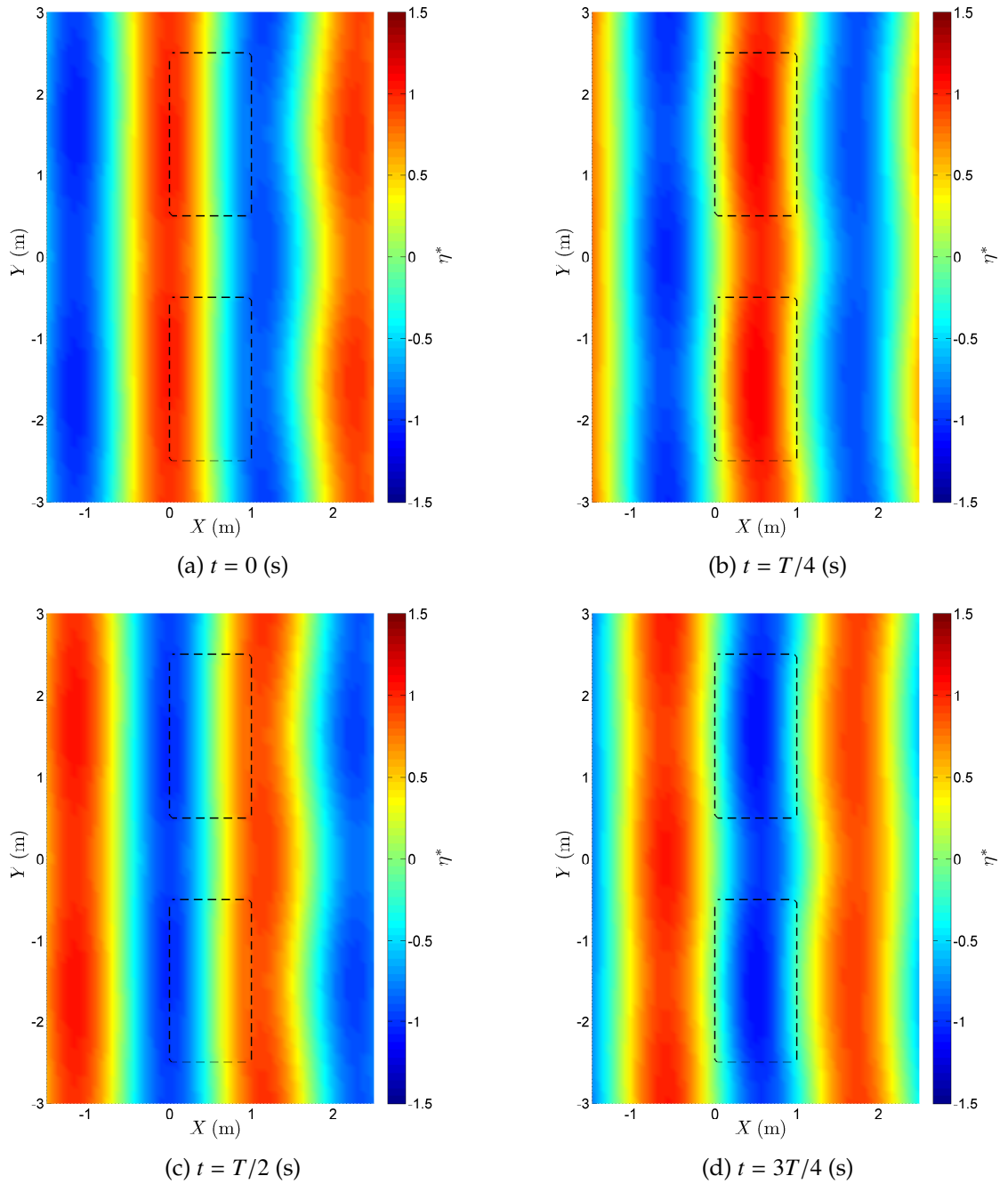


Figure 3.33: Snapshots of dimensionless free surface elevation over two rectangular patches within one wave period. The incident wave condition has $T = 1.50$ s and $H_{\text{inc}} = 5.34$ cm with constant water depth $h_0 = 30$ cm. The dashed line shows the boundary of the forest patches.

In addition to multiple patches, a single circular region with two subzones

as sketched in Fig.3.34 is used to demonstrate the numerical results. The semi-analytical solutions can be obtained as presented in Sec.3.6.2.1. For open water, the solution is in (3.126):

$$\begin{aligned} \phi_S = A_0 \sum_{m=0}^{\infty} \epsilon_m i^m \cos m\theta & \left\{ \left[J_m(k_0 r) + C_{m0} H_m^{(1)}(k_0 r) \right] \frac{\cosh k_0(Z+h)}{\cosh k_0 h} \right\} \\ & + A_0 \sum_{m=0}^{\infty} \epsilon_m i^m \cos m\theta \left[\sum_{p=1}^{\infty} C_{mp} K_m(\kappa_p r) \frac{\cos \kappa_p(Z+h)}{\cos \kappa_p h} \right], \quad r > R \quad (3.136) \end{aligned}$$

in which J_m , $H_m^{(1)}$ and K_m represent respectively the Bessel function of the first kind, the Hankel function of the first kind and the modified Bessel function of the second kind. ϵ_m is the Jacobi symbol, defined in (3.123): $\epsilon_0 = 1$ and $\epsilon_m = 2$ when $m \geq 1$. Note that $k_p = i\kappa_p$ (when $p \geq 1$). For two subzones, the solutions are

$$\begin{aligned} \phi_1 = A_0 \sum_{m=0}^{\infty} \epsilon_m i^m \cos m\theta & \left\{ \sum_{q=0}^{\infty} \left[B_{mq} J_m(\gamma_1 \hat{k}_{1q} r) + B'_{mq} Y_m(\gamma_1 \hat{k}_{1q} r) \right] \frac{\cosh \hat{k}_{1q}(Z+h)}{\cosh \hat{k}_{1q} h} \right\}, \\ & R_2 < r < R \quad (3.137) \end{aligned}$$

and

$$\phi_2 = A_0 \sum_{m=0}^{\infty} \epsilon_m i^m \cos m\theta \left[\sum_{e=0}^{\infty} D_{me} J_m(\gamma_2 \hat{k}_{2e} r) \frac{\cosh \hat{k}_{2e}(Z+h)}{\cosh \hat{k}_{2e} h} \right], \quad r < R_2 \quad (3.138)$$

where Y_m denotes the Bessel function of the second kind. The dispersion relationships for \hat{k}_{1q} and \hat{k}_{2e} are respectively

$$1 = \left(\frac{n_1 + N_1}{n_1} \right) \hat{k}_{1q} \tanh \hat{k}_{1q} h \quad \text{and} \quad 1 = \left(\frac{n_2 + N_2}{n_2} \right) \hat{k}_{2e} \tanh \hat{k}_{2e} h \quad (3.139)$$

The matching conditions along the exterior boundary (i.e. $r = R$) are in (3.66) and (3.68) while the conditions along the interface between two subzones (i.e. $r = R_2$) are in (3.75) and (3.77). With the application of orthogonality as pre-

sented in (3.70), (3.73) and (3.74), a system of algebraic equations can be obtained for solving the unknown coefficients C_{m0} , C_{mp} , B_{mq} , B'_{mq} and D_{me} :

$$[\mathbb{A}] \{\mathbb{C}\} = \{\mathbb{RHS}\} \quad (3.140)$$

in which

$$\mathbb{C} = \begin{Bmatrix} C_{m0} \\ C_{mp} \\ B_{mq} \\ B'_{mq} \\ D_{me} \end{Bmatrix} \quad \text{and} \quad \mathbb{RHS} = \begin{Bmatrix} -J_m(k_0 R) \frac{\Gamma_{01q}}{\cosh k_0 h} \\ \mathbf{0} \\ j_m(k_0 R) \frac{\Pi(k_0)}{\cosh k_0 h} \\ \mathbf{0} \\ \mathbf{0} \end{Bmatrix}. \quad (3.141)$$

The nonzero elements of the coefficient matrix \mathbb{A} are

$$\begin{aligned} \mathbb{A}_{11} &= H_m^{(1)}(k_0 R) \frac{\Gamma_{01q}}{\cosh k_0 h}, & \mathbb{A}_{12} &= \sum_{p=1}^{n_p} K_m(\kappa_p R) \frac{\Gamma_{p1q}}{\cos \kappa_p h} \\ \mathbb{A}_{13} &= -J_m(\gamma_1 \hat{k}_{1q} R) \frac{\Pi(\hat{k}_{1q})}{\cosh \hat{k}_{1q} h}, & \mathbb{A}_{14} &= -Y_m(\gamma_1 \hat{k}_{1q} R) \frac{\Pi(\hat{k}_{1q})}{\cosh \hat{k}_{1q} h}, \\ \mathbb{A}_{22} &= -\dot{K}_m(\kappa_p R) \frac{\Pi(\kappa_p)}{\cos \kappa_p h}, & \mathbb{A}_{23} &= M'_1 \sum_{q=0}^{n_q} j_m(\gamma_1 \hat{k}_{1q} R) \frac{\Gamma_{p1q}}{\cosh \hat{k}_{1q} h}, \\ \mathbb{A}_{24} &= M'_1 \sum_{q=0}^{n_q} \dot{Y}_m(\gamma_1 \hat{k}_{1q} R) \frac{\Gamma_{p1q}}{\cosh \hat{k}_{1q} h}, & \mathbb{A}_{31} &= -\dot{H}_m^{(1)}(k_0 R) \frac{\Pi(k_0)}{\cosh k_0 h}, \\ \mathbb{A}_{33} &= M'_1 \sum_{q=0}^{n_q} j_m(\gamma_1 \hat{k}_{1q} R) \frac{\Gamma_{01q}}{\cosh \hat{k}_{1q} h}, & \mathbb{A}_{34} &= M'_1 \sum_{q=0}^{n_q} \dot{Y}_m(\gamma_1 \hat{k}_{1q} R) \frac{\Gamma_{01q}}{\cosh \hat{k}_{1q} h}, \\ \mathbb{A}_{43} &= \sum_{q=0}^{n_q} J_m(\gamma_1 \hat{k}_{1q} R_2) \frac{\Gamma_{1q2e}}{\cosh \hat{k}_{1q} h}, & \mathbb{A}_{44} &= \sum_{q=0}^{n_q} Y_m(\gamma_1 \hat{k}_{1q} R_2) \frac{\Gamma_{1q2e}}{\cosh \hat{k}_{1q} h}, \\ \mathbb{A}_{45} &= -J_m(\gamma_2 \hat{k}_{2e} R_2) \frac{\Pi(\hat{k}_{2e})}{\cosh \hat{k}_{2e} h}, & \mathbb{A}_{53} &= -M'_1 j_m(\gamma_1 \hat{k}_{1q} R_2) \frac{\Pi(\hat{k}_{1q})}{\cosh \hat{k}_{1q} h}, \\ \mathbb{A}_{54} &= -M'_1 \dot{Y}_m(\gamma_1 \hat{k}_{1q} R_2) \frac{\Pi(\hat{k}_{1q})}{\cosh \hat{k}_{1q} h}, & \mathbb{A}_{55} &= M'_2 \sum_{e=0}^{n_e} j_m(\gamma_2 \hat{k}_{2e} R_2) \frac{\Gamma_{2e1q}}{\cosh \hat{k}_{2e} h} \end{aligned}$$

where $M'_1 \equiv n_1 + M_1$ and $M'_2 \equiv n_2 + M_2$. Other elements (i.e. \mathbb{A}_{15} , \mathbb{A}_{21} , \mathbb{A}_{25} , \mathbb{A}_{32} , \mathbb{A}_{35} , \mathbb{A}_{41} , \mathbb{A}_{42} , \mathbb{A}_{51} & \mathbb{A}_{52}) are all zeros. The derivatives of Bessel functions of the first and second kind are defined in (C.15) while the derivatives of modified Bessel function and Hankel function can be found in (C.16). The functions Π

and Γ have been introduced in (3.73) and (3.74). It should also be noted that the infinite p , q and e need to be truncated to finite numbers, i.e. n_p , n_q and n_e . Once the unknown coefficients are solved, the wave solutions for different zones can then be obtained by (3.136), (3.137) and (3.138).

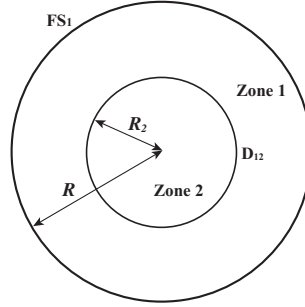


Figure 3.34: Sketch of a single circular patch with two subzones. D_{12} shows the interfaces and FS_1 indicates the exterior boundary adjacent to the open water region. The cell configuration for Zone 1 is the same as that used in Sec.3.6.2 – $\ell = 9$ cm, $d = 3$ cm, and the porosities $n = 0.9127$. Two special configurations are applied to Zone 2: $n = 0$ (solid) and $n = 1$ (empty).

In the following, the incident waves with period $T = 1.00$ s and wave height $H_{inc} = 4.89$ cm under a constant water depth $h_0 = 40$ cm are used for demonstration. The radius of Zone 2 is set as $R_2 = R/2$. Two special configurations for Zone 2 are applied – (I) an impermeable region ($n = 0$) ; (II) an empty region ($n = 1$). As shown in Fig.3.35, the inner zone is assumed as a solid area such that zero fluxes normal to the inner boundary (R_2) is required, i.e. $\partial\phi_1/\partial r = 0$. For this case, no solutions for Zone 2 is needed. Fig.3.36 shows the spatial variation of dimensionless wave amplitude along different profiles. It can be observed that the wave scattering by the solid Zone 2 alters the wave fields in Zone 1 as well as the open water region. For example, along the centerline $Y = 0$ m, the reflected waves by the solid wall of Zone 2 directly result in an increased

wave amplitude as shown in Fig.3.36a(1). The scattered waves by Zone 2 can also be observed in Fig.3.36. The wave diffraction converging behind Zone 2 is observed as well. In this case, Zone 1 dissipates both the incident waves and the scattered waves by Zone 2. On the other hand, assuming no cylinders in Zone 2, the dimensionless wave fields are presented in Fig.3.37. The spatial variation of dimensionless wave amplitude along different profiles is shown in Fig.3.38 in comparison with the solution for a homogeneous forest. Without cylinders in Zone 2, the diffracted waves over the forest region are not as obvious as those for a homogeneous patch.

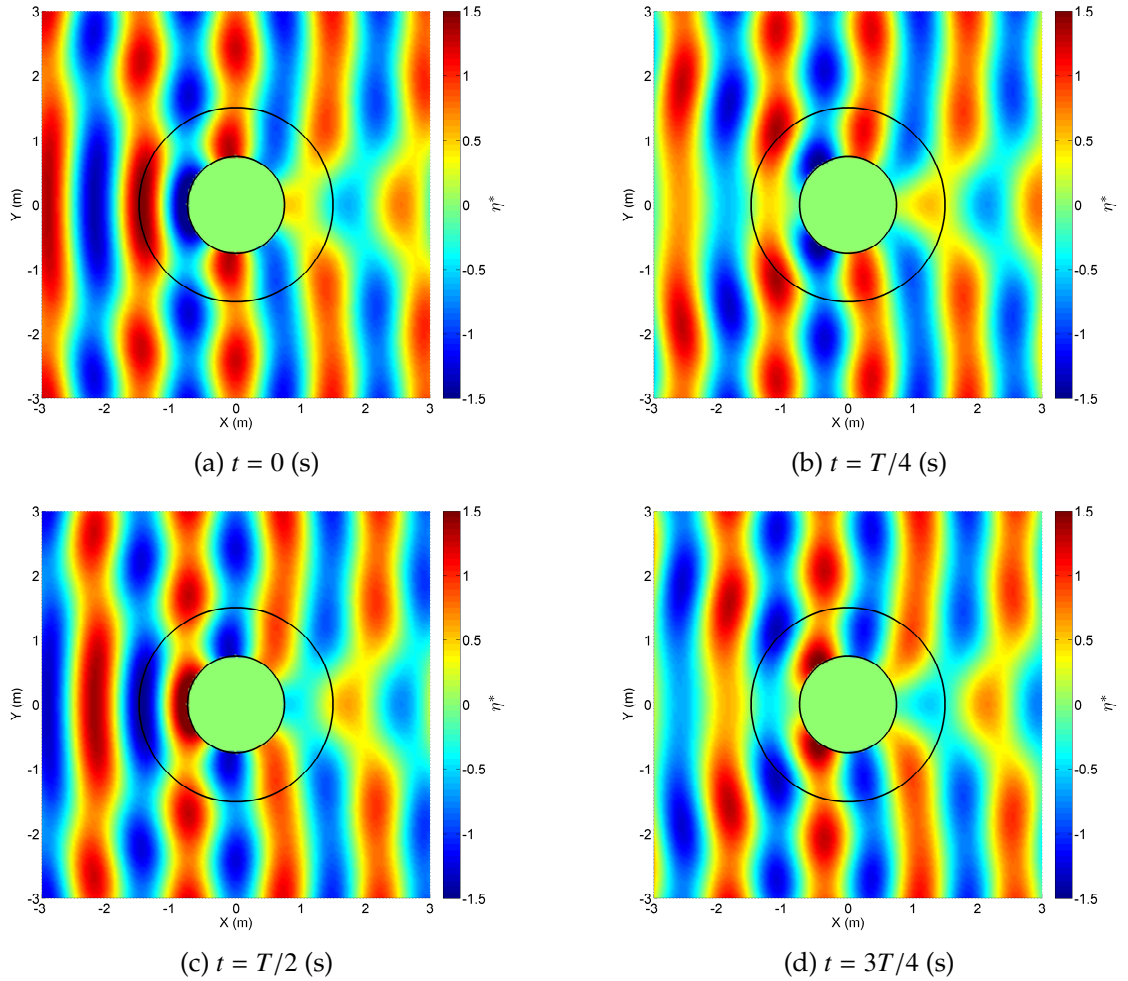
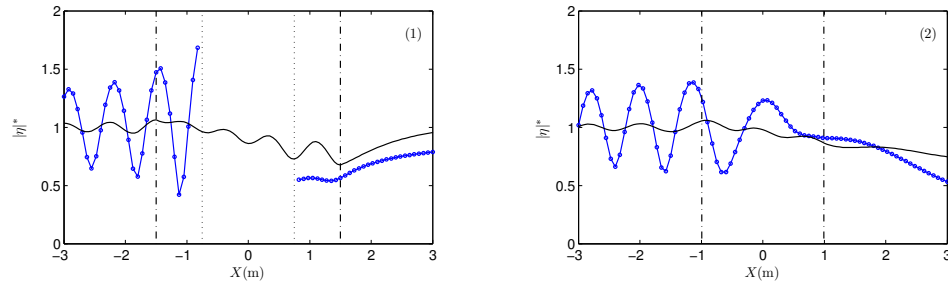
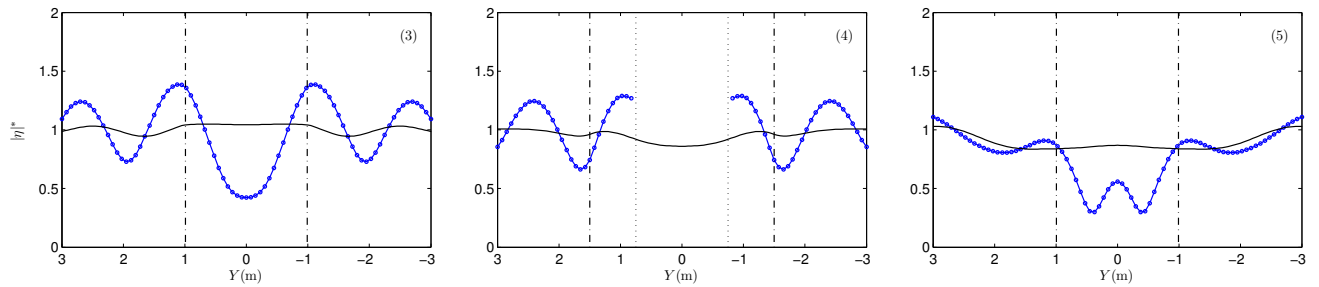


Figure 3.35: Snapshots of dimensionless free surface elevation over a single circular patch with two subzones within one wave period – Case I. The boundary of the forest patch and the interface between two subzones are indicated by solid lines. The incident wave condition is $T = 1.00$ s and $H_{\text{inc}} = 4.89$ cm with constant water depth $h_0 = 40$ cm.



(a) Along different Y : (1) $Y = 0$ m, (2) $Y = 1.125$ m



(b) Along different X : (3) $X = -1.125$ m, (4) $X = 0$ m, and (5) $X = 1.125$ m

Figure 3.36: Spatial variation of dimensionless wave amplitude along different profiles – Case I. The circle lines show the numerical results; the solid lines indicate the solutions for one homogeneous patch (i.e. Sec.3.6.2). Dot-dashed vertical lines indicate the forest edges and dotted vertical lines show the interfaces between two subzones. The incident wave condition is $T = 1.00$ s and $H_{inc} = 4.89$ cm with constant water depth $h_0 = 40$ cm.

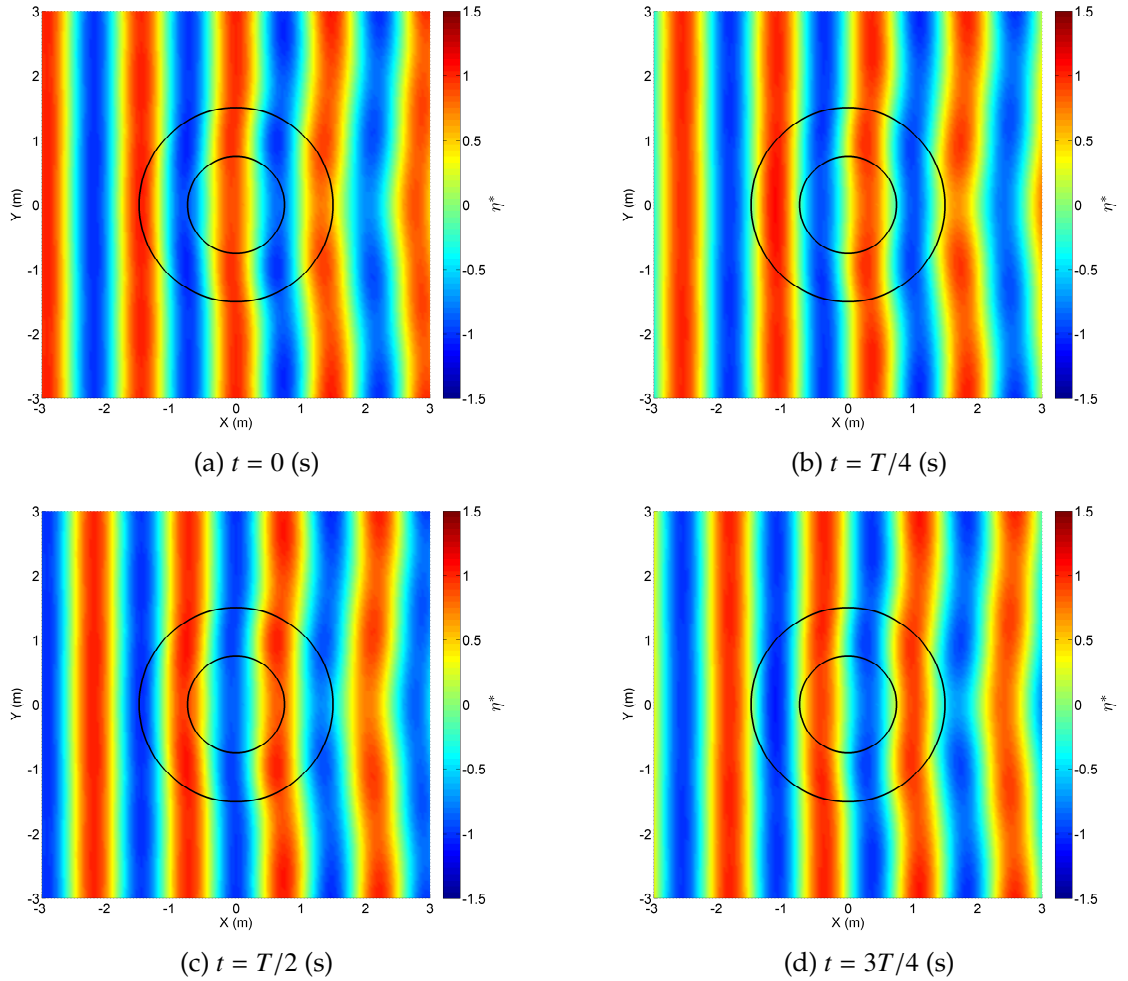
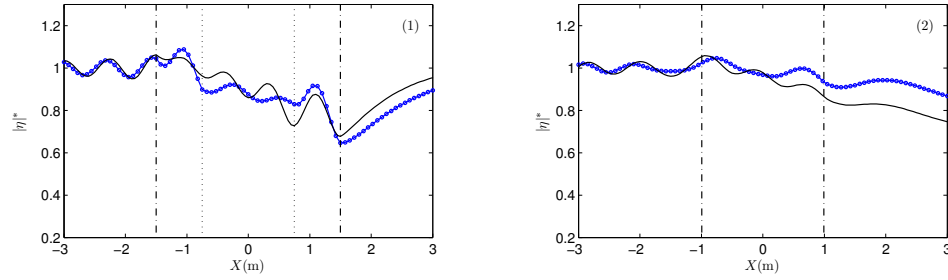
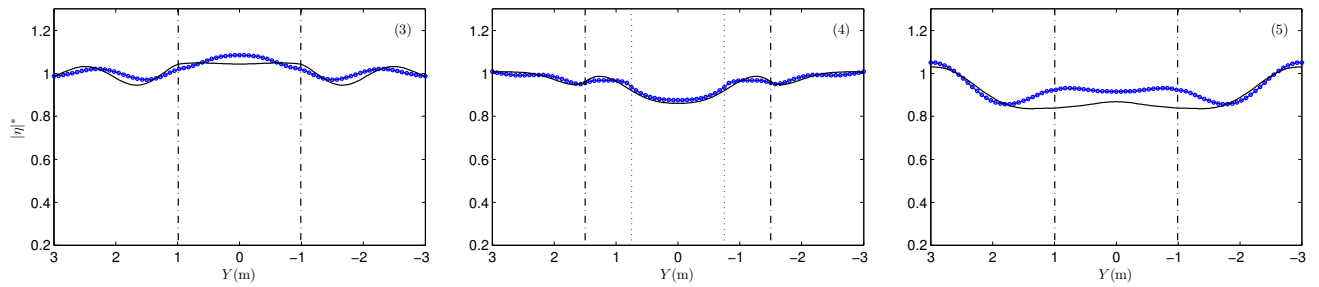


Figure 3.37: Snapshots of dimensionless free surface elevation over a single circular patch with two subzones within one wave period – Case II. The boundary of the forest patch and the interface between two subzones are indicated by solid lines. The incident wave condition is $T = 1.00$ s and $H_{\text{inc}} = 4.89$ cm with constant water depth $h_0 = 40$ cm.



(a) Along different Y : (1) $Y = 0$ m, (2) $Y = 1.125$ m



(b) Along different X : (3) $X = -1.125$ m, (4) $X = 0$ m, and (5) $X = 1.125$ m

Figure 3.38: Spatial variation of dimensionless wave amplitude along different profiles – Case II. The circle lines show the numerical results; the solid lines indicate the solutions for one homogeneous patch (i.e. Sec.3.6.2). Dot-dashed vertical lines indicate the forest edges and dotted vertical lines show the interfaces between two subzones. The incident wave condition is $T = 1.00$ s and $H_{\text{inc}} = 4.89$ cm with constant water depth $h_0 = 40$ cm.

3.7 Concluding remarks and discussions

Focusing on small-amplitude periodic waves, this chapter extends the theoretical model in [Mei et al. \(2014\)](#) to study wave propagation through a general coastal forest, which can have multiple patches of arbitrary shape. Each patch may consist of several subzones with different properties (e.g. vegetation types, planting patterns and cell porosity). Namely, a subzone is considered as a homogeneous region, which could be surrounded by other subzones and/or the open water region. Assuming a strong contrast between wavelength and tree spacing, the multiple-scale perturbation method is applied. Driven by the macro-scale pressure gradient, the micro-scale flow fields within cells are solved numerically. The equations governing macro-scale (wavelength-scale) wave dynamics are derived with cell effects being included. Considering a possible arbitrary shape of any forest subzone, the boundary integral equation method is employed to discretize the boundary of forest region and to solve the macro-scale problem numerically. To estimate the wave attenuation by the forest region, the eddy viscosity and drag coefficient are both considered as constant bulk quantities within each subzone of the entire forest region and are allowed to be changed in different subzones. Here we use the energy model in [Mei et al. \(2014\)](#), requiring a balance between the time-averaged dissipation rate and the time-averaged rate of work done by the wave forces on the cylinders within a certain subzone. Different from [Mei et al. \(2014\)](#), who adopted the empirical formula for steady unidirectional flows to prescribe the drag coefficient, a new drag formula is proposed based on the experimental measurements in [Hu et al. \(2014\)](#) with the Reynolds number defined with vegetation-related hydraulic radius. The bulk eddy viscosity over a certain subzone is then determined by

using the new drag coefficient formula to overcome the inadequate estimation of drag coefficient and the consequent necessity of introducing a fitting coefficient for each wave condition in [Mei et al. \(2014\)](#). A computing program is established based on the present numerical model, which can be applied to different forest configurations and to solve the macro-scale wave solutions with required inputs.

To check the numerical model, different forest configurations are tested. A forest belt with a finite width is first used to investigate the wave decay inside the model forest. The semi-analytical solutions are provided instead of using the integral equation method due to the infinite length. For normal incidence, good agreements are found between model results and the experimental data in [Hu et al. \(2014\)](#). Obliquely incident waves are also tested although no experimental data is available. Other laboratory experimental works mentioned in [Mei et al. \(2014\)](#) have been revisited and reasonable agreements have been observed for the cases with insignificant nonlinearity. According to all the data-model comparisons, it is concluded that the present model performs well as long as the basic assumptions of the theory are satisfied, i.e. the nonlinearity is weak ($A_{\text{inc}}/h_0 < 0.1$) and the ratio of tree spacing to wavelength is small ($\ell/L \leq 0.05$).

The present approach is further applied to another two special forest configurations with finite extent. The first one is a single homogeneous circular forest and the second one includes multiple patches. For a single circular forest, the semi-analytical solutions are provided where negligible differences are found when comparing with the numerical results. The data-model comparisons show reasonable agreements. For multiple patches, we first use the constant value of eddy viscosity for the single circular forest and assign it to all the patches. The

iterative scheme is then used to find the eddy viscosity for each patch. The differences among them are within 0.5 %. The model results and experimental data are also in reasonable agreement. However, due to the arrangement of wave gauges and the limited wave conditions in the experiments, detailed comparisons of the variation of wave amplitude within each patch are not allowed. The effectiveness of these two special forest configurations on wave attenuation is compared. As expected, the circular forest has the higher efficiency in damping the incoming waves than multiple smaller patches. Furthermore, larger waves yield more wave dissipation for both forest configurations. As a demonstration, we present the numerical results for two different non-circular forest configurations, i.e. one single rectangle and two rectangular patches. We also use one single circular patch with two subzones to show the numerical results. For all the forest conditions, the wave attenuation and diffraction when propagating through the forest region can both be captured by the present model.

It should be noted that in [Mei et al. \(2014\)](#) the drag coefficient and eddy viscosity are both considered to vary spatially within a homogeneous area. This is different from the present model, which assumes a constant bulk eddy viscosity for each subzone. Therefore, it is of interest to investigate the importance of varying eddy viscosity/drag coefficient. Here we use the forest belt as an example, following [Mei et al. \(2014\)](#)'s approach but using the new drag coefficient formula in this study, i.e. (3.100). The variation of eddy viscosity is shown in [Fig.3.39](#) and [3.40](#) for tests in [Table 3.1](#). The constant bulk eddy viscosity is also plotted in the same figure. The deviation of varying eddy viscosity from the bulk value is within $\pm 4\%$. As indicated in [Mei et al. \(2014\)](#), wave amplitude and the corresponding variations inside the forest region must be solved

numerically when the eddy viscosity is spatial-varying. Thus, numerical calculations are conducted and the resulting wave solutions are compared with the present model results, which are based on the concept of bulk eddy viscosity. As shown in Fig.3.41, the difference is insignificant for the cases where the wave nonlinearity is small. On the other hand, the difference starts increasing when the nonlinearity becomes higher, i.e. Fig.3.42. As mentioned previously, when the nonlinearity is important, the discrepancies between model results and experimental data could become noticeable. Since the drag coefficient formula is originally obtained based on the bulk eddy viscosity assumption, it is consistent with [Hu et al. \(2014\)](#)'s experiments when using bulk eddy viscosity (and drag coefficient). Furthermore, it should also be noted that the semi-analytical solutions only allow constant coefficients in use.

Due to the scattering of available drag coefficient data and the lack of measurements for lower Reynolds number, more experimental work is needed in the future to develop a more comprehensive empirical formula. The effects of KC number also deserve attention. In conclusion, using the multi-scale perturbation method, it has been shown that the present numerical model is able to predict the propagations of small-amplitude waves over a general vegetated water, which can be composed of multiple forest patches of arbitrary shape. In addition, the present model reduces computational efforts comparing with direct numerical simulation.

Most of the contents presented in this chapter have been included in [Liu et al. \(2015\)](#) and [Chang et al. \(2017a\)](#).

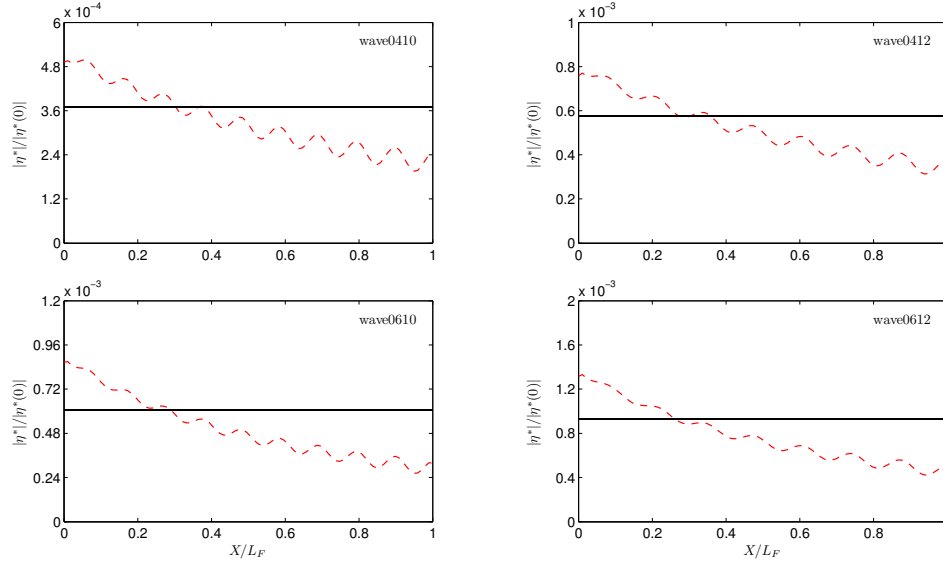


Figure 3.39: Comparison of spatial-varying dimensionless eddy viscosity (dashed line) and the spatial-averaged bulk value (solid line) inside the model forest belt for the cases with normal incidence. The wave conditions can be found in Table 3.1 (wave0410, 0412, 0610, 0612).

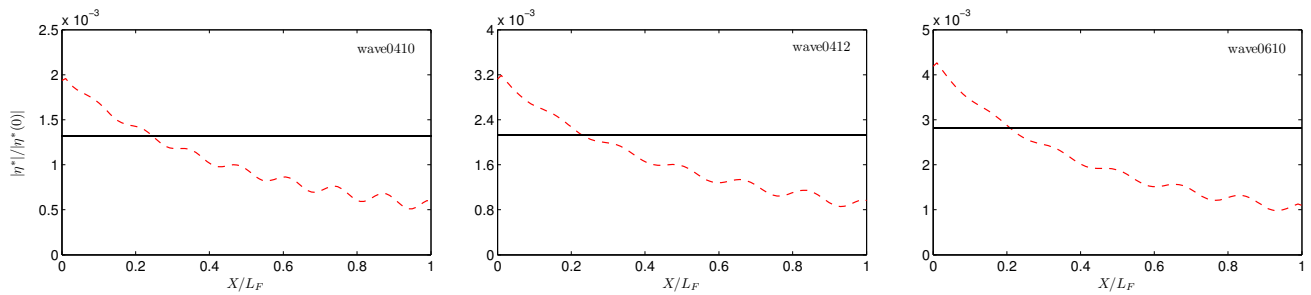


Figure 3.40: Comparison of spatial-varying dimensionless eddy viscosity (dashed line) and the spatial-averaged bulk value (solid line) inside the model forest belt for the cases with normal incidence. The wave conditions can be found in Table 3.1 (wave0812, 0815, 1015).

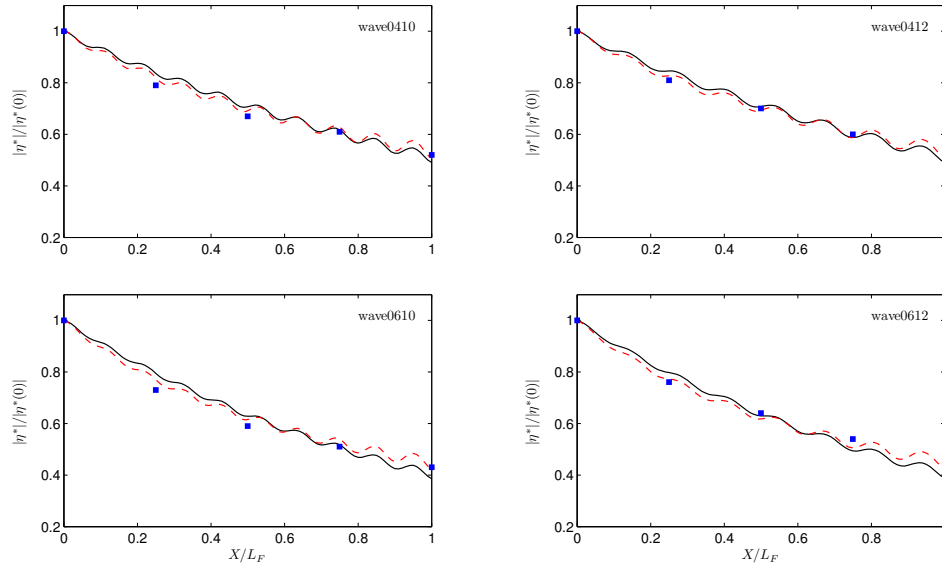


Figure 3.41: Comparison of predicted spatial variation of normalized dimensionless wave amplitude inside the model forest, based on varying (dashed line) and bulk eddy viscosity (solid line). Solid squares shows the laboratory data by [Hu et al. \(2014\)](#). The wave conditions can be found in Table 3.1 (wave0410, 0412, 0610, 0612).

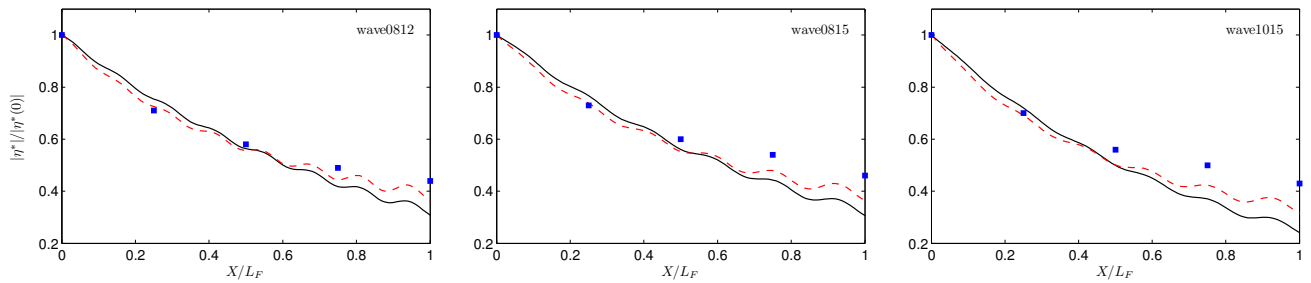


Figure 3.42: Comparison of predicted spatial variation of normalized dimensionless wave amplitude inside the model forest, based on varying (dashed line) and bulk eddy viscosity (solid line). Solid squares shows the laboratory data by [Hu et al. \(2014\)](#). The wave conditions can be found in Table 3.1 (wave0812, 0815, 1015).

CHAPTER 4

SMALL-AMPLITUDE TRANSIENT LONG WAVES THROUGH COASTAL FORESTS

In this chapter, we continue to study small-amplitude waves but switch to focus on transient long waves through a heterogeneous forest of arbitrary shape. Similarly, the homogenization theory is applied to separate two contrasting physical length scales: the scale characterizing transient waves and the scale representing spacing among cylinders. Fourier transform is employed so that the free surface elevation and velocity field are solved in the frequency domain. For each harmonic, the flow motion within a unit cell, consisting of one or more cylinders, is obtained by solving the micro-scale boundary-value problem, which is driven by the macro-scale (wavelength scale) pressure gradient. The cell-averaged equations governing the macro-scale wave amplitude spectrum are derived with consideration of the effects from cell problem solutions.

As presented in Chap.3, a vegetated area can have an arbitrary shape and shall be further divided into subzones according to different properties. The boundary integral equation method is again employed to solve the macro-scale wave amplitude spectrum numerically. Within each homogeneous subzone, a constant bulk eddy viscosity is assumed and can be determined by a modified empirical formula. Once the solutions of the wave amplitude spectrum are obtained, the free surface elevation can be computed by the inverse Fourier transform. A computing program for transient waves is also developed based on the present approach.

To check the numerical model, three special forest configurations, as used in

Chap.3, are investigated. We focus on incident waves with a soliton-like shape. The semi-analytical solutions of wave amplitude spectrum for a forest belt and a single circular patch are respectively provided, which are used as a preliminary validation of the numerical model. The comparisons with experimental data show very good agreements. The effects of different wave parameters on normalized damping height are investigated. Different arrangements of cylinders are discussed as well. The numerical model is further compared with the experiments for a forest region consisting of multiple circular patches. Good agreements are also observed between the simulated free surface elevations and the experimental measurements. The effectiveness of different forest configurations on wave attenuation is discussed.

4.1 Governing equations and boundary conditions

Considering small-amplitude long waves propagating in a constant water depth h_0 , the free surface elevation can be expressed as $z = \eta(\vec{x}, t)$. The leading-order velocities are on the horizontal plane and are independent of z , i.e. $u_i(\vec{x}, t)$, $i = 1, 2$. Therefore, the depth-averaged equations in (2.11) and (2.12) can be linearized (with double bars being dropped) as

$$\frac{\partial \eta}{\partial t} + h_0 \frac{\partial u_i}{\partial x_i} = 0, \quad i = 1, 2 \quad (4.1)$$

and

$$\frac{\partial u_i}{\partial t} = -g \frac{\partial \eta}{\partial x_i} + \nu_e \left(\frac{\partial^2 u_i}{\partial x_j \partial x_j} \right), \quad i \& j = 1, 2 \quad (4.2)$$

where the bottom friction has been neglected and the eddy viscosity ν_e is assumed as a constant. Here we use the Fourier transform to solve the governing

equations and boundary conditions. As an example, the Fourier transform of free surface elevation η can be expressed as

$$\hat{\eta}(x_i, \omega) = \int_{-\infty}^{\infty} \eta(x_i, t) e^{i\omega t} dt \quad (4.3)$$

where $\hat{\eta}(x_i, \omega)$ is called wave amplitude spectrum. The inverse Fourier transform of wave amplitude spectrum gives back the expression of wave surface profile:

$$\eta(x_i, t) = \frac{1}{2\pi} \int_{-\infty}^{\infty} \hat{\eta}(x_i, \omega) e^{-i\omega t} d\omega \quad (4.4)$$

Based on the long-wave assumption and associated scales, we introduce the dimensionless variables as

$$x_i^* = \frac{x_i}{\ell}, \quad t^* = \omega t, \quad \eta^* = \frac{\eta}{H_{\text{inc}}} \quad \text{and} \quad u_i^* = \frac{u_i}{\sqrt{g(h_0 + H_{\text{inc}})H_{\text{inc}}/(h_0 + H_{\text{inc}})}} \quad (4.5)$$

where the horizontal coordinates are scaled by the characteristic tree spacing ℓ (micro-length) and the free surface elevation is scaled by the incident wave height H_{inc} . The wave speed of a solitary wave, i.e. $\sqrt{g(h_0 + H_{\text{inc}})}$, is assumed. We first apply Fourier transform to the linearized equations (4.1) and (4.2), and then normalize the variables with proper scales as indicated in (4.5) to yield

$$-i\varepsilon\hat{\eta}^* + \frac{\partial \hat{u}_i^*}{\partial x_i^*} = 0, \quad i \ \& \ j = 1, 2 \quad (4.6)$$

and

$$-i\varepsilon\hat{u}_i^* = -\frac{\partial \hat{\eta}^*}{\partial x_i^*} + \varepsilon\sigma \frac{\partial^2 \hat{u}_i^*}{\partial x_j^* \partial x_j^*}, \quad i \ \& \ j = 1, 2 \quad (4.7)$$

where \hat{u}_i^* is the dimensionless velocity spectrum and the small parameter ε is defined as

$$\varepsilon = \frac{\omega\ell}{\sqrt{g(h_0 + H_{\text{inc}})}} \equiv k\ell \ll O(1) \quad (4.8)$$

We remark here that since the linear long wave theory is used, the incident wave height must be reasonably small, i.e. $H_{\text{inc}}/h_0 \ll O(1)$ has been applied. The

wave dispersion is also assumed to be negligible. Therefore, the size of forest region should be in the same order of magnitude as the characteristic wavelength, which has to be much greater than the tree spacing.

Similar to Chap.3, we propose that each homogeneous forest subzone has a constant bulk value of dimensional eddy viscosity ν_e , which can be determined by modifying the empirical formula in Mei et al. (2011):

$$\nu_e = 1.86(1 - n)^{2.06} U_0 \ell \quad \text{with} \quad U_0 = \sqrt{g(h_0 + H_{\text{inc}})} \left(\frac{H_{\text{inc}}}{h_0 + H_{\text{inc}}} \right) \quad (4.9)$$

where U_0 represents the depth-averaged horizontal water particle velocity. The corresponding dimensionless eddy viscosity can then be written as

$$\sigma = \frac{\nu_e}{\omega \ell^2} = 1.86(1 - n)^{2.06} \frac{1}{k_\omega \ell} \left(\frac{H_{\text{inc}}}{h_0 + H_{\text{inc}}} \right), \quad k_\omega = \frac{\omega}{\sqrt{g(h_0 + H_{\text{inc}})}} \quad (4.10)$$

Obviously, the dimensionless eddy viscosity σ is a function of ω . It should be noted that in Mei et al. (2011), $U_0 = \sqrt{gh_0} H_{\text{inc}} / 2h_0$ was specified in their empirical formula.

In this chapter we shall focus on soliton-like incident waves. The free surface profile can be expressed as

$$\eta_{\text{inc}}(x_1, t) = H_{\text{inc}} \text{sech}^2 [k_s(x_1 - ct)] \quad (4.11)$$

where the effective wavenumber k_s and wave speed c are defined as

$$k_s = \frac{1}{h_0} \sqrt{\frac{3H_{\text{inc}}}{4h_0}} \quad \text{and} \quad c = \sqrt{g(h_0 + H_{\text{inc}})} \quad (4.12)$$

The incident soliton has the wave amplitude spectrum (Miles 1976) as

$$\hat{\eta}_{\text{inc}}(x_1, \omega) = A_s e^{ik_\omega x_1}, \quad A_s(\omega) = \frac{4}{3} \pi h_0^3 \left(\frac{\omega}{c^2} \right) \text{csch} \left[\pi \left(\frac{h_0^3}{3H_{\text{inc}}} \right)^{1/2} \frac{\omega}{c} \right] \quad (4.13)$$

in which $k_\omega = \omega/c$. For an incident soliton, where the wave amplitude spectrum is an even function in ω , the inverse Fourier transform in (4.4) can also be modified as

$$\eta(x_i, t) = \frac{1}{\pi} \int_0^\infty \hat{\eta}(x_i, \omega) e^{-i\omega t} d\omega \quad (4.14)$$

Note that in the numerical computations, the infinite components of harmonic ω need to be truncated to a finite number with proper convergence tests. The details will be discussed later in Sec.4.3.4.

4.2 Homogenization method

Similar to Sec.3.2, we introduce two coordinates to capture the physics of flows in the vicinity of cylinders and the wave motions propagating through the entire forest region:

$$X_i^* = \varepsilon x_i^* = kx_i, \quad i = 1, 2 \quad (4.15)$$

Employing the multiple-scale perturbation method and dropping the asterisks for brevity, the dimensionless velocity and wave amplitude spectrum can be expressed as

$$\hat{u}_i = \hat{u}_i^{(0)} + \varepsilon \hat{u}_i^{(1)} + \varepsilon^2 \hat{u}_i^{(2)} + \dots \quad \text{and} \quad \hat{\eta} = \hat{\eta}^{(0)} + \varepsilon \hat{\eta}^{(1)} + \varepsilon^2 \hat{\eta}^{(2)} + \dots \quad (4.16)$$

in which \hat{u}_i and $\hat{\eta}$ are functions of (x_i, X_i, ω) . Note again that in this chapter only dimensionless variables are presented from here on. Following the classical perturbation procedures, the governing equations in different orders of magnitude are separated:

- $O(\varepsilon^0)$:

$$\frac{\partial \hat{u}_i^{(0)}}{\partial x_i} = 0, \quad i = 1, 2 \quad (4.17)$$

and

$$\frac{\partial \hat{\eta}^{(0)}}{\partial x_i} = 0, \quad i = 1, 2 \quad (4.18)$$

which shows the leading-order wave amplitude spectrum is independent of micro-scale, i.e. $\hat{\eta}^{(0)} = \hat{\eta}^{(0)}(X_i, \omega)$.

- $O(\varepsilon^1)$:

$$-i\hat{\eta}^{(0)} + \frac{\partial \hat{u}_i^{(0)}}{\partial X_i} + \frac{\partial \hat{u}_i^{(1)}}{\partial x_i} = 0, \quad i = 1, 2 \quad (4.19)$$

and

$$-i\hat{u}_i^{(0)} = -\frac{\partial \hat{\eta}^{(1)}}{\partial x_i} - \frac{\partial \hat{\eta}^{(0)}}{\partial X_i} + \sigma \left(\frac{\partial^2 \hat{u}_i^{(0)}}{\partial x_j \partial x_j} \right), \quad i \& j = 1, 2 \quad (4.20)$$

in which the bottom shear stress has been neglected due to the assumption that $h_0 \gg \ell$.

4.2.1 Micro-scale (cell) problem

To solve the flow motions around cylinders within a unit cell, we express the leading-order velocities and the free surface fluctuation in terms of convolution integrals (Mei and Vernescu 2010; Mei et al. 2011):

$$u_i^{(0)}(\vec{x}, \vec{X}, t) = - \int_0^t K_{ij}(\vec{x}, t - \tau) \frac{\partial \eta^{(0)}(\vec{X}, \tau)}{\partial X_j} d\tau, \quad \vec{x} \in \Omega_f \quad (4.21)$$

and

$$\eta^{(1)}(\vec{x}, \vec{X}, t) = - \int_0^t A_j(\vec{x}, t - \tau) \frac{\partial \eta^{(0)}(\vec{X}, \tau)}{\partial X_j} d\tau, \quad \vec{x} \in \Omega_f \quad (4.22)$$

For transient waves, K_{ij} , A_j and $\eta^{(0)}$ are nonzero when time is greater than or equal to zero. Equations (4.21) and (4.22) can be rewritten in the general convolution form by integrating from negative infinity to positive infinity:

$$u_i^{(0)}(\vec{x}, \vec{X}, t) = - \int_{-\infty}^{\infty} K_{ij}(\vec{x}, t - \tau) \frac{\partial \eta^{(0)}(\vec{X}, \tau)}{\partial X_j} d\tau, \quad \vec{x} \in \Omega_f \quad (4.23)$$

and

$$\eta^{(1)}(\vec{x}, \vec{X}, t) = - \int_{-\infty}^{\infty} A_j(\vec{x}, t - \tau) \frac{\partial \eta^{(0)}(\vec{X}, \tau)}{\partial X_j} d\tau, \quad \vec{x} \in \Omega_f \quad (4.24)$$

Applying Fourier transform to (4.23) and (4.24), the convolution property provides the transformed relationships as

$$\hat{u}_i^{(0)} = -\hat{K}_{ij} \frac{\partial \hat{\eta}^{(0)}}{\partial X_j} \quad \text{and} \quad \hat{\eta}^{(1)} = -\hat{A}_j \frac{\partial \hat{\eta}^{(0)}}{\partial X_j}, \quad \vec{x} \in \Omega_f \quad (4.25)$$

where Ω_f represents the fluid part within a unit cell Ω . From the mass conservation of $O(1)$ and the momentum equations of $O(\varepsilon)$, \hat{K}_{ij} and \hat{A}_j satisfy

$$\frac{\partial \hat{K}_{ij}}{\partial x_i} = 0 \quad (4.26)$$

and

$$i\hat{K}_{ij} = -\delta_{ij} + \frac{\partial \hat{A}_j}{\partial x_i} - \sigma \frac{\partial^2 \hat{K}_{ij}}{\partial x_k \partial x_k}, \quad \vec{x} \in \Omega_f \quad (4.27)$$

in which \hat{K}_{ij} and \hat{A}_j are subject to the cell-periodicity (Mei et al. 2011). δ_{ij} denotes the Kronecker delta. No-slip boundary conditions along the solid surface of cylinders are also valid. As noted, we consider each forest subzone as a homogeneous area where a dimensional bulk eddy viscosity ν_e is determined by (4.9), while the corresponding dimensionless eddy viscosity σ in (4.10) shall vary with different harmonics. Accordingly, within a forest subzone the cell problem for each harmonic has to be solved separately. Similar to Sec.3.2.1, finite element approach is applied to solve the micro-scale boundary-value problem numerically. The related details have been presented in Mei et al. (2011) and should not be repeated here.

4.2.2 Macro-scale (wavelength-scale) problem

With the cell problem solutions, the leading-order cell-averaged velocity spectrum can be obtained from (4.25):

$$\langle \hat{u}_i^{(0)} \rangle = -\langle \hat{K}_{ij} \rangle \frac{\partial \hat{\eta}^{(0)}}{\partial X_j}, \quad i \& j = 1, 2 \quad (4.28)$$

and the cell-averaged mass equation of $\mathcal{O}(\varepsilon)$ gives

$$-in\hat{\eta}^{(0)} + \frac{\partial \langle \hat{u}_i^{(0)} \rangle}{\partial X_i} = 0, \quad i = 1, 2 \quad (4.29)$$

in which Gauss's theorem and the cell-periodic conditions are invoked with the cell porosity n being defined in (3.42) as $n = \Omega_f/\Omega$. The cell-averaged quantity $\langle \cdot \rangle$ has also been defined in (3.39). Combining (4.28) and (4.29), the leading-order cell-averaged equation governing the wave amplitude spectrum becomes

$$-in\hat{\eta}^{(0)} - \hat{\mathcal{K}} \left(\frac{\partial^2 \hat{\eta}^{(0)}}{\partial X_i \partial X_i} \right) = 0, \quad i = 1, 2 \quad (4.30)$$

in which $\langle \hat{K}_{ij} \rangle = \hat{\mathcal{K}}\delta_{ij}$ has been applied. In the absence of vegetation, the porosity becomes unity (i.e. $n = 1$) and $\hat{K}_{ij} \rightarrow i\delta_{ij}$ following from (4.27). Therefore, in open water the governing equation becomes

$$\hat{\eta}^{(0)} + \frac{\partial^2 \hat{\eta}^{(0)}}{\partial X_i \partial X_i} = 0, \quad i = 1, 2 \quad (4.31)$$

4.3 Boundary integral equation method

Like Sec.3.3, we employ the boundary integral equation method to solve the macro-scale wave amplitude spectrum. The integral formulation for a forest subzone and for the open water region are presented, respectively. The required matching conditions along the interfaces of two adjacent subzones and along the boundary between the forest region and open water are introduced.

4.3.1 Integral formulation for a forest subzone

Let us first consider a forest subzone ξ of an arbitrary shape. As sketched in Fig.1.1, a forest subzone can be adjacent to other subzones and/or open water. The leading-order equation governing the macro-scale wave amplitude spectrum, as shown in (4.30), is rewritten as

$$\frac{\partial^2 \hat{\eta}_\xi^{(0)}}{\partial X_1 \partial X_1} + \frac{\partial^2 \hat{\eta}_\xi^{(0)}}{\partial X_2 \partial X_2} + \hat{\beta}_\xi^2 \hat{\eta}_\xi^{(0)} = 0, \quad \hat{\beta}_\xi = \sqrt{\frac{in}{\mathcal{K}_\xi}} \quad (4.32)$$

Comparing (4.32) with (3.57), they are both well-known Helmholtz equations but with different complex coefficients in front of the 3rd term of the equations, which contain information from the respective cell problem solutions. In (4.32) the wave amplitude spectrum $\hat{\eta}_\xi^{(0)}$ depends on the frequency (ω) and has to be solved independently for each ω . We convert (4.32) into the integral equation (Liggett and Liu 1983) as

$$\hat{\eta}_\xi^{(0)}(\vec{X}_i) = \frac{-i\pi}{2\alpha} \int_{S_\xi + D_{\xi\psi}} \left\{ \hat{\eta}_\xi^{(0)}(\vec{X}_j) \frac{\partial [H_0^{(1)}(\hat{\beta}_\xi r)]}{\partial \hat{n}_\xi} - H_0^{(1)}(\hat{\beta}_\xi r) \frac{\partial \hat{\eta}_\xi^{(0)}(\vec{X}_j)}{\partial \hat{n}_\xi} \right\} dS \quad (4.33)$$

where the boundary of subzone ξ can include the boundary to open water (i.e. S_ξ) and/or the interfaces with other subzones ψ (i.e. $D_{\xi\psi}$). \vec{X}_i denotes the coordinate of a point on the boundary of subzone ξ with its interior angle α sketched in Fig.3.3. \vec{X}_j is another boundary point of the subzone with $r = |\vec{X}_i - \vec{X}_j|$ yielding the distance between these two boundary points. $H_0^{(1)}$ is the Hankel function of the first kind and \hat{n}_ξ represents the outward normal direction to the boundary of subzone ξ . Note again that $\hat{\beta}_\xi$ is obtained from the cell problem solution and (4.33) will be used to solve the wave amplitude spectrum as well as its normal derivative along the boundary. After obtaining the wave amplitude spectrum and its normal derivative along the boundary, the solutions inside the subzone

can be readily computed by assigning \vec{X}_i as an interior point with its interior angle = 2π :

$$\hat{\eta}_\xi^{(0)}(\vec{X}_i) = \frac{-i}{4} \int_{S_\xi + D_{\xi\psi}} \left\{ \hat{\eta}_\xi^{(0)}(\vec{X}_j) \frac{\partial [H_0^{(1)}(\hat{\beta}_\xi \underline{r})]}{\partial \hat{n}_\xi} - H_0^{(1)}(\hat{\beta}_\xi \underline{r}) \frac{\partial \hat{\eta}_\xi^{(0)}(\vec{X}_j)}{\partial \hat{n}_\xi} \right\} dS \quad (4.34)$$

Note that \vec{X}_i is now an interior point of subzone ξ while \vec{X}_j is on its boundary.

4.3.2 Integral formulation for open water

For open water the governing equation is given in (4.31) with subscript S denoting the scattered wave amplitude spectrum:

$$\frac{\partial^2 \hat{\eta}_S^{(0)}}{\partial X_1 \partial X_1} + \frac{\partial^2 \hat{\eta}_S^{(0)}}{\partial X_2 \partial X_2} + \hat{\eta}_S^{(0)} = 0 \quad (4.35)$$

Equation (4.35) has the same form as (3.63) with the coefficient in front of the 3rd term, k_p , being replaced by 1. Note that $\hat{\eta}_S^{(0)}$ in (4.35) for each harmonic is solved separately. Equation (4.35) can also be converted into the following integral equation:

$$\hat{\eta}_S^{(0)}(\vec{X}_i) = \frac{-i\pi}{2(2\pi - \alpha)} \int_S \left\{ \hat{\eta}_S^{(0)}(\vec{X}_j) \frac{\partial [H_0^{(1)}(\underline{r})]}{\partial \hat{n}_S} - H_0^{(1)}(\underline{r}) \frac{\partial \hat{\eta}_S^{(0)}(\vec{X}_j)}{\partial \hat{n}_S} \right\} dS \quad (4.36)$$

where \vec{X}_i and \vec{X}_j are both located on the boundary between open water and the forest region. S denotes the combination of external boundaries of all the forest patches. Again, once the wave amplitude spectrum $\hat{\eta}_S^{(0)}$ and its normal derivatives along the boundary S are solved, we can assign \vec{X}_i as any interior point within the open water region and modify (4.36) as

$$\hat{\eta}_S^{(0)}(\vec{X}_i) = \frac{-i}{4} \int_S \left\{ \hat{\eta}_S^{(0)}(\vec{X}_j) \frac{\partial [H_0^{(1)}(\underline{r})]}{\partial \hat{n}_S} - H_0^{(1)}(\underline{r}) \frac{\partial \hat{\eta}_S^{(0)}(\vec{X}_j)}{\partial \hat{n}_S} \right\} dS \quad (4.37)$$

Note that the outward normal directions of the boundary for forest subzone and open water are opposite to each other, i.e. $\hat{n}_\xi = -\hat{n}_S$.

4.3.3 Matching conditions along the boundaries

As noted in Sec.3.3.3, the boundary of a forest subzone can be in contact with other subzones and/or with open water. Referring the former as the interface with other subzones and the latter as the exterior boundary, the continuity of wave amplitude spectrum and velocity spectrum is required.

We first consider the exterior boundary of subzone ξ , i.e. S_ξ . The continuity of wave amplitude and normal velocity spectrum respectively yields

$$\hat{\eta}_\xi^{(0)} = \hat{\eta}_I^{(0)} + \hat{\eta}_S^{(0)} \quad \text{and} \quad -i\hat{\mathcal{K}}_\xi \frac{\partial \hat{\eta}_\xi^{(0)}}{\partial \hat{n}_\xi} = \frac{\partial \hat{\eta}_I^{(0)}}{\partial \hat{n}_\xi} + \frac{\partial \hat{\eta}_S^{(0)}}{\partial \hat{n}_\xi} \quad (4.38)$$

in which $\hat{\mathcal{K}} \rightarrow i$ for the open water region has been applied. Note that in (4.38) the incident wave amplitude spectrum, i.e. $\hat{\eta}_I^{(0)} = \hat{A}_0 e^{iX}$ with $\hat{A}_0 = A_s/H_{\text{inc}}$, and the scattered wave amplitude spectrum $\hat{\eta}_S^{(0)}$ are both included within the open water region.

On the other hand, along the interface between subzone ξ and its adjacent subzone ψ (i.e. $D_{\xi\psi}$), the wave amplitude and normal velocity spectrum have to be continuous:

$$\hat{\eta}_\xi^{(0)} = \hat{\eta}_\psi^{(0)} \quad \text{and} \quad \hat{\mathcal{K}}_\xi \frac{\partial \hat{\eta}_\xi^{(0)}}{\partial \hat{n}_\xi} = -\hat{\mathcal{K}}_\psi \frac{\partial \hat{\eta}_\psi^{(0)}}{\partial \hat{n}_\psi} \quad (4.39)$$

Note that the negative sign reflects the opposite directions of \hat{n}_ξ and \hat{n}_ψ .

4.3.4 Numerical implementation

In the numerical computations, we discretize the boundary of a forest subzone ξ into elements with a constant length ΔS . Accordingly, (4.33) in discrete form becomes

$$\hat{\eta}_\xi^{(0)}(\vec{X}_i) = \frac{-i\pi}{2\alpha} \sum_{j=1}^{\mathbb{N}_\xi} \left\{ \hat{\eta}_\xi^{(0)}(\vec{X}_j) \frac{\partial [H_0^{(1)}(\hat{\beta}_\xi r)]}{\partial \hat{n}_\xi} - H_0^{(1)}(\hat{\beta}_\xi r) \frac{\partial \hat{\eta}_\xi^{(0)}(\vec{X}_j)}{\partial \hat{n}_\xi} \right\} \Delta S \quad (4.40)$$

in which \vec{X}_j denotes the middle point of each boundary element (see Fig.3.3). \mathbb{N}_ξ represents the total number of elements on the boundary of subzone ξ , which can include the exterior boundary S_ξ and/or interfaces with other subzones $D_{\xi\psi}$. The wave amplitude spectrum can also be expressed in terms of its normal derivatives in the following index notation formulation:

$$\left(\hat{\eta}_\xi^{(0)} \right)_i = \left(\hat{\mathcal{G}}_\xi \right)_{ij} \left(\frac{\partial \hat{\eta}_\xi^{(0)}}{\partial \hat{n}_\xi} \right)_j \quad \text{with } i \ \& \ j = 1 \cdots \mathbb{N}_\xi \quad (4.41)$$

where the coefficient matrix $[\hat{\mathcal{G}}_\xi] = [I + \hat{C}_\xi]^{-1} [\hat{D}_\xi]$ with I being the identity matrix while \hat{C}_ξ and \hat{D}_ξ are respectively defined as

$$\left(\hat{C}_\xi \right)_{ij} = \frac{i\pi}{2\alpha} \left[-\hat{\beta}_\xi H_1^{(1)}(\hat{\beta}_\xi r_{ij}) \right] \frac{\partial r_{ij}}{\partial \hat{n}_\xi} \Delta S, \quad \left(\hat{D}_\xi \right)_{ij} = \frac{i\pi}{2\alpha} H_0^{(1)}(\hat{\beta}_\xi r_{ij}) \Delta S \quad (4.42)$$

On the other hand, the wave amplitude spectrum for open water as shown in (4.36) also needs to be expressed in discrete form as

$$\hat{\eta}_S^{(0)}(\vec{X}_i) = \frac{-i\pi}{2(2\pi - \alpha)} \sum_{j=1}^{\mathbb{N}_S} \left\{ \hat{\eta}_S^{(0)}(\vec{X}_j) \frac{\partial [H_0^{(1)}(r)]}{\partial \hat{n}_S} - H_0^{(1)}(r) \frac{\partial \hat{\eta}_S^{(0)}(\vec{X}_j)}{\partial \hat{n}_S} \right\} \Delta S \quad (4.43)$$

where \mathbb{N}_S denotes the total number of elements along the exterior boundary of all the forest patches, i.e. the boundary separating the forest region from open water ($S = \sum S_\xi$). Likewise, we express the wave amplitude spectrum for open

water in terms of its normal derivatives as

$$\left(\hat{\eta}_S^{(0)}\right)_i = \left(\hat{Q}_S\right)_{ij} \left(\frac{\partial \hat{\eta}_S^{(0)}}{\partial \hat{n}_S}\right)_j \quad \text{with } i \& j = 1 \cdots \mathbb{N}_S \quad (4.44)$$

in which the coefficient matrix $\left[\hat{Q}_S\right] = \left[\mathcal{I} + \hat{\mathcal{E}}_S\right]^{-1} \left[\hat{\mathcal{F}}_S\right]$ with

$$\left(\hat{\mathcal{E}}_S\right)_{ij} = \frac{-i\pi}{2(2\pi - \alpha)} H_1^{(1)}(r_{ij}) \frac{\partial r_{ij}}{\partial \hat{n}_S} \Delta S, \quad \left(\hat{\mathcal{F}}_S\right)_{ij} = \frac{i\pi}{2(2\pi - \alpha)} H_0^{(1)}(r_{ij}) \Delta S. \quad (4.45)$$

As introduced in Sec.4.3.3, the matching conditions must be imposed for solving the wave amplitude spectrum along the boundaries, including both the interfaces and exterior boundaries. In (4.38), the continuity of wave and normal velocity spectrum along the exterior boundary S_ξ of a forest subzone respectively yields

$$\left(\hat{\mathcal{G}}_\xi\right)_{ij} \left(\frac{\partial \hat{\eta}_\xi^{(0)}}{\partial \hat{n}_\xi}\right)_j = \left(\hat{A}_0 e^{iX_1}\right)_i + \left(\hat{Q}_S\right)_{im} \left(\frac{\partial \hat{\eta}_S^{(0)}}{\partial \hat{n}_S}\right)_m \quad (4.46)$$

and

$$-i\hat{\mathcal{K}} \left(\frac{\partial \hat{\eta}_\xi^{(0)}}{\partial \hat{n}_\xi}\right)_i = \hat{A}_0 \left(\frac{\partial e^{iX_1}}{\partial \hat{n}_\xi}\right)_i + \left(\frac{\partial \hat{\eta}_S^{(0)}}{\partial \hat{n}_\xi}\right)_i \quad (4.47)$$

where the substitution of (4.41) and (4.44) has been made in (4.46). Assuming the incident waves in X_1 direction, X_{1i} in (4.46) and (4.47) denotes the X_1 coordinate of point i . Note that ξ in (4.46) and (4.47) can be any subzone that is exposed to open water such that \vec{X}_i is located on the exterior boundary of subzone ξ . In (4.46), $\vec{X}_j \in S_\xi + D_{\xi\psi}$ (with $j = 1 \cdots \mathbb{N}_\xi$) denotes the boundary points of subzone ξ while $\vec{X}_m \in \mathbf{S}$ (with $m = 1 \cdots \mathbb{N}_S$) is on the boundary of open water.

Along the interfaces between subzones, (4.39) also requires the continuity of wave amplitude and normal velocity spectrum such that

$$\left(\hat{\mathcal{G}}_\xi\right)_{ij} \left(\frac{\partial \hat{\eta}_\xi^{(0)}}{\partial \hat{n}_\xi}\right)_j = \left(\hat{\mathcal{G}}_\psi\right)_{ik} \left(\frac{\partial \hat{\eta}_\psi^{(0)}}{\partial \hat{n}_\psi}\right)_k \quad (4.48)$$

and

$$\hat{\mathcal{K}}_{\xi} \left(\frac{\partial \hat{\eta}_{\xi}^{(0)}}{\partial \hat{n}_{\xi}} \right)_i = -\hat{\mathcal{K}}_{\psi} \left(\frac{\partial \hat{\eta}_{\psi}^{(0)}}{\partial \hat{n}_{\psi}} \right)_i \quad (4.49)$$

in which \vec{X}_j (with $j = 1 \cdots \mathbb{N}_{\xi}$) and \vec{X}_k (with $k = 1 \cdots \mathbb{N}_{\psi}$) represent the boundary points of subzones ξ and ψ , respectively. Also note the outward normal directions along the interface with respect to these two adjacent subzones (ξ and ψ) are opposite, i.e. $\hat{n}_{\xi} = -\hat{n}_{\psi}$.

With (4.46), (4.47), (4.48) and (4.49), a system of equations is formulated for solving the leading-order wave amplitude spectrum $\hat{\eta}_{\xi}^{(0)}$, $\hat{\eta}_{\psi}^{(0)}$ and $\hat{\eta}_S^{(0)}$ as well as their normal derivatives along the exterior boundaries of forest patches and the interfaces between subzones. Once the solutions along boundaries are known, the wave amplitude spectrum within any subzone and open water can be readily obtained from (4.34) and (4.37), respectively. As noted previously, the wave amplitude spectrums $\hat{\eta}_{\xi}^{(0)}$ and $\hat{\eta}_S^{(0)}$ are solved independently for each harmonic. The free surface elevation can then be obtained by the inverse transform in (4.14). In the numerical computations, the infinite range of harmonics ω needs to be truncated to a finite number. It has been found that the harmonics ranging from 10^{-3} to 10 (i.e. $10^{-3} \leq \omega \leq 10$) with 40 equally-distributed terms in total is sufficient to reconstruct the shape of incident soliton in (4.11). Therefore, we start with this arrangement in the numerical computations and perform convergence tests. According to the results, it shows that this arrangement is able to bring about convergent free surface elevations for small amplitude waves. For relatively larger waves, however, the range of harmonic components needs to be adjusted and higher values have to be included. The details for each forest configuration will be presented.

An example sketching the discretization of forest boundary has been provided in Fig.3.3. The definition of interior angle and element length are presented in the same figure. The outward normal directions along the boundaries of subzones and of open water can both be found. The direction of integration along the boundary of subzones is specified as well. Comparing the present model for transient waves with that for periodic waves in Sec.3.3, both models share the integral formulation for the well-known Helmholtz equation but with different contributions from the respective cell effects. As mentioned in Sec.4.3.1 and 4.3.2, the wave amplitude spectrum for each harmonic needs to be solved separately.

4.4 Cornell HomogEnization model for WAve-VEgetation interaction – Transient waves

Similar to Sec.3.5, a computing program named CHEWAVE-T (Cornell HomogEnization model on WAve-VEgetation interaction-Transient wave) is also developed based on the present approach. Applying Fourier transform, the model is able to solve the propagation of transient long waves through a general forest region, which has multiple patches of arbitrary shape. The numerical solver on the micro-scale problem is also provided. Inputs for the numerical computations include the conditions of incident soliton, forest configurations, properties and the discretization of boundaries. Most of the input files have the same contents and formats as those in Sec.3.5 except the incident wave condition file *WaveInc.dat*, which has to be modified as $\rightarrow \{h_0 ; H_{inc} ; N_\omega\}$ with N_ω

denoting the total number of harmonics being used in the computation. In addition, one more input file including an array of the harmonic components is required: *Omega.dat* – $\{\omega\}$. On the other hand, the output of the model has only one file – *etaG.dat*, which is a three-dimensional array containing the leading-order dimensionless free surface elevation in the entire computational domain at different time. It has size $N_{Yc} \times N_{Xc} \times N_T$ where N_T denotes the number of grids in time. More details can be referred to Appendix B.2. Besides, the cell problem solver is provided based on an open source finite element software – FreeFEM++ (Hecht 2012). Several different cell configurations have been tested.

4.5 Model validation and numerical results

The infinitely long forest belt studied in Mei et al. (2011) is first re-examined. The homogeneous circular forest presented in Sec.3.6.2 (for studying periodic waves) is then used to check the numerical model. Semi-analytical solutions for these two special forest configurations are provided. Negligible differences are observed when comparing with numerical results, which serve as a preliminary validation of the numerical model. To further investigate the present model, the experiments on multiple circular patches (as shown in Sec.3.6.3) are used as another special forest configuration. Numerically-simulated free surfaces elevation compared with the experimental measurements for three forest configurations are presented herein.

4.5.1 Solitary wave through a forest belt

Considering transient long waves with a soliton-like shape propagating through a forest belt with an infinite length (i.e. $-\infty < Y < \infty$) but a finite width (i.e. $0 \leq X \leq L_F$). Due to the infinite length, we here present the semi-analytical solutions of wave amplitude spectrum instead of using the boundary integral equation method. The comparisons with experimental data reported in [Mei et al. \(2011\)](#) are provided. The nonlinearity effect on the wave attenuation is also discussed.

4.5.1.1 Semi-analytical solutions

The leading-order wave amplitude spectrum inside the forest (with subscript F) can be obtained by solving (4.30):

$$\hat{\eta}_F^{(0)} = C_1 e^{\gamma_s X} + C_2 e^{-\gamma_s X} \quad \text{with} \quad \gamma_s = i\hat{\beta} = \sqrt{-in/\hat{\mathcal{K}}} \quad (4.50)$$

The cell-averaged leading-order velocity spectrum can then be derived from (4.28):

$$\langle \hat{u}_F^{(0)} \rangle = -\hat{\mathcal{K}} \frac{\partial \hat{\eta}_F^{(0)}}{\partial X} = -\gamma_s \hat{\mathcal{K}} [C_1 e^{\gamma_s X} - C_2 e^{-\gamma_s X}] \quad (4.51)$$

where C_1 and C_2 are undetermined coefficients. In open water, the solutions in the incidence region (i.e. $X < 0$) are

$$\hat{\eta}_I^{(0)} + \hat{\eta}_R^{(0)} = \hat{A}_0 e^{iX} + \hat{A}_0 R_s e^{-iX}, \quad \langle \hat{u}_I^{(0)} \rangle + \langle \hat{u}_R^{(0)} \rangle = \hat{A}_0 e^{iX} - \hat{A}_0 R_s e^{-iX} \quad (4.52)$$

while in the transmission region (i.e. $X > L_F$) the solutions become

$$\hat{\eta}_T^{(0)} = \hat{A}_0 T_s e^{iX}, \quad \langle \hat{u}_T^{(0)} \rangle = \hat{A}_0 T_s e^{iX} \quad (4.53)$$

where $|R_s|$ and $|T_s|$ respectively represent the reflection and transmission coefficients of each harmonic in the transformed domain. Note that $\hat{A}_0 = A_s/H_{\text{inc}}$ with $A_s(\omega)$ defined in (4.13) and H_{inc} is the incident wave height. The unknown coefficients C_1 , C_2 , R_s and T_s are to be determined by requiring the wave amplitude and velocity spectrum to be continuous along the edges of forest:

$$\hat{\eta}_{\text{F}}^{(0)} = \hat{\eta}_{\text{I}}^{(0)} + \hat{\eta}_{\text{R}}^{(0)}, \quad \langle \hat{u}_{\text{F}}^{(0)} \rangle = \langle \hat{u}_{\text{I}}^{(0)} \rangle + \langle \hat{u}_{\text{R}}^{(0)} \rangle \quad \text{at } X = 0 \quad (4.54)$$

and

$$\hat{\eta}_{\text{F}}^{(0)} = \hat{\eta}_{\text{T}}^{(0)}, \quad \langle \hat{u}_{\text{F}}^{(0)} \rangle = \langle \hat{u}_{\text{T}}^{(0)} \rangle \quad \text{at } X = L_{\text{F}} \quad (4.55)$$

Substituting the wave amplitude and velocity spectrum into these two conditions (4.54) and (4.55), the coefficients are derived as

$$C_1 = \frac{2\hat{A}_0(1 - \gamma_s \hat{\mathcal{K}})}{(1 - \gamma_s \hat{\mathcal{K}})^2 - (1 + \gamma_s \hat{\mathcal{K}})^2 e^{2\gamma_s L_{\text{F}}}}, \quad C_2 = \frac{-2\hat{A}_0(1 + \gamma_s \hat{\mathcal{K}}) e^{2\gamma_s L_{\text{F}}}}{(1 - \gamma_s \hat{\mathcal{K}})^2 - (1 + \gamma_s \hat{\mathcal{K}})^2 e^{2\gamma_s L_{\text{F}}}} \quad (4.56)$$

and

$$R_s = \frac{2(1 - \gamma_s \hat{\mathcal{K}}) - 2(1 + \gamma_s \hat{\mathcal{K}}) e^{2\gamma_s L_{\text{F}}}}{(1 - \gamma_s \hat{\mathcal{K}})^2 - (1 + \gamma_s \hat{\mathcal{K}})^2 e^{2\gamma_s L_{\text{F}}}} - 1, \quad T_s = \frac{-4\gamma_s \hat{\mathcal{K}} e^{(\gamma_s - i)L_{\text{F}}}}{(1 - \gamma_s \hat{\mathcal{K}})^2 - (1 + \gamma_s \hat{\mathcal{K}})^2 e^{2\gamma_s L_{\text{F}}}} \quad (4.57)$$

With the wave amplitude spectrum for each region, the free surface elevation can then be obtained by the inverse Fourier transform in (4.14).

4.5.1.2 Numerical results

To check the approach, we compare the above semi-analytical solutions with the experimental data reported by Mei et al. (2011). The experimental setup and the wave conditions can be found in Mei et al. (2011)'s Fig.8 and Table 5, respectively. The model forest has 1.08 m in width.

In numerical computations, as stated in Sec.4.3.4, we start with the truncated range of harmonics as $10^{-3} \leq \omega \leq 10$ where totally 40 equally-distributed values are included. To test the numerical results, here we modify the range of harmonics by increasing the highest value by one at each time and compute the relative error of the maximum wave heights obtained from two successive arrangements. The convergence criterion requires the error to be less than 0.1 %. It is shown that this range (i.e. $10^{-3} \leq \omega \leq 10$) provides convergent results for the cases with relatively smaller waves (e.g. $H_{\text{inc}}/h_0 = 0.0413$ and 0.0744). However, for the cases with larger waves (e.g. $H_{\text{inc}}/h_0 = 0.1113, 0.1487, 0.1864$), we need to adopt $10^{-3} \leq \omega \leq 15$ with 40 equally-distributed values to have convergent free surface elevation. For both ranges, the small parameter in (4.8) is still satisfied. Comparing with the data at the end of forest (i.e. wave gauge 6 in Mei et al. 2011's Fig.8), the relative errors of numerical results for all the reported cases are always less than 10 %. Two wave conditions are selected to present the comparisons between the predicted free surface elevation and the experimental measurements in Fig.4.1.

In addition, defining the normalized damping height as

$$\Delta H^* (\%) = \frac{|H_{\text{end}} - H_{\text{inc}}|}{H_{\text{inc}}} \times 100\% \quad (4.58)$$

where H_{end} denotes the wave height measured at wave gauge 6, the comparisons of different cases (with different H_{inc}/h_0) are presented in Fig.4.2. When the nonlinearity (i.e. H_{inc}/h_0) becomes larger, the prediction seems to overestimate the wave attenuation by the forest. The eddy viscosity ν_e in (4.9), which directly affects the dissipation rate, is approximately linear with the incident wave nonlinearity when H_{inc}/h is small enough, i.e. $O(H_{\text{inc}}/h_0) \ll 1$. This may explain the numerical damping height and the reported data have different be-

haviors when the nonlinearity of incident waves becomes higher. The limitation of the present linear model also contributes to the discrepancy between numerical results and measurements, which may not be clear here due to the lack of cases with higher nonlinearity. Further discussions on the nonlinearity of incident waves will be presented later for other forest configurations. It is also observed that the forest has a higher efficiency for damping larger waves. In addition to the wave crest attenuation, the reflection by the forest belt is also detected by the present model at wave gauge 2, where the reflected wave height ranges from 15% to 20% of the incident wave.

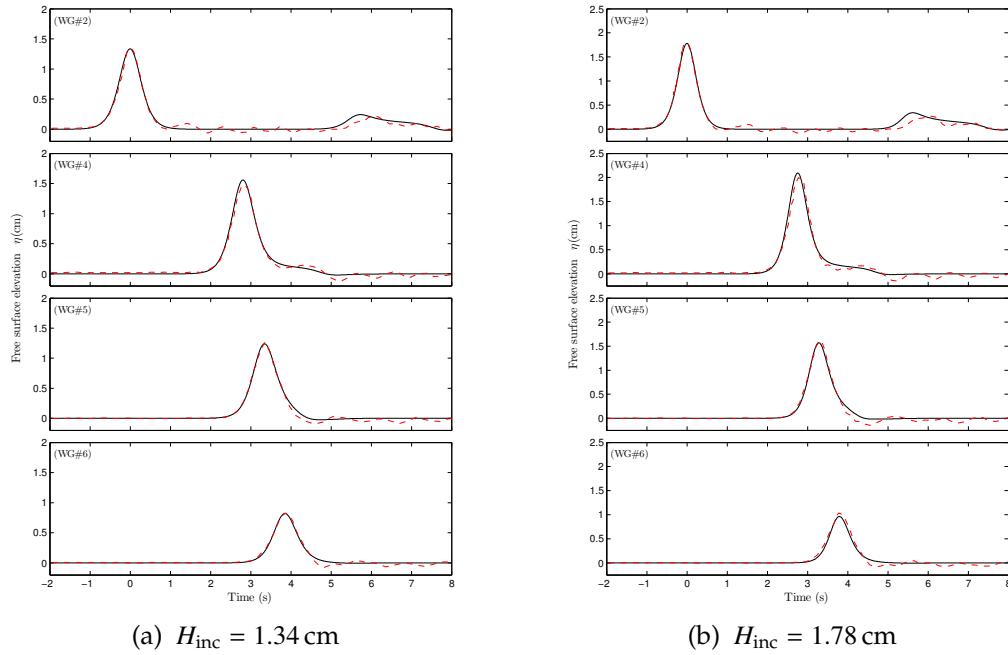


Figure 4.1: Comparison of wave heights by numerical simulations (solid lines) with experimental data (dashed lines) through the forest belt. For both cases, the water depth $h_0 = 12$ cm, the width of forest belt $L_F = 1.08$ m and the cylinder size $d = 1$ cm with porosity $n \approx 91.27\%$.

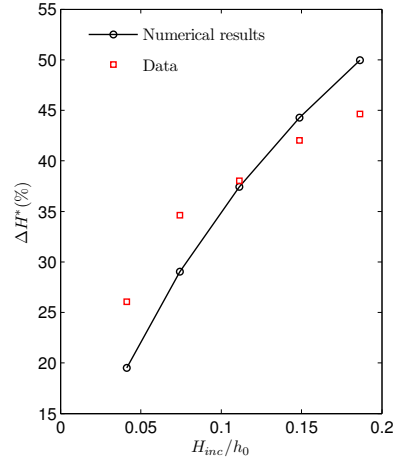


Figure 4.2: Comparison of normalized damping height as defined in (4.58): circles show the model results and squares represent the experimental measurements.

4.5.2 Solitary wave through a circular forest

To check the present numerical model, we consider a circular forest with radius R , as used in Sec.3.6.2 for studying periodic waves. The laboratory experiments were conducted by using the same facility at the University of Cantabria. The experimental setup and the detailed arrangement of wave gauges have been given in Fig.3.16. Two water depths with different wave conditions were tested (Table 4.1 and 4.2). In the following, we first present the semi-analytical solutions for wave amplitude spectrum. The numerical results obtained by the present model agree very well with the semi-analytical solutions and the comparisons will not be shown here. Instead, the comparisons between the model simulations and experimental data will be presented and discussed.

Table 4.1: Experimental conditions and dimensionless parameters – Solitary Test I

Case	h_0 (cm)	H_{inc} (cm)	k_s (1/m)	L (m)	$k_s h_0$	$k_s H_{\text{inc}}$	H_{inc}/h_0	ν_e (m ² /s)
3S1	30	3.54	0.9916	6.3362	0.2975	0.0351	0.1180	2.1101E-04
3S2		4.42	1.1081	5.6705	0.3324	0.0490	0.1473	2.6007E-04
3S3		5.35	1.2191	5.1541	0.3657	0.0652	0.1783	3.1063E-04
3S4		7.34	1.4279	4.4003	0.4284	0.1048	0.2447	4.1466E-04
3S5		8.32	1.5202	4.1330	0.4561	0.1265	0.2773	4.6397E-04
3S6		9.21	1.5995	3.9283	0.4798	0.1473	0.3070	5.0774E-04
3S7		10.92	1.7416	3.6076	0.5225	0.1902	0.3640	5.8930E-04
3S8		11.26	1.7686	3.5527	0.5306	0.1991	0.3753	6.0514E-04

Table 4.2: Experimental conditions and dimensionless parameters – Solitary Test II

Case	h_0 (cm)	H_{inc} (cm)	k_s (1/m)	L (m)	$k_s h_0$	$k_s H_{\text{inc}}$	H_{inc}/h_0	ν_e (m ² /s)
4S1	40	3.58	0.6477	9.7006	0.2591	0.0232	0.0895	1.8721E-04
4S2		4.54	0.7294	8.6141	0.2918	0.0331	0.1135	2.3483E-04
4S3		5.44	0.7984	7.8694	0.3194	0.0434	0.1360	2.7859E-04
4S4		7.42	0.9325	6.7381	0.3730	0.0692	0.1855	3.7197E-04
4S5		8.40	0.9922	6.3329	0.3969	0.0833	0.2099	4.1681E-04
4S6		9.44	1.0518	5.9738	0.4207	0.0993	0.2359	4.6346E-04
4S7		11.39	1.1553	5.4385	0.4621	0.1316	0.2848	5.4848E-04
4S8		11.61	1.1664	5.3867	0.4666	0.1354	0.2903	5.5789E-04

The above h_0 represents the constant water depth and the incident wave height H_{inc} is obtained from the averaged wave height measured by wave gauges 1, 2 and 3. k_s denotes the effective wavenumber defined in (4.12) and the wave length $L = 2\pi/k_s$. For all the cases, the diameter of the circular forest is 3 m and the cell porosity is approximately 91.27 %.

4.5.2.1 Semi-analytical solutions

The governing equation (4.30) for wave amplitude spectrum within the forest region (with subscript F) can be expressed in cylindrical coordinates as

$$\frac{1}{r} \frac{\partial}{\partial r} \left(r \frac{\partial \hat{\eta}_F^{(0)}}{\partial r} \right) + \frac{1}{r^2} \frac{\partial^2 \hat{\eta}_F^{(0)}}{\partial \theta^2} + \hat{\beta}^2 \hat{\eta}_F^{(0)} = 0, \quad \hat{\beta} = \sqrt{in/\hat{\mathcal{K}}} \quad (4.59)$$

where the semi-analytical solution can be readily obtained as

$$\hat{\eta}_F^{(0)} = \hat{A}_0 \sum_{m=0}^{\infty} \epsilon_m i^m \cos m\theta C_m J_m(\hat{\beta}r) \quad (4.60)$$

For the open water region, the wave amplitude spectrum, including the incident and scattered waves, gives

$$\hat{\eta}_I^{(0)} + \hat{\eta}_S^{(0)} = \hat{A}_0 \sum_{m=0}^{\infty} \epsilon_m i^m \cos m\theta \left[J_m(r) + B_m H_m^{(1)}(r) \right] \quad (4.61)$$

where $\hat{\mathcal{K}} = i$ and $n = 1$ have been applied. In (4.61), J_m and H_m denote respectively the Bessel function of the first kind and the Hankel function of the first kind. The Jacobi symbol has the following definition: ϵ_m has $\epsilon_0 = 1$ and $\epsilon_m = 2$ when $m \geq 1$. The unknown coefficients B_m and C_m are determined by the matching conditions at $r = R$, requiring the wave amplitude and velocity spectrum to be continuous:

$$\hat{\eta}_F^{(0)} = \hat{\eta}_I^{(0)} + \hat{\eta}_S^{(0)} \quad \text{and} \quad -i\hat{\mathcal{K}} \frac{\partial \hat{\eta}_F^{(0)}}{\partial r} = \frac{\partial \hat{\eta}_I^{(0)}}{\partial r} + \frac{\partial \hat{\eta}_S^{(0)}}{\partial r}. \quad (4.62)$$

Substituting (4.60) and (4.61) into (4.62) yields

$$B_m = \frac{-\Delta J / (i\hat{\beta}\hat{\mathcal{K}}\Delta J_{\hat{\beta}}) - J_m(R)/J_m(\hat{\beta}R)}{H_m^{(1)}(R)/J_m(\hat{\beta}R) + 2\Delta H^{(1)} / (i\hat{\beta}R\hat{\mathcal{K}}\Delta J_{\hat{\beta}})} \quad \text{and} \quad C_m = \frac{\Delta J + 2B_m\Delta H^{(1)}/R}{-i\hat{\beta}\hat{\mathcal{K}}\Delta J_{\hat{\beta}}} \quad (4.63)$$

where $\Delta J = [J_{m-1}(R) - J_{m+1}(R)]$, $\Delta J_{\hat{\beta}} = [J_{m-1}(\hat{\beta}R) - J_{m+1}(\hat{\beta}R)]$ and $\Delta H^{(1)} = [mH_m^{(1)}(R) - RH_{m+1}^{(1)}(R)]$. The solutions for the free surface elevation can be obtained by the inverse Fourier transform of the wave amplitude spectrum.

4.5.2.2 Numerical results

In numerical computations, the circular forest boundary is discretized as shown in Fig.3.18. For each harmonic, we adopt the same discretization with 180

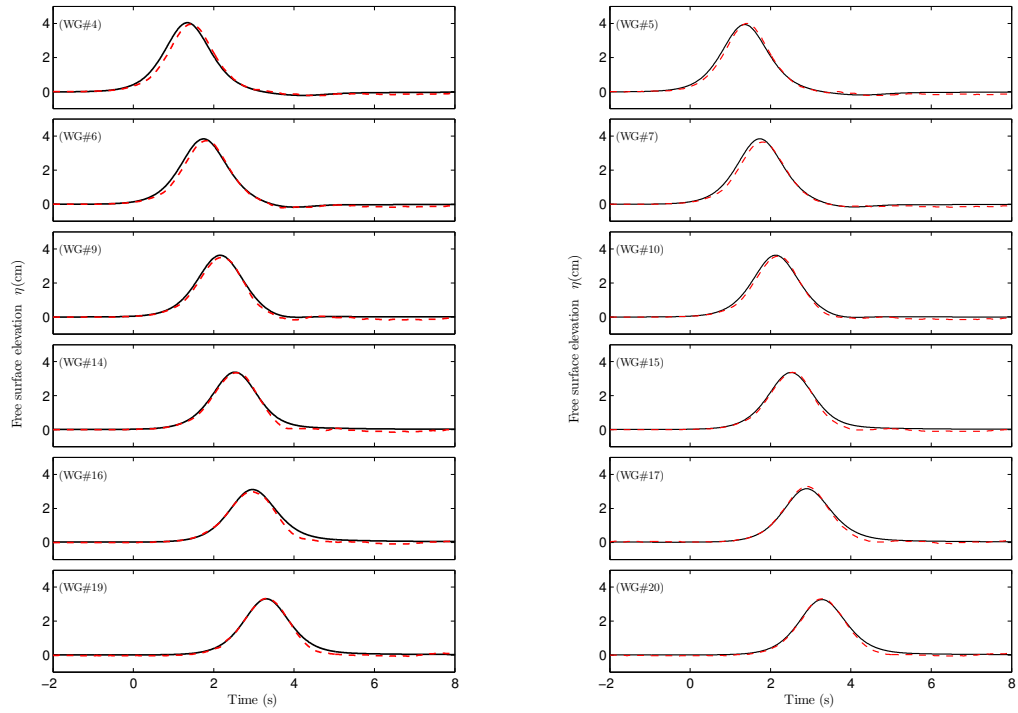
boundary elements ($\mathbb{N}_F = \mathbb{N}_S = 180$) in total. This was confirmed by a convergence test in Sec.3.6.2.3. We first compare the numerical results with the semi-analytical solutions in the above. The agreements are excellent. Thus, the detailed comparisons are skipped.

Here we compare the numerical results with the experimental measurements. Two cases with lowest values of H_{inc}/h_0 are first shown in Fig.4.3 and 4.4. On the other hand, Fig.4.5 and 4.6 present the comparisons of two other cases with higher values of H_{inc}/h_0 . Comparisons are made at gauges along the centerline ($Y = 0$) as well as the off-centerline ($Y = -R/2$). The wave crest attenuation is evident in both sets of cases. The wave height in front of the forest increases slightly due to the wave scattering and reflection. In addition, the diffracted wave converging behind the forest is also evident at wave gauge 19 and 20, resulting in a slightly increased wave height. The wave height variations along the centerline of the circular forest are shown in Fig.4.7. Overall, the numerically-simulated wave heights agree well with the measured wave heights. The relative differences are always below 17 %. More specifically, for the cases with smaller nonlinearity (i.e. $H_{\text{inc}}/h_0 \leq 0.2$), the relative error is lower than 10 %. More comparisons are presented from Fig.D.1 – D.12 in Appendix D.

Further investigation is conducted on the normalized damping height along the centerline of the circular forest, which is defined as (4.58) with H_{end} representing H_{16} , i.e. the measured height by wave gauge 16. Fig.4.8 shows the variation of normalized damping height along the centerline with the nonlinearity of incident wave. Obviously, the relative differences between the predicted and measured damping height are smaller when $H_{\text{inc}}/h_0 \leq 0.3$. On the other hand,

the discrepancy becomes noticeable when the nonlinearity is beyond 0.3, which confirms the limitation of the present linear model. It is also shown that the forest is more efficient on damping larger waves.

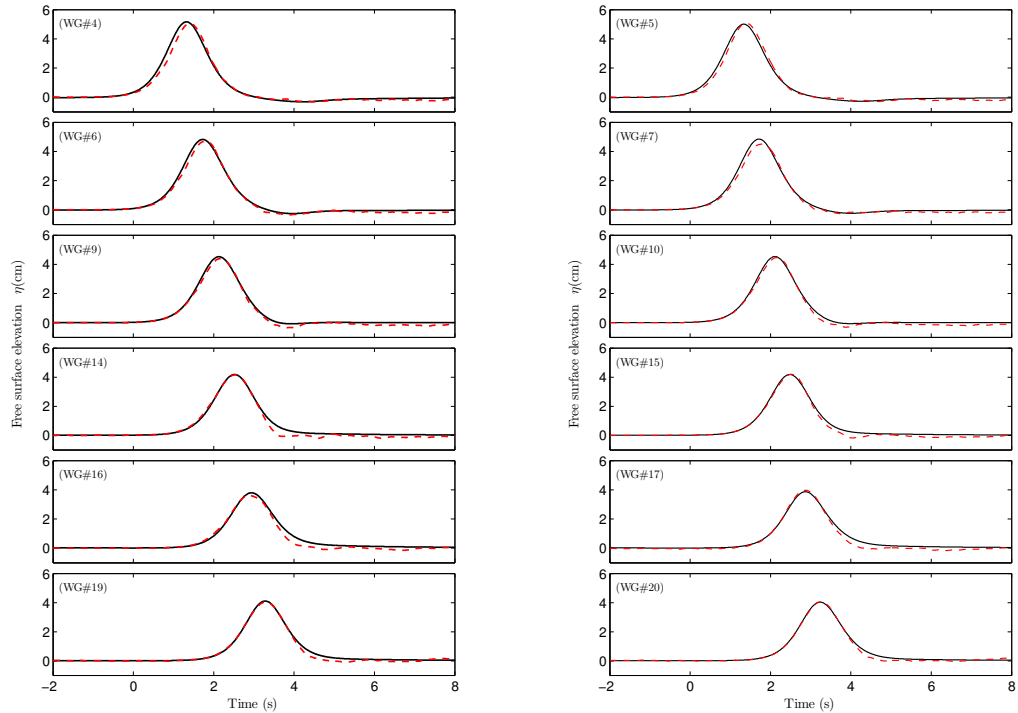
It should be noted that during the calibration tests (i.e. test runs without cylinders), wave gauge 10 shows irregularities. Namely, the wave height measurements at gauge 10 are approximately +5 to +10 % of the incident wave height for the wave tests in Table 4.1. On the other hand, for Table 4.2 the wave height measurements at gauge 10 are approximately -5 to -8 % of the incident wave height during the calibration tests.



(a) $Y = 0$: along WG #4, 6, 9, 14, 16, 19

(b) $Y = -R/2$: along WG #5, 7, 10, 15, 17, 20

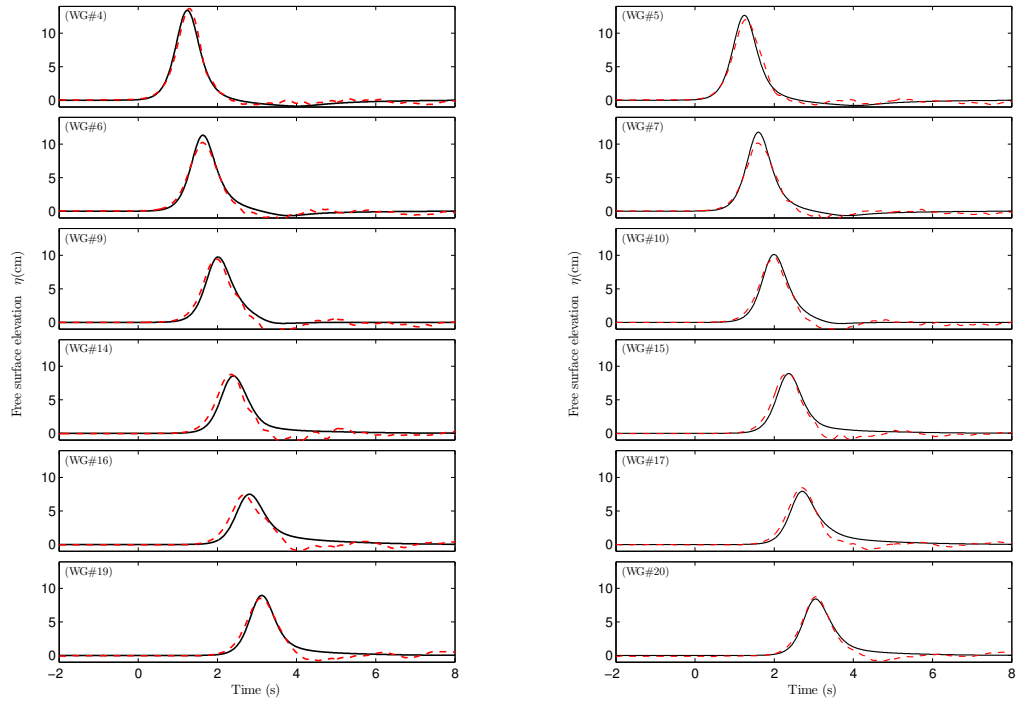
Figure 4.3: Comparison of wave heights by numerical simulations (solid lines) with experimental data (dashed lines) for Case 4S1.



(a) $Y = 0$: along WG #4, 6, 9, 14, 16, 19

(b) $Y = -R/2$: along WG #5, 7, 10, 15, 17, 20

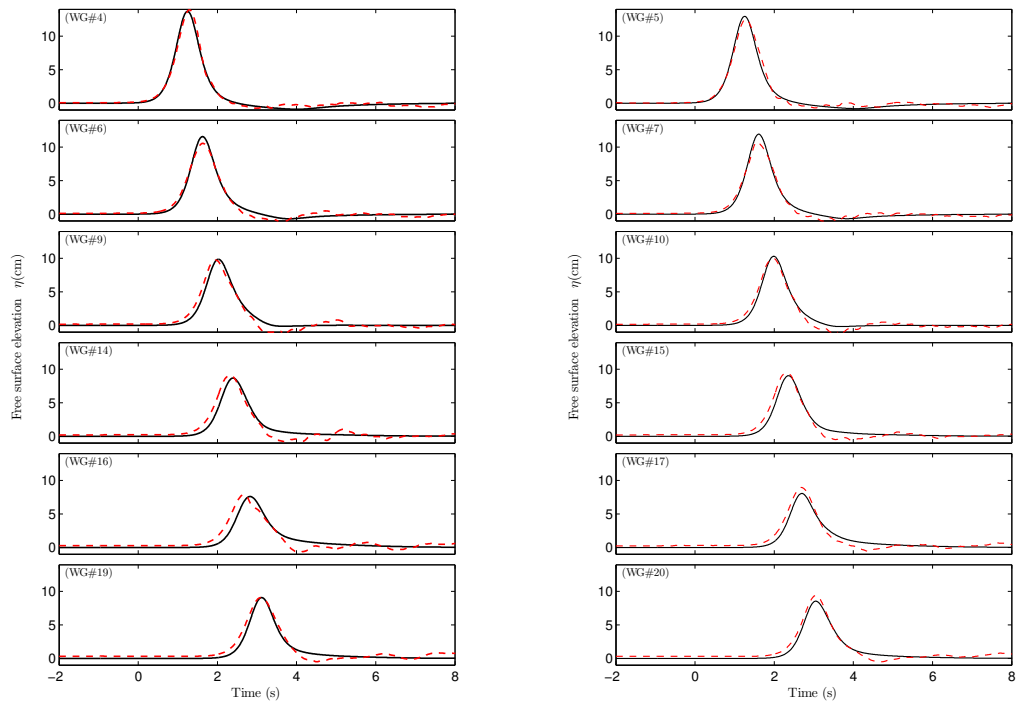
Figure 4.4: Comparison of wave heights by numerical simulations (solid lines) with experimental data (dashed lines) for Case 4S2.



(a) $Y = 0$: along WG #4, 6, 9, 14, 16, 19

(b) $Y = -R/2$: along WG #5, 7, 10, 15, 17, 20

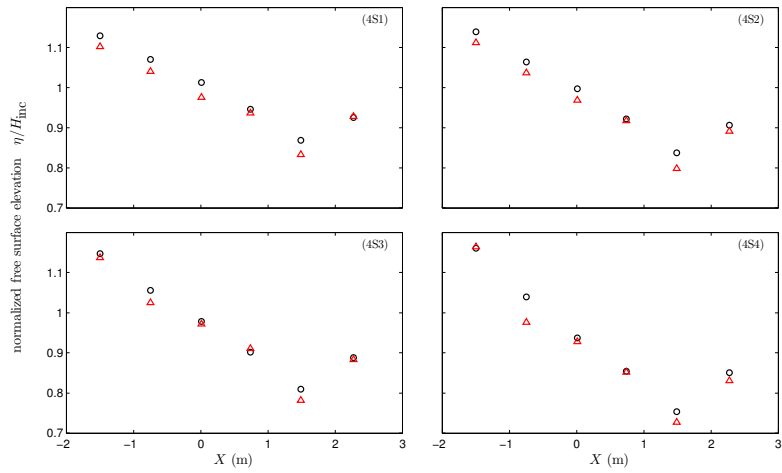
Figure 4.5: Comparison of wave heights by numerical simulations (solid lines) with experimental data (dashed lines) for Case 4S7.



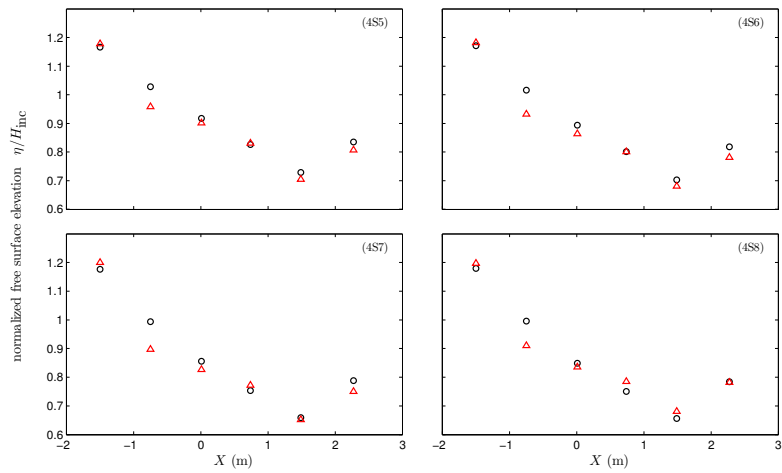
(a) $Y = 0$: along WG #4, 6, 9, 14, 16, 19

(b) $Y = -R/2$: along WG #5, 7, 10, 15, 17, 20

Figure 4.6: Comparison of wave height by numerical simulations (solid lines) with experimental data (dashed lines) for Case 4S8.



(a) 4S1–4S4



(b) 4S5–4S8

Figure 4.7: Comparison of simulated and measured wave height profiles along the centerline for cases in Table 4.2: circles – model results; triangles – data.

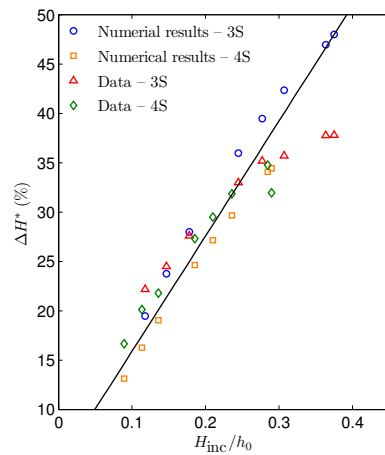


Figure 4.8: Comparison of normalized damping height along the centerline. 3S and 4S represent the wave conditions in Table 4.1 and 4.2 respectively. Linear fitting (solid) line for numerical simulation is $\Delta H^*(\%) = 166.66 (H_{inc}/h_0) + 4.22$ with $R^2 = 0.9541$.

4.5.3 Solitary wave through multiple circular forest patches

To further test the present numerical model, we employ multiple circular patches as another special forest configuration. The detailed experimental setup has been provided in Fig.3.26. Note that the experimental facility is the same as that presented in Sec.4.5.2 but with a different arrangement of wave gauges. The experimental conditions can be found in Table 4.3.

Table 4.3: Experimental conditions and dimensionless parameters for multiple circular forest patches

Case	h_0 (cm)	H_{inc} (cm)	k_s (1/m)	L (m)	$k_s h_0$	$k_s H_{inc}$	H_{inc}/h_0	ν_e (m ² /s)
1	30	4.59	1.1292	5.5645	0.3387	0.0518	0.1530	2.6941E-04
2		6.98	1.3924	4.5124	0.4177	0.0972	0.2327	3.9623E-04
3		9.16	1.5951	3.9390	0.4785	0.1461	0.3053	5.0531E-04

The above h_0 represents the constant water depth and the incident wave height H_{inc} is obtained from the wave height measured by wave gauges 1. k_s denotes the effective wavenumber defined in (4.12) and the wave length $L = 2\pi/k_s$. For all the cases, the cell porosity is approximately 91.27 %.

4.5.3.1 Numerical results

Considering each patch as a homogeneous subzone of the entire forest region, a constant bulk value of dimensional eddy viscosity is assumed and determined by (4.9). Due to the same properties (cylinder arrangement and cell porosity) over four patches, the bulk value of dimensional eddy viscosity is assigned to each patch. Therefore, the cell problem corresponding to each harmonic needs to be solved only once. Note again that the cell problem for different harmonic components (ω) has to be solved independently as the dimensionless eddy viscosity depends on ω . Following the convergence tests, we here

adopt $10^{-3} \leq \omega \leq 15$ (with 40 equally-distributed values) as the arrangement of truncated harmonic components in numerical computations. For each harmonic, the same discretization of forest boundary (see Fig.3.18) is applied for each patch with 720 boundary elements in total (i.e. $\mathbb{N}_\xi = 180$ and $\mathbb{N}_S = 720$). Uniform solution along each element is assumed. For each patch (i.e. patch ξ), the outward normal direction of the boundary can be represented by r_ξ which is shown in Fig.3.18, i.e. $\hat{n}_\xi = -\hat{n}_S \equiv r_\xi$. Therefore, the matching conditions in (4.46) and (4.47) become

$$\left(\hat{\mathcal{G}}_\xi\right)_{ij} \left(\frac{\partial \hat{\eta}_\xi^{(0)}}{\partial r_\xi}\right)_j = \hat{A}_0 e^{iX_i} - \left(\hat{\mathcal{Q}}_S\right)_{im} \left(\frac{\partial \hat{\eta}_S^{(0)}}{\partial r_\xi}\right)_m \quad (4.64)$$

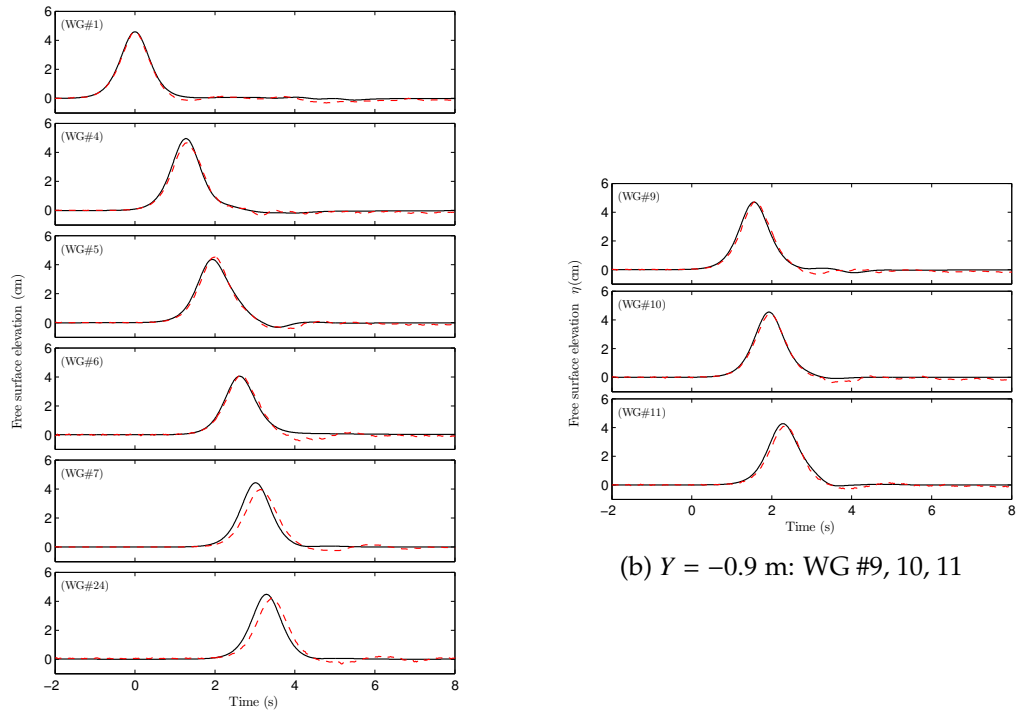
and

$$-i\hat{\mathcal{K}} \left(\frac{\partial \hat{\eta}_\xi^{(0)}}{\partial r_\xi}\right)_i = \hat{A}_0 \frac{\partial e^{iX_i}}{\partial r_\xi} + \left(\frac{\partial \hat{\eta}_S^{(0)}}{\partial r_\xi}\right)_i \quad (4.65)$$

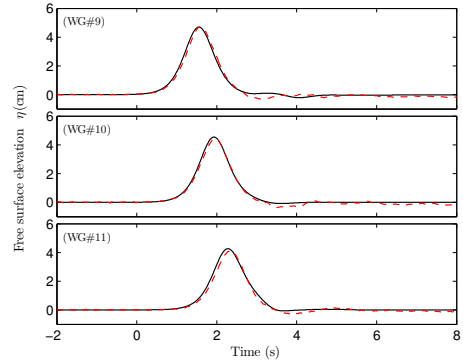
where i & $j = 1 \cdots \mathbb{N}_\xi$ and $m = 1 \cdots \mathbb{N}_S$ with $\mathbb{N}_S = \sum_1^4 \mathbb{N}_\xi$. A system of equations for solving $\partial \hat{\eta}_\xi^{(0)} / \partial r_\xi$ and $\partial \hat{\eta}_S^{(0)} / \partial r_\xi$ is formulated. After the unknown $\hat{\eta}_\xi^{(0)}$ and $\hat{\eta}_S^{(0)}$ and their normal derivatives along the boundaries are solved, the wave amplitude spectrum in each patch as well as in open water can be obtained from (4.34) and (4.37), respectively. Once again, we note that the wave amplitude spectrum for each harmonic is solved separately and the free surface elevation can be computed by the inverse Fourier transform in (4.14) with numerical integration.

The comparisons of numerically-simulated free surface elevations with gauge measurements are presented in Fig.4.9 – 4.11. As concluded previously for a circular forest, the nonlinearity of incident wave plays an essential role in the accuracy of model prediction. Similar results can also be observed in Fig.4.9 – 4.11. For smaller waves (e.g. Case 1: $H_{\text{inc}}/h_0 \approx 0.15$), the largest relative wave

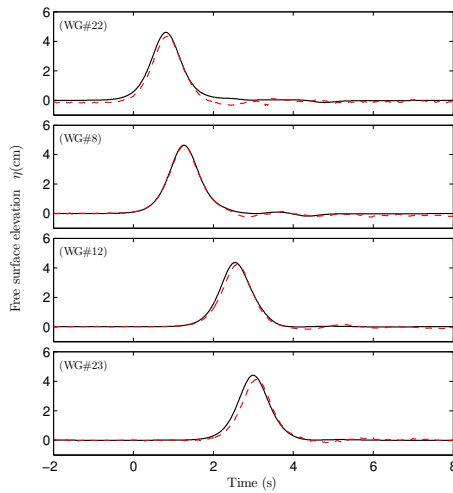
height difference appears to be 10 % at wave gauge 7. For larger wave (e.g. Case 2: $H_{\text{inc}}/h_0 \approx 0.23$ and Case 3: $H_{\text{inc}}/h_0 \approx 0.31$), on the other hand, the relative errors increase to 14 % at wave gauge 7. Furthermore, the discrepancy at wave gauge 4, which is close to the entry of the vegetated area, is higher than expected while the measurements at wave gauge 10 for Case 2 and 3 present lower values than expected. It is also obvious that the phase differences between the model predictions and the data become noticeable for all the cases when the wave gauges are outside the vegetated area (i.e. wave gauges 7 & 24). In fact, the phase differences for three cases are almost the same (i.e. ≈ 0.13 s at wave gauges 7 & 24). Finally, we also compare the numerically-simulated wave heights along the centerline with those for the single circular forest (Sec.4.5.2) in Fig.4.12. As more cylinders are used for the single circular forest than those for four smaller patches, higher attenuation of the advancing wave crest (around 10 % for Case 1 and 15 % for Case 2) is observed in the single patch case. Also, the phase differences due to the existence of more cylinders (i.e. higher porosity) are recognized.



(a) $Y = 0$ m (Centerline): WG #1, 4, 5, 6, 7, 24

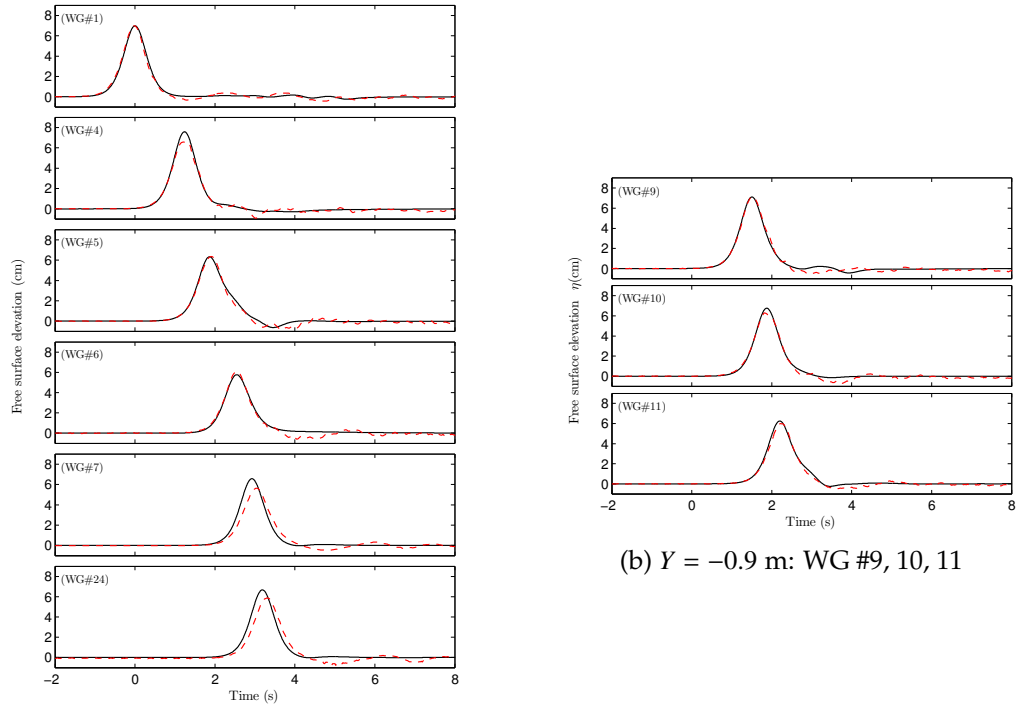


(b) $Y = -0.9$ m: WG #9, 10, 11

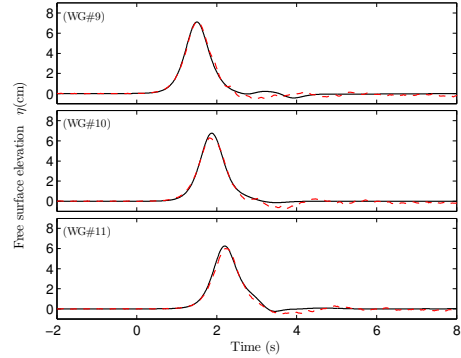


(c) $Y = -1.17$ m: WG #22, 8, 12, 23

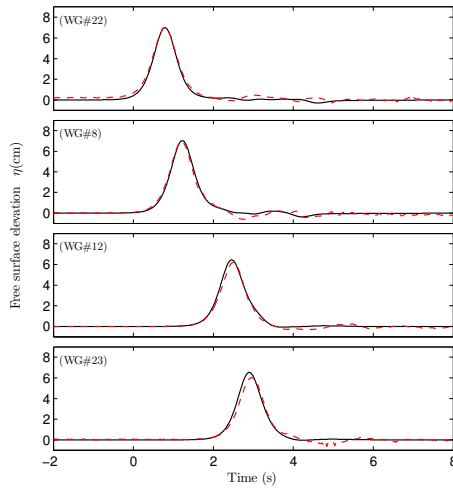
Figure 4.9: Comparison of wave height by numerical simulation (solid lines) with experimental data (dashed lines) for multiple patches – Case 1.



(a) $Y = 0$ m (Centerline): WG #1, 4, 5, 6, 7, 24

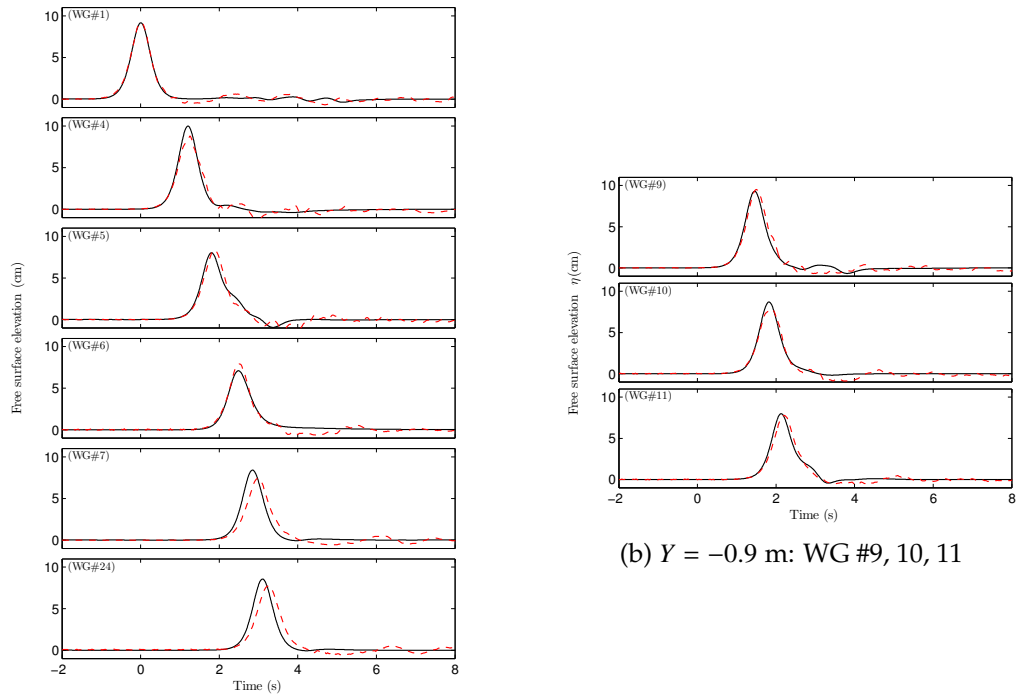


(b) $Y = -0.9$ m: WG #9, 10, 11

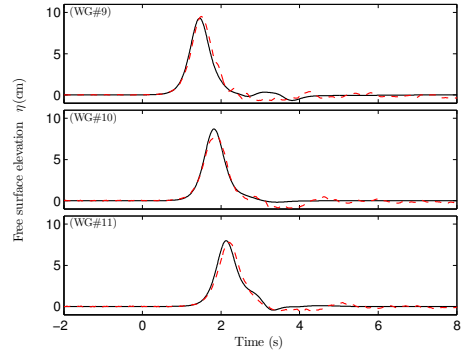


(c) $Y = -1.17$ m: WG #22, 8, 12, 23

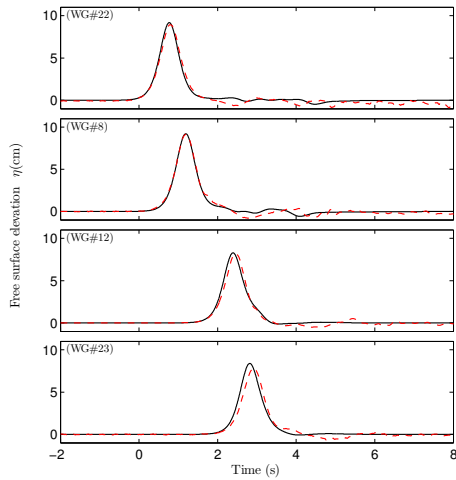
Figure 4.10: Comparison of wave height by numerical simulation (solid lines) with experimental data (dashed lines) for multiple patches – Case 2.



(a) $Y = 0$ m (Centerline): WG #1, 4, 5, 6, 7, 24



(b) $Y = -0.9$ m: WG #9, 10, 11



(c) $Y = -1.17$ m: WG #22, 8, 12, 23

Figure 4.11: Comparison of wave height by numerical simulation (solid lines) with experimental data (dashed lines) for multiple patches – Case 3.

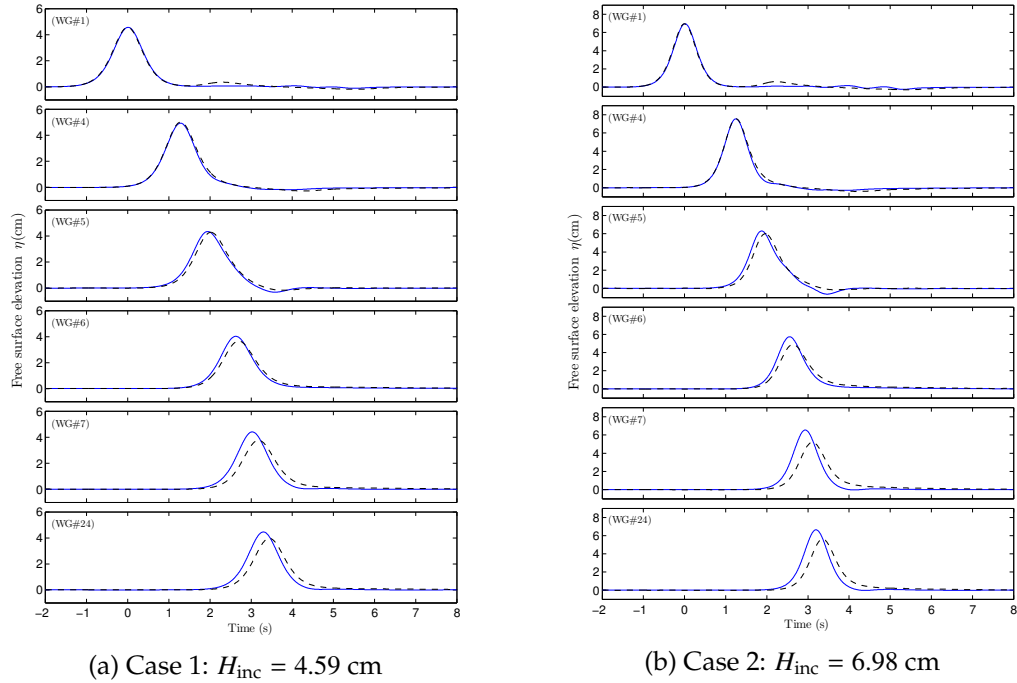


Figure 4.12: Comparison of numerical-simulated wave heights through the centerline of single circular forest (dashed lines) and of multiple patches (solid lines).

4.6 Concluding remarks and discussions

Transient long waves with a soliton-like impulse propagating through a coastal forest are studied in this chapter. The multi-scale perturbation method is applied to separate the cylinder and wavelength scales. Starting with linearized equations, Fourier transform is used for solving the transient problem, which is different from the approach used in [Mei et al. \(2011\)](#). The micro- and macro-scale problems for each harmonic are solved independently. Once the wave amplitude spectrum for each harmonic is obtained, the free surface elevation can be computed by inverse Fourier transform. It should be remarked again that the incident wave height has to be reasonably small due to the use of

linear wave theory. To determine the finite number of harmonic components used in the numerical computations, we first perform a test and conclude that $10^{-3} \leq \omega \leq 10$ (with equally-distributed 40 values in total) is sufficient to reconstruct the incident soliton in (4.11). Using this arrangement in the numerical computations shows convergent simulated free surface elevation for relatively smaller waves. For larger waves, on the other hand, higher values of harmonics (e.g. $10^{-3} \leq \omega \leq 15$) are needed such that the range of harmonics has to be modified.

Similar to Sec.3.3, the boundary integral equation method is employed for resolving the arbitrary forest shape such that the leading-order wave amplitude spectrum is solved numerically. Each forest subzone is considered as a homogeneous region where a dimensional bulk eddy viscosity is determined by an empirical formula. It is reiterated here that while the dimensional eddy viscosity is a constant in a subzone, the dimensionless eddy viscosity depends on the harmonic component. A computing program has been written based on the present numerical model and can be applied to different configurations of forest patches. The required inputs of the numerical model are described in Appendix B.2.1.

To check the present approach, the forest belt studied in Mei et al. (2011) is first examined with new semi-analytical solutions being provided. A modification of the empirical formula for eddy viscosity in Mei et al. (2011) shows better agreement between the semi-analytical results and reported data. By checking the normalized damping height, the model limitation on the non-linearity of incident wave is observed. We also test the efficiency of different forest sizes on damping the incident wave energy. As expected, thicker forest

belts can have higher wave dissipation. For the largest wave in their cases (i.e. $H_{\text{inc}}/h_0 \approx 0.1864$), approximately 90 % of incident wave height is damped out when the forest width becomes four times of the original size (i.e. $4 \times L_F$). The circular forest, as presented in Sec.3.6.2, is then used to check the numerical model. The numerical results show very good agreement with the experimental data. The relative differences between measured and simulated wave heights are less than 17 %. For the cases with smaller nonlinearity, i.e. $H_{\text{inc}}/h_0 \leq 0.2$, the relative errors become less than 10 %. Focusing on the normalized damping height along the centerline, the relative errors are less than 12 % for most of the cases (i.e. $H_{\text{inc}}/h_0 \leq 0.3$), which confirms the linear limitation of the present model on the nonlinearity of incident wave. Further investigation on the present model is conducted by using the forest configuration in Sec.3.6.3, which contains four smaller circular patches. Again, good agreements between model results and the data are found and the effects of the nonlinearity of incident wave are also observed. Similarly, the discrepancy between numerical simulations and the data starts increasing when $H_{\text{inc}}/h_0 > 0.2$. The comparisons of wave attenuation by the single circular forest and by multiple patches are also presented, showing higher attenuation of incoming waves by the former.

As we know, a solitary wave, with a finite wave height, can propagate at a constant speed without changing its shape over a fairly long distance. As mentioned in Mei et al. (2005), a linear and non-dispersive approximation could be used over a certain length of time, which could be estimated by $t \sim \sqrt{h_0/g}(L/H_{\text{inc}})$. Using the effective wavelength of a solitary wave as the length scale L , the time t can range from $O(10)$ to $O(100)$ secs for the wave conditions presented in Sec.4.5.1 – 4.5.3. An approximate traveling distance dur-

ing this time t can be obtained by using the wave speed of a solitary wave $= \sqrt{g(h_0 + H_{\text{inc}})}$, which gives $O(10)$ m for larger wave height and $O(100)$ m for smaller wave height. Apparently, the distance is much longer than that from the wavemaker to the forest area in the laboratory experiments, especially for lower incident wave nonlinearity. This may justify the comparisons between the present linear model and the experimental data of solitary wave, which actually has nonlinear and dispersive characteristics. On the other hand, for the cases with largest values of H_{inc}/h_0 (e.g. 3S7 & 3S8 in Table 4.1), the distance for linear non-dispersive approximation being hold is around 12 m, which is just slightly longer than that between wavemaker and the circular forest. This may also explain the discrepancy between the present linear model and experimental measurements for incident waves with higher nonlinearity. A nonlinear model shall then be considered as a future work for model expansion.

To test the effects of different cylinder configurations on wave attenuation, the staggered arrangement as shown in Fig.3.1a is adopted. With the same size of cylinder and cell porosity as used for aligned configuration (Sec.4.5.1 & 4.5.2), the spacing (i.e. micro-length scale ℓ_{st} where the subscript "st" denotes the staggered arrangement) has to be $\sqrt{2}\ell$. For the forest belt, $d = 1$ cm and $\ell_{\text{st}} = 3\sqrt{2}$. For the single circular forest, $d = 3$ cm and $\ell_{\text{st}} = 9\sqrt{2}$. In Fig.4.13, the comparisons of wave height evolution through the forest belt for two different cylinder arrangements are presented. It can be seen that the staggered arrangement brings about 5–10 % more of the wave height dissipation than the aligned cylinders although the staggered arrangement has larger cell size. Similarly, the staggered cylinder arrangement is applied to the single circular forest. The comparisons are presented in Fig.4.14 and 4.15. Up to 20 % more of the normalized

damping height is also observed in Fig.4.16.

Most of the contents in this chapter have been presented in Chang et al. (2017b).

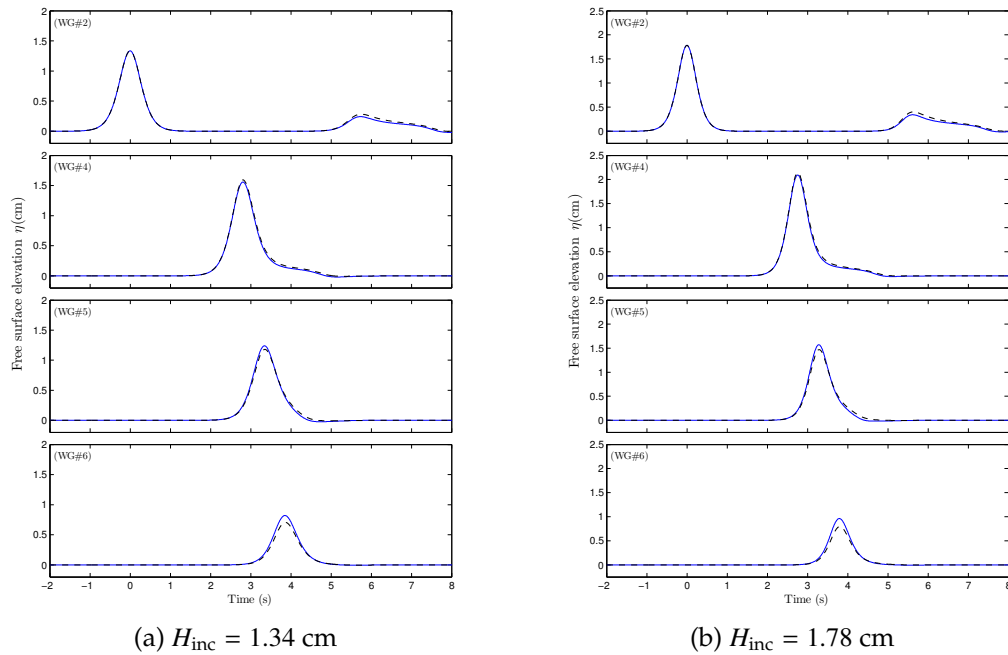
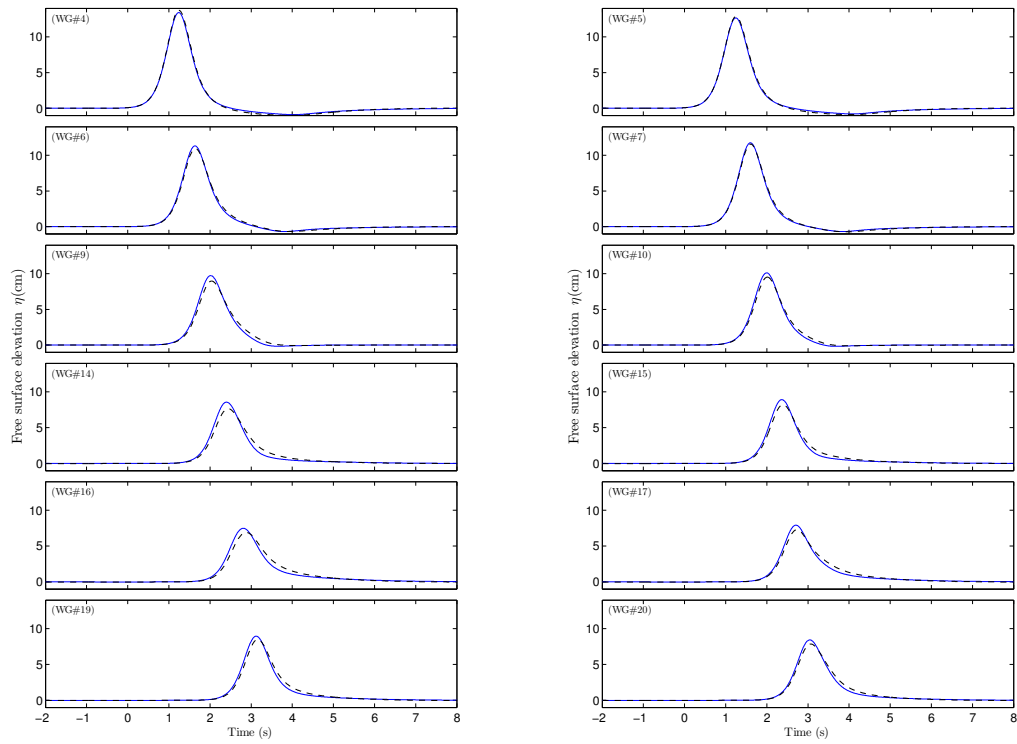


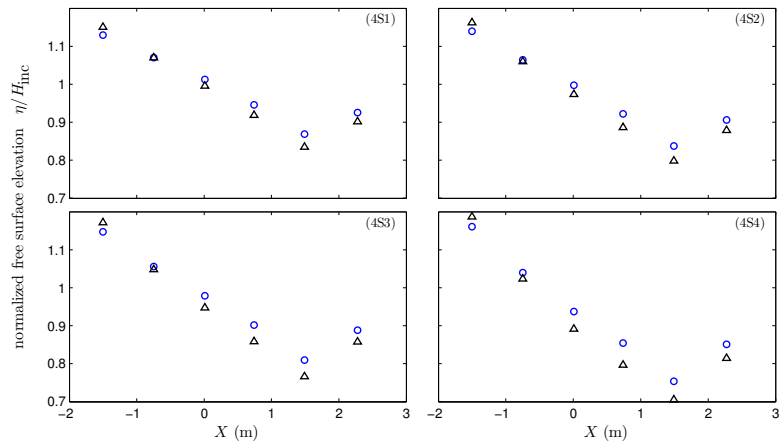
Figure 4.13: Comparison of simulated wave height between aligned and staggered cylinder arrangements for the forest belt test (Case 3 & 4): solid lines – aligned, dashed lines – staggered.



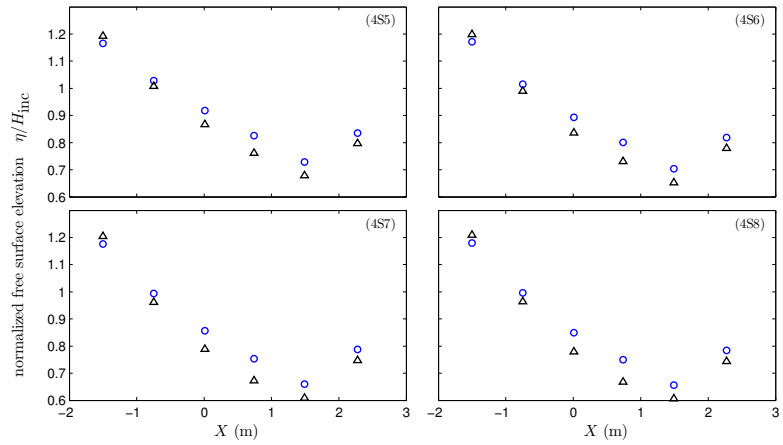
(a) $Y = 0$: along WG #4, 6, 9, 14, 16, 19

(b) $Y = -R/2$: along WG #5, 7, 10, 15, 17, 20

Figure 4.14: Comparison of simulated wave height between aligned and staggered cylinder arrangements for single circular forest test 4S7: solid lines – aligned, dashed lines – staggered.



(a) 4S1–4S4



(b) 4S5–4S8

Figure 4.15: Comparison of simulated wave height profiles along the centerline of single circular forest between aligned and staggered cylinder arrangements for cases in Table 4.2: circles – aligned; triangles – staggered.

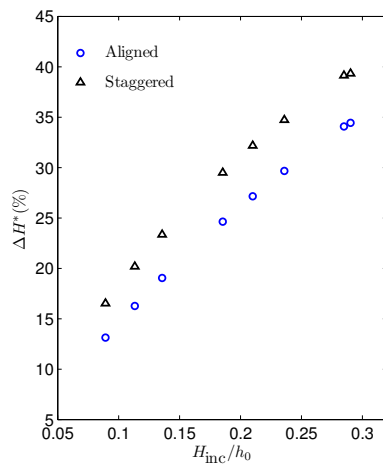


Figure 4.16: Comparison of normalized damping height along the centerline of single circular forest between aligned and staggered cylinder arrangements for cases in Table 4.2.

CHAPTER 5

HARMONICS GENERATION BY A COASTAL FOREST

In the previous chapters, we have shown the capability of the linear models on estimating wave attenuation by coastal forests. However, the limitation on the nonlinearity of incident waves has been confirmed in the data-model comparisons for both types of waves (i.e. periodic and transient waves). Accordingly, this chapter aims to take nonlinear effects into account by including the convection term in the momentum equations and to investigate the possible differences from the results obtained by the linear model.

Assuming incident waves as simple harmonic with weakly nonlinearity, higher harmonic waves are expected to be generated within the vegetated area and propagate to open water. The homogenization theory is again applied such that the micro-scale flow in the vicinity of cylinders is separated from the macro-scale wave dynamics. Different from the linear model presented in Chap.3, the leading-order cell problem now becomes a nonlinear boundary-value-problem while the macro-scale problem still remains linear. Expressing the solutions (e.g. velocity, free surface elevation) as a superposition of different harmonics, the governing equations for each mode can be separated while different harmonics are still interacting with each other due to the nonlinearity in cell problem. To solve the nonlinear boundary-value-problem, a modified pressure correction method is introduced with the use of finite difference discretization. The modified pressure correction method is an iterative approach where an appropriate initial guess is needed. A staggered grid discretization is used such that the unknown pressure locates at all the inner grid points. After obtaining the micro-scale solutions, the macro-scale wave dynamics can then be solved nu-

merically. As the cell problem is driven by the macro-scale pressure gradient, another iterative scheme is needed to solve this coupled system. The details of the numerical algorithms for both micro- and macro-scale problems are provided.

Focusing on shallow-water waves propagating through a forest belt as a special case, the leading-order wave solutions for different harmonic components are solved numerically. The present model results are first compared with the linear model results to investigate the nonlinear effects. Higher harmonic components are then presented. The reflection and transmission coefficients are also compared with existing experimental data. The effects of different parameters and varying nonlinearity on the wave solutions are further discussed.

5.1 Governing equations and boundary conditions

Starting with the shallow-water wave equations, the leading-order velocities are on the horizontal plane and are independent of z , i.e. $u_i(\vec{x}, t)$, $i = 1 \& 2$. The nonlinearity is now included in the governing equations as shown in (2.11) and (2.12), where double bars are dropped for brevity:

$$\frac{\partial \eta}{\partial t} + \frac{\partial}{\partial x_i} [u_i (h_0 + \eta)] = 0, \quad i = 1, 2 \quad (5.1)$$

and

$$\frac{\partial u_i}{\partial t} + u_j \frac{\partial u_i}{\partial x_j} = -g \frac{\partial \eta}{\partial x_i} + \nu_e \frac{\partial^2 u_i}{\partial x_j \partial x_j}, \quad i \& j = 1, 2 \quad (5.2)$$

in which h_0 and η respectively denote the constant water depth and the free surface elevation. The bottom friction has been neglected in (5.2) and the eddy viscosity ν_e is assumed to be a constant across a homogeneous forest region.

With shallow-water wave conditions, the variables can be normalized by the characteristic scales as

$$x_i^* = \frac{x_i}{\ell}, \quad \eta^* = \frac{\eta}{A_{\text{inc}}}, \quad t^* = t\omega, \quad u_i^* = \frac{u_i}{\sqrt{gh_0}A_{\text{inc}}/h_0} \quad (5.3)$$

in which the horizontal coordinates are scaled by the micro-length ℓ , and the free surface elevation is normalized by the incident wave amplitude A_{inc} . Here the constant water depth is assumed to be greater than the tree spacing but less than the wavelength, i.e. $\ell \ll h_0 \ll 1/k_{\text{inc}}$, where k_{inc} denotes the wavenumber of incident waves. The small parameter ε can be defined as

$$\varepsilon = k_{\text{inc}}\ell \equiv \omega\ell / \sqrt{gh_0} \ll \mathcal{O}(1) \quad (5.4)$$

where the typical wavenumber for shallow-water waves has been adopted, i.e. $k_{\text{inc}} \approx \omega / \sqrt{gh_0}$. To introduce the weakly nonlinearity, we define another parameter:

$$\alpha_n = \frac{A_{\text{inc}}/h_0}{\varepsilon} \quad \text{with} \quad \mathcal{O}(\alpha_n) = \mathcal{O}(1) \quad (5.5)$$

which indicates the weakly nonlinearity as

$$\mathcal{O}(A_{\text{inc}}/h_0) = \mathcal{O}(\varepsilon) \quad (5.6)$$

Based on the above scales, the normalized governing equations become:

$$\varepsilon \frac{\partial \eta^*}{\partial t^*} + \frac{\partial}{\partial x_i^*} [u_i^* (1 + \alpha_n \varepsilon \eta^*)] = 0, \quad j = 1, 2 \quad (5.7)$$

and

$$\varepsilon \frac{\partial u_i^*}{\partial t^*} + (\alpha_n \varepsilon) u_j^* \frac{\partial u_i^*}{\partial x_j^*} = -\frac{\partial \eta^*}{\partial x_i^*} + \sigma \varepsilon \frac{\partial^2 u_i^*}{\partial x_j \partial x_j}, \quad i \& j = 1, 2 \quad (5.8)$$

where the dimensionless eddy viscosity has been defined in (3.11). The normalized no-slip boundary condition along cylinder surfaces remains valid:

$$u_i^* = 0 \quad \text{when} \quad \vec{x}^* \in S_c \quad (5.9)$$

Due to the long-wave assumption, we here adopt the empirical formula in [Mei et al. \(2011\)](#) to determine the eddy viscosity ν_e :

$$\nu_e = 1.86(1 - n)^{2.06} U_0 \ell \quad \text{with} \quad U_0 = \sqrt{gh_0} (A_{\text{inc}}/h_0) \quad (5.10)$$

where U_0 represents the depth-averaged horizontal water particle velocity. The corresponding dimensionless eddy viscosity is

$$\sigma = \frac{\nu_e}{\omega \ell^2} = 1.86(1 - n)^{2.06} \frac{1}{k_{\text{inc}} \ell} \left(\frac{A_{\text{inc}}}{h_0} \right), \quad k_{\text{inc}} = \omega / \sqrt{gh_0} \quad (5.11)$$

5.2 Homogenization method

Due to the contrast between tree spacing and wavelength, we apply the multi-scale perturbation theory and introduce two coordinates as shown in [\(3.17\)](#):

$$X_i^* \equiv \varepsilon x_i^* = k_{\text{inc}} x_i \quad (5.12)$$

where the micro-scale x_i^* is used to describe flow motions in the vicinity of cylinders and the macro-scale X_i^* is for the wave dynamics over the forest area. Accordingly, the dimensionless velocity and free surface elevation can be expanded as

$$u_i^* = u_i^{*(0)} + \varepsilon u_i^{*(1)} + \varepsilon^2 u_i^{*(2)} + \dots, \quad \eta^* = \eta^{*(0)} + \varepsilon \eta^{*(1)} + \varepsilon^2 \eta^{*(2)} + \dots \quad (5.13)$$

in which u_i^* and η^* are functions of (x_i^*, X_i^*, t^*) . From here on, only dimensionless variables are used and the asterisks $(\cdot)^*$ are to be dropped for brevity. Substituting [\(5.13\)](#) back into [\(5.7\)](#) and [\(5.8\)](#), the governing equations at different orders of magnitude can be obtained as follows.

- $O(\varepsilon^0)$

$$\frac{\partial u_i^{(0)}}{\partial x_i} = 0, \quad i = 1, 2 \quad (5.14)$$

and

$$\frac{\partial \eta^{(0)}}{\partial x_i} = 0, \quad i = 1, 2 \quad (5.15)$$

In (5.15), the leading-order free surface elevation is independent of the micro-scale coordinates, i.e. $\eta^{(0)} = \eta^{(0)}(X_i, t)$.

- $O(\varepsilon^1)$

$$\frac{\partial \eta^{(0)}}{\partial t} + \frac{\partial u_i^{(0)}}{\partial X_i} + \frac{\partial u_i^{(1)}}{\partial x_i} + \alpha_n \frac{\partial (u_i^{(0)} \eta^{(0)})}{\partial x_i} = 0 \quad (5.16)$$

and

$$\frac{\partial u_i^{(0)}}{\partial t} + \alpha_n u_j^{(0)} \frac{\partial u_i^{(0)}}{\partial x_j} = -\frac{\partial \eta^{(0)}}{\partial X_i} - \frac{\partial \eta^{(1)}}{\partial x_i} + \sigma \frac{\partial^2 u_i^{(0)}}{\partial x_j \partial x_j} \quad (5.17)$$

Considering a simple harmonic incident wave train, higher harmonics will be generated because of the nonlinearity. To anticipate the growth of higher harmonics, we express the velocity components and free surface elevation as

$$u_i = \frac{1}{2} \sum_{m=-\infty}^{\infty} \tilde{u}_{i,m} e^{-im\tau} \quad \text{with} \quad \tilde{u}_{i,-m} = (\tilde{u}_{i,m})' \quad (5.18)$$

and

$$\eta = \frac{1}{2} \sum_{m=-\infty}^{\infty} \tilde{\eta}_m e^{-im\tau} \quad \text{with} \quad \tilde{\eta}_{-m} = (\tilde{\eta}_m)' \quad (5.19)$$

in which m denotes different harmonic modes and $(\cdot)'$ represents the complex conjugate operator. Focusing on the leading-order flows, the micro and macro-scale governing equations are derived in the following sections.

5.2.1 Micro-scale (cell) problem

Let's focus on the flow motion in a micro-scale cell first. Substituting (5.18) – (5.19) into the mass conservation of $O(1)$ in (5.14) and the momentum equations of $O(\varepsilon)$ in (5.17) yields:

$$\sum_{m=-\infty}^{\infty} \frac{\partial \tilde{u}_{i,m}^{(0)}}{\partial x_i} e^{-im\tau} = 0 \quad (5.20)$$

and

$$\begin{aligned} \sum_{m=-\infty}^{\infty} (-im) \tilde{u}_{i,m}^{(0)} e^{-im\tau} + \frac{\alpha_n}{2} \left(\sum_{m_1=-\infty}^{\infty} \tilde{u}_{j,m_1}^{(0)} e^{-im_1\tau} \right) \left(\sum_{m_2=-\infty}^{\infty} \frac{\partial \tilde{u}_{i,m_2}^{(0)}}{\partial x_j} e^{-im_2\tau} \right) \\ = - \sum_{m=-\infty}^{\infty} \frac{\partial \tilde{\eta}_m^{(0)}}{\partial X_i} e^{-im\tau} - \sum_{m=-\infty}^{\infty} \frac{\partial \tilde{\eta}_m^{(1)}}{\partial x_i} e^{-im\tau} + \sigma \sum_{m=-\infty}^{\infty} \frac{\partial^2 \tilde{u}_{i,m}^{(0)}}{\partial x_j \partial x_j} e^{-im\tau} \end{aligned} \quad (5.21)$$

For each mode m , the above two equations give

$$\frac{\partial \tilde{u}_{i,m}^{(0)}}{\partial x_i} = 0 \quad (5.22)$$

and

$$(-im) \tilde{u}_{i,m}^{(0)} + \frac{\alpha_n}{2} \sum_{m_1=-\infty}^{\infty} \left(\tilde{u}_{j,m_1}^{(0)} \frac{\partial \tilde{u}_{i,m-m_1}^{(0)}}{\partial x_j} \right) = - \frac{\partial \tilde{\eta}_m^{(0)}}{\partial X_i} - \frac{\partial \tilde{\eta}_m^{(1)}}{\partial x_i} + \sigma \frac{\partial^2 \tilde{u}_{i,m}^{(0)}}{\partial x_j \partial x_j} \quad (5.23)$$

in which the forcing term $\partial \tilde{\eta}_m^{(0)} / \partial X_i$ is given by the macro-scale solutions. Along the surface of cylinders, no-slip boundary condition gives

$$\tilde{u}_{i,m}^{(0)} = 0, \quad x_i \in S_c \quad (5.24)$$

In addition, $\tilde{u}_{i,m}^{(0)}$ and $\tilde{\eta}_m^{(1)}$ are subject to cell-periodicity. Apparently, equations (5.22) and (5.23), governing the cell problem of mode m , are nonlinear equations. Higher harmonics are to be generated through the nonlinearity in (5.23), where different harmonics are interacting with each other.

5.2.1.1 Modified pressure correction method

Here we employ a modified pressure correction method to solve the nonlinear cell problem. The pressure correction method, i.e. Semi-Implicit Method for Pressure Linked Equations, is basically an iterative approach and is commonly used for solving nonlinear Navier-Stokes equations (Anderson 1995, Ferziger and Peric 2012). The iteration process requires a proper initial guess of both pressure and velocity fields. Within each step of the iteration, the corrections on pressure and velocity are constructed until convergent solutions are achieved. To implement the iteration process, a pseudo-transient term needs to be introduced to the momentum equation in (5.23) as

$$\frac{\partial \tilde{u}_{i,m}^{(0)}}{\partial t} - \text{im} \tilde{u}_{i,m}^{(0)} + \frac{\alpha_n}{2} \sum_{m_1=-\infty}^{\infty} \frac{\partial (\tilde{u}_{j,m_1}^{(0)} \tilde{u}_{i,m-m_1}^{(0)})}{\partial x_j} = -\frac{\partial \tilde{\eta}_m^{(0)}}{\partial X_i} - \frac{\partial \tilde{\eta}_m^{(1)}}{\partial x_i} + \sigma \frac{\partial^2 \tilde{u}_{i,m}^{(0)}}{\partial x_j \partial x_j} \quad (5.25)$$

where the conservation form is used. Note that the unknown $\tilde{u}_{i,m}^{(0)}$ is independent of time. The pseudo-time derivative term is actually used for the iteration procedures. Once the convergent solutions are obtained, the pseudo-time derivative term should be negligible.

A finite difference approach with staggered grid discretization, as sketched in Fig.5.1, is applied in the numerical computations. Using staggered grid arrangement, the unknown $\tilde{\eta}_m^{(1)}$ are all located at the inner grid points, which can avoid unspecified boundary conditions. Only the grid points of velocity components are along the boundary of the cylinder, where the no-slip boundary conditions are then applied. Choosing a forward difference in time and central differences for spatial derivatives, the momentum equation in (5.25) can be

expressed as

$$\begin{aligned} \frac{(\tilde{u}_{i,m}^{(0)})^{n_t+1} - (\tilde{u}_{i,m}^{(0)})^{n_t}}{\Delta t} = \text{im}(\tilde{u}_{i,m}^{(0)})^{n_t} - \frac{\alpha_n}{2} \sum_{m_1=-\infty}^{\infty} \left(\frac{\partial \tilde{u}_{j,m_1}^{(0)} \tilde{u}_{i,m-m_1}^{(0)}}{\partial x_j} \right)^{n_t} \\ - \frac{\partial \tilde{\eta}_m^{(0)}}{\partial X_i} - \left(\frac{\partial \tilde{\eta}_m^{(1)}}{\partial x_i} \right)^{n_t} + \sigma \left(\frac{\partial^2 \tilde{u}_{i,m}^{(0)}}{\partial x_j \partial x_j} \right)^{n_t} \end{aligned} \quad (5.26)$$

in which $n_t + 1$ and n_t respectively denote the $(n_t + 1)$ _{th} and (n_t) _{th} iterations. The convergence criterion requires the spatial average of relative errors between two successive iterations (on both pressure and velocity) to be less than 0.1 % for each m :

$$\left| \frac{(\tilde{u}_{i,m}^{(0)})^{n_t+1} - (\tilde{u}_{i,m}^{(0)})^{n_t}}{(\tilde{u}_{i,m}^{(0)})^{n_t}} \right| \leq 0.1 \% \quad , \quad \left| \frac{(\tilde{\eta}_{i,m}^{(1)})^{n_t+1} - (\tilde{\eta}_{i,m}^{(1)})^{n_t}}{(\tilde{\eta}_{i,m}^{(1)})^{n_t}} \right| \leq 0.1 \% \quad (5.27)$$

An example of convergence histories can be found in Fig.5.10. The satisfaction of continuity equation also needs to be assured. When the solutions are converged, the pseudo-time derivative term in (5.26) can be neglected, i.e. $(\tilde{u}_{i,m}^{(0)})^{n_t+1} \approx (\tilde{u}_{i,m}^{(0)})^{n_t}$. The convergent results shall satisfy the cell problem equations in (5.22) and (5.23). To initiate the iteration process, a proper guess of pressure and velocity fields is needed. Here we use the linear problem solutions (i.e. $\alpha_n = 0$) as the initial guess to start the iteration in numerical computations.

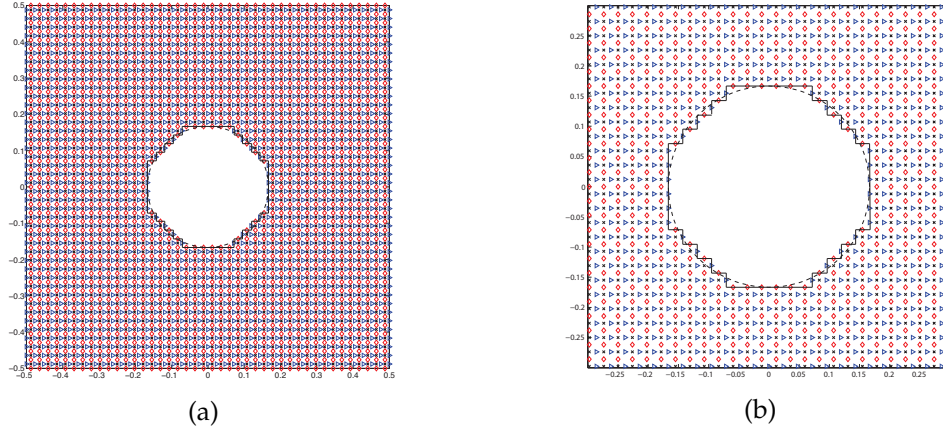


Figure 5.1: A sketch of staggered grid discretization: crosses – $\eta_m^{(1)}$, triangles – $u_{1,m}^{(0)}$ and diamonds – $u_{2,m}^{(0)}$. The dashed line indicates the boundary of cylinder while the solid line shows the real boundary in finite difference computations. (a) – a unit cell; (b) – partial enlarged view. Note: the number of grids in this figure only serves the purpose of illustration.

As mentioned above, the modified pressure correction method is an iterative approach. Within the iteration process, the velocity field is obtained from the guessed pressure (or from the previous iteration) and does not necessarily satisfy the continuity equation. Accordingly, the correction on pressure aims to make the velocity field in better agreement with the continuity equation through the iteration process. The pseudo-time derivative term is also expected to be decreasing until negligible. To construct the formula for pressure correction, we first substitute the pressure and velocity fields at step n_t into the momentum equation in (5.26). The uncorrected velocity at next "pseudo-time" step (i.e. $n_t + 1$) can then be obtained explicitly:

$$\begin{aligned}
 (\tilde{u}_{i,m}^{(0)**})^{n_t+1} = & (\tilde{u}_{i,m}^{(0)})^{n_t} + \text{im}\Delta t (\tilde{u}_{i,m}^{(0)})^{n_t} - \frac{\alpha_n}{2}\Delta t \sum_{m_1=-\infty}^{\infty} \left(\frac{\partial \tilde{u}_{j,m_1}^{(0)} \tilde{u}_{i,m-m_1}^{(0)}}{\partial x_j} \right)^{n_t} \\
 & - \Delta t \frac{\partial \tilde{\eta}_m^{(0)}}{\partial X_i} - \Delta t \left(\frac{\partial \tilde{\eta}_m^{(1)**}}{\partial x_i} \right)^{n_t} + \sigma \Delta t \left(\frac{\partial^2 \tilde{u}_{i,m}^{(0)}}{\partial x_j \partial x_j} \right)^{n_t} \quad (5.28)
 \end{aligned}$$

in which the double asterisks (**) are used to denote the uncorrected terms. It is

reminded that the uncorrected velocity $\tilde{u}_{i,m}^{(0)**}$ is computed based on the guessed (or the previous-iterated) pressure field $\tilde{\eta}_m^{(1)**}$ such that the continuity equation is not necessarily satisfied. Therefore, the corrections need to be constructed:

$$\tilde{\eta}_m^{(1)} = \tilde{\eta}_m^{(1)**} + \tilde{\eta}_m^{(1)c}, \quad \tilde{u}_{i,m}^{(0)} = \tilde{u}_{i,m}^{(0)**} + \tilde{u}_{i,m}^{(0)c} \quad (5.29)$$

where the superscript c is used to represent the corrections on pressure and velocity fields. To derive a formula for computing these corrections, we subtract (5.28) from (5.26) and obtain

$$\left(\tilde{u}_{i,m}^{(0)}\right)^{n_t+1} - \left(\tilde{u}_{i,m}^{(0)**}\right)^{n_t+1} = \tilde{u}_{i,m}^{(0)c} = -\Delta t \left(\frac{\partial \tilde{\eta}_m^{(1)c}}{\partial x_i} \right) \quad (5.30)$$

Through the iteration process, it is required that the velocity after each correction shall satisfy the continuity equation. Accordingly, substituting (5.30) into (5.22), the formula for pressure correction can be obtained:

$$\frac{\partial^2 \tilde{\eta}_m^{(1)c}}{\partial x_1 \partial x_1} + \frac{\partial^2 \tilde{\eta}_m^{(1)c}}{\partial x_2 \partial x_2} = \frac{1}{\Delta t} \left(\frac{\partial \tilde{u}_{1,m}^{(0)**}}{\partial x_1} + \frac{\partial \tilde{u}_{2,m}^{(0)**}}{\partial x_2} \right)^{n_t+1} \quad (5.31)$$

in which the RHS are known from (5.28). Note that we impose the following condition to ensure unique solutions:

$$\langle \tilde{\eta}_m^{(1)c} \rangle = 0 \quad (5.32)$$

where the angle brackets denote the cell-averaged operator defined in (3.39). The cell-periodicity condition is also applied. Using staggered-type grid discretization (e.g. Fig.5.1), the unknown $\tilde{\eta}_m^{(1)c}$ are located at all the inner points and can be readily obtained by solving the Poisson equation in (5.31). The velocity corrections $\tilde{u}_{i,m}^{(0)c}$ can then be obtained by (5.30). When the pressure and velocity are corrected by (5.29), the new values are designated to the RHS of (5.28) and the process will be repeated until the convergent solutions are achieved

and the continuity equation is satisfied. The iterations procedures can be found in Fig.5.2. Note that a factor of under-relaxation (Anderson 1995) on pressure correction is applied to avoid divergent results:

$$\left(\tilde{\eta}_m^{(1)}\right)^{n_t+1} = \left(\tilde{\eta}_m^{(1)**}\right)^{n_t} + \kappa_{\tilde{\eta}} \left(\tilde{\eta}_m^{(1)c}\right) \quad (5.33)$$

where $\kappa_{\tilde{\eta}}$ denotes the under-relaxation factor. A value of 0.8 is used in the numerical computations.

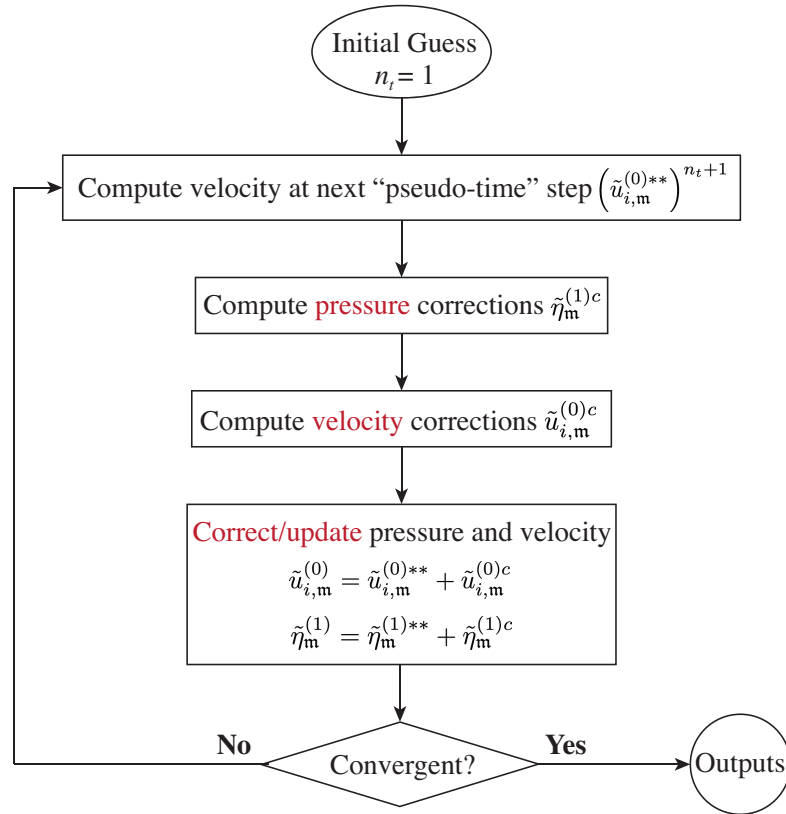


Figure 5.2: Iteration steps for solving cell problem by the modified pressure correction method

In addition to the present approach, it should be noted that several other numerical methods could be alternatives to solve the nonlinear cell problem and should deserve future explorations. One example is the projection method

(Chorin 1968), which has been widely used for solving nonlinear Navier-Stokes equations. Separating the momentum equations into two parts, the projection method is basically a fractional-step approach. An intermediate velocity is first obtained by excluding the pressure gradient term, i.e. $\partial \tilde{\eta}_m^{(1)} / \partial x_i$ in (5.25). The second step is to solve the updated velocity by including the pressure gradient, in which the divergence-free condition is required. This is similar to the present approach. To avoid the unknown boundary conditions of $\tilde{\eta}_m^{(1)}$, a staggered discretization could be used. The pseudo-time derivative term in (5.25) will also be needed to conduct the iteration. More discussions could be included in future works.

5.2.2 Macro-scale (wavelength scale) problem

With the cell problem solutions, now we turn to the macro-scale problem for wave dynamics. Taking cell average, as shown in (3.39), over the mass conservation of $O(\varepsilon)$ in (5.16):

$$n \frac{\partial \eta^{(0)}}{\partial t} + \frac{\partial \langle u_i^{(0)} \rangle}{\partial X_i} = 0 \quad (5.34)$$

in which (5.14) and (5.15) have been applied. The Gauss's theorem and cell-periodicity are also used. The above n denotes the cell porosity and has been defined in (3.42). Substituting (5.18) and (5.19) into (5.34) yields

$$n \left(\sum_{m=-\infty}^{\infty} -im \tilde{\eta}_m^{(0)} e^{-imt} \right) + \sum_{m=-\infty}^{\infty} \frac{\partial \langle \tilde{u}_{i,m}^{(0)} \rangle}{\partial X_i} e^{-imt} = 0 \quad (5.35)$$

For each mode m , we have

$$n \left(-im \tilde{\eta}_m^{(0)} \right) + \frac{\partial \langle \tilde{u}_{i,m}^{(0)} \rangle}{\partial X_i} = 0 \quad (5.36)$$

Likewise, taking cell average over momentum equation of $O(\varepsilon)$ in (5.17) gives

$$\begin{aligned} \frac{\partial \langle u_i^{(0)} \rangle}{\partial t} + \frac{1}{\Omega} \iint_{\Omega_f} \left(\alpha_n u_j^{(0)} \frac{\partial u_i^{(0)}}{\partial x_j} \right) d\Omega \\ = -n \frac{\partial \eta^{(0)}}{\partial X_i} - \frac{1}{\Omega} \iint_{\Omega_f} \left(\frac{\partial \eta^{(1)}}{\partial x_i} \right) d\Omega + \frac{1}{\Omega} \iint_{\Omega_f} \left(\sigma \frac{\partial^2 u_i^{(0)}}{\partial x_j \partial x_j} \right) d\Omega \end{aligned} \quad (5.37)$$

in which Ω is the total cross-sectional area projected on the horizontal plane and Ω_f represents the area occupied by fluid inside Ω . Substituting the solution forms in (5.18) and (5.19) into the above equation, then for each mode m we have

$$\begin{aligned} -im \langle \tilde{u}_{i,m}^{(0)} \rangle + \frac{\alpha_n}{2\Omega} \iint_{\Omega_f} \left[\sum_{m_1=-\infty}^{\infty} \left(\tilde{u}_{j,m_1}^{(0)} \frac{\partial \tilde{u}_{i,m-m_1}^{(0)}}{\partial x_j} \right) \right] d\Omega \\ = -n \frac{\partial \tilde{\eta}_m^{(0)}}{\partial X_i} - \frac{1}{\Omega} \left(\iint_{\Omega_f} \frac{\partial \tilde{\eta}_m^{(1)}}{\partial x_i} d\Omega \right) + \frac{\sigma}{\Omega} \left(\iint_{\Omega_f} \frac{\partial^2 \tilde{u}_{i,m}^{(0)}}{\partial x_j \partial x_j} d\Omega \right) \end{aligned} \quad (5.38)$$

in which the Gauss's theorem and cell-periodicity are applied. Combining (5.36) with (5.38), the governing equation for the leading-order free surface elevation $\tilde{\eta}_m^{(0)}$ of each mode inside the forest is derived as:

$$\frac{\partial^2 \tilde{\eta}_m^{(0)}}{\partial X_i^2} + (m^2) \tilde{\eta}_m^{(0)} = - \left(\frac{\alpha_n}{n} \right) \frac{\partial \tilde{M}_m}{\partial X_i} - \left(\frac{1}{n} \right) \frac{\partial \tilde{N}_m}{\partial X_i} + \left(\frac{\sigma}{n} \right) \frac{\partial \tilde{Q}_m}{\partial X_i} \quad (5.39)$$

where \tilde{M}_m , \tilde{N}_m and \tilde{Q}_m on the RHS are all from the cell (micro-scale) problem solutions:

$$\tilde{M}_m = \frac{1}{2\Omega} \iint_{\Omega_f} \left[\sum_{m_1=-\infty}^{\infty} \left(\tilde{u}_{j,m_1}^{(0)} \frac{\partial \tilde{u}_{i,m-m_1}^{(0)}}{\partial x_j} \right) \right] d\Omega \quad (5.40)$$

and

$$\tilde{N}_m = \frac{1}{\Omega} \iint_{\Omega_f} \frac{\partial \tilde{\eta}_m^{(1)}}{\partial x_i} d\Omega, \quad \tilde{Q}_m = \frac{1}{\Omega} \iint_{\Omega_f} \frac{\partial^2 \tilde{u}_{i,m}^{(0)}}{\partial x_j \partial x_j} d\Omega \quad (5.41)$$

For open water, on the other hand, the incident wavelength $1/k_{\text{inc}}$ instead of tree spacing is used to scale the horizontal coordinates. The corresponding leading-order governing equations are derived as

$$\frac{\partial \eta^{(0)}}{\partial t} + \frac{\partial \langle u_i^{(0)} \rangle}{\partial X_i} = 0 \quad (5.42)$$

and

$$\frac{\partial \langle u_i^{(0)} \rangle}{\partial t} = -\frac{\partial \eta^{(0)}}{\partial X_i} \quad (5.43)$$

Substituting (5.18) and (5.19) into (5.42) and (5.43), for each mode we have

$$-im\tilde{\eta}_m^{(0)} + \frac{\partial \langle \tilde{u}_{i,m}^{(0)} \rangle}{\partial X_i} = 0 \quad (5.44)$$

and

$$-im\langle \tilde{u}_{i,m}^{(0)} \rangle = -\frac{\partial \tilde{\eta}_m^{(0)}}{\partial X_i} \quad (5.45)$$

Combining (5.44) with (5.45), the equation governing the leading-order free surface elevation outside the forest is obtained:

$$\frac{\partial^2 \tilde{\eta}_m^{(0)}}{\partial X_i^2} + (m^2) \tilde{\eta}_m^{(0)} = 0 \quad (5.46)$$

5.3 Shallow-water waves through a forest belt

Here we consider shallow-water waves propagating through a homogeneous forest belt (as used in Sec.3.6.1) with an infinite length (i.e. $-\infty < Y < \infty$) but a finite width (i.e. $0 \leq X \leq L_F$). Assuming normal incident waves of simple harmonic, higher harmonics will be developed inside the forest region by non-linearity and be radiated into open water as reflected and transmitted waves. Accordingly, the solutions within incidence and transmission regions can be readily obtained by solving (5.46):

- Incidence region:

$$\tilde{\eta}_{1,m}^{(0)} = e^{imX} + R_m e^{-imX}, \quad \tilde{u}_{1,m}^{(0)} = e^{imX} - R_m e^{-imX} \quad \text{when } X < 0 \quad (5.47)$$

- Transmission region:

$$\tilde{\eta}_{T,m}^{(0)} = T_m e^{imX}, \quad \tilde{u}_{T,m}^{(0)} = T_m e^{imX} \quad \text{when } X > L_F \quad (5.48)$$

Inside the forest region, the numerical solutions to (5.39) can be found by a second-order finite difference approach and shall match the open-water solutions along the edges of the forest felt. Requiring the continuity of free surface and horizontal velocity at discrete points on the interfaces, i.e.

$$\eta_{I,m}^{(0)} = \eta_{F,m}^{(0)}, \quad \tilde{u}_{I,m}^{(0)} = \tilde{u}_{F,m}^{(0)} \quad \text{at } X = 0 \quad (5.49)$$

and

$$\eta_{F,m}^{(0)} = \eta_{T,m}^{(0)}, \quad \tilde{u}_{F,m}^{(0)} = \tilde{u}_{T,m}^{(0)} \quad \text{at } X = L_F \quad (5.50)$$

, a matrix equation for the unknowns inside and the coefficients R_m, T_m outside can be formulated and be solved numerically. Note that we assume the mean water level does not change in the incidence region such that the reflection coefficient of zero-th mode is set as $R_0 = 0$.

As indicated above, the gradient of leading-order free surface elevation, i.e. $\partial \tilde{\eta}_m^{(0)} / \partial X$, is serving as the driving force for cell problem. On the other hand, when solving the macro-scale problem, those cell-averaged terms \tilde{M}_m, \tilde{N}_m and \tilde{Q}_m need to be computed based on the micro-scale solutions. Accordingly, an iterative scheme must be introduced for this coupled system, solving both the micro- and macro-scale problems. Starting with linear problem solutions in Chap.3 to initiate the iteration process, the macro-scale pressure gradient is given as an input for cell problem in (5.22) & (5.23). Once the micro-scale solution is found, the cell-averaged \tilde{M}_m, \tilde{N}_m and \tilde{Q}_m can be obtained. The macro-scale free surface elevation $\tilde{\eta}_m^{(0)}$ and the coefficients R_m, T_m for each mode m can

be solved numerically. Afterwards, we go back to the cell problem with the updated pressure gradient (i.e. gradient of leading-order free surface elevation $\partial\tilde{\eta}_m^{(0)}/\partial X$). Solving the micro- and macro-scale problem in order, the iterative process is to be repeated until the convergent results are achieved, which requires the spatial-averaged relative differences between the wave solutions obtained from two successive iteration steps to be less than 1.0 %:

$$\frac{1}{N_{X_p}} \sum_{iX_p}^{N_{X_p}} \left| \frac{\tilde{\eta}_{m_}(k+1)^{(0)} - \tilde{\eta}_{m_}(k)^{(0)}}{\tilde{\eta}_{m_}(k)^{(0)}} \right| \leq 1.0 \% \quad (5.51)$$

where k and $k + 1$ respectively denote the $(k)_{\text{th}}$ and $(k + 1)_{\text{th}}$ iteration. N_{X_p} gives the total number of discrete grid points inside the forest. Note that the infinite number of harmonics (i.e. m) needs to be truncated to a certain number in the numerical computations. Fig.5.3 shows the iteration steps for solving the coupled micro- and macro-scale problem. An example of convergence histories for macro-scale iterations is given in Fig.5.13.

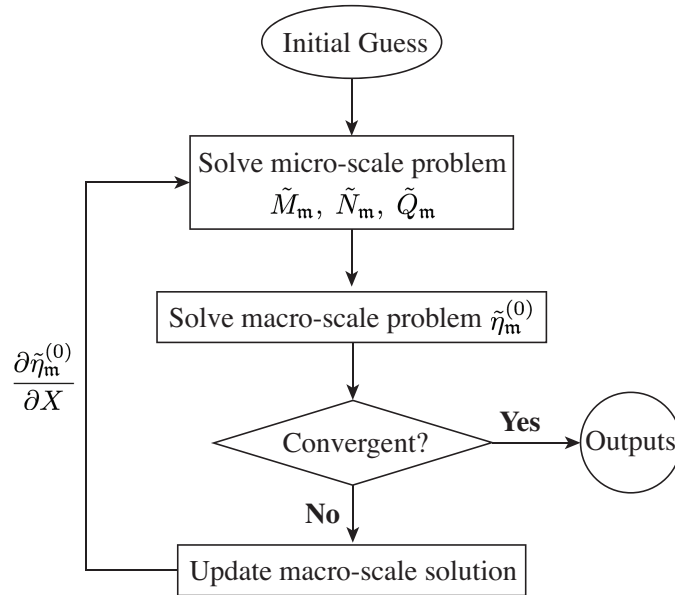


Figure 5.3: Iteration steps for solving the coupled micro- and macro-scale problem.

In the following, we use the experimental conditions reported in [Mei et al. \(2011\)](#) to study the nonlinearity effects. As shown in [Table 5.1](#), a range of wave periods is included in their experiments, in which Case 7 & 8 have shallow-water-wave conditions ($h_0/L < 0.05$) while the rest have relatively shorter waves. We first exclude the nonlinearity by setting $\alpha_n = 0$ and compare the numerical results with the linear problem solutions in [Mei et al. \(2011\)](#). The differences on both micro- and macro-scale results due to different numerical algorithms for solving the cell problem are presented and discussed. Afterwards, using the present model with α_n in [Table 5.1](#), the effects of nonlinearity on the wave solutions are studied. The behaviors of different harmonics are also discussed. The comparisons of reflection/transmission coefficients with experimental data are then presented. The impacts of different parameters on the wave amplitude evolutions are shown as well.

Table 5.1: Experimental conditions and dimensionless parameters in [Mei et al. \(2011\)](#)

Case	h_0 (cm)	T (s)	A_{inc} (cm)	L (m)	$k_{\text{inc}}h_0$	$k_{\text{inc}}A_{\text{inc}}$	A_{inc}/h_0	α_n	σ
1	12	1.2	1.36	1.236	0.61	0.070	0.1133	0.7432	0.0096
2		1.4	1.23	1.450	0.52	0.053	0.1025	0.7885	0.0101
3		1.6	1.20	1.676	0.45	0.045	0.1000	0.8889	0.0113
4		1.8	1.22	1.885	0.40	0.040	0.1017	1.0167	0.0129
5		1.9	1.22	2.038	0.37	0.038	0.1017	1.0991	0.0136
6		2.0	0.34	2.094	0.36	0.010	0.0283	0.3148	0.0040
7		2.5	0.33	2.692	0.28	0.008	0.0275	0.3928	0.0048
8		3.0	0.25	3.278	0.23	0.005	0.0208	0.3623	0.0044

The above h_0 , T , A_{inc} and L represent the constant water depth, the incident wave period, wave amplitude and wavelength, respectively. k_{inc} denotes the incident wavenumber. For all the cases, the width of the forest region L_F is 1.08 m and the porosity n is 91.27% ($d=1\text{cm}$, $\ell=3\text{cm}$).

5.3.1 Linear results

To check the present model, we first set $\alpha_n = 0$ for the cases in Table 5.1 and compare the numerical results with the semi-analytical solutions in Mei et al. (2011), where the cell problem is solved by using finite element approach. The normalized wave amplitude variation through the forest for two cases with relatively longer wavelength is presented in Fig.5.4. It can be observed that the present model results have slightly higher wave amplitude inside the forest. Slightly larger reflected waves are also observed while negligible differences are found in transmitted waves. Overall, the spatial-averaged relative differences between two model results are about 1 – 2 %. This is mainly because different numerical algorithms are employed for solving the cell problem in two models. The discretization used in two numerical models have been presented in Fig.3.2b and Fig.5.1, respectively. Obviously, the staggered grid system used in the present approach does not perfectly fit the boundary of the central cylinder. This shall be the main contribution to the differences observed in Fig.5.4.

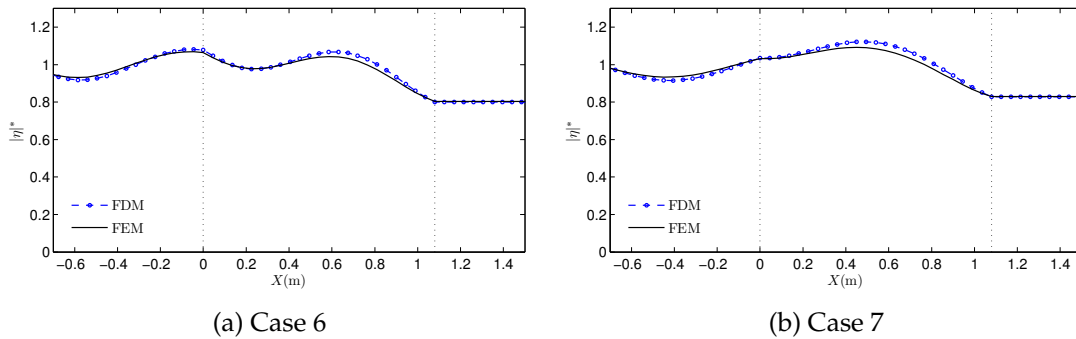


Figure 5.4: Comparison of linear model results. Solid lines is obtained by using finite element model (Mei et al. 2011) to solve the cell problem. Dashed lines with circles show the results by the present approach. The wave conditions can be found in Table 5.1.

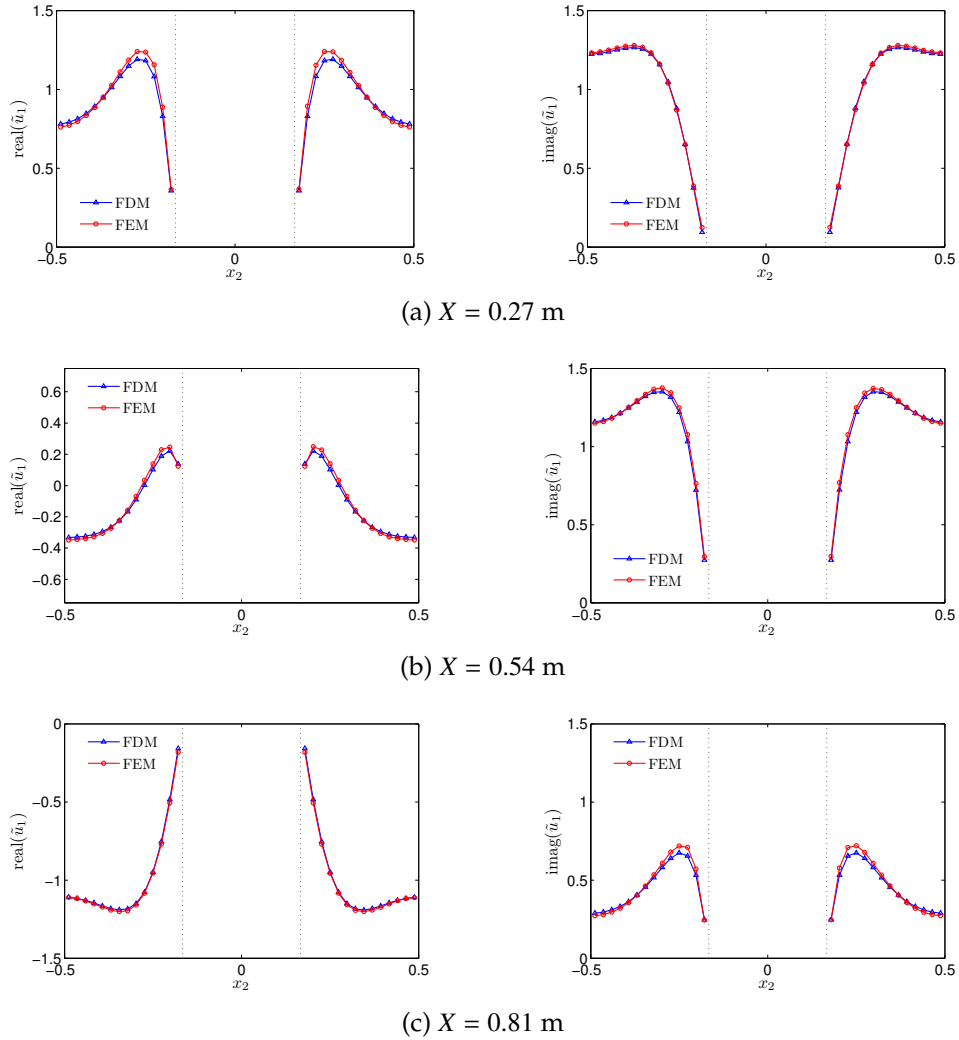


Figure 5.5: Profiles of dimensionless flow velocity $\tilde{u}_{1,m=1}^{(0)}$ along $x_1 = 0$ at three locations within the forest. The wave condition is Case 6 in Table 5.1. The vertical dotted lines show the edges of cylinder. FDM: finite different method (the present approach), FEM: finite element model used in Mei et al. (2011).

For further investigation, three different locations within the forest belt ($X = L_F/4, L_F/2$ & $3L_F/4$) are selected and the corresponding micro-scale velocity profiles $\tilde{u}_{1,m=1}^{(0)}$ along $x_1 = 0$ obtained by two numerical models are compared. As shown in Fig.5.5, the discrepancy between two model results can be observed, especially when close to the central cylinder. Besides, the cell-averaged veloci-

ties $\langle \tilde{u}_{i,m=1}^{(0)} \rangle$ within the model forest are also compared, yielding similar relative errors (i.e. 1–2 %) as presented in macro-scale wave amplitude comparisons. Linear micro-scale flow fields within unit cells have been presented in Sec.3.6 and Mei et al. (2014) and shall not be repeated here.

5.3.2 Nonlinear results

Using the values of α_n in Table 5.1, we conduct the numerical computations by the present model to investigate the nonlinear effects on micro-scale flow fields and macro-scale wave solutions. Two cases with long-wave conditions (Case 7 and 8 in Table 5.1) are first presented in Fig.5.6, showing the normalized wave amplitude through the forest belt. In the same figures, the linear solutions (i.e. $\alpha_n = 0$) are also plotted for comparison. The corresponding wave profiles for each harmonic component m are presented in Fig.5.8. As expected, higher harmonics are grown inside the forest by nonlinearity and are radiated into open water as reflected and transmitted waves. For both cases, it can be observed that the first harmonic ($m = 1$) is the dominant mode for the total solution based on the assumption of simple harmonic incidence. Due to smaller nonlinearity (A_{inc}/h_0), the amplitude of higher harmonic waves is quite small. The nonlinear effects are not obvious in the total solutions and yield only about 2 % as the spatial-averaged relative differences in comparison with linear model results. Note that the infinite number of harmonics m is truncated as $m = 5$ in the numerical computations.

To investigate higher nonlinearity, Case 4 and 5 in Table 5.1 are selected although the corresponding wavelength is relatively shorter and is not within

shallow-water wave regime. For both cases, the nonlinear effects become obvious and can be observed in the total solutions (Fig.5.7), in which higher spatial-averaged relative differences $\approx 10\%$ are found when comparing with linear model results. It can also be observed in Fig.5.9 that the first harmonic ($m = 1$) is still dominant although the order of magnitude for the second and third modes ($m = 2, 3$) becomes greater than those of Case 7 & 8: $O(10^{-2})$.

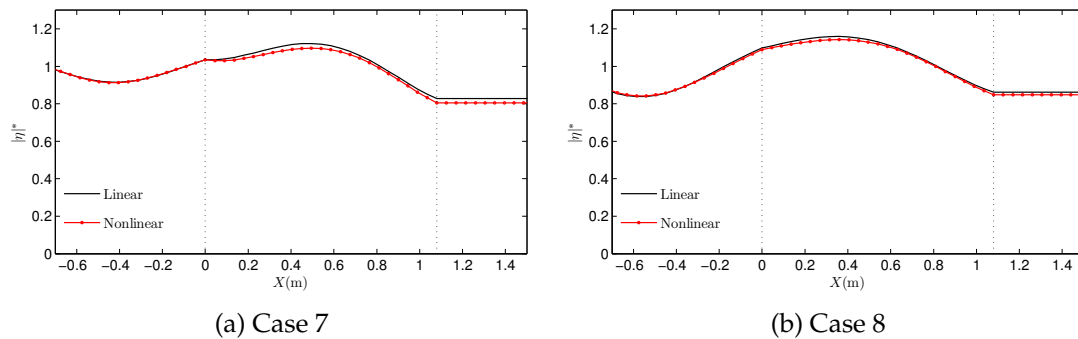


Figure 5.6: Comparison of nonlinear wave amplitude variation – Case 7 & 8. The linear model uses σ in Table 5.1.

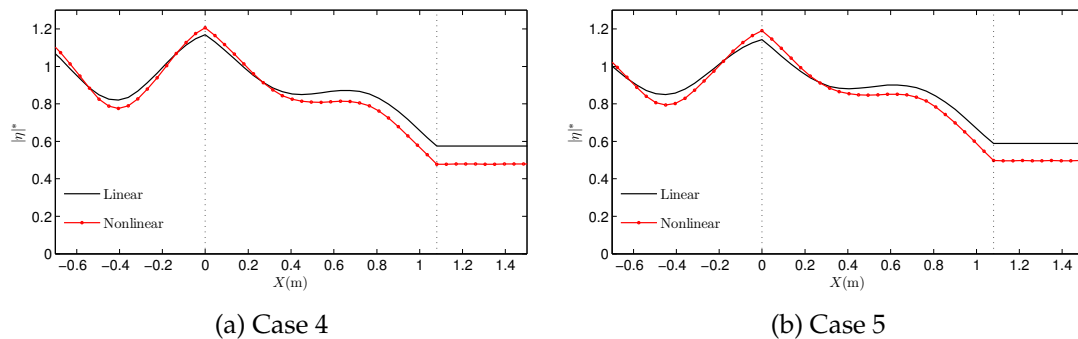
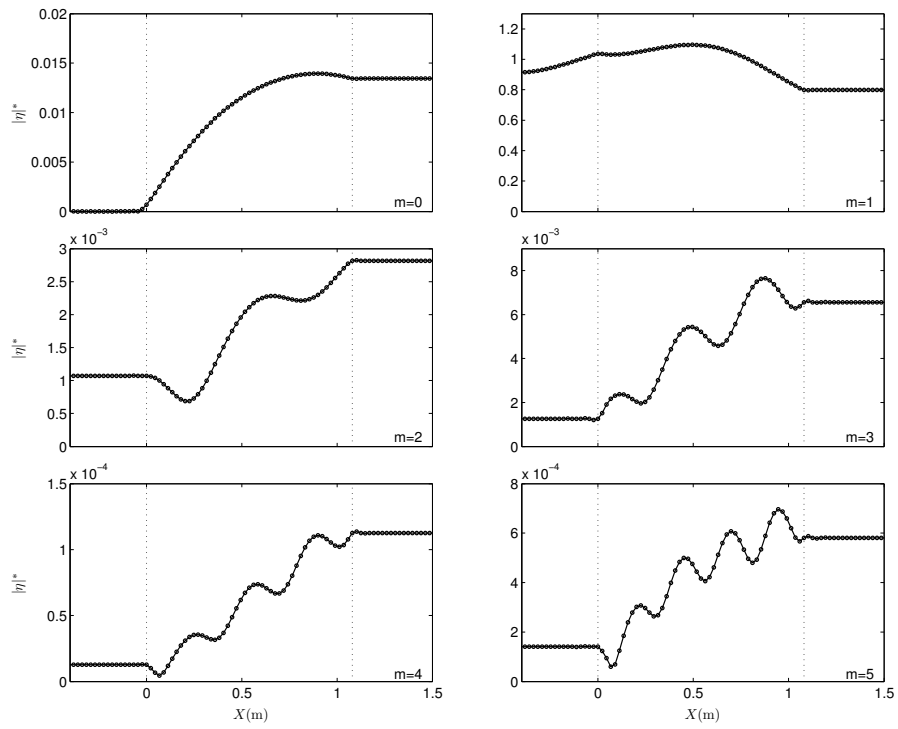
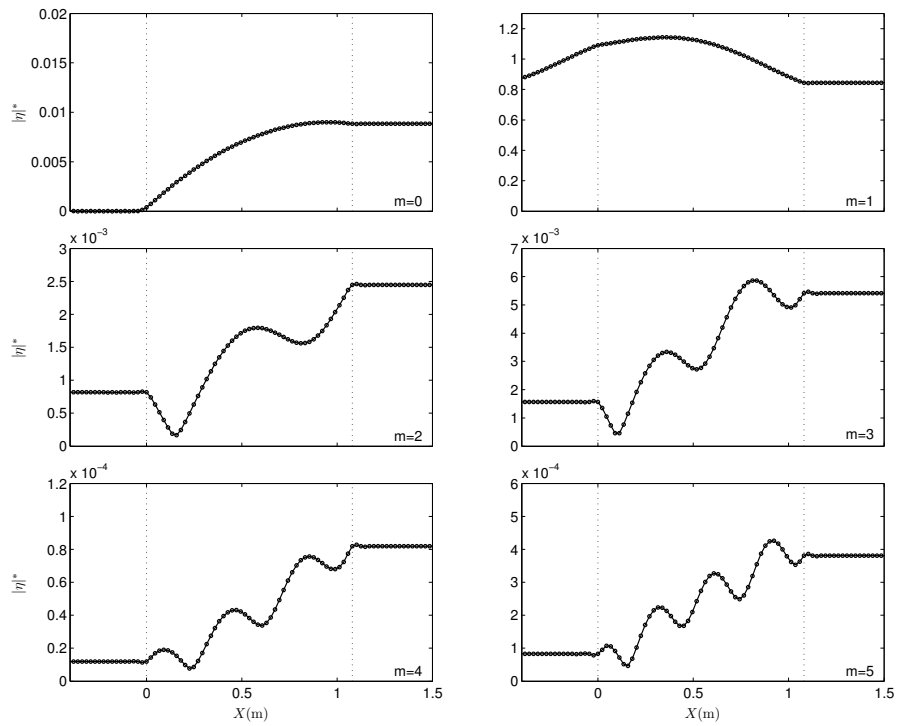


Figure 5.7: Comparison of nonlinear wave amplitude variation – Case 4 & 5. The linear model uses σ in Table 5.1.

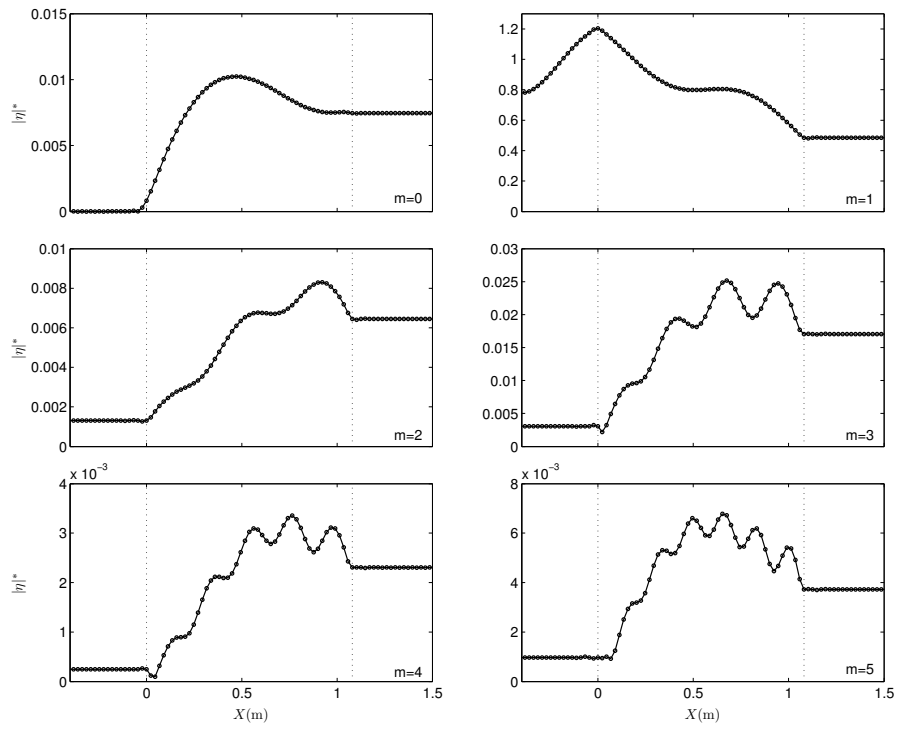


(a) Case 7

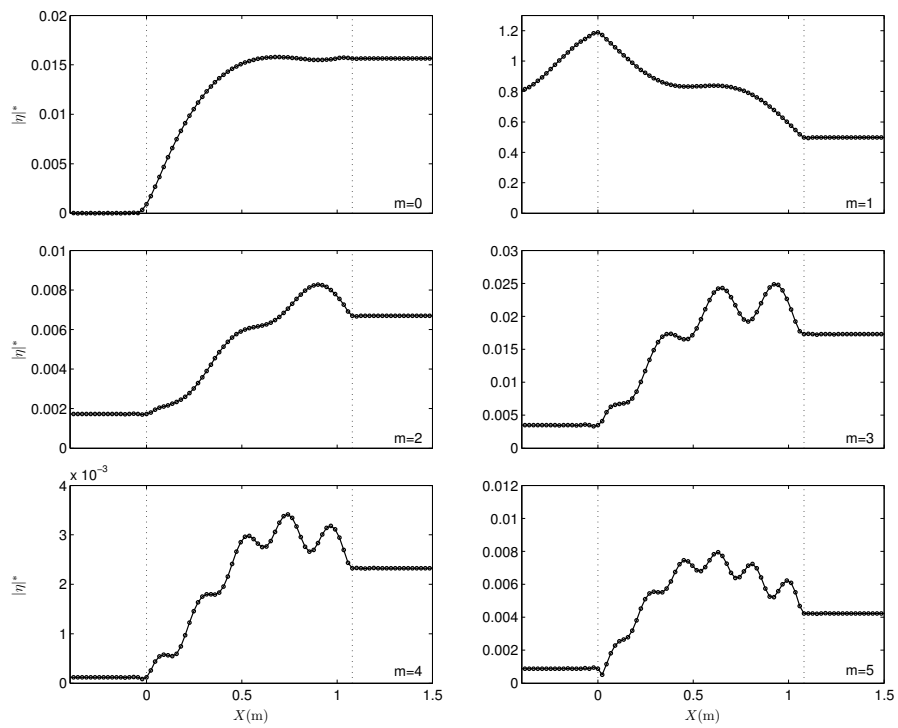


(b) Case 8

Figure 5.8: Wave amplitude variation for each mode – Case 7 & 8



(a) Case 4



(b) Case 5

Figure 5.9: Wave amplitude variation for each mode – Case 4 & 5

It is also worthy of exploring the micro-scale flow fields within cells by the present model. Using Case 5 & 7, which have two different values of nonlinearity parameter α_n , we respectively present the velocity fields of each harmonic component at the middle of forest belt ($X = L_F/2$). Fig.E.1 first shows the velocity fields of zero-th mode ($m = 0$) for both cases. The instantaneous velocity fields for higher modes can be found from Fig.E.2 to E.11 in Appendix E.1. Symmetric eddies can be observed near the central cylinder due to the boundary effects. The differences after including nonlinearity can also be found when comparing with the linear flow fields in Sec.3.6. For higher modes, more eddies with smaller sizes are formed close to the central cylinder and travel towards the cell boundaries. The different patterns for Case 5 & 7 can also be observed. It should be noted that only Reynolds-averaged velocity fields are presented.

As mentioned in Sec.5.2.1.1, the modified pressure correction method employed for solving the nonlinear cell problem is an iteration approach. In the numerical computations, it is required that the spatial-averaged relative errors for each mode m between two successive iterations are less than 0.1 % as indicated in (5.27). By setting $\alpha_n = 1.0$, Fig.5.10 shows an example of the convergence histories for micro-scale problem iteration. It can be observed that the spatial-averaged relative errors for different modes are decreasing and the convergence criteria can be achieved after around 500 – 600 iterations.

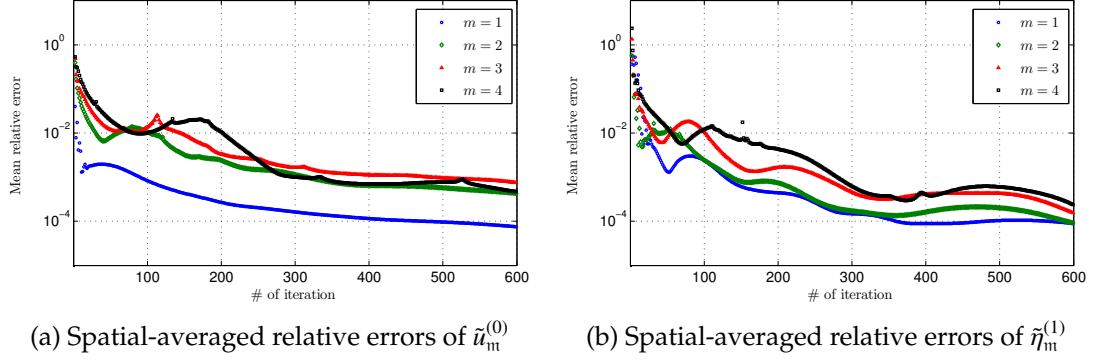


Figure 5.10: Convergence histories of micro-scale iterations on $\tilde{u}_m^{(0)}$ and $\tilde{\eta}_m^{(1)}$ for different modes when $\alpha_n = 1.0$.

Although the gauge data inside the model forest is not available such that the comparisons of wave profiles are not allowed, we here present the comparisons of the reflection/transmission coefficients and the percentage of energy dissipation with experimental data in Fig.5.11. The linear model results are plotted in the same figures. For long waves (i.e. $h_0/L < 0.05$) – Case 7 & 8, the present model yields lower dissipation by the forest region with larger reflected and transmitted waves being observed. On the other hand, for relatively short waves ($h_0/L > 0.05$), the discrepancy between model results and experimental data become noticeable where higher energy dissipation can be observed. Obviously, using the present shallow-water wave model does not consider vertical variations, which can be important for relatively shorter waves. In addition, the estimation of eddy viscosity by the empirical formula may not be appropriate and could be the main contribution to the disagreement. In Chap.3, it has been shown the energy model with a new drag coefficient formula can be used to determine the eddy viscosity for shorter waves, in which reasonable agreements have been found in data-model comparisons. As we know, the value of eddy viscosity directly affects the energy dissipation and the resulting wave

profiles within the forest. Thus, it is suggested that the present model should be expanded by including short wave conditions in future works. A proper estimation of eddy viscosity as shown in Sec.3.4 should also be made. Available experimental data for relatively short waves can then be used for model validation.

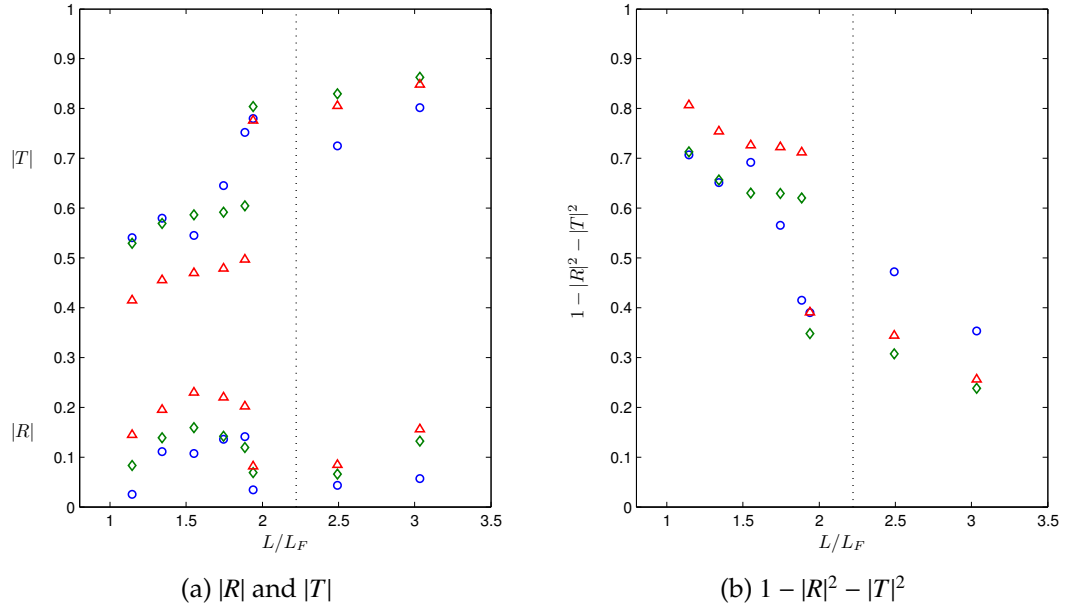


Figure 5.11: Comparisons of reflection $|R|$ and transmission coefficients $|T|$. $1 - |R|^2 - |T|^2$ shows the percentage of energy dissipation by the forest. Circles – data; diamonds – linear results by present model; triangles – nonlinear results by present model. The vertical dotted lines show the shallow-water wave condition, i.e. $h_0/L \leq 0.05$.

As indicated in (5.11), higher values of nonlinearity parameter α_n lead to greater values of eddy viscosity σ , which would increase the dissipation within the forest region. This has been presented in the above results. However, we know the values of α_n are determined by both the wave nonlinearity A_{inc}/h_0 and the small parameter $\varepsilon = k_{\text{inc}}\ell$. Therefore, to explore the effects of these two parameters on wave solutions, more analyses are carried out here. Selecting six values of α_n with different combinations of A_{inc}/h_0 and $k_{\text{inc}}\ell$, we compare the

corresponding reflection and transmission coefficients. As shown in Fig.5.12a and 5.12b, with the same value of α_n (i.e. the same σ), larger wave nonlinearity A_{inc}/h_0 brings about higher energy dissipation. On the other hand, longer waves show less dissipation by the forest region in Fig.5.12c and 5.12d. As expected, the forest region is a more efficient damper for shorter waves, which has also been presented by the linear model (Chap.3). Besides, larger waves have higher normalized energy dissipation in comparison with smaller waves. Some of the corresponding wave profiles can be found from Fig.E.12 to E.15 in Appendix E.2. It can also be observed that for all the tested cases, the first mode ($m = 1$) is always dominant and higher modes ($m > 1$) are less important.

An example of convergence histories for macro-scale iterations (Fig.5.3) with different values of α_n is given in Fig.5.13. It can be observed that more iteration steps are needed for higher values of α_n . For all the cases tested in this chapter, the convergence criteria in (5.51) can be achieved within 30 iterations.

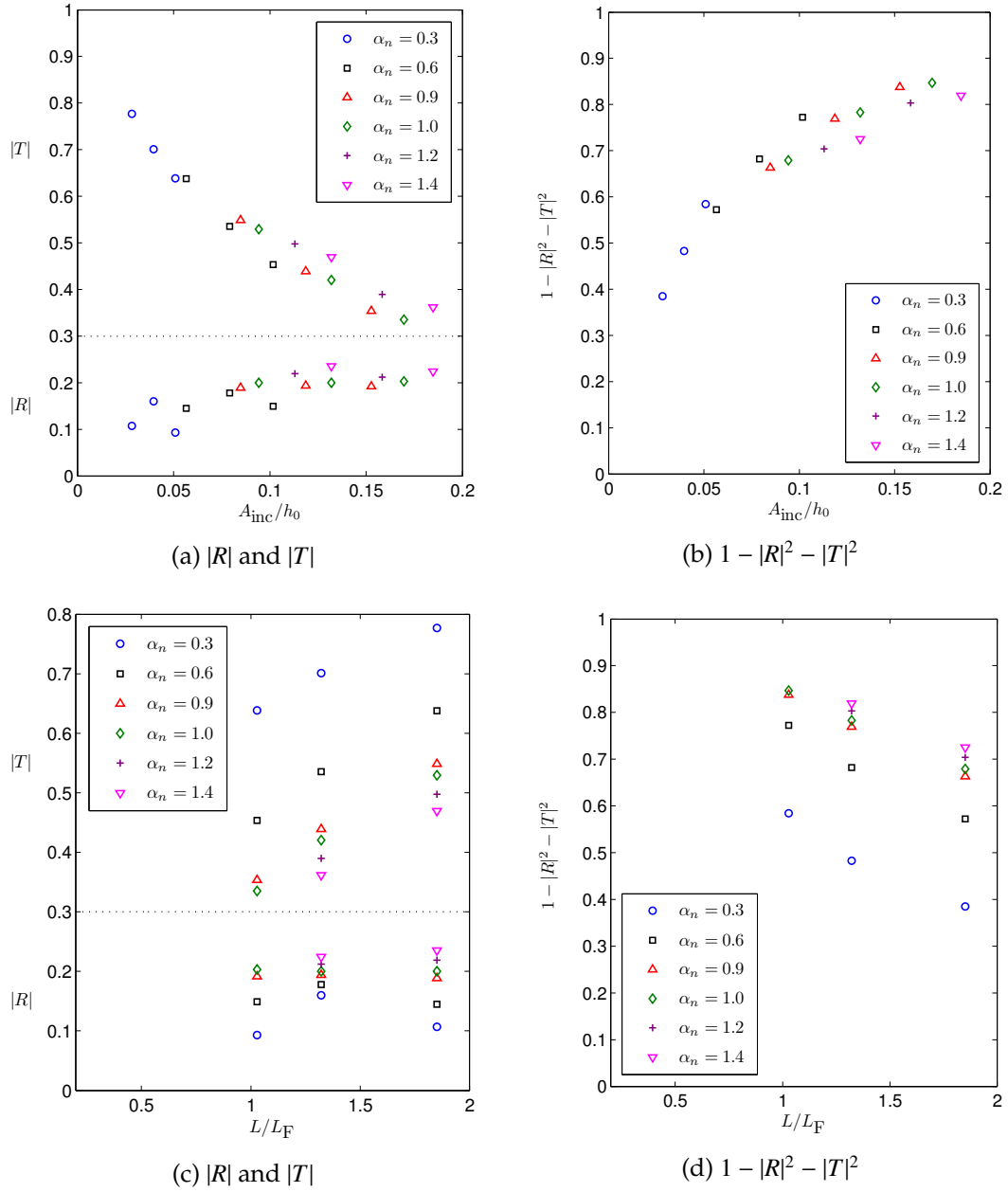


Figure 5.12: Comparisons of reflection $|R|$ and transmission coefficients $|T|$. $1 - |R|^2 - |T|^2$ shows the percentage of energy dissipation by the forest. Six values of α_n are selected with different combinations of A_{inc}/h_0 and $k_{\text{inc}}\ell$. Horizontal dotted line is used to separate reflection and transmission coefficients.

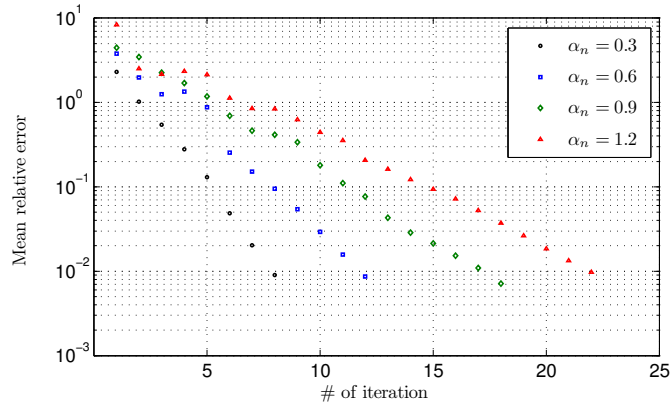


Figure 5.13: Convergence histories of macro-scale iterations for different values of α_n with $k\ell = 0.094$.

5.4 Concluding remarks and discussions

In this chapter, the nonlinear effects and the resulting harmonics generation within a coastal forest are investigated. Assuming incident waves as simple harmonic with weakly nonlinearity, higher harmonic waves are expected to be developed inside the forest and be radiated to the outside region. Without ignoring the convection terms in the momentum equations, the multi-scale perturbation technique is applied and the governing equations for each harmonic component are derived. The leading-order cell (micro-scale) problem becomes a nonlinear boundary-value-problem and can be solved by employing a modified pressure correction method. A staggered grid discretization with finite difference approach is used in the numerical computations. With micro-scale solutions, the linear wavelength-scale (macro-scale) problem for each harmonic can then be solved numerically. An iterative scheme is proposed for solving this coupled system.

Considering shallow-water waves propagating through an infinitely long forest belt of finite width, the linear model results in [Mei et al. \(2011\)](#) are first used to check the present numerical approach by neglecting the nonlinearity, i.e. $\alpha_n = 0$. The comparisons are made for both micro- and macro-scale results. Overall, the spatial-averaged relative differences of 1 – 2 % are observed in the comparisons of two macro-scale results. The velocity profiles within unit cells and the corresponding cell-averaged velocities are compared, in which the same range of relative errors is also found. The differences between these two approaches could mainly be caused by the different numerical algorithms and the corresponding discretization for solving the micro-scale problem. It should be noted that the staggered grid system used in the present finite difference approach does not perfectly fit the boundary of the cylinder within a cell (e.g. [Fig.5.1](#)). Therefore, a boundary-fitting discretization will be suggested in future works.

Using the experimental conditions in [Mei et al. \(2011\)](#), which have both long waves and relatively short waves, the nonlinear and linear model results are compared. Higher harmonic components for different wave conditions are also presented. It can be observed that higher harmonic waves are generated within the forest belt as expected. Due to the assumption of simple-harmonic incidences, the first harmonic component is dominant while higher modes are relatively smaller. Assuming that the mean water level does not change in the far field of the incidence region (i.e. the normalized mean depth is unity), a wave setup can be observed within the forest such that an increase of the mean water level appears in the transmission region. For all the cases, higher reflection coefficients but lower transmission coefficients are observed when taking nonlinear

terms into account.

The numerical results are also compared with the experimental data reported in [Mei et al. \(2011\)](#). Without gauge data within the model forest, the data-model comparisons are only allowed in the incidence and transmission regions. For long waves (i.e. $h_0/L < 0.05$), larger reflected and transmitted waves are observed in the model results when comparing with the measurements. For relatively short waves ($h_0/L > 0.05$), the obvious discrepancy between model results and data are observed and can be attributed to the use of present shallow-water wave model, which does not take vertical variation into account for short waves. The way to determine the value of eddy viscosity also deserves a further investigation. As presented in [Chap.3](#), the eddy viscosity is determined by an energy model with a drag coefficient formula for short waves. On the other hand, in [Chap.4](#) and this chapter, an empirical formula is used to estimate the eddy viscosity. As we know, the numerical results are directly affected by the values of eddy viscosity. Therefore, the possible misinterpretation of eddy viscosity for short waves by using the empirical formula for long waves may also directly lead to the discrepancy. In future works, the present model needs to be expanded such that the vertical variation can be included. A proper estimation of eddy viscosity as shown in [Sec.3.4](#) shall then be used for relatively short waves. Also, several existing sets of experimental data for short waves can then be used to further check the developed model.

To explore the effects of nonlinearity, different wave parameters are tested. It has been shown that higher values of α_n (larger σ) result in more wave dissipation. As shown in [\(5.11\)](#), it should be noted that the dimensionless eddy viscosity in the present model is directly proportional to the values of α_n , which

are determined by the incident wave nonlinearity A_{inc}/h_0 and the small parameter $k_{\text{inc}}\ell$. Therefore, several values of α_n with different combinations of A_{inc}/h_0 and $k_{\text{inc}}\ell$ are selected to compare the model results. It is observed that with the same value of α_n and σ , larger wave nonlinearity A_{inc}/h_0 leads to higher energy dissipation. In addition, the forest area is shown to damp less energy for longer waves. Similar results have also been presented by the linear model, which indicates that a coastal forest is a more efficient damper for shorter waves. Also, larger waves have higher normalized energy dissipation when compared with smaller waves. Again, the first harmonic waves remain dominant for all the cases.

CHAPTER 6

SUMMARY AND SUGGESTED FUTURE WORKS

In this dissertation, the theoretical model developed in [Mei et al. \(2011, 2014\)](#) is extended to study wave propagating through a heterogeneous coastal forest, which can have multiple vegetation patches of arbitrary shape. Each patch can be composed of several subzones due to different properties, e.g. vegetation species/sizes, planting patterns. A forest subzone, which could be surrounded by other subzones and/or open water, is then considered as a homogeneous region, where a constant bulk value of eddy viscosity can be yielded. With a strong contrast between wavelength and tree spacing, the multiple-scale perturbation technique (homogenization theory) is applied such that the micro-scale flow motion within unit cells and macro-scale wave dynamics are solved separately. Driven by the macro-scale pressure gradient, the micro-scale flow fields within a unit cell, with one or more cylinders inside, is obtained by numerically solving the boundary-value cell problem. The equations governing macro-scale wave dynamics are derived based on the micro-scale solutions. The boundary integral equation method is employed to discretize the boundary of a forest patch with arbitrary shape and to solve the macro-scale problem numerically.

Small-amplitude waves are considered in the first part. Two types of waves are included – periodic short waves (Chap.3) and transient long waves (Chap.4). For periodic waves, an energy model is applied with the wave forces being determined by a new drag coefficient formula based on [Hu et al. \(2014\)](#)'s experiments. For transient long waves, only incidences of a soliton-like impulse are considered. Fourier transform is used and the bulk eddy viscosity is determined by a modified empirical formula. Two computing programs are re-

spectively established based on the numerical models and can be applied to a general coastal forest and to solve both micro- and macro-scale problems. Information of required inputs for conducting numerical computations is also provided. Three different forest configurations with existing experimental data are tested for both types of waves. An infinitely long forest belt with a finite width is first used to check the present models. The semi-analytical solutions are provided. For periodic waves, both normally and obliquely incidences are discussed. The data-model comparisons show good agreements for the cases with smaller nonlinearity ($A_{\text{inc}}/h_0 < 0.1$). The limitation of the present model on the ratio of tree spacing to wavelength is also found ($\ell/L \leq 0.05$). For transient waves, the model limitation on the nonlinearity of incident waves is confirmed. A single homogeneous circular forest is used to establish a benchmark case for a coastal forest of finite area. The semi-analytical solutions are also provided. The laboratory experiments were conducted at the University of Cantabria and good agreements are shown in the comparisons between model results and experimental data. The suggestion on the incident wave nonlinearity of transient waves for better model predictions is also presented ($H_{\text{inc}}/h_0 < 0.3$). The experiments in [Maza \(2015\)](#), consisting of multiple circular patches, are used for further model validation. Again, good agreements are found between model results and experimental measurements. It is also concluded that larger waves yield more wave dissipation. Moreover, a coastal forest is shown to be more efficient to damp out shorter waves.

In the last part of this dissertation (Chap.5), the nonlinear effects are investigated by including the convection terms in the momentum equations, which have been ignored in the linear models. Considering shallow-water incident

waves of simple harmonic, we anticipate that higher harmonic components are to be generated due to the nonlinearity. With multi-scale perturbation technique, the micro- and macro-scale equations for each harmonic are derived. The cell problem for micro-scale flow motion becomes a nonlinear boundary-value-problem while the macro-scale problem for wave dynamics is still linear. A modified pressure correction method is introduced with the use of staggered grid discretization of finite difference to solve the nonlinear cell problem. Considering a forest belt as a special case, the comparisons of numerical results obtained by linear and nonlinear models are presented. The numerical results are also compared with the experimental data reported in [Mei et al. \(2011\)](#). However, due to the inaccurate estimation of eddy viscosity for relatively shorter waves, the discrepancy between model results and data is noticeable. To explore the numerical model and the effects of nonlinearity, different parameters are tested and higher harmonic waves are also presented. As a result, higher energy dissipation appears with larger waves, i.e. greater wave nonlinearity A_{inc}/h_0 . In addition, the coastal forest is shown to be more efficient at damping shorter waves. For all the tested cases, the first harmonic waves are always dominant while higher harmonic components are relatively smaller.

In this dissertation, it has been shown that the present approach based on the multi-scale perturbation method is able to predict the propagation and dissipation of waves over a general vegetated water, which can be composed of multiple forest patches of arbitrary shape. However, there are still several improvements shall be suggested and be carried out in future works. As pointed out in [Chap.3](#) for short periodic waves, a new drag coefficient formula has been proposed based on the direct measurements of wave forces on a cylinder ar-

ray (Hu et al. 2014). However, its application is limited by the lack of data for lower Reynolds number (long wave cases). Also, due to the scattering of available data, more laboratory/numerical experiments will be suggested for future works, which shall cover a wider range of Reynolds number. The effects of KC number on drag coefficients also need further investigation. As we know, drag coefficients depend on both Reynolds number and Keulegan-Carpenter number, especially for oscillatory flows (Sumer and Fredsøe 2006). Some of the literature (e.g. Ozeren et al. 2014) have discussed the respective significance of Re and KC under different wave conditions. However, more experiments and discussions are still demanded to develop a more comprehensive formula in terms of both Reynolds number and Keulegan-Carpenter number.

The present numerical models for both types of waves have been validated by laboratory experiments of different types of forest configurations. Simplified conditions have been applied to isolate each dynamic factor and help understand the physics. In future works, it could be valuable to check the present models with field data. Instead of using idealized shapes of cylinder patches, the realistic information of forest configurations in natural fields can be useful input to perform some model tests. In addition, the wave-vegetation processes are more complicated and are usually coupled with sediment transport and wave-driven and tidal mean flows, which also deserves further investigation. Moreover, the bathymetry (water depth variation) should be included in future model improvements. Wave-current combined flows propagating through a general vegetated area can also be the next step of model development.

Another interesting future work can be landed with testing different shapes of elements in cylinder arrays. To study the protection of shore regions, the

impacts of waves, especially long waves (e.g. tsunami waves or storm surges), are essential to the construction sites (buildings) and deserve further discussions. Replacing the circular cylinders with rectangular columns (or other elements of different shapes), the present model can provide a preliminary study on the interactions between long waves and model buildings along shorelines. Of course, more field surveys on the arrangements and spacing between buildings will be needed.

As shown in Chap.5, some model improvements must be performed in future works. For example, a boundary-fitting discretization will be needed when solving the nonlinear cell problem. Different numerical approaches (e.g. projection method) can also be explored. In addition, the macro-scale model including nonlinear effects needs to be expanded to relatively short wave cases, in which vertical variation is included. For short waves, the estimation of eddy viscosity should follow the energy model and the iterative scheme instead of using the empirical formula for long waves. The expanded model shall then be checked by existing experimental data (e.g. [Hu et al. 2014](#), [Wu et al. 2011, 2012](#), [Augustin et al. 2009](#)). As suggested above, of course, more experiments are needed to establish a more comprehensive drag formula including both long-waves and short-wave conditions.

Overall, the present model has been shown its capability of predicting wave attenuation when propagating through a vegetated water. Using the multi-scale perturbation technique is able to resolve macro-scale wave amplitude variations through the model forest. The detailed flow fields can also be obtained in micro-scale (cell) solutions, which provide more physical insights than the existing macro-scale schemes. Furthermore, comparing with direct numerical

approaches, the present model shows its computational efficiency and can be applied to a general (more realistic) coastal forest region.

APPENDIX A
DETAILED DERIVATIONS OF INTEGRAL FORMULATION

A.1 Derivation of Helmholtz equation

■ Forest subzone

As stated in Sec.3.3.1, the solutions to macro-scale equation (3.54) can be expressed as

$$\phi_\xi = \mathcal{A}_\xi(X_i)\mathcal{Z}_\xi(Z), \quad i = 1, 2 \quad (\text{A.1})$$

which separates the horizontal and vertical variables due to the possible arbitrary shape of subzone ξ . Substituting (A.1) into (3.54), then

$$\frac{1}{\mathcal{A}_\xi} \left(\frac{\partial^2 \mathcal{A}_\xi}{\partial X_1^2} + \frac{\partial^2 \mathcal{A}_\xi}{\partial X_2^2} \right) = -\frac{\gamma_\xi^2}{\mathcal{Z}_\xi} \left(\frac{\partial^2 \mathcal{Z}_\xi}{\partial Z^2} \right) \quad (\text{A.2})$$

In the above equation, both LHS and RHS must be equal to constant (e.g. \hat{k}_ξ).

Therefore, we have

$$\frac{1}{\mathcal{Z}_\xi} \left(\frac{\partial^2 \mathcal{Z}_\xi}{\partial Z^2} \right) = (\hat{k}_\xi)^2 \quad \implies \quad \mathcal{Z}_\xi = \frac{\cosh \hat{k}_\xi(Z + h)}{\cosh \hat{k}_\xi h} \quad (\text{A.3})$$

in which the no-slip boundary condition along the seabed in (3.50) has been used. The complex potential in (A.1) then becomes

$$\phi_\xi = \mathcal{A}_\xi(X_i) \frac{\cosh \hat{k}_\xi(Z + h)}{\cosh \hat{k}_\xi h}, \quad i = 1, 2 \quad (\text{A.4})$$

Using the kinematic boundary condition along the free surface in (3.48), the dispersion relationship can be obtained as

$$1 = \left(\frac{n_\xi + N_\xi}{n_\xi} \right) \hat{k}_{\xi_d} \tanh \hat{k}_{\xi_d} h \quad (\text{A.5})$$

where \hat{k}_q (with $q = 0, \dots, \infty$) gives the infinite number of complex roots. (A.4) shall then be rewritten as

$$\phi_\xi = \sum_{q=0}^{\infty} \mathcal{A}_{\xi_q}(X_i) \frac{\cosh \hat{k}_{\xi_q}(Z+h)}{\cosh \hat{k}_{\xi_q} h}, \quad i = 1, 2 \quad (\text{A.6})$$

And the equation governing the horizontal variable \mathcal{A}_{ξ_q} is the well-known Helmholtz equation:

$$\left(\frac{\partial^2 \mathcal{A}_{\xi_q}}{\partial X_1 \partial X_1} + \frac{\partial^2 \mathcal{A}_{\xi_q}}{\partial X_2 \partial X_2} \right) + (\gamma_{\xi_q} \hat{k}_{\xi_q})^2 \mathcal{A}_{\xi_q} = 0 \quad (\text{A.7})$$

■ Open water

Likewise, expressing the solution for open water as

$$\phi_S = \mathcal{B}(X_i) \mathcal{Z}_S(Z), \quad i = 1, 2 \quad (\text{A.8})$$

and substituting back into (3.60), then we obtain

$$\frac{1}{\mathcal{B}} \left(\frac{\partial^2 \mathcal{B}}{\partial X_1^2} + \frac{\partial^2 \mathcal{B}}{\partial X_2^2} \right) = -\frac{1}{\mathcal{Z}_S} \left(\frac{\partial^2 \mathcal{Z}_S}{\partial Z^2} \right) \quad (\text{A.9})$$

Again, LHS and RHS in the above equation must be constant. Then

$$\frac{1}{\mathcal{Z}_S} \left(\frac{\partial^2 \mathcal{Z}_S}{\partial Z^2} \right) = k_p^2 \implies \mathcal{Z}_S = \frac{\cosh k_p(Z+h)}{\cosh k_p h} \quad (\text{A.10})$$

where k_p satisfies the following dispersion relationship:

$$1 = k_p \tanh k_p h \quad (\text{A.11})$$

with one real root k_0 and infinite number of imaginary roots $k_p = ik_p$ ($p \geq 1$). The complex solution for open water becomes

$$\phi_S = \sum_{p=0}^{\infty} \mathcal{B}_p(\vec{X}_i) \frac{\cosh k_p(Z+h)}{\cosh k_p h}, \quad i = 1, 2 \quad (\text{A.12})$$

and the corresponding Helmholtz equation for \mathcal{B}_p is

$$\left(\frac{\partial^2 \mathcal{B}_p}{\partial X_1 \partial X_1} + \frac{\partial^2 \mathcal{B}_p}{\partial X_2 \partial X_2} \right) + k_p^2 \mathcal{B}_p = 0 \quad (\text{A.13})$$

A.2 Boundary integral formulation

In this section, the derivations of converting the Helmholtz equations into integral equations for both the forest region and open water are presented respectively.

A.2.1 Forest region (bounded domain)

Assuming \mathcal{A}_{ξ_q} and \mathcal{R}_{ξ_q} both satisfy the Helmholtz equation in (A.7):

$$\nabla^2 \mathcal{A}_{\xi_q} + (\gamma_\xi \hat{k}_{\xi_q})^2 \mathcal{A}_{\xi_q} = 0 \quad \text{and} \quad \nabla^2 \mathcal{R}_{\xi_q} + (\gamma_\xi \hat{k}_{\xi_q})^2 \mathcal{R}_{\xi_q} = 0 \quad (\text{A.14})$$

where $\nabla^2 = \frac{\partial^2}{\partial X_1 \partial X_1} + \frac{\partial^2}{\partial X_2 \partial X_2}$. From Green's identity, we know

$$\int_{\partial \xi} \left(\mathcal{A}_{\xi_q} \frac{\partial \mathcal{R}_{\xi_q}}{\partial \hat{n}_\xi} - \mathcal{R}_{\xi_q} \frac{\partial \mathcal{A}_{\xi_q}}{\partial \hat{n}_\xi} \right) dS = \iint_{\xi} \left(\mathcal{A}_{\xi_q} \nabla^2 \mathcal{R}_{\xi_q} - \mathcal{R}_{\xi_q} \nabla^2 \mathcal{A}_{\xi_q} \right) dX_1 dX_2 = 0 \quad (\text{A.15})$$

where $\partial \xi$ is the boundary of the forest subzone ξ and \hat{n}_ξ denotes the outward normal direction of the boundary (see Fig.3.3). In particular, we propose

$$\mathcal{R}_{\xi_q} = H_0^{(1)}(\gamma_\xi \hat{k}_{\xi_q} \underline{r}) \quad (\text{A.16})$$

where $H_0^{(1)}$ is the Hankel function of the first kind and \underline{r} gives the distance from a point \vec{X}_i to the boundary $\partial \xi$. When the point \vec{X}_i is outside of the subzone ξ , then (A.15) yields

$$\int_{\partial \xi} \left\{ \mathcal{A}_{\xi_q} \frac{\partial}{\partial \hat{n}_\xi} \left[H_0^{(1)}(\gamma_\xi \hat{k}_{\xi_q} \underline{r}) \right] - H_0^{(1)}(\gamma_\xi \hat{k}_{\xi_q} \underline{r}) \frac{\partial \mathcal{A}_{\xi_q}}{\partial \hat{n}_\xi} \right\} dS = 0 \quad (\text{A.17})$$

On the other hand, if the point \vec{X}_i is inside the subzone, a logarithmic singularity at the point exists:

$$\lim_{\underline{r} \rightarrow 0} H_0^{(1)}(\gamma_\xi \hat{k}_{\xi_q} \underline{r}) \equiv \lim_{\underline{r} \rightarrow 0} \left[J_0(\gamma_\xi \hat{k}_{\xi_q} \underline{r}) + iY_0(\gamma_\xi \hat{k}_{\xi_q} \underline{r}) \right] \rightarrow 1 + i \frac{2}{\pi} \left[\ln \left(\frac{1}{2} \gamma_\xi \hat{k}_{\xi_q} \underline{r} \right) + a_e \right] \quad (\text{A.18})$$

where $a_e \approx 0.5772$ is the Euler-Mascheroni constant (Lee 1971). To avoid this singularity, the point \vec{X}_i needs to be excluded and the Green's identity in (A.15) can be rewritten as

$$\begin{aligned} \int_{\partial\xi} \left(\mathcal{A}_{\xi_q} \frac{\partial \mathcal{R}_{\xi_q}}{\partial \hat{n}_\xi} - \mathcal{R}_{\xi_q} \frac{\partial \mathcal{A}_{\xi_q}}{\partial \hat{n}_\xi} \right) dS + \int_{\rho_0} \left(\mathcal{A}_{\xi_q} \frac{\partial \mathcal{R}_{\xi_q}}{\partial \hat{n}_\xi} - \mathcal{R}_{\xi_q} \frac{\partial \mathcal{A}_{\xi_q}}{\partial \hat{n}_\xi} \right) dS \\ = \iint_{\xi'} \left(\mathcal{A}_{\xi_q} \nabla^2 \mathcal{R}_{\xi_q} - \mathcal{R}_{\xi_q} \nabla^2 \mathcal{A}_{\xi_q} \right) dX_1 dX_2 \quad (\text{A.19}) \end{aligned}$$

in which ρ_0 is a small circle of radius r_0 and the point \vec{X}_i locates at its center. ξ' becomes the domain between ξ and r_0 . Note that the outward normal direction on the small circle ρ_0 is from ξ and points inward toward the center \vec{X}_i . Since the point \vec{X}_i is now outside the domain ξ' , the RHS in (A.19) becomes zero:

$$\begin{aligned} \int_{\partial\xi} \left\{ \mathcal{A}_{\xi_q} \frac{\partial}{\partial \hat{n}_\xi} \left[H_0^{(1)}(\gamma_\xi \hat{k}_{\xi_q} r) \right] - H_0^{(1)}(\gamma_\xi \hat{k}_{\xi_q} r) \frac{\partial \mathcal{A}_{\xi_q}}{\partial \hat{n}_\xi} \right\} dS \\ = \int_{\rho_0} \left\{ \mathcal{A}_{\xi_q} \frac{\partial}{\partial \hat{r}_0} \left[H_0^{(1)}(\gamma_\xi \hat{k}_{\xi_q} r) \right] - H_0^{(1)}(\gamma_\xi \hat{k}_{\xi_q} r) \frac{\partial \mathcal{A}_{\xi_q}}{\partial \hat{r}_0} \right\} dS \quad (\text{A.20}) \end{aligned}$$

where (A.16) has been used. Along the boundary ρ_0 , \hat{n}_ξ has been replaced with $-\hat{r}_0$ where \hat{r}_0 denotes the outward normal direction of ρ_0 .

Now let's make the radius of ρ_0 as small as possible and (A.20) becomes

$$\begin{aligned} \lim_{r_0 \rightarrow 0} \int_{\rho_0} \left\{ \mathcal{A}_{\xi_q} \frac{\partial}{\partial \hat{r}_0} \left[H_0^{(1)}(\gamma_\xi \hat{k}_{\xi_q} r_0) \right] - H_0^{(1)}(\gamma_\xi \hat{k}_{\xi_q} r_0) \frac{\partial \mathcal{A}_{\xi_q}}{\partial \hat{r}_0} \right\} dS \\ = \lim_{r_0 \rightarrow 0} \int_0^{2\pi} \left\{ \mathcal{A}_{\xi_q} \frac{2i}{\pi} \frac{1}{r_0} - \left(1 + i \frac{2}{\pi} \left[\ln(\gamma_\xi \hat{k}_{\xi_q} r_0) + a \right] \right) \frac{\partial \mathcal{A}_{\xi_q}}{\partial \hat{r}_0} \right\} r_0 d\theta \rightarrow 4i \mathcal{A}_{\xi_q} \quad (\text{A.21}) \end{aligned}$$

in which the asymptotic behavior of Hankel function is recalled:

$$\lim_{r_0 \rightarrow 0} H_0^{(1)}(\gamma_\xi \hat{k}_{\xi_q} r_0) \rightarrow 1 + i \frac{2}{\pi} \left[\ln \left(\frac{1}{2} \gamma_\xi \hat{k}_{\xi_q} r_0 \right) + a_e \right] \quad (\text{A.22})$$

and

$$\lim_{r_0 \rightarrow 0} \frac{\partial}{\partial \hat{r}_0} \left[H_0^{(1)}(\gamma_\xi \hat{k}_{\xi_q} r_0) \right] \rightarrow i \frac{2}{\pi} \frac{1}{r_0} \quad (\text{A.23})$$

Substituting Eq.(A.21) into Eq.(A.20), then

$$\mathcal{A}_{\xi_q}(\vec{X}_i) = \frac{-i}{4} \int_{\partial\xi} \left\{ \mathcal{A}_{\xi_q} \frac{\partial}{\partial \hat{n}_\xi} [H_0^{(1)}(\gamma_\xi \hat{k}_{\xi_q} \underline{r})] - H_0^{(1)}(\gamma_\xi \hat{k}_{\xi_q} \underline{r}) \frac{\partial \mathcal{A}_{\xi_q}}{\partial \hat{n}_\xi} \right\} dS \quad (\text{A.24})$$

where \underline{r} gives the distance from the interior point \vec{X}_i to the boundary $\partial\xi$. The same equation is shown in (3.59).

If we make \vec{X}_i approach to the boundary, then (A.24) becomes

$$\begin{aligned} \mathcal{A}_{\xi_q}(\vec{X}_i) &= -\frac{i}{4} \int_{\partial\xi-\rho_0} \left\{ \mathcal{A}_{\xi_q} \frac{\partial}{\partial \hat{n}_\xi} [H_0^{(1)}(\gamma_\xi \hat{k}_{\xi_q} \underline{r})] - H_0^{(1)}(\gamma_\xi \hat{k}_{\xi_q} \underline{r}) \frac{\partial \mathcal{A}_{\xi_q}}{\partial \hat{n}_\xi} \right\} dS \\ &= -\frac{i}{4} \int_{\rho_0} \left\{ \mathcal{A}_{\xi_q} \frac{\partial}{\partial \hat{n}_\xi} [H_0^{(1)}(\gamma_\xi \hat{k}_{\xi_q} \underline{r})] - H_0^{(1)}(\gamma_\xi \hat{k}_{\xi_q} \underline{r}) \frac{\partial \mathcal{A}_{\xi_q}}{\partial \hat{n}_\xi} \right\} dS \end{aligned} \quad (\text{A.25})$$

The 2nd integral on the RHS of (A.25) can also be obtained by making the circle ρ_0 as small as possible:

$$\begin{aligned} &\lim_{r_0 \rightarrow 0} \left(-\frac{i}{4} \right) \int_{\rho_0} \left\{ \mathcal{A}_{\xi_q} \frac{\partial}{\partial \hat{n}_\xi} [H_0^{(1)}(\gamma_\xi \hat{k}_{\xi_q} r_0)] - H_0^{(1)}(\gamma_\xi \hat{k}_{\xi_q} r_0) \frac{\partial \mathcal{A}_{\xi_q}}{\partial \hat{n}_\xi} \right\} dS \\ &\rightarrow \lim_{r_0 \rightarrow 0} \left(-\frac{i}{4} \right) \int_0^{2\pi-\alpha} \left\{ \mathcal{A}_{\xi_q} \frac{2i}{\pi} \frac{1}{r_0} - \left(1 + \frac{2i}{\pi} [\ln(\gamma_\xi \hat{k}_{\xi_q} r_0) + a_e] \right) \frac{\partial \mathcal{A}_{\xi_q}}{\partial \hat{n}_\xi} \right\} r_0 d\theta \\ &= \mathcal{A}_{\xi_q}(\vec{X}_i) \frac{1}{2\pi} (2\pi - \alpha) \end{aligned} \quad (\text{A.26})$$

in which α denotes the interior angle of point \vec{X}_i (see Fig.3.3). Both (A.22) and (A.23) are applied. The outward normal direction of small circle ρ_0 now is equivalent to that of the subzone ξ , i.e. $\hat{r}_0 = \hat{n}_\xi$. Thus, (A.25) becomes

$$\mathcal{A}_{\xi_q}(\vec{X}_i) = \frac{-i}{4} \int_{\partial\xi} \left\{ \mathcal{A}_{\xi_q} \frac{\partial [H_0^{(1)}(\gamma_\xi \hat{k}_{\xi_q} \underline{r})]}{\partial \hat{n}_\xi} - H_0^{(1)}(\gamma_\xi \hat{k}_{\xi_q} \underline{r}) \frac{\partial \mathcal{A}_{\xi_q}}{\partial \hat{n}_\xi} \right\} dS + \left(1 - \frac{\alpha}{2\pi} \right) \mathcal{A}_{\xi_q}(\vec{X}_i) \quad (\text{A.27})$$

or

$$\mathcal{A}_{\xi_q}(\vec{X}_i) = \frac{-i\pi}{2\alpha} \int_{\partial\xi} \left\{ \mathcal{A}_{\xi_q} \frac{\partial [H_0^{(1)}(\gamma_\xi \hat{k}_{\xi_q} \underline{r})]}{\partial \hat{n}_\xi} - H_0^{(1)}(\gamma_\xi \hat{k}_{\xi_q} \underline{r}) \frac{\partial \mathcal{A}_{\xi_q}}{\partial \hat{n}_\xi} \right\} dS \quad (\text{A.28})$$

The same equation has also been presented in (3.58). The point \vec{X}_i is now a point along the boundary of subzone ξ .

A.2.2 Open water (unbounded domain)

Similar to (A.24), the integral formulation to the Helmholtz equation for open water is

$$\begin{aligned} \mathcal{B}_p(\vec{X}_i) = & \frac{-i}{4} \int_{\mathbf{S}} \left\{ \mathcal{B}_p \frac{\partial}{\partial \hat{n}_S} [H_0^{(1)}(k_p r)] - H_0^{(1)}(k_p r) \frac{\partial \mathcal{B}_p}{\partial \hat{n}_S} \right\} dS \\ & - \frac{i}{4} \int_{\mathbf{S}_0} \left\{ \mathcal{B}_p \frac{\partial}{\partial \hat{n}_S} [H_0^{(1)}(k_p r)] - H_0^{(1)}(k_p r) \frac{\partial \mathcal{B}_p}{\partial \hat{n}_S} \right\} dS \end{aligned} \quad (\text{A.29})$$

in which \mathbf{S} represents the internal boundary of open water (i.e. the combination of the boundaries of all forest patches) while \mathbf{S}_0 is a circle with radius $R_0 \rightarrow \infty$ enclosing the open water region. \hat{n}_S denotes the outward normal direction of open water (see Fig.3.3) and the point \vec{X}_i is an interior point within open water. Along the outside circle \mathbf{S}_0 , the outward normal direction can be expressed as $\hat{n}_S = \hat{R}_0$. Recalling the asymptotic behavior of Hankel function:

$$\lim_{R_0 \rightarrow \infty} H_0^{(1)}(k_p R_0) \rightarrow \sqrt{\frac{2}{\pi(k_p R_0)}} e^{i(k_p R_0 - \frac{\pi}{4})} \quad (\text{A.30})$$

and

$$\lim_{R_0 \rightarrow \infty} \frac{\partial}{\partial \hat{R}_0} [H_0^{(1)}(k_p R_0)] = \lim_{R_0 \rightarrow \infty} [-k_p H_1^{(1)}(k_p R_0)] \rightarrow -k_p \sqrt{\frac{2}{\pi(k_p R_0)}} e^{i(k_p R_0 - \frac{\pi}{4} - \frac{\pi}{2})} \quad (\text{A.31})$$

, the 2nd integral on the RHS of (A.29) can be obtained as

$$\begin{aligned} & \lim_{R_0 \rightarrow \infty} \frac{-i}{4} \int_{\mathbf{S}_0} \left\{ \mathcal{B}_p \frac{\partial}{\partial \hat{R}_0} [H_0^{(1)}(k_p R_0)] - H_0^{(1)}(k_p R_0) \frac{\partial \mathcal{B}_p}{\partial \hat{R}_0} \right\} dS \\ & = \lim_{R_0 \rightarrow \infty} \frac{i}{4} \int_0^{2\pi} \left[\mathcal{B}_p \cdot k_p \sqrt{\frac{2}{\pi(k_p R_0)}} e^{i(k_p R_0 - \frac{\pi}{4} - \frac{\pi}{2})} + \sqrt{\frac{2}{\pi(k_p R_0)}} e^{i(k_p R_0 - \frac{\pi}{4})} \frac{\partial \mathcal{B}_p}{\partial \hat{R}_0} \right] R_0 d\theta \\ & = \frac{i}{4} \lim_{R_0 \rightarrow \infty} \sqrt{\frac{2}{\pi k_p}} \int_0^{2\pi} \left[e^{i(k_p R_0 - \frac{\pi}{4})} \sqrt{R_0} \left(-ik_p \mathcal{B}_p + \frac{\partial \mathcal{B}_p}{\partial \hat{R}_0} \right) \right] d\theta \rightarrow 0 \end{aligned} \quad (\text{A.32})$$

in which the Sommerfeld radiation condition has been applied:

$$\lim_{R_0 \rightarrow \infty} \sqrt{R_0} \left(-ik_p + \frac{\partial}{\partial \hat{R}_0} \right) \mathcal{B}_p \rightarrow 0 \quad (\text{A.33})$$

Accordingly, (A.29) becomes

$$\mathcal{B}_p(\vec{X}_i) = \frac{-i}{4} \int_{\mathbf{S}} \left\{ \mathcal{B}_p \frac{\partial}{\partial \hat{n}_{\mathbf{S}}} [H_0^{(1)}(k_p \underline{r})] - H_0^{(1)}(k_p \underline{r}) \frac{\partial \mathcal{B}_p}{\partial \hat{n}_{\mathbf{S}}} \right\} dS \quad (\text{A.34})$$

where \underline{r} gives the distance from the interior point \vec{X}_i to the boundary \mathbf{S} . The same equation can be found in (3.65).

Again, let's make \vec{X}_i approaches to the boundary of open water \mathbf{S} , then

$$\begin{aligned} \mathcal{B}_p(\vec{X}_i) = & -\frac{i}{4} \int_{\mathbf{S}-\rho_0} \left\{ \mathcal{B}_p \frac{\partial}{\partial \hat{n}_{\mathbf{S}}} [H_0^{(1)}(k_p \underline{r})] - H_0^{(1)}(k_p \underline{r}) \frac{\partial \mathcal{B}_p}{\partial \hat{n}_{\mathbf{S}}} \right\} dS \\ & - \frac{i}{4} \int_{\rho_0} \left\{ \mathcal{B}_p \frac{\partial}{\partial \hat{n}_{\mathbf{S}}} [H_0^{(1)}(k_p \underline{r})] - H_0^{(1)}(k_p \underline{r}) \frac{\partial \mathcal{B}_p}{\partial \hat{n}_{\mathbf{S}}} \right\} dS \quad (\text{A.35}) \end{aligned}$$

Likewise, the 2nd integral on the RHS of (A.35) can be obtained by making the circle ρ_0 as small as possible:

$$\begin{aligned} & \lim_{r_0 \rightarrow 0} \left(-\frac{i}{4} \right) \int_{\rho_0} \left\{ \mathcal{B}_p \frac{\partial}{\partial \hat{n}_{\mathbf{S}}} [H_0^{(1)}(k_p r_0)] - H_0^{(1)}(k_p r_0) \frac{\partial \mathcal{B}_p}{\partial \hat{n}_{\mathbf{S}}} \right\} dS \\ & \rightarrow \lim_{r_0 \rightarrow 0} \left(-\frac{i}{4} \right) \int_0^\alpha \left\{ \mathcal{B}_p \left(i \frac{2}{\pi} \frac{1}{r_0} \right) - \left(1 + i \frac{2}{\pi} [\ln(k_p r_0) + a_e] \right) \frac{\partial \mathcal{B}_p}{\partial \hat{n}_{\mathbf{S}}} \right\} r_0 d\theta = \mathcal{B}_p(\vec{X}_i) \frac{\alpha}{2\pi} \quad (\text{A.36}) \end{aligned}$$

in which (A.22) and (A.23) have been applied, and α denotes the interior angle of point \vec{X}_i . The outward normal direction of small circle ρ_0 now is equivalent to that of the open water region, i.e. $\hat{r}_0 = \hat{n}_{\mathbf{S}}$. Thus, (A.35) becomes

$$\mathcal{B}_p(\vec{X}_i) = \frac{-i}{4} \int_{\mathbf{S}} \left\{ \mathcal{B}_p \frac{\partial}{\partial \hat{n}_{\mathbf{S}}} [H_0^{(1)}(k_p \underline{r})] - H_0^{(1)}(k_p \underline{r}) \frac{\partial \mathcal{B}_p}{\partial \hat{n}_{\mathbf{S}}} \right\} dS + \frac{\alpha}{2\pi} \mathcal{B}_p(\vec{X}_i) \quad (\text{A.37})$$

or

$$\mathcal{B}_p(\vec{X}_i) = \frac{-i\pi}{2(2\pi - \alpha)} \int_{\mathbf{S}} \left\{ \mathcal{B}_p \frac{\partial [H_0^{(1)}(k_p \underline{r})]}{\partial \hat{n}_{\mathbf{S}}} - H_0^{(1)}(k_p \underline{r}) \frac{\partial \mathcal{B}_p}{\partial \hat{n}_{\mathbf{S}}} \right\} dS \quad (\text{A.38})$$

which has also been presented in (3.64). \vec{X}_i is now a point along the boundary of open water, i.e. the exterior boundary of any subzone ξ .

APPENDIX B
FURTHER INFORMATION FOR THE NUMERICAL MODEL

B.1 Small-amplitude periodic waves

As noted in Sec.3.5, the numerical model, based on the boundary integral equation method, is capable of solving wave propagation through a general forest configuration, which can be composed of multiple patches of arbitrary shape. To conduct the numerical computations by the present model, users are required to prepare several inputs in advance, such as the incident wave conditions, forest properties, as well as the desired computational domain. In the following, we provide the details of each input file. On the other hand, the outputs of this numerical program include the free surface elevation over the specified domain as well as the values of dimensionless parameters (i.e. Reynolds number, drag coefficient and eddy viscosity) for each subzone. Note that different columns in the following inputs/outputs are separated by semicolons. The corresponding size of each file can be found in Table B.1.

In addition to the macro-scale numerical program, the micro-scale (cell) problem solver is needed and introduced here. Different cell configurations (e.g. Mei et al. 2014, Liu et al. 2015) have been tested and prepared. Note the macro-scale program is written in Fortran and the use of linear algebra solver packages, i.e. LAPACK & BLAS (Anderson et al. 1999), is needed.

B.1.1 Inputs/outputs for the numerical model

B.1.1.1 Incident wave conditions and forest configurations

1. *WaveInc.dat* – $\{h_0 ; T_{\text{inc}} ; H_{\text{inc}}\}$

- h_0 – constant water depth
- T_{inc} – incident wave period
- H_{inc} – incident wave height

2. *PZnum.dat* – $\{\mathbb{P} ; N^Z|_{\mathbb{P}}\}$

- \mathbb{P} – patch index ($\mathbb{P} = 1 \cdots N_{\text{patch}}$, N_{patch} denotes the total number of forest patches)
- $N^Z|_{\mathbb{P}}$ – number of subzones within Patch \mathbb{P}

3. *PZidndl.dat* – $\{\mathbb{P} ; \xi, N_{\xi} ; \ell_{\xi}, d_{\xi} ; n_{\xi} ; A_{\xi}\}$

- \mathbb{P} – patch index
- ξ – subzone index ($\xi = 1 \cdots N_{\text{zone}}$, N_{zone} gives the total number of subzones in the entire forest region. i.e. $N_{\text{zone}} = \sum_{\mathbb{P}=1}^{N_{\text{patch}}} N^Z|_{\mathbb{P}}$)
- N_{ξ} – total number of boundary elements used in subzone ξ
- ℓ_{ξ} – cell size (i.e. tree spacing) in subzone ξ
- d_{ξ} – diameter of cylinders in subzone ξ
- n_{ξ} – cell porosity in subzone ξ
- A_{ξ} – area of subzone ξ

4. *PZcoor.dat* – $\{\mathbb{P} ; \xi ; \psi ; X_j|_{\text{bp}} ; Y_j|_{\text{bp}} ; X_j|_{\text{les}} ; Y_j|_{\text{les}} ; X_j|_{\text{lee}} ; Y_j|_{\text{lee}} ; \alpha_j ; \Delta S_j\}$

- \mathbb{P} – patch index
- ξ – subzone index
- ψ – adjacent subzone index (= 0 if open water)
- (X_j, Y_j) – coordinates of boundary points for subzones. The definitions of subscripts bp, es and ee can be found in Fig.2).
- α_j – interior angle of boundary point (Fig.2)
- ΔS_j – element length (Fig.2)

5. *PZcoorEX.dat* – $\{\mathbb{P}; \psi; X_s|_{bp}; Y_s|_{bp}; X_s|_{es}; Y_s|_{es}; X_s|_{ee}; Y_s|_{ee}; \alpha_s; \Delta S_s\}$

- \mathbb{P} – patch index
- ξ – subzone index
- (X_s, Y_s) – coordinates of boundary points for the open water region.
- α_s – interior angle of boundary point ($\equiv \alpha_j$)
- ΔS_s – element length

B.1.1.2 Computational domain and grid points

1. *XYCinfo.dat* – $\{N_{Xc}; N_{Yc}; \Delta X_c; \Delta Y_c\}$

- N_{Xc} – total number of grid points in X direction for computing the macro-scale wave solutions
- N_{Yc} – total number of grid points in Y direction for computing the macro-scale wave solutions
- $\Delta X_c / \Delta Y_c$ – grid size in X / Y direction

2. *XC.dat* & *YC.dat* – coordinates of grid points in the entire computational domain (for macro-scale wave solutions)
3. *XYCpid.dat* & *XYCzid.dat* – patch & subzone indices (= 0 if open water) of grid points (X_c , Y_c)

B.1.1.3 Dimensionless parameters and computed free surface elevation

1. *ReCDsigma.dat* – $\{Re_v ; C_D ; \sigma\}$
 - Re_v – Reynolds number for subzone ξ
 - C_D – drag coefficient for subzone ξ
 - σ – dimensionless eddy viscosity for subzone ξ
2. *etaZOR.dat* & *etaZOI.dat* – real & imaginary parts of the dimensionless free surface elevations at all grid points

Table B.1: Size of each input file

Inputs/Outputs	File Name	Number of rows	Number of columns
Inputs	WaveInc.dat	1	3
	PZnum.dat	N_{patch}	2
	PZidndl.dat	N_{zone}	7
	PZcoor.dat	$N_{\text{bp} fs}$	11
	PZcoorEX.dat	$N_{\text{bp} low}$	10
	XYCinfo.dat	1	4
	XC.dat	N_{Y_c}	N_{X_c}
	YC.dat	N_{Y_c}	N_{X_c}
	XYCpid.dat	N_{Y_c}	N_{X_c}
	XYCzid.dat	N_{Y_c}	N_{X_c}
Outputs	ReCDSigma.dat	N_{zone}	3
	etaZOR.dat	N_{Y_c}	N_{X_c}
	etaZOI.dat	N_{Y_c}	N_{X_c}

$N_{\text{bp}|fs} = \sum N_{\xi}$ and $N_{\text{bp}|low} = \sum N_{p_k}$ denote the total number of boundary points belonging to forest subzones and open water, respectively.

B.1.2 Cell problem solver

The cell problem solver is an open source finite element software – FreeFEM++ (Hecht 2012). Several special cell configurations with one or a few cylinders inside as presented in Liu et al. (2015) and Mei et al. (2011, 2014) have been tested. The scripts can be obtained along with the macro-scale numerical model and can also be edited by users. Note that the present theory only allows the cell configuration to be symmetric in both x and y directions.

B.2 Small-amplitude transient long waves

As mentioned in the Sec.4.4, most of the input files for running this numerical model are the same as those given in Appendix B.1. Since the model employs Fourier transform to solve the transient problem, the total number of harmonics being used in the computation needs to be specified. In addition, the range of harmonic components is required. In the following, we again specify the contents of each input/output. Note that different columns in each input/output are separated by semicolons. The corresponding size of each file can be found in Table B.2.

B.2.1 Inputs/outputs for the numerical model

B.2.1.1 Incident wave conditions and forest configurations

1. *WaveInc.dat* – $\{h_0 ; H_{\text{inc}} ; N_\omega\}$

- h_0 – constant water depth
- H_{inc} – incident wave height
- N_ω – total number of harmonics

2. *Omega.dat* – $\{\omega\}$

- ω – harmonic

3. *PZnum.dat* – $\{\mathbb{P} ; N^Z|_{\mathbb{P}}\}$

- \mathbb{P} – patch index ($\mathbb{P} = 1 \cdots N_{\text{patch}}$, N_{patch} denotes the total number of forest patches)
- $N^Z|_{\mathbb{P}}$ – number of subzones within Patch \mathbb{P}

4. *PZidndl.dat* – $\{\mathbb{P} ; \xi, N_\xi ; \ell_\xi, d_\xi ; n_\xi ; A_\xi\}$

- \mathbb{P} – patch index
- ξ – subzone index ($\xi = 1 \cdots N_{\text{zone}}$, N_{zone} gives the total number of subzones in the entire forest region. i.e. $N_{\text{zone}} = \sum_{\mathbb{P}=1}^{N_{\text{patch}}} N^Z|_{\mathbb{P}}$)
- N_ξ – total number of boundary elements used in subzone ξ
- ℓ_ξ – cell size (i.e. tree spacing) in subzone ξ
- d_ξ – diameter of cylinders in subzone ξ
- n_ξ – cell porosity in subzone ξ
- A_ξ – area of subzone ξ

5. *PZcoor.dat* – $\{\mathbb{P} ; \xi ; \psi ; X_j|_{\text{bp}} ; Y_j|_{\text{bp}} ; X_j|_{\text{les}} ; Y_j|_{\text{les}} ; X_j|_{\text{lee}} ; Y_j|_{\text{lee}} ; \alpha_j ; \Delta S_j\}$

- \mathbb{P} – patch index
- ξ – subzone index

- ψ – adjacent subzone index (= 0 if open water)
- (X_j, Y_j) – coordinates of boundary points for subzones. The definitions of subscripts bp, es and ee can be found in Fig.2).
- α_j – interior angle of boundary point (Fig.2)
- ΔS_j – element length (Fig.2)

6. *PZcoorEX.dat* – $\{\mathbb{P}; \psi; X_s|_{\text{bp}}; Y_s|_{\text{bp}}; X_s|_{\text{es}}; Y_s|_{\text{es}}; X_s|_{\text{ee}}; Y_s|_{\text{ee}}; \alpha_s; \Delta S_s\}$

- \mathbb{P} – patch index
- ξ – subzone index
- (X_s, Y_s) – coordinates of boundary points for the open water region.
- α_s – interior angle of boundary point ($\equiv \alpha_j$)
- ΔS_s – element length

B.2.1.2 Computational domain and free surface elevation

1. *XYCinfo.dat* – $\{N_{Xc}; N_{Yc}; \Delta X_c; \Delta Y_c\}$

- N_{Xc} – total number of grid points in X direction for computing the macro-scale wave solutions
- N_{Yc} – total number of grid points in Y direction for computing the macro-scale wave solutions
- $\Delta X_c / \Delta Y_c$ – grid size in X / Y direction

2. *XC.dat* & *YC.dat* – coordinates of grid points in the entire computational domain (for macro-scale wave solutions)

3. *XYCpid.dat* & *XYCzid.dat* – patch & subzone indices (= 0 if open water) of grid points (X_c , Y_c)
4. *etaG.dat* – dimensionless free surface elevations at all grid points at different time

Table B.2: Size of each input file

File Name	Number of rows	Number of columns
WaveInc.dat	1	3
Omega.dat	N_ω	1
PZnum.dat	N_{patch}	2
PZidndl.dat	N_{zone}	7
PZcoor.dat	$N_{\text{bp} fs}$	11
PZcoorEX.dat	$N_{\text{bp} low}$	10
XYCinfo.dat	1	4
XC.dat	N_{Y_c}	N_{X_c}
YC.dat	N_{Y_c}	N_{X_c}
XYCpid.dat	N_{Y_c}	N_{X_c}
XYCzid.dat	N_{Y_c}	N_{X_c}

$N_{\text{bp}|fs} = \sum N_{\xi}$ and $N_{\text{bp}|low} = \sum N_{P_k}$ denote the total number of boundary points belonging to forest subzones and open water, respectively.

APPENDIX C

DERIVATIONS OF MATCHING CONDITIONS FOR TWO SPECIAL FOREST CONFIGURATIONS

C.1 Water waves propagating through a forest belt

The semi-analytical solutions for the incidence, transmission and forest regions are presented in (3.110), (3.111) and (3.114). The unknown coefficients are to be solved by matching the pressure and normal fluxes along the edges of the forest, i.e. (3.118) and (3.119).

Along $X = 0$, substituting the solutions (3.110) and (3.114) into (3.118) yields

$$A_0 (1 + R) \frac{\cosh k_0(Z + h)}{\cosh k_0 h} + \sum_{p=1}^{\infty} A_p \frac{\cos \kappa_p(Z + h)}{\cos \kappa_p h} = \sum_{q=0}^{\infty} \frac{\cosh \hat{k}_q(Z + h)}{\cosh \hat{k}_q h} [C_q + D_q] \quad (\text{C.1})$$

and

$$\begin{aligned} i\alpha A_0 (1 - R) \frac{\cosh k_0(Z + h)}{\cosh k_0 h} + \sum_{p=1}^{\infty} A_p \lambda_p \frac{\cos \kappa_p(Z + h)}{\cos \kappa_p h} \\ = (n + M) \sum_{q=0}^{\infty} i\hat{\alpha}_q \frac{\cosh \hat{k}_q(Z + h)}{\cosh \hat{k}_q h} [C_q - D_q] \end{aligned} \quad (\text{C.2})$$

Applying the orthogonality condition, presented in (3.70), to the above (C.1) and (C.2), then

$$A_0 (1 + R) \frac{\Gamma_{0q}}{\cosh k_0 h} + \sum_{p=1}^{\infty} A_p \frac{\Gamma_{pq}}{\cos \kappa_p h} = \frac{\Pi(\hat{k}_q)}{\cosh \hat{k}_q h} [C_q + D_q] \quad (\text{C.3})$$

$$i\alpha A_0 (1 - R) \frac{\Pi(k_0)}{\cosh k_0 h} = (n + M) \sum_{q=0}^{\infty} i\hat{\alpha}_q \frac{\Gamma_{0q}}{\cosh \hat{k}_q h} [C_q - D_q] \quad (\text{C.4})$$

and

$$(A_p \lambda_p) \frac{\Pi_2(\kappa_p)}{\cos \kappa_p h} = (n + M) \sum_{q=0}^{\infty} i\hat{\alpha}_q \frac{\Gamma_{pq}}{\cosh \hat{k}_q h} [C_q - D_q] \quad (\text{C.5})$$

in which the definitions of Π and Γ have been given in (3.73) and (3.74). Note that since $k_p \equiv i\kappa_p$ when $p \geq 1$, then we know

$$\begin{aligned}\Gamma_{pq} &= \frac{k_p \sinh(k_p h) \cosh(\hat{k}_q h) - \hat{k}_q \cosh(k_p h) \sinh(\hat{k}_q h)}{k_p^2 - \hat{k}_q^2} \\ &= \frac{-\kappa_p \sin(\kappa_p h) \cosh(\hat{k}_q h) - \hat{k}_q \cos(\kappa_p h) \sinh(\hat{k}_q h)}{-\kappa_p^2 - \hat{k}_q^2}\end{aligned}\quad (\text{C.6})$$

And we also define

$$\Pi_2(\kappa_p) \equiv \Pi(k_p) = \frac{h}{2} \left(1 + \frac{\sin 2\kappa_p h}{2\kappa_p h} \right) \quad (\text{C.7})$$

Likewise, along the interface between the forest and the transmission region (i.e. $X = L_F$), the matching conditions are also required. Substituting (3.111) and (3.114) into (3.119) yields

$$\begin{aligned}\sum_{q=0}^{\infty} \frac{\cosh \hat{k}_q(Z+h)}{\cosh \hat{k}_q h} [C_q e^{i\hat{\alpha}_p L_F} + D_q e^{-i\hat{\alpha}_p L_F}] \\ = (A_0 T) \frac{\cosh k_0(Z+h)}{\cosh k_0 h} e^{i\alpha L_F} + \sum_{p=1}^{\infty} B_p \frac{\cos \kappa_p(Z+h)}{\cos \kappa_p h} e^{-\lambda_p L_F}\end{aligned}\quad (\text{C.8})$$

and

$$\begin{aligned}(n+M) \sum_{q=0}^{\infty} \frac{\cosh \hat{k}_q(Z+h)}{\cosh \hat{k}_q h} i\hat{\alpha}_q [C_q e^{i\hat{\alpha}_p L_F} - D_q e^{-i\hat{\alpha}_p L_F}] \\ = i\alpha (A_0 T) \frac{\cosh k_0(Z+h)}{\cosh k_0 h} e^{i\alpha L_F} - \sum_{p=1}^{\infty} B_p \lambda_p \frac{\cos \kappa_p(Z+h)}{\cos \kappa_p h} e^{-\lambda_p L_F}\end{aligned}\quad (\text{C.9})$$

Again, we apply the orthogonality condition to (C.8) and (C.9), three equations are given as

$$\frac{\Pi(\hat{k}_q)}{\cosh \hat{k}_q h} [C_q e^{i\hat{\alpha}_p L_F} + D_q e^{-i\hat{\alpha}_p L_F}] = (A_0 T) \frac{\Gamma_{0q}}{\cosh k_0 h} e^{i\alpha L_F} + \sum_{p=1}^{\infty} B_p \frac{\Gamma_{pq}}{\cos \kappa_p h} e^{-\lambda_p L_F} \quad (\text{C.10})$$

$$(n+M) \sum_{q=0}^{\infty} \frac{\Gamma_{pq}}{\cosh \hat{k}_q h} i\hat{\alpha}_q [C_q e^{i\hat{\alpha}_p L_F} - D_q e^{-i\hat{\alpha}_p L_F}] = -B_p \lambda_p \frac{\Pi_2(\kappa_p)}{\cos \kappa_p h} e^{-\lambda_p L_F} \quad (\text{C.11})$$

and

$$(n + M) \sum_{q=0}^{\infty} \frac{\Gamma_{0q}}{\cosh \hat{k}_q h} \hat{\alpha}_q \left[C_q e^{i\hat{\alpha}_q L_F} - D_q e^{-i\hat{\alpha}_q L_F} \right] = \alpha (A_0 T) \frac{\Pi(k_0)}{\cosh k_0 h} e^{i\alpha L_F} \quad (\text{C.12})$$

Solving the above system of algebraic equations, i.e. (C.3), (C.4), (C.5), (C.10), (C.11) and (C.12), then the unknown coefficients A_p , C_q , D_q , B_p as well as the reflection coefficient $|R|$ and transmission coefficient $|T|$ can be obtained. It may be noted that the infinite p and q need to be truncated to finite numbers by performing the convergence test.

C.2 Water waves scattered by a circular forest

Following the same procedures presented in the previous section, the unknown coefficients in the solution forms (3.122) and (3.126) can be determined by invoking the matching conditions in (3.128) and (3.129) along $r = R$:

$$\begin{aligned} A_0 \sum_{m=0}^{\infty} \epsilon_m i^m \cos m\theta & \left\{ \left[J_m(k_0 R) + C_{m0} H_m^{(1)}(k_0 R) \right] \frac{\cosh k_0 (Z + h)}{\cosh k_0 h} \right\} \\ & + A_0 \sum_{m=0}^{\infty} \epsilon_m i^m \cos m\theta \left[\sum_{p=1}^{\infty} C_{mp} K_m(\kappa_p R) \frac{\cos \kappa_p (Z + h)}{\cos \kappa_p h} \right] \\ & = A_0 \sum_{m=0}^{\infty} \epsilon_m i^m \cos m\theta \left[\sum_{q=0}^{\infty} B_{mq} J_m(\gamma \hat{k}_q R) \frac{\cosh \hat{k}_q (Z + h)}{\cosh \hat{k}_q h} \right] \end{aligned} \quad (\text{C.13})$$

and

$$\begin{aligned} A_0 \sum_{m=0}^{\infty} \epsilon_m i^m \cos m\theta & \left\{ j_m(k_0 R) + C_{m0} \dot{H}_m^{(1)}(k_0 R) \right\} \frac{\cosh k_0 (Z + h)}{\cosh k_0 h} \\ & + A_0 \sum_{m=0}^{\infty} \epsilon_m i^m \cos m\theta \left\{ \sum_{p=1}^{\infty} C_{mp} \dot{K}_m(\kappa_p R) \frac{\cos \kappa_p (Z + h)}{\cos \kappa_p h} \right\} \\ & = (n + M) A_0 \sum_{m=0}^{\infty} \epsilon_m i^m \cos m\theta \left\{ \sum_{q=0}^{\infty} B_{mq} j_m(\gamma \hat{k}_q R) \frac{\cosh \hat{k}_q (Z + h)}{\cosh \hat{k}_q h} \right\} \end{aligned} \quad (\text{C.14})$$

in which the derivatives of Bessel functions of the first and second kind are defined as

$$J_m(ax) = \frac{1}{2}a [J_{m-1}(ax) - J_{m+1}(ax)] \quad \text{and} \quad \dot{Y}_m(ax) = \frac{1}{2}a [Y_{m-1}(ax) - Y_{m+1}(ax)] \quad (\text{C.15})$$

The derivatives of modified Bessel function and Hankel function are respectively defined as

$$\dot{K}_m(ax) = -\frac{1}{2}a [K_{m-1}(ax) - K_{m+1}(ax)] \quad \text{and} \quad \dot{H}_m^{(1)}(ax) = a \left(\frac{mH_m^{(1)}(ax)}{ax} - H_{m+1}^{(1)}(ax) \right) \quad (\text{C.16})$$

Applying the orthogonality condition as shown in (3.70) to the above (C.13) and (C.14) gives

$$\begin{aligned} A_0 \sum_{m=0}^{\infty} \epsilon_m i^m \cos m\theta \left\{ \left[J_m(k_0 R) + C_{m0} H_m^{(1)}(k_0 R) \right] \frac{\Gamma_{0q}}{\cosh k_0 h} + \sum_{p=1}^{\infty} C_{mp} K_m(\kappa_p R) \frac{\Gamma_{pq}}{\cos \kappa_p h} \right\} \\ = A_0 \sum_{m=0}^{\infty} \epsilon_m i^m \cos m\theta \left[B_{mq} J_m(\gamma \hat{k}_q R) \frac{\Pi(\hat{k}_q)}{\cosh \hat{k}_q h} \right] \quad (\text{C.17}) \end{aligned}$$

$$\begin{aligned} A_0 \sum_{m=0}^{\infty} \epsilon_m i^m \cos m\theta \left\{ -\frac{1}{2} C_{mp} \kappa_p \left[K_{m-1}(\kappa_p R) + K_{m+1}(\kappa_p R) \right] \right\} \frac{\Pi_2(\kappa_p)}{\cos \kappa_p h} \\ = (n + M) A_0 \sum_{m=0}^{\infty} \epsilon_m i^m \cos m\theta \left\{ \sum_{q=0}^{\infty} \frac{1}{2} B_{mq} \gamma \hat{k}_q \left[J_{m-1}(\gamma \hat{k}_q R) - J_{m+1}(\gamma \hat{k}_q R) \right] \frac{\Gamma_{pq}}{\cosh \hat{k}_q h} \right\} \quad (\text{C.18}) \end{aligned}$$

and

$$\begin{aligned} A_0 \sum_{m=0}^{\infty} \epsilon_m i^m \cos m\theta \left\{ \frac{k_0}{2} [J_{m-1}(k_0 R) - J_{m+1}(k_0 R)] + C_{m0} k_0 \left[\frac{mH_m^{(1)}(k_0 R)}{k_0 R} - H_{m+1}^{(1)}(k_0 R) \right] \right\} \frac{\Pi(k_0)}{\cosh k_0 h} \\ = (n + M) A_0 \sum_{m=0}^{\infty} \epsilon_m i^m \cos m\theta \left\{ \sum_{q=0}^{\infty} \frac{1}{2} B_{mq} \gamma \hat{k}_q \left[J_{m-1}(\gamma \hat{k}_q R) - J_{m+1}(\gamma \hat{k}_q R) \right] \frac{\Gamma_{0q}}{\cosh \hat{k}_q h} \right\} \quad (\text{C.19}) \end{aligned}$$

where Γ_{0q} , Γ_{pq} , $\Pi(k_0)$, $\Pi(\hat{k}_q)$ and $\Pi_2(\kappa_p)$ are defined in (3.73), (3.74) and (C.7). Solving (C.17), (C.18) and (C.19) simultaneously, the unknown coefficients C_{m0} , C_{mp} and B_{mq} can be obtained.

APPENDIX D
MORE DATA-MODEL COMPARISONS FOR SOLITARY WAVE
THROUGH A CIRCULAR FOREST

D.1 Cases in Table 4.1

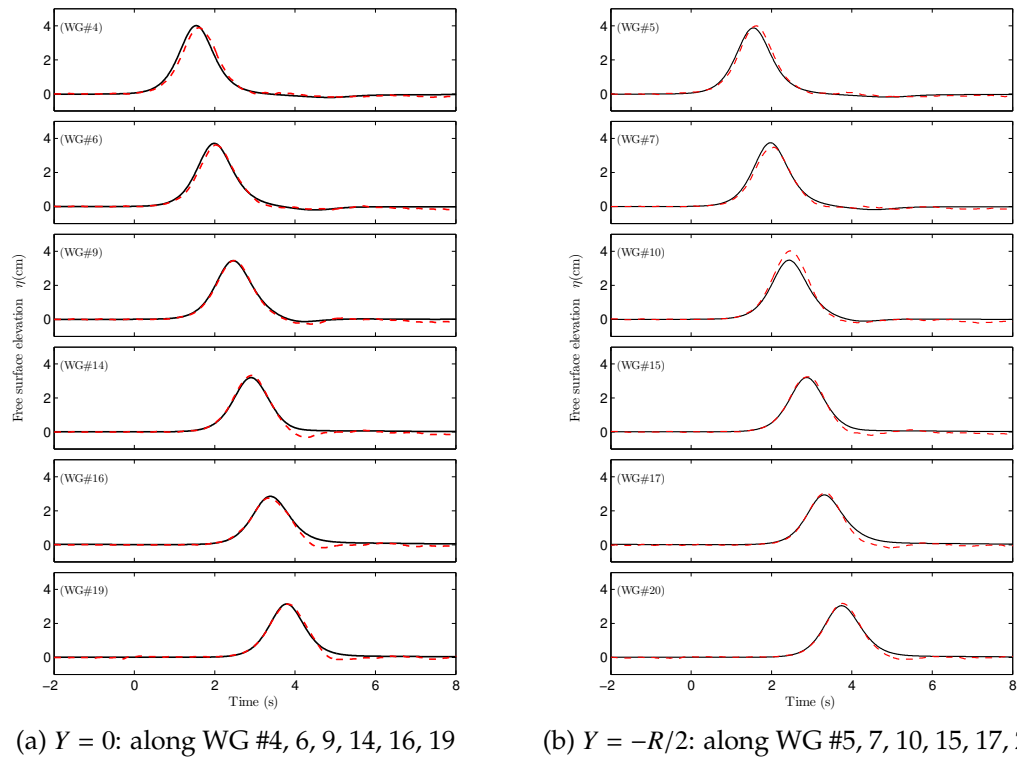


Figure D.1: Comparison of wave heights by numerical simulations (solid lines) with experimental data (dashed lines) for Case 3S1.

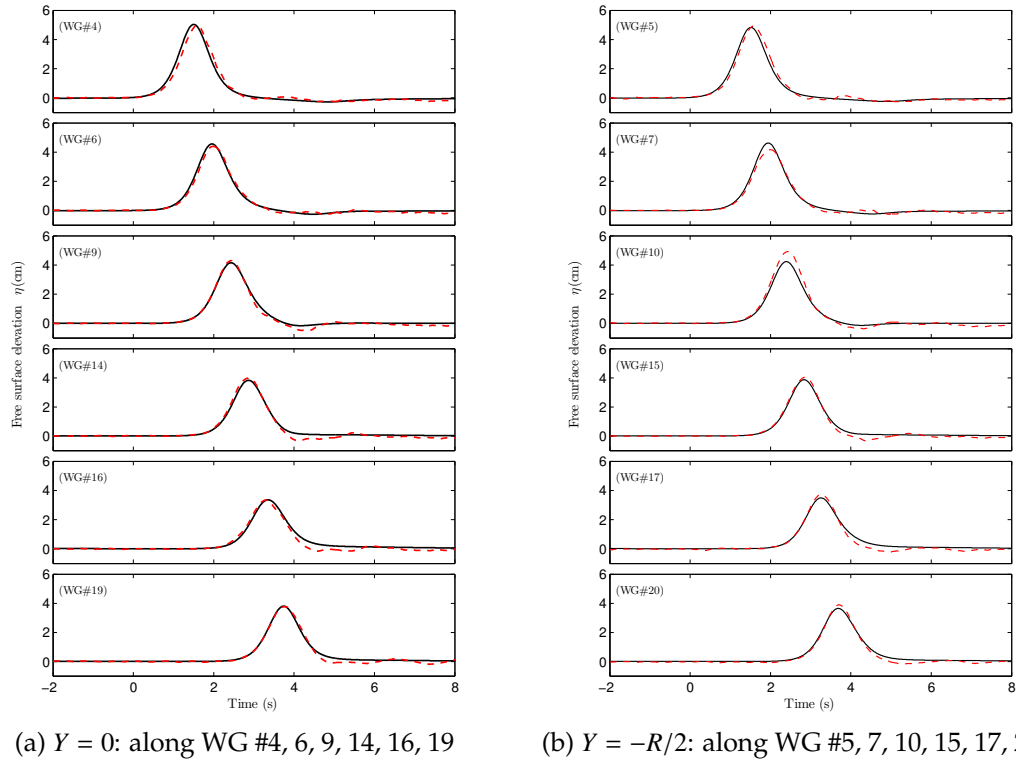


Figure D.2: Comparison of wave heights by numerical simulations (solid lines) with experimental data (dashed lines) for Case 3S2.

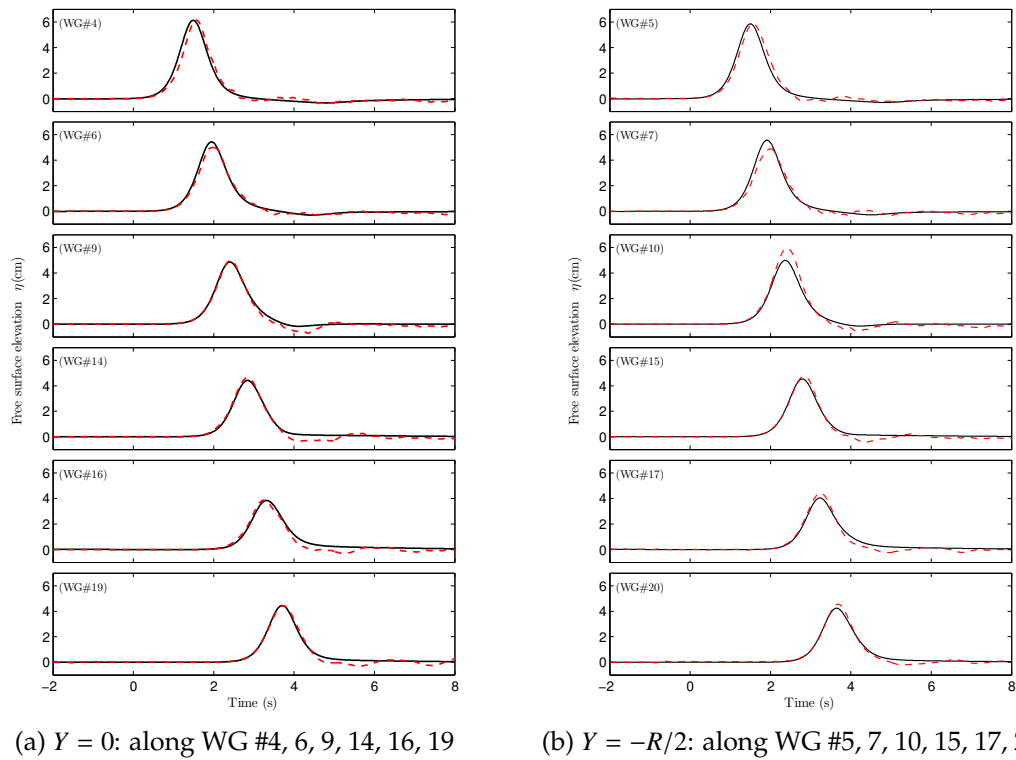
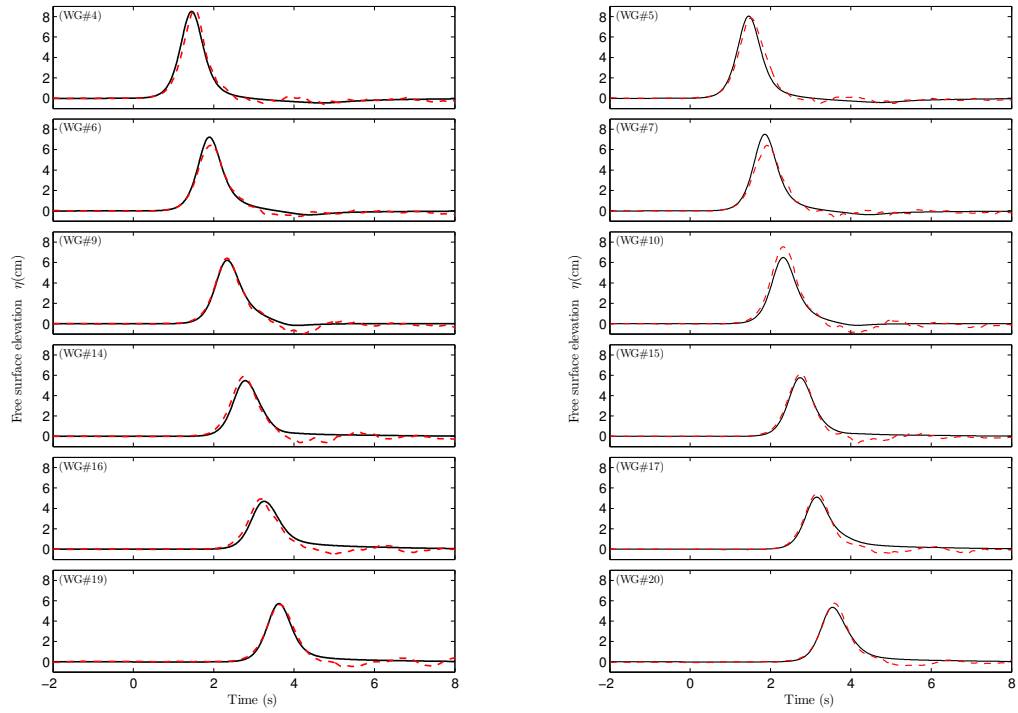


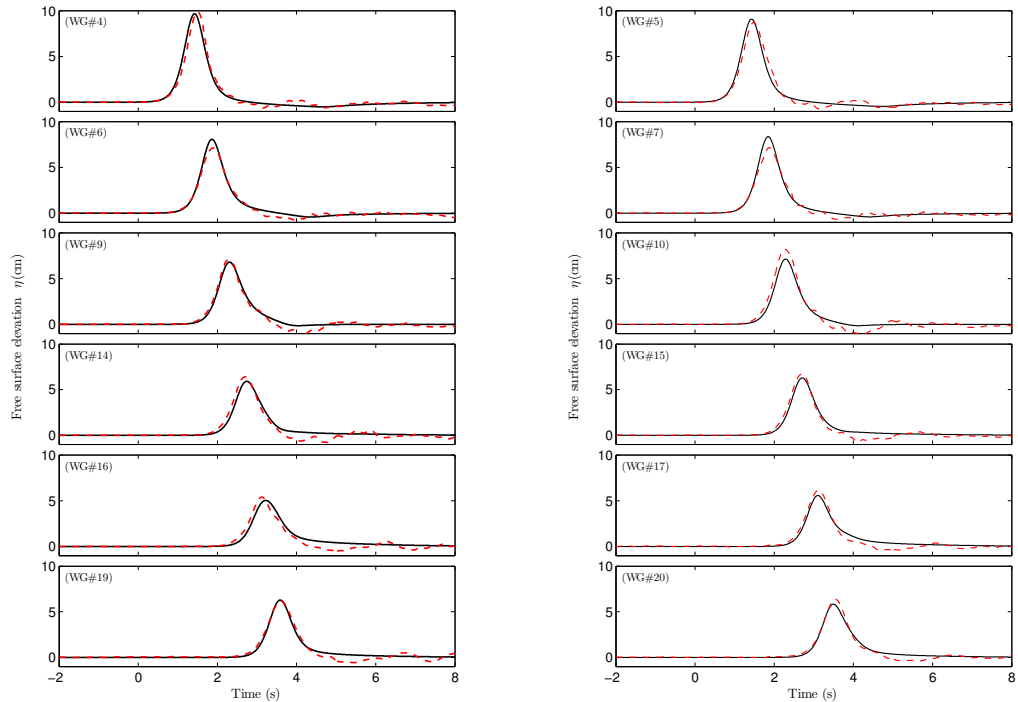
Figure D.3: Comparison of wave heights by numerical simulations (solid lines) with experimental data (dashed lines) for Case 3S3.



(a) $Y = 0$: along WG #4, 6, 9, 14, 16, 19

(b) $Y = -R/2$: along WG #5, 7, 10, 15, 17, 20

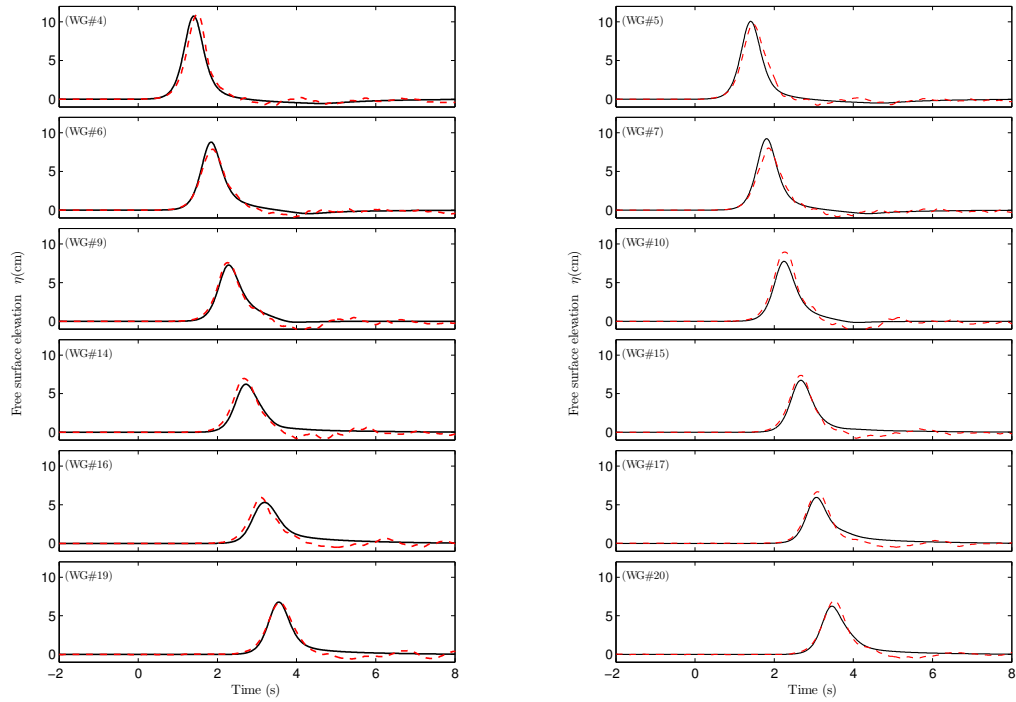
Figure D.4: Comparison of wave heights by numerical simulations (solid lines) with experimental data (dashed lines) for Case 3S4.



(a) $Y = 0$: along WG #4, 6, 9, 14, 16, 19

(b) $Y = -R/2$: along WG #5, 7, 10, 15, 17, 20

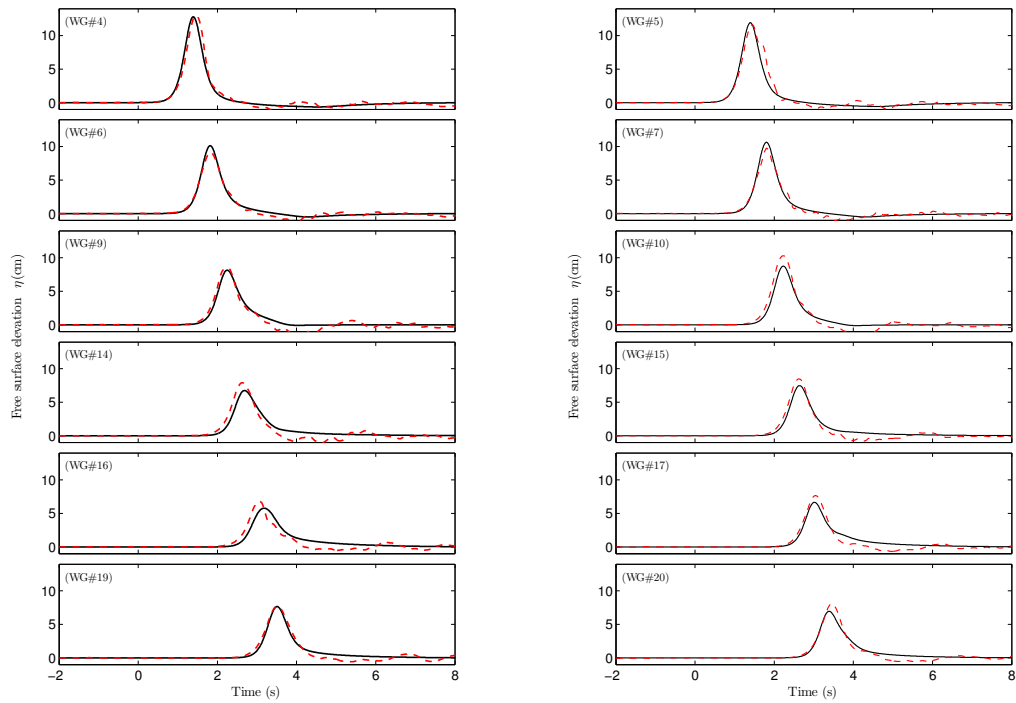
Figure D.5: Comparison of wave heights by numerical simulations (solid lines) with experimental data (dashed lines) for Case 3S5.



(a) $Y = 0$: along WG #4, 6, 9, 14, 16, 19

(b) $Y = -R/2$: along WG #5, 7, 10, 15, 17, 20

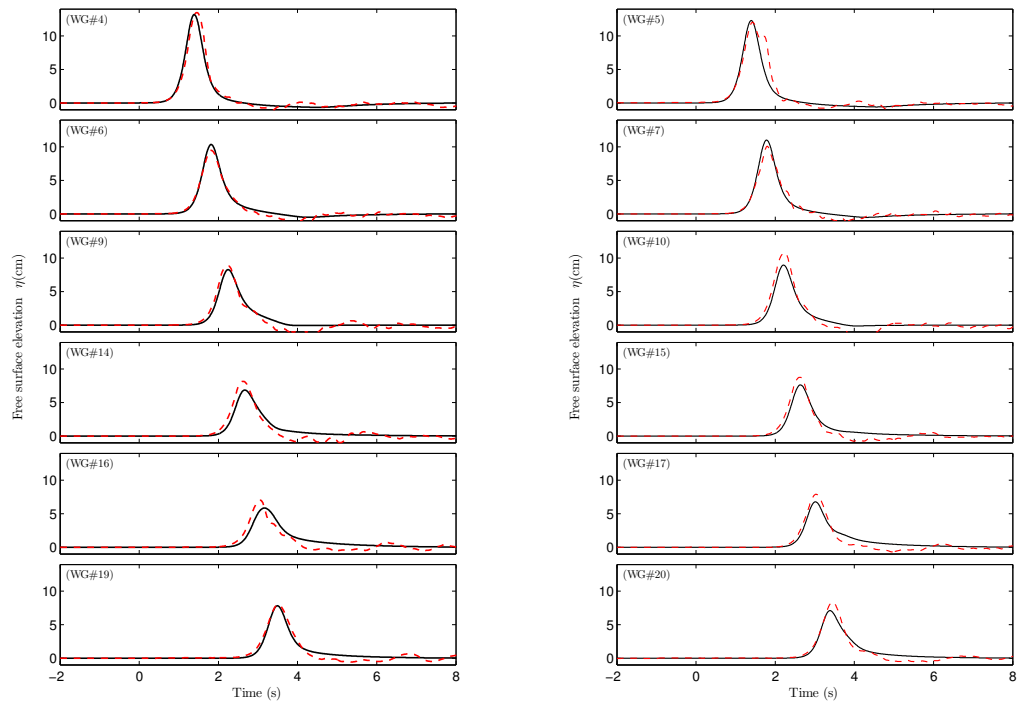
Figure D.6: Comparison of wave heights by numerical simulations (solid lines) with experimental data (dashed lines) for Case 3S6.



(a) $Y = 0$: along WG #4, 6, 9, 14, 16, 19

(b) $Y = -R/2$: along WG #5, 7, 10, 15, 17, 20

Figure D.7: Comparison of wave heights by numerical simulations (solid lines) with experimental data (dashed lines) for Case 3S7.



(a) $Y = 0$: along WG #4, 6, 9, 14, 16, 19

(b) $Y = -R/2$: along WG #5, 7, 10, 15, 17, 20

Figure D.8: Comparison of wave heights by numerical simulations (solid lines) with experimental data (dashed lines) for Case 3S8.

D.2 Cases in Table 4.2

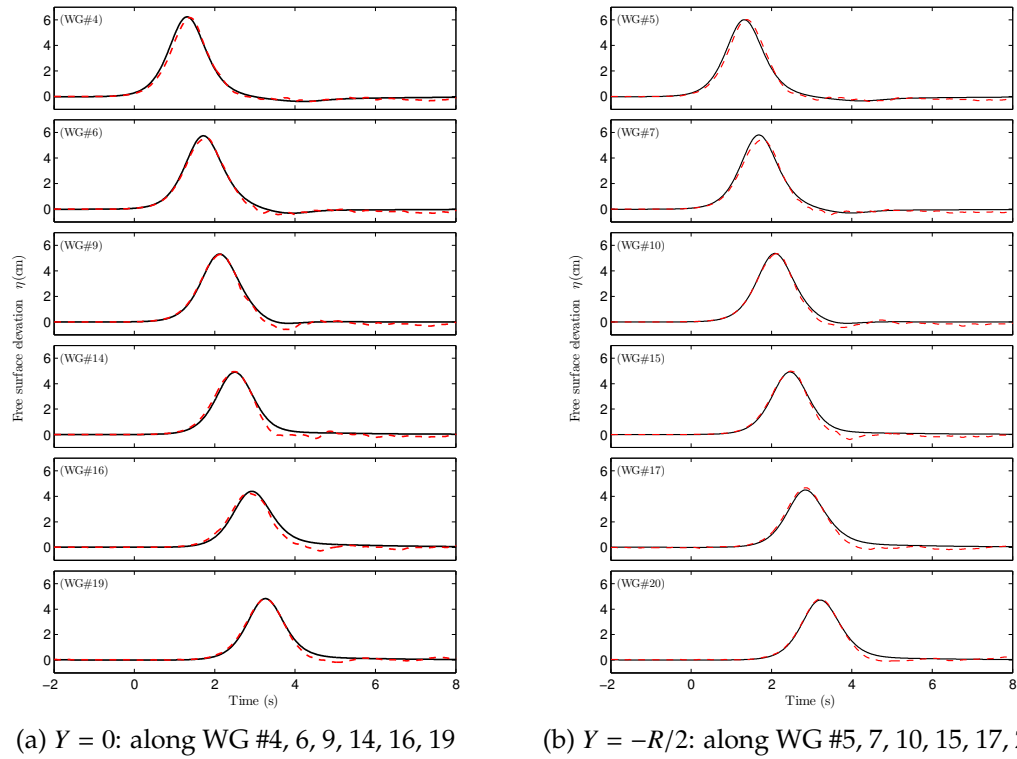
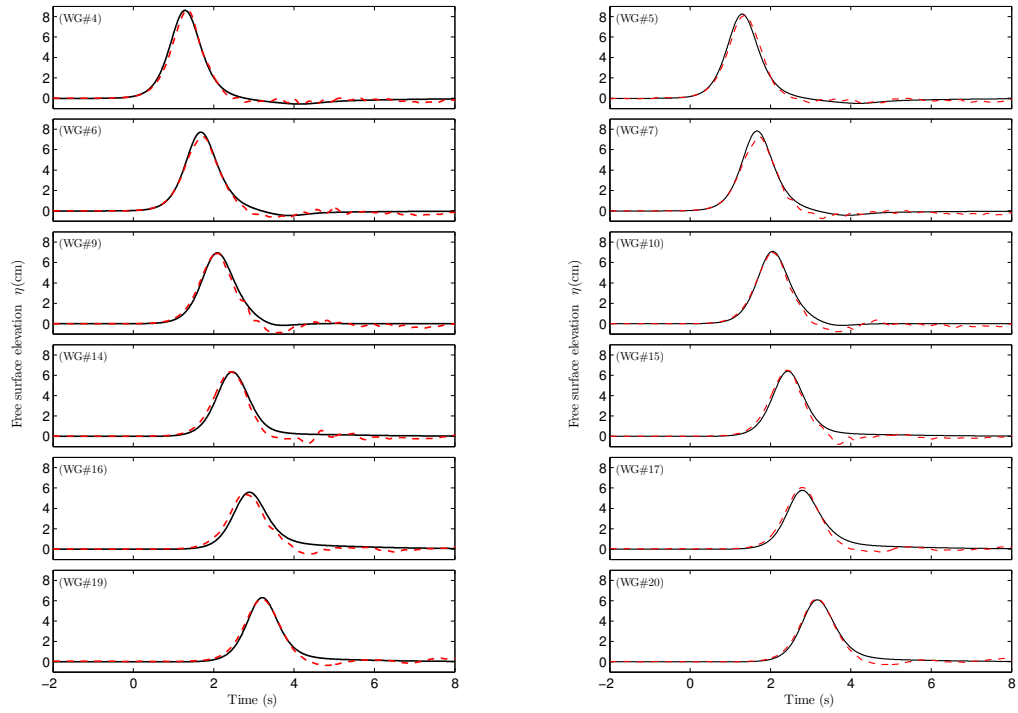


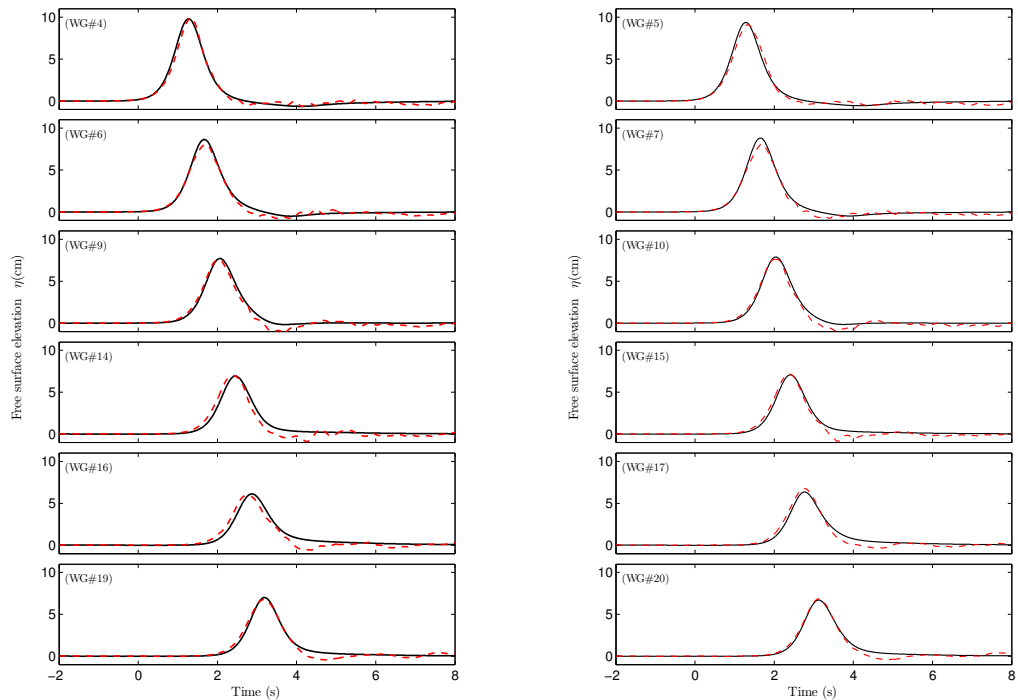
Figure D.9: Comparison of wave heights by numerical simulations (solid lines) with experimental data (dashed lines) for Case 4S3.



(a) $Y = 0$: along WG #4, 6, 9, 14, 16, 19

(b) $Y = -R/2$: along WG #5, 7, 10, 15, 17, 20

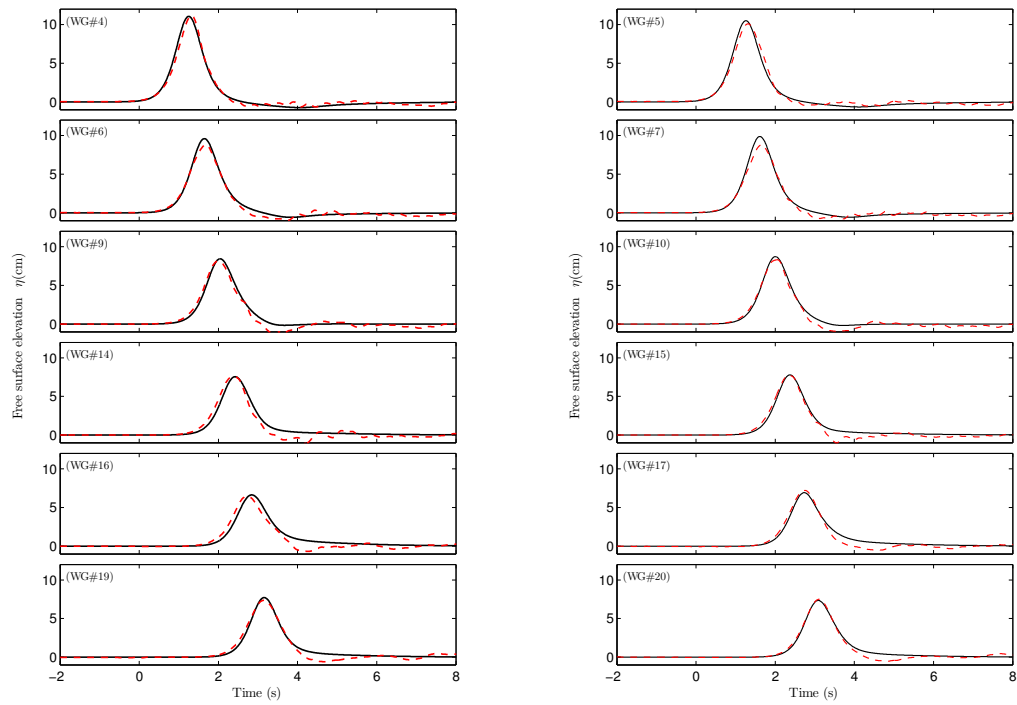
Figure D.10: Comparison of wave heights by numerical simulations (solid lines) with experimental data (dashed lines) for Case 4S4.



(a) $Y = 0$: along WG #4, 6, 9, 14, 16, 19

(b) $Y = -R/2$: along WG #5, 7, 10, 15, 17, 20

Figure D.11: Comparison of wave heights by numerical simulations (solid lines) with experimental data (dashed lines) for Case 4S5.



(a) $Y = 0$: along WG #4, 6, 9, 14, 16, 19

(b) $Y = -R/2$: along WG #5, 7, 10, 15, 17, 20

Figure D.12: Comparison of wave heights by numerical simulations (solid lines) with experimental data (dashed lines) for Case 4S6.

APPENDIX E
MORE NUMERICAL RESULTS FOR HARMONICS GENERATION
PROBLEM

E.1 Micro-scale velocity fields

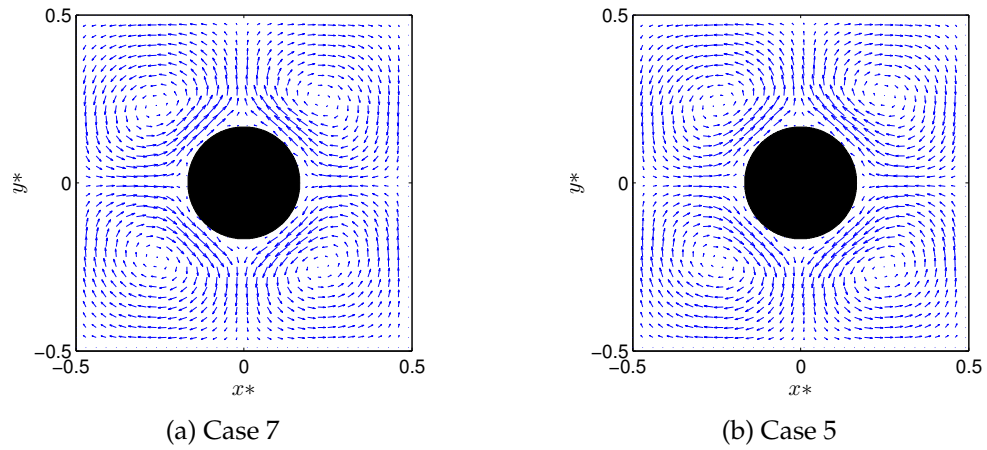


Figure E.1: Horizontal velocity fields of 0_{th} mode ($m = 0$) at the middle of forest belt ($X = L_F/2$) – Case 5 & 7.

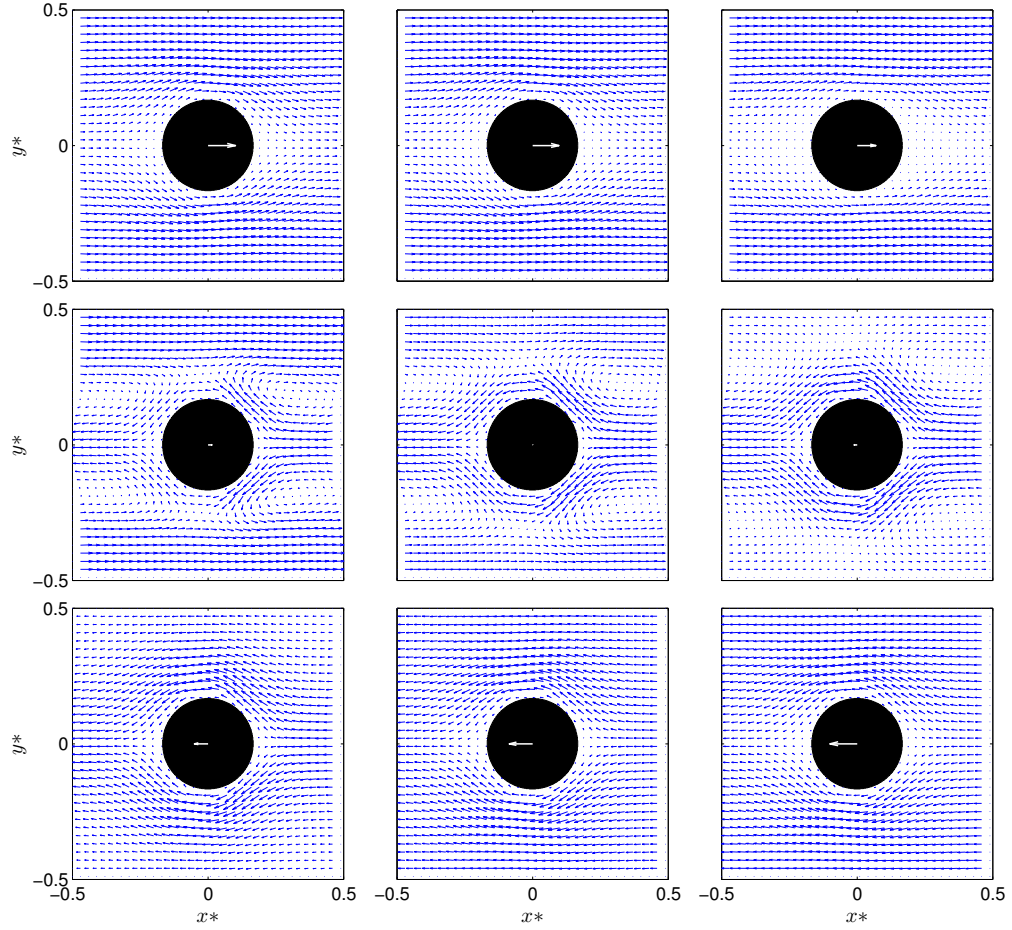


Figure E.2: Snapshots of horizontal velocity fields of 1_{st} mode ($m = 1$) at the middle of forest belt ($X = L_F/2$) – Case 7. From left to right and top to bottom, the dimensionless time is $mt/T = 0.25, 0.27, 0.34, 0.43, 0.45, 0.47, 0.53, 0.60, 0.65$. Note that the central arrows are used to indicate the evolution and directions of horizontal cell-averaged velocity $\langle u_{m=1}^{(0)} \rangle$. The length of arrows have been enlarged for illustration and do not indicate the real magnitude.

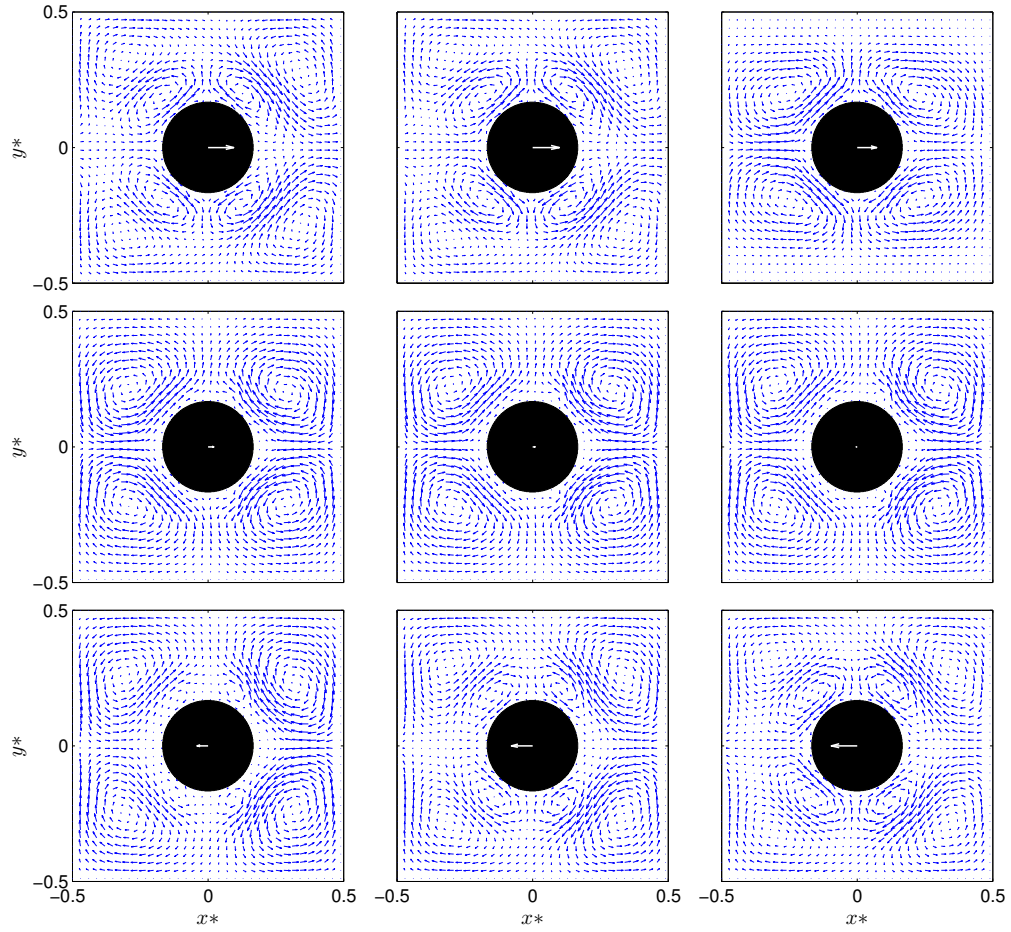


Figure E.3: Snapshots of horizontal velocity fields of 2_{nd} mode ($m = 2$) at the middle of forest belt ($X = L_F/2$) – Case 7. From left to right and top to bottom, the dimensionless time is $mt/T = 0.35, 0.37, 0.54, 0.63, 0.65, 0.67, 0.73, 0.80, 0.85$. Note that the central arrows are used to indicate the evolution and directions of horizontal cell-averaged velocity $\langle u_{m=2}^{(0)} \rangle$. The length of arrows have been enlarged for illustration and do not indicate the real magnitude.

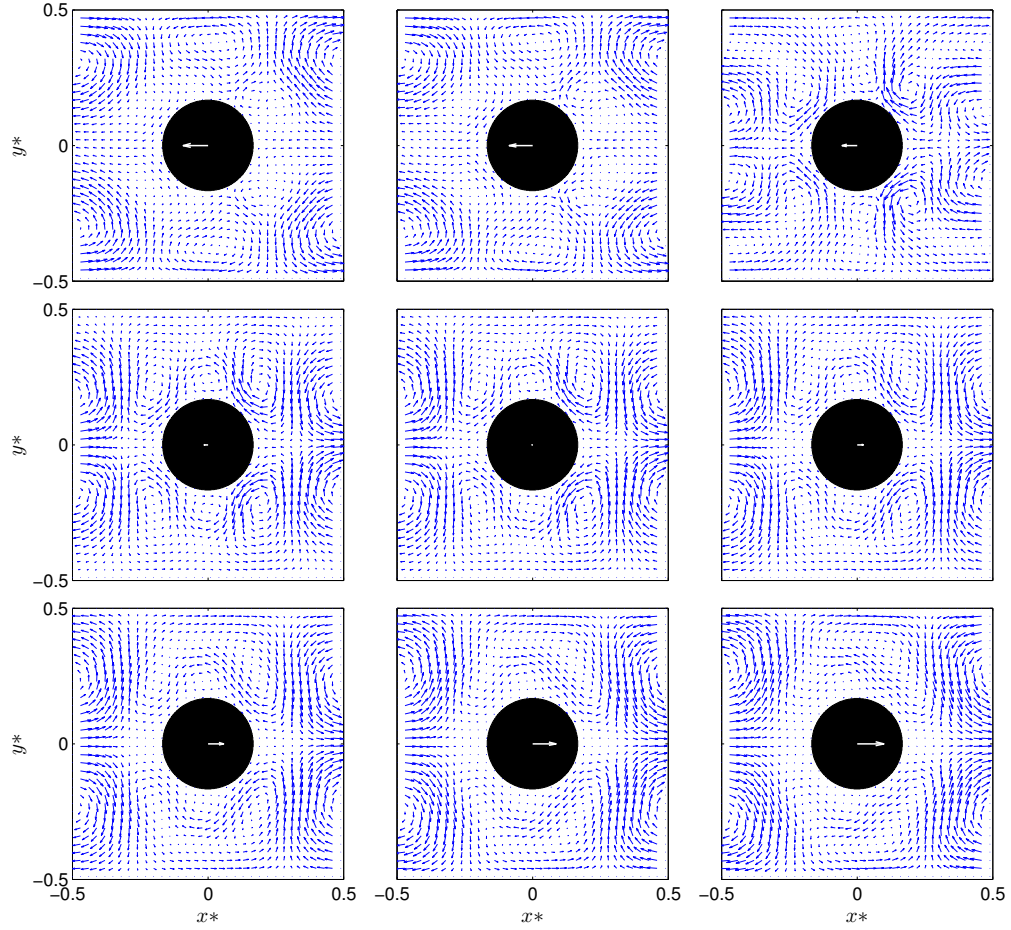


Figure E.4: Snapshots of horizontal velocity fields of 3_{rd} mode ($m = 3$) at the middle of forest belt ($X = L_F/2$) – Case 7. From left to right and top to bottom, the dimensionless time is $mt/T = 0.35, 0.37, 0.44, 0.51, 0.53, 0.57, 0.63, 0.70, 0.75$. Note that the central arrows are used to indicate the evolution and directions of horizontal cell-averaged velocity $\langle u_{m=3}^{(0)} \rangle$. The length of arrows have been enlarged for illustration and do not indicate the real magnitude.

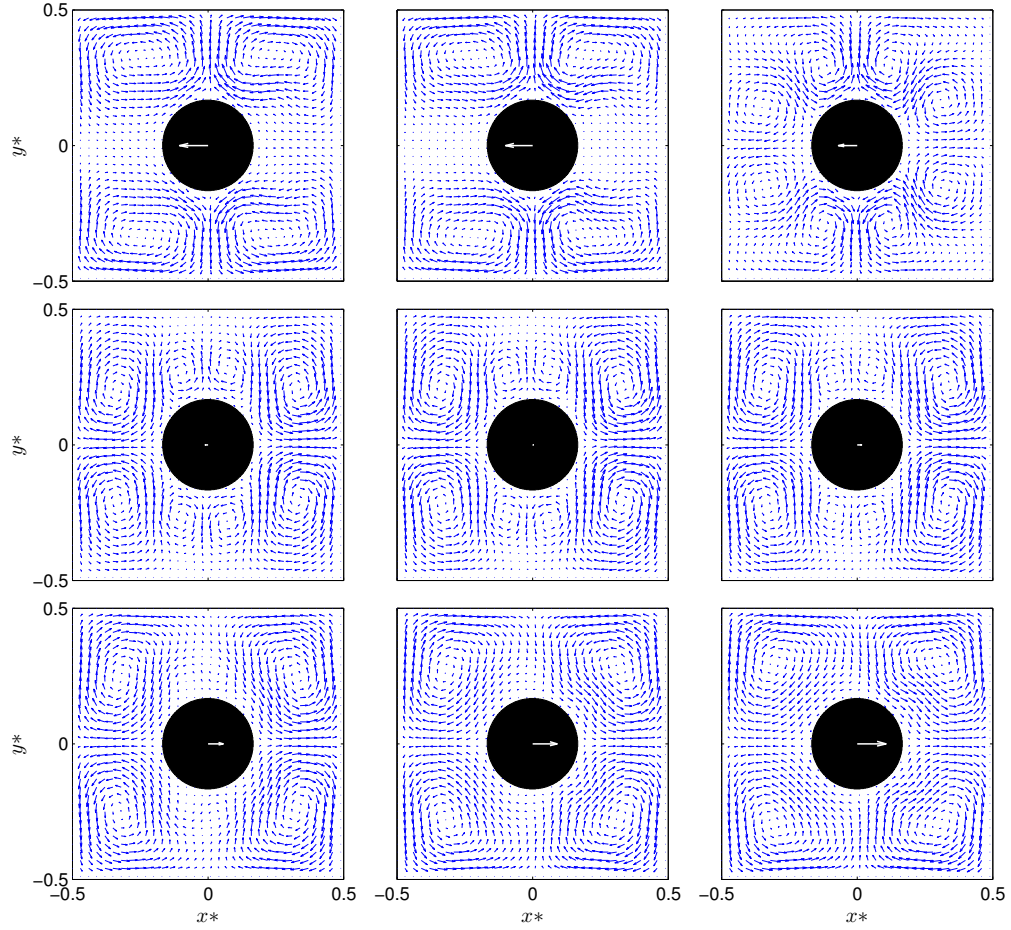


Figure E.5: Snapshots of horizontal velocity fields of 4th mode ($m = 4$) at the middle of forest belt ($X = L_F/2$) – Case 7. From left to right and top to bottom, the dimensionless time is $mt/T = 0.25, 0.27, 0.34, 0.43, 0.45, 0.47, 0.53, 0.60, 0.65$. Note that the central arrows are used to indicate the evolution and directions of horizontal cell-averaged velocity $\langle u_{m=4}^{(0)} \rangle$. The length of arrows have been enlarged for illustration and do not indicate the real magnitude.

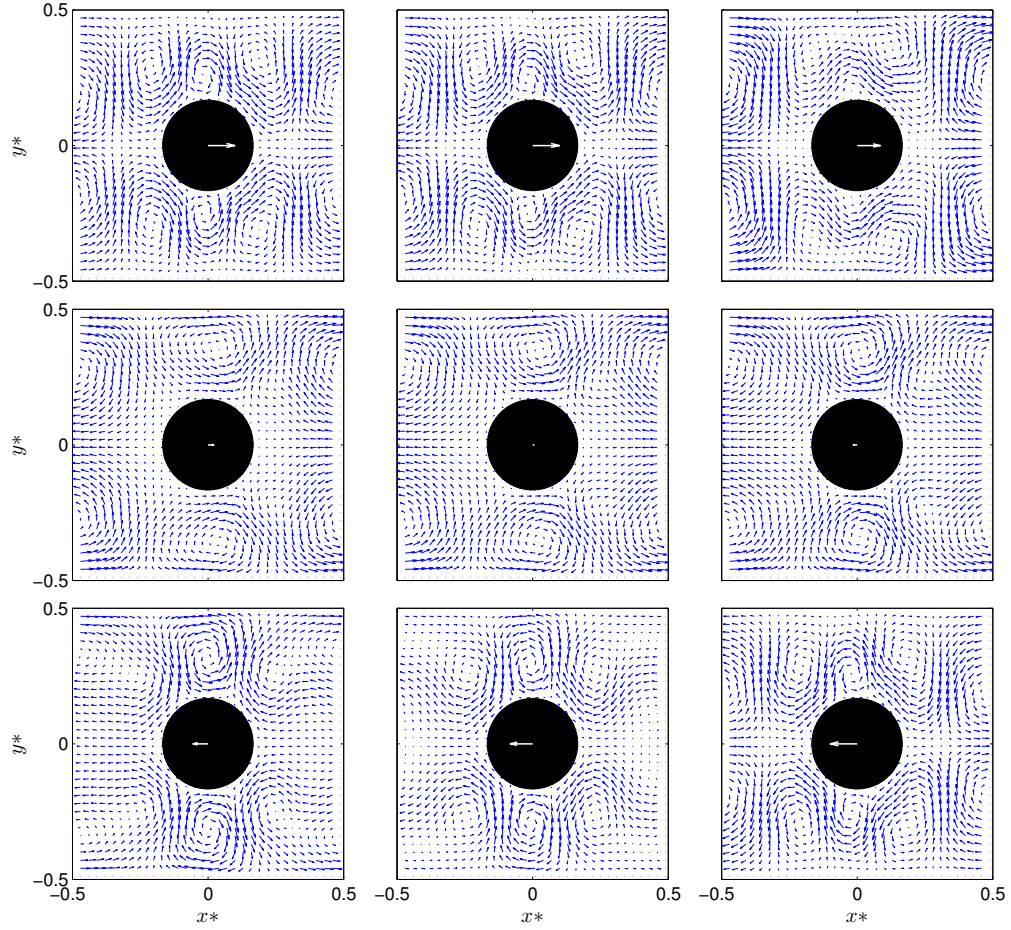


Figure E.6: Snapshots of horizontal velocity fields of 5th mode ($m = 5$) at the middle of forest belt ($X = L_F/2$) – Case 7. From left to right and top to bottom, the dimensionless time is $mt/T = 0.35, 0.37, 0.44, 0.57, 0.60, 0.63, 0.70, 0.76, 0.85$. Note that the central arrows are used to indicate the evolution and directions of horizontal cell-averaged velocity $\langle u_{m=5}^{(0)} \rangle$. The length of arrows have been enlarged for illustration and do not indicate the real magnitude.

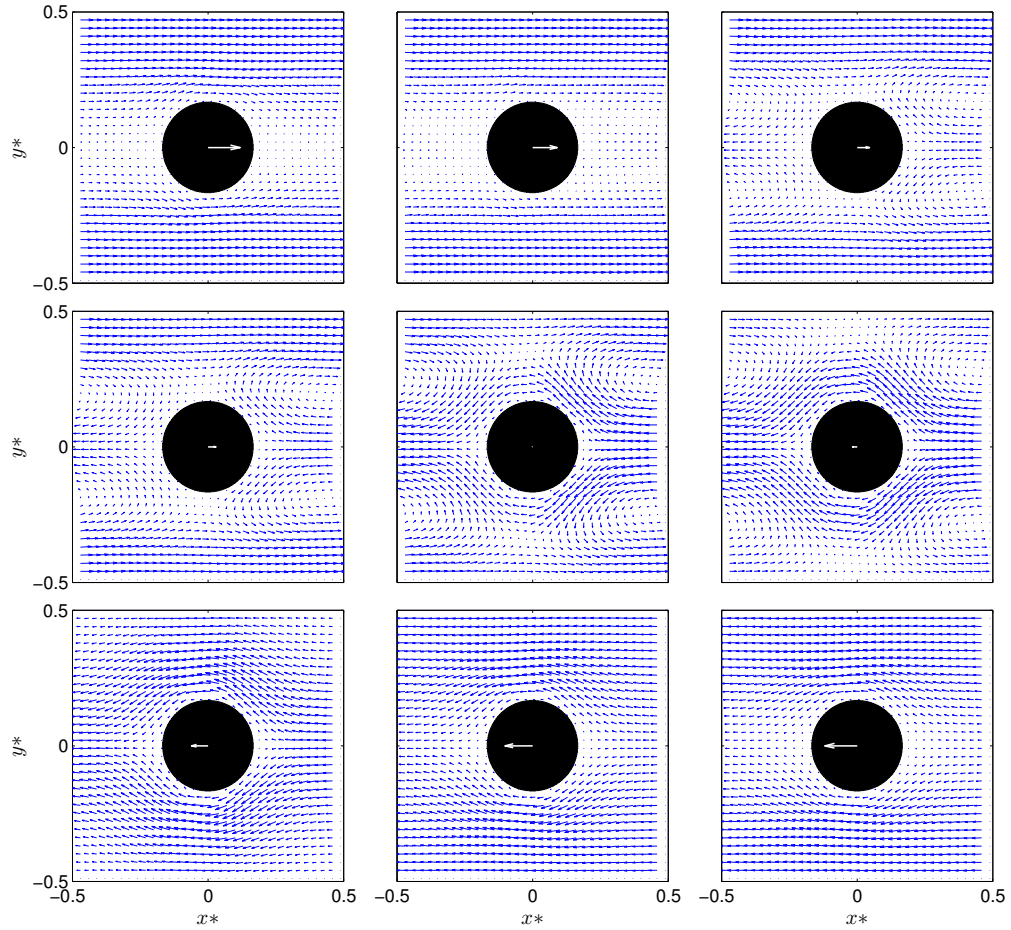


Figure E.7: Snapshots of horizontal velocity fields of 1st mode ($m = 1$) at the middle of forest belt ($X = L_F/2$) – Case 5. From left to right and top to bottom, the dimensionless time is $mt/T = 0.32, 0.39, 0.46, 0.48, 0.52, 0.54, 0.60, 0.67, 0.72$. Note that the central arrows are used to indicate the evolution and directions of horizontal cell-averaged velocity $\langle u_{m=1}^{(0)} \rangle$. The length of arrows have been enlarged for illustration and do not indicate the real magnitude.

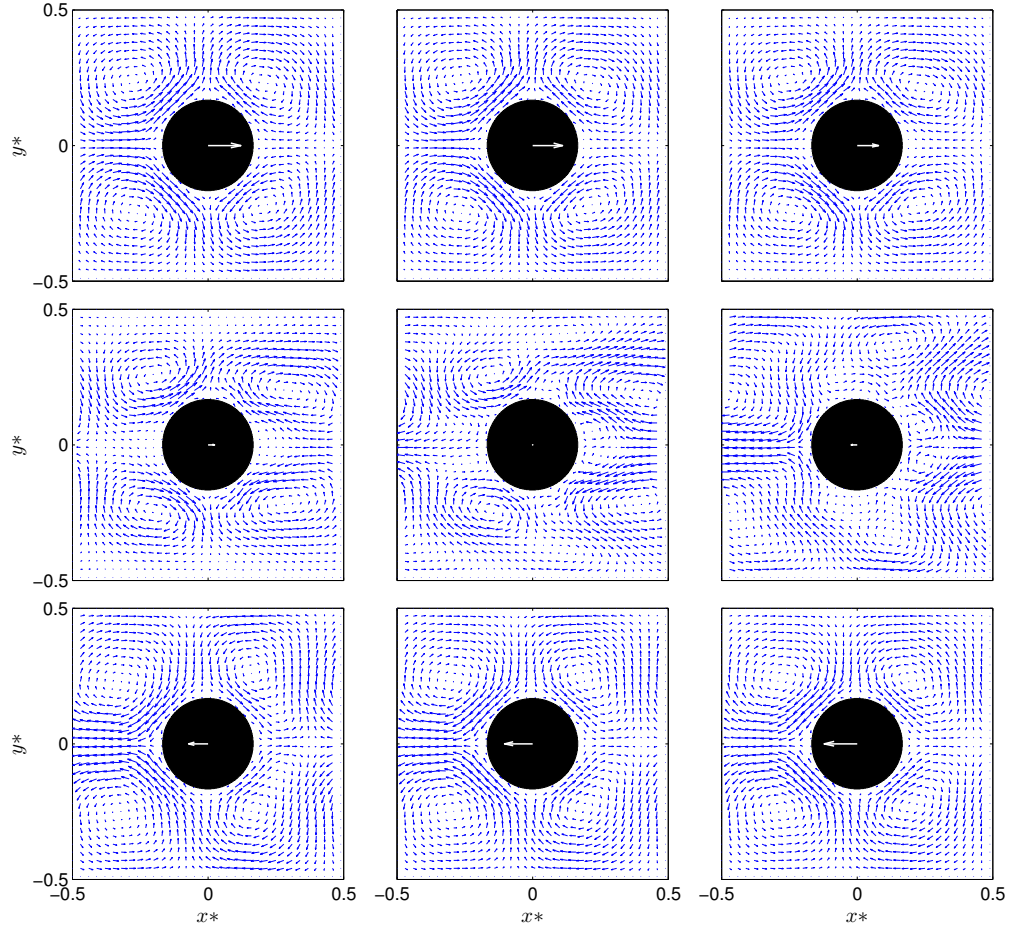


Figure E.8: Snapshots of horizontal velocity fields of 2_{nd} mode ($m = 2$) at the middle of forest belt ($X = L_F/2$) – Case 5. From left to right and top to bottom, the dimensionless time is $mt/T = 0.46, 0.51, 0.58, 0.66, 0.69, 0.72, 0.79, 0.85, 0.92$. Note that the central arrows are used to indicate the evolution and directions of horizontal cell-averaged velocity $\langle u_{m=2}^{(0)} \rangle$. The length of arrows have been enlarged for illustration and do not indicate the real magnitude.

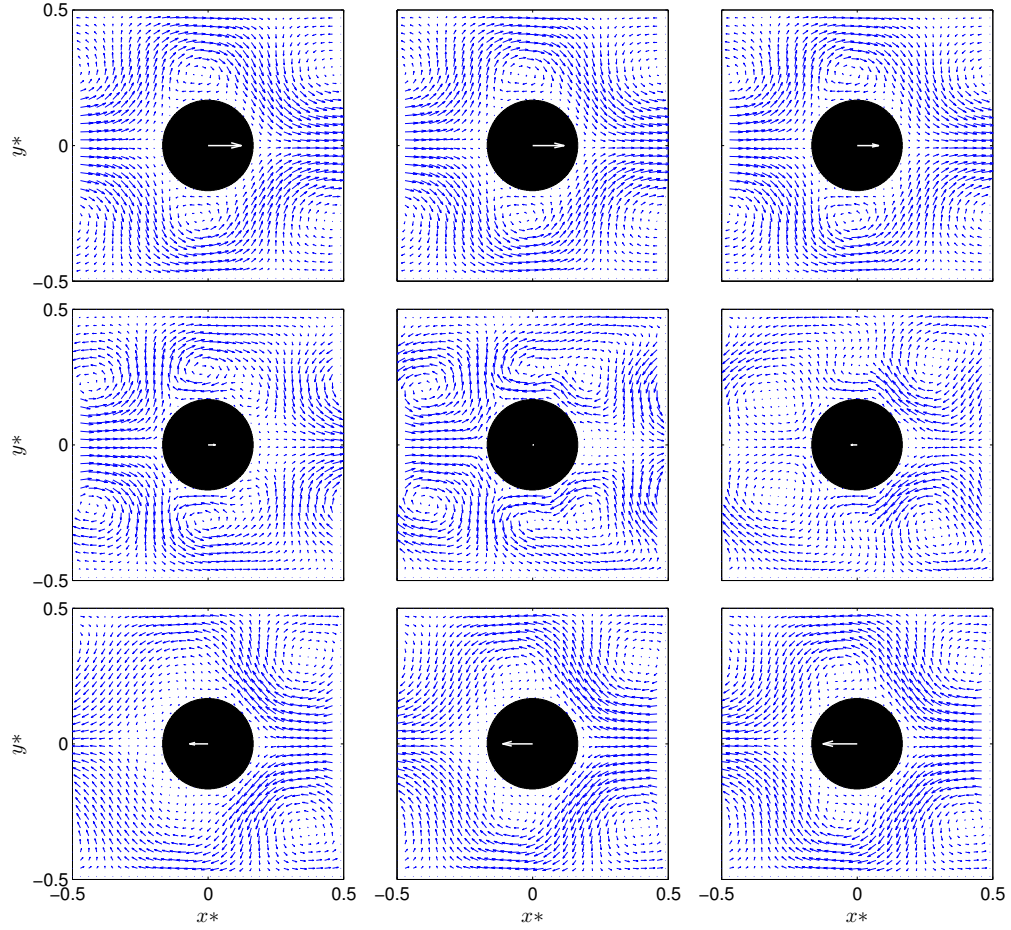


Figure E.9: Snapshots of horizontal velocity fields of 3_{rd} mode ($m = 3$) at the middle of forest belt ($X = L_F/2$) – Case 5. From left to right and top to bottom, the dimensionless time is $mt/T = 0.35, 0.37, 0.44, 0.51, 0.54, 0.57, 0.63, 0.70, 0.75$. Note that the central arrows are used to indicate the evolution and directions of horizontal cell-averaged velocity $\langle u_{m=3}^{(0)} \rangle$. The length of arrows have been enlarged for illustration and do not indicate the real magnitude.

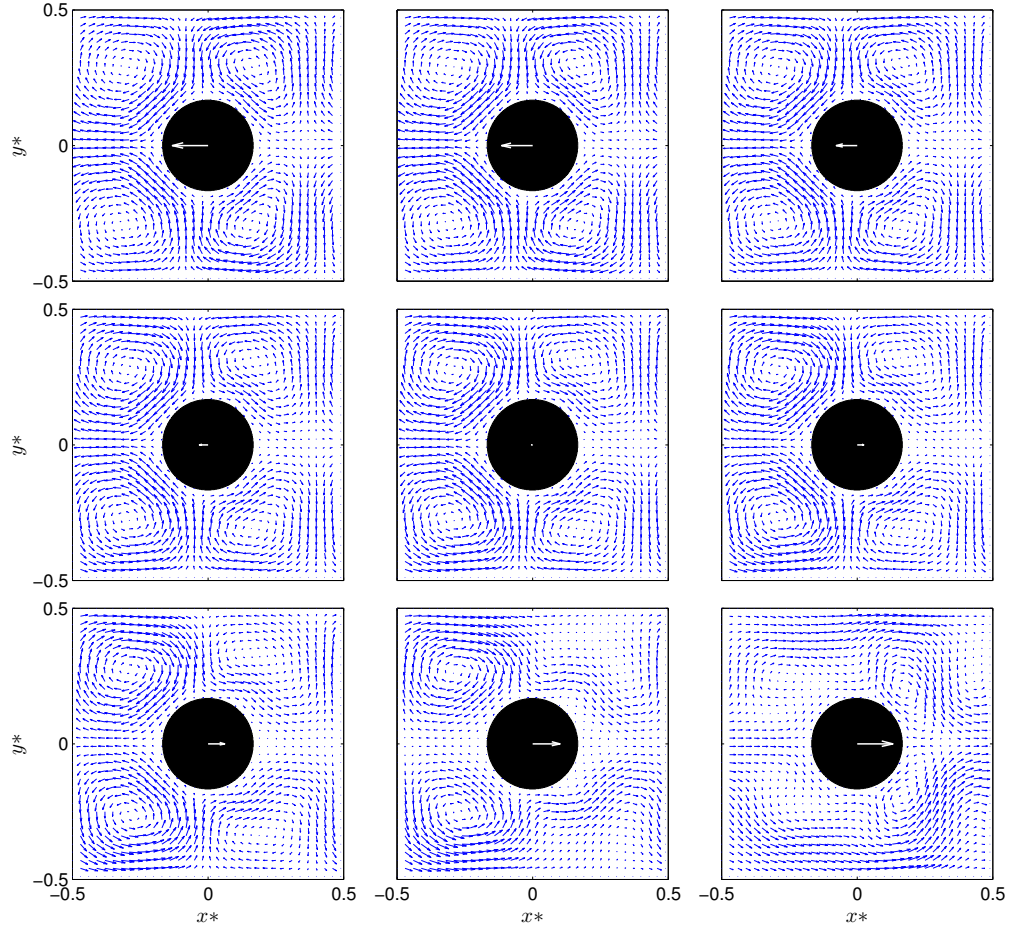


Figure E.10: Snapshots of horizontal velocity fields of 4th mode ($m = 4$) at the middle of forest belt ($X = L_F/2$) – Case 5. From left to right and top to bottom, the dimensionless time is $mt/T = 0.07, 0.10, 0.15, 0.20, 0.23, 0.26, 0.30, 0.35, 0.40$. Note that the central arrows are used to indicate the evolution and directions of horizontal cell-averaged velocity $\langle u_{m=4}^{(0)} \rangle$. The length of arrows have been enlarged for illustration and do not indicate the real magnitude.

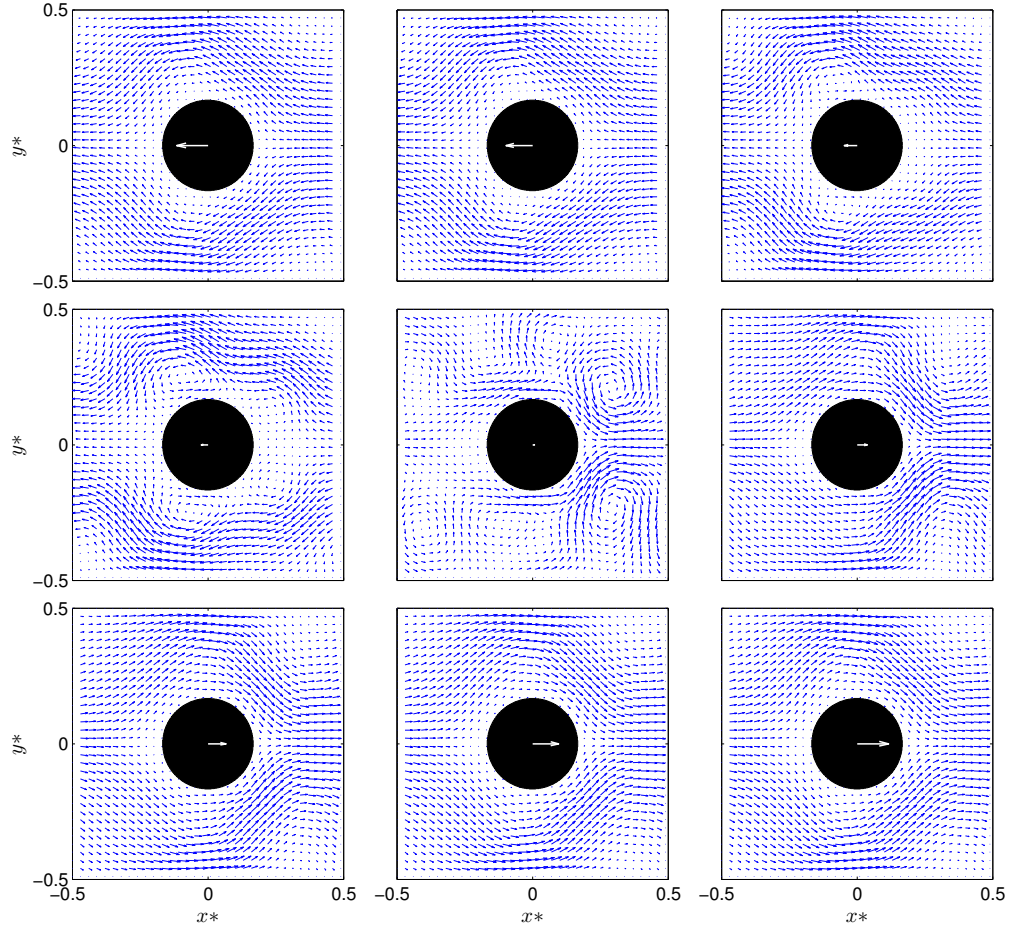
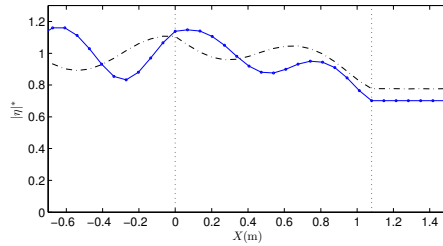
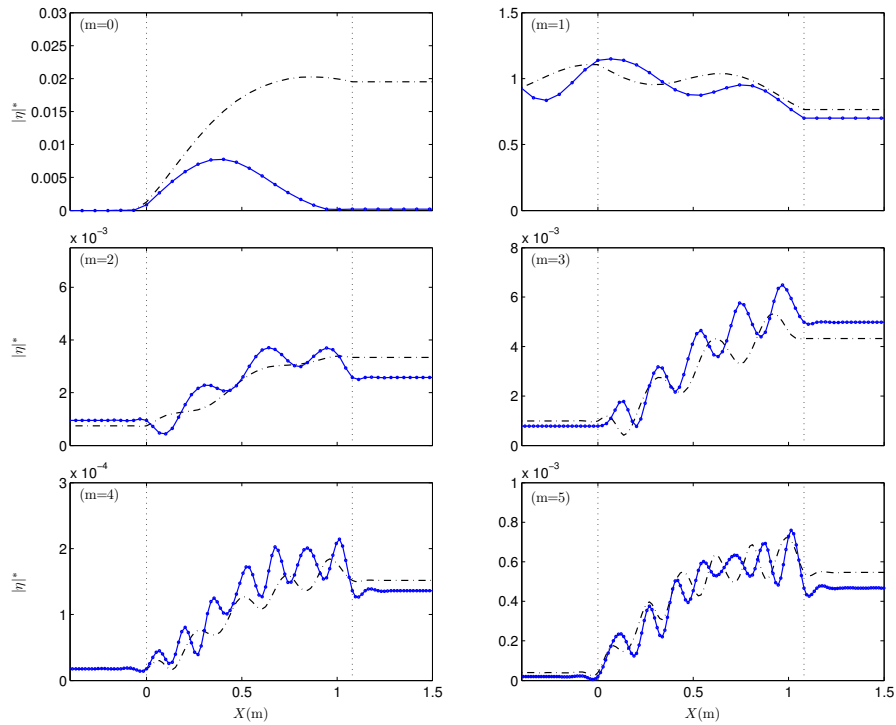


Figure E.11: Snapshots of horizontal velocity fields of 5th mode ($m = 5$) at the middle of forest belt ($X = L_F/2$) – Case 5. From left to right and top to bottom, the dimensionless time is $mt/T = 0.13, 0.17, 0.25, 0.28, 0.32, 0.36, 0.40, 0.45, 0.50$. Note that the central arrows are used to indicate the evolution and directions of horizontal cell-averaged velocity $\langle u_{m=5}^{(0)} \rangle$. The length of arrows have been enlarged for illustration and do not indicate the real magnitude.

E.2 Macro-scale wave amplitude variations through the forest belt

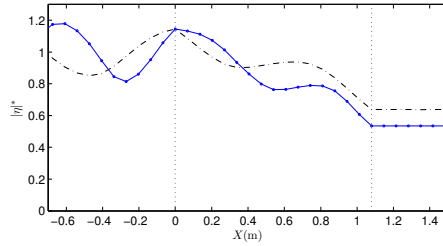


(a) Total solutions

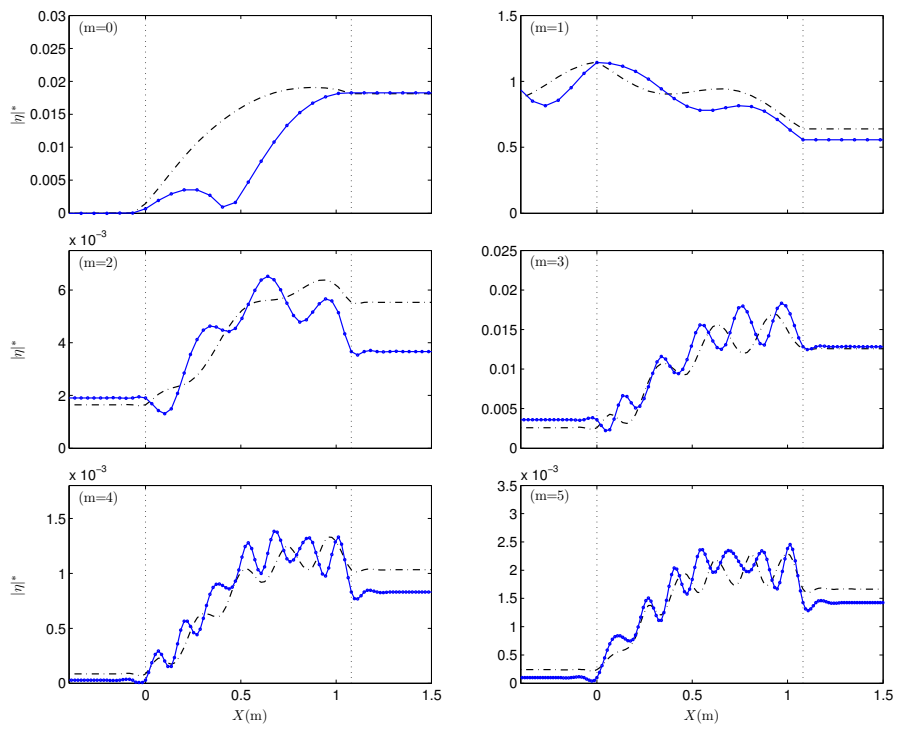


(b) Each harmonic component

Figure E.12: Wave amplitude variation of different harmonic components – $\alpha_n = 0.3$. Dot-dashed lines: $k_{inc}\ell = 0.0942$, $A_{inc}/h_0 = 0.0283$; circled lines: $k_{inc}\ell = 0.1319$, $A_{inc}/h_0 = 0.0396$

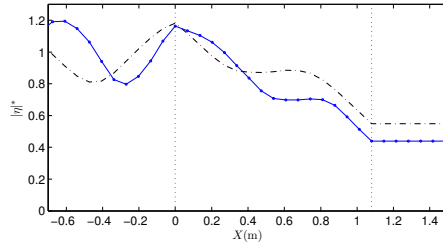


(a) Total solutions

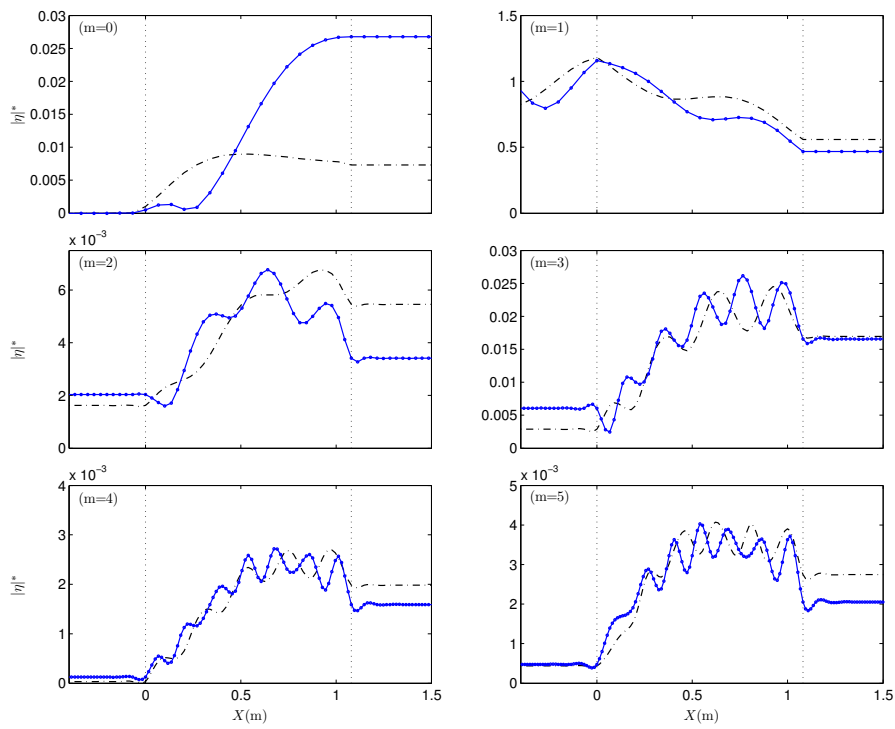


(b) Each harmonic component

Figure E.13: Wave amplitude variation of different harmonic components – $\alpha_n = 0.6$. Dot-dashed lines: $k_{inc}\ell = 0.0942$, $A_{inc}/h_0 = 0.0565$; circled lines: $k_{inc}\ell = 0.1319$, $A_{inc}/h_0 = 0.0792$

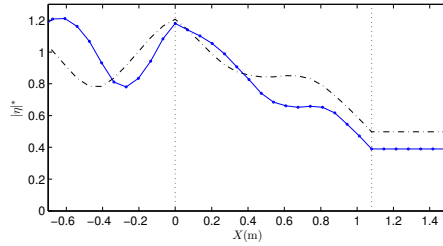


(a) Total solutions

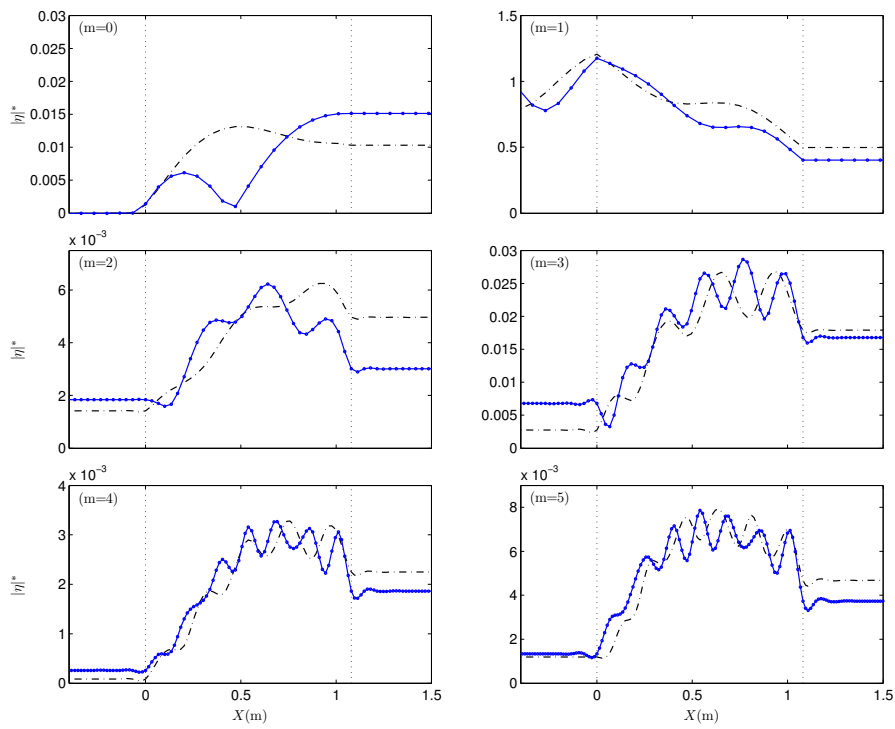


(b) Each harmonic component

Figure E.14: Wave amplitude variation of different harmonic components – $\alpha_n = 0.9$. Dot-dashed lines: $k_{inc}\ell = 0.0942$, $A_{inc}/h_0 = 0.0848$; circled lines: $k_{inc}\ell = 0.1319$, $A_{inc}/h_0 = 0.1188$



(a) Total solutions



(b) Each harmonic component

Figure E.15: Wave amplitude variation of different harmonic components – $\alpha_n = 1.2$. Dot-dashed lines: $k_{inc}\ell = 0.0942$, $A_{inc}/h_0 = 0.1131$; circled lines: $k_{inc}\ell = 0.1319$, $A_{inc}/h_0 = 0.1583$

BIBLIOGRAPHY

- Anderson, E., Bai, Z., Bischof, C., Blackford, S., Demmel, J., Dongarra, J., Du Croz, J., Greenbaum, A., Hammarling, S., McKenney, A., and Sorensen, D. *LAPACK Users' Guide*. Society for Industrial and Applied Mathematics, third edition, 1999.
- Anderson, J., John D. *Computational Fluid Dynamics – The Basics with Applications*. McGraw-Hill Inc., 1995.
- Anderson, M. E. and Smith, J. M. Wave attenuation by flexible, idealized salt marsh vegetation. *Coastal Engineering*, 83:82–92, 2014.
- Anderson, M. E. and Smith, J. M. Implementation of wave dissipation by vegetation in STWAVE. Technical Report ERDC/CHL CHETN-I-85, US Army Engineer Research and Development Center, Vicksburg, MS, February 2015.
- Augustin, L. N. Laboratory experiments and numerical modeling of wave attenuation through artificial vegetation. Master's thesis, Texas A&M University, 2007.
- Augustin, L. N., Irish, J. L., and Lynett, P. Laboratory and numerical studies of wave damping by emergent and near-emergent wetland vegetation. *Coastal Engineering*, 56:332–340, 2009.
- Bagchi, P. and Balachandar, S. Response of the wake of an isolated particle to an isotropic turbulent flow. *Journal of Fluid Mechanics*, 518:95–123, 2004.
- Chakrabarti, A., Chen, Q., Smith, H. D., and Liu, D. Large eddy simulation of unidirectional and wave flows through vegetation. *Journal of Engineering Mechanics*, 142:04016048, 2016.

- Chang, C.-W., Liu, P. L.-F., Mei, C. C., and Maza, M. Periodic water waves through a heterogeneous coastal forest of arbitrary shape. *Coastal Engineering*, 122:141–157, 2017a.
- Chang, C.-W., Liu, P. L.-F., Mei, C. C., and Maza, M. Modeling transient long waves propagating through a heterogeneous coastal forest of arbitrary shape. *Coastal Engineering*, 122:124–140, 2017b.
- Cheng, N.-S. and Nguyen, H. T. Hydraulic radius for evaluating resistance induced by simulated emergent vegetation in open-channel flows. *Journal of Hydraulic Engineering*, 137:995–1004, 2011.
- Chorin, A. J. Numerical solution of the navier-stokes equations. *Mathematics of Computation*, 22:745–762, 1968.
- Cui, J. and Neary, V. S. LES study of turbulent flows with submerged vegetation. *Journal of Hydraulic Research*, 46:307–316, 2008.
- Dalrymple, R. A., Kirby, J. T., and Hwang, P. A. Wave diffraction due to areas of energy dissipation. *Journal of Waterway, Port, Coastal, and Ocean Engineering*, 100:67–79, 1984.
- Danielsen, F., Sorensen, M. K., Olwig, M. F., Selvam, V., Parish, F., Burgess, N. D., Hiraishi, T., Karunagaran, V. M., Rasmussen, M. S., Hansen, L. B., Quarto, A., and Suryadiputra, N. The asian tsunami: A protective role for coastal vegetation. *Science*, 310:643, 2005.
- Das, S. and Vincent, J. R. Mangroves protected villages and reduced death toll during indian super cyclone. In *Proceedings of the National Academy of Sciences of the United States of America*, pages 7357–7360, 2009.

- de Lima, P. H. S., Janzen, J. G., and Nepf, H. M. Flow patterns around two neighboring patches of emergent vegetation and possible implications for deposition and vegetation growth. *Environmetnal Fluid Mechanics*, 15:881–898, 2015.
- Fernando, H., Samarawickrama, S., Balasubramanian, S., Hettiarachchi, S., and Voropayev, S. Effects of porous barriers such as coral reefs on coastal wave propagation. *Journal of Hydro-environment Research*, 1:187–194, 2008.
- Ferziger, J. H. and Peric, M. *Computational Methods for Fluid Dynamics*. Springer, third edition, 2012.
- Hecht, F. New development in freefem++. *Journal of Numerical Mathematics*, 20: 251–265, 2012.
- Horstman, E. M., Dohmen-Janssen, C. M., Narra, P. M. F., van den Berg, N. J. F., Siemerink, M., and Hulscher, S. J. M. H. Wave attenuation in mangroves: A quantitative approach to field observations. *Coastal Engineering*, 94:47–62, 2014.
- Hu, Z., Suzuki, T., Zitman, T., Uittewaal, W., and Stive, M. Laboratory study on wave dissipation by vegetation in combined current-wave flow. *Coastal Engineering*, 88:131–142, 2014.
- Huang, Z., Yao, Y., Sim, S. Y., and Yao, Y. Interaction of solitary waves with emergent, rigid vegetation. *Ocean Engineering*, 38:1080–1088, 2011.
- Husrin, S., Strusinska, A., and Oumeraci, H. Experimental study on tsunami attenuation by mangrove forest. *Earth, Planets and Space*, 64:973–989, 2012.

- Irish, J. L., Weiss, R., Yang, Y., Song, Y. K., Zainali, A., and Marivela-Colmenarejo, R. Laboratory experiments of tsunami run-up and withdrawal in patchy coastal forest on a steep beach. *Natural Hazards*, 74:1933–1949, 2014.
- Irtem, E., Gedik, N., Kabdasli, M. S., and Yasa, N. E. Coastal forest effects on tsunami run-up heights. *Ocean Engineering*, 36:313–320, 2009.
- Isaacson, M. Measurement of regular wave reflection. *Journal of Waterway, Port, Coastal and Ocean Engineering*, 117:553–569, 1991.
- Ismail, H., Wahab, A. K. A., and Alias, N. E. Determination of mangrove forest performance in reducing tsunami run-up using physical models. *Natural Hazards*, 63:939–963, 2012.
- Kathiresan, K. and Rajendran, N. Coastal mangrove forests mitigated tsunami. *Estuarine, Coastal and Shelf Science*, 65:601–606, 2005.
- Lara, J. L., Maza, M., Ondiviela, B., Trinogga, J., Losada, I., Bouma, T., and Gordejuela, N. Large-scale 3-d experiments of wave and current interaction with real vegetation. part 1: Guidelines for physical modeling. *Coastal Engineering*, 107:70–83, 2016.
- Lee, J.-J. Wave-induced oscillations in harbours of arbitrary geometry. *Journal of Fluid Mechanics*, 45:375–394, 1971.
- Lee, J.-J. and Ayer, R. M. Wave propagation over a rectangular trench. *Journal of Fluid Mechanics*, 110:335–347, 1981.
- Li, C. and Yan, K. Numerical investigation of wave-current-vegetation interaction. *Journal of Hydraulic Engineering*, 133:794–803, 2007.

- Liggett, J. A. and Liu, P. L.-F. *The boundary integral equation method for porous media flow*. Allen & Unwin, 1983.
- Liu, D., Diplas, P., Fairbanks, J. D., and Hodges, C. C. An experimental study of flow through rigid vegetation. *Journal of Geophysical Research*, 113:F04015, 2008.
- Liu, P. L.-F., Chang, C.-W., Mei, C. C., Lomonaco, P., Martin, F. L., and Maza, M. Periodic water waves through an aquatic forest. *Coastal Engineering*, 96: 100–117, 2015.
- Ma, G., Kirby, J. T., Su, S.-F., Figlus, J., and Shi, F. Numerical study of turbulence and wave damping induced by vegetation canopies. *Coastal Engineering*, 80: 68–78, 2013.
- Massel, S. R., Furukawa, K., and Brinkman, R. M. Surface wave propagation in mangrove forests. *Fluid Dynamics Research*, 24:219–249, 1999.
- Maza, M. *Experimental and numerical modelling of flow interaction with natural ecosystems for coastal protection*. PhD thesis, University of Cantabria, 2015.
- Maza, M., Lara, J. L., and Losada, I. J. A coupled model of submerged vegetation under oscillatory flow using navier-stokes equations. *Coastal Engineering*, 80: 16–34, 2013.
- Maza, M., Lara, J. L., Losada, I., Ondiviela, B., Trinogga, J., and Bouma, T. Large-scale 3-d experiments of wave and current interaction with real vegetation. part 2: Experimental analysis. *Coastal Engineering*, 106:73–86, 2015a.
- Maza, M., Lara, J. L., and Losada, I. J. Tsunami wave interaction with mangrove forests: A 3-d numerical approach. *Coastal Engineering*, 98:33–54, 2015b.

- Maza, M., Lara, J. L., and Losada, I. J. Solitary wave attenuation by vegetation patches. *Advances in Water Resources*, 98:159–172, 2016.
- Mazda, Y., Kobashi, D., and Okada, S. Tidal-scale hydrodynamics within mangrove swamps. *Wetlands Ecology and Management*, 13:647–655, 2005.
- Mei, C. C. and Vernescu, B. *Homogenization methods for multiscale mechanics*. World Scientific, 2010.
- Mei, C. C., Stiassnie, M., and Yue, D. K.-P. *Theory and Applications of Ocean Surface Waves: Nonlinear Aspects*. World Scientific, 2005.
- Mei, C. C., Chan, I.-C., Liu, P. L.-F., Huang, Z., and Zhang, W. Long waves through emergent coastal vegetation. *Journal of Fluid Mechanics*, 687:461–491, 2011.
- Mei, C. C., Chan, I.-C., and Liu, P. L.-F. Waves of intermediate length through an array of vertical cylinders. *Environmental Fluid Mechanics*, 14:235–261, 2014.
- Meire, D. W. S. A., Kondziolka, J. M., and Nepf, H. M. Interaction between neighboring vegetation patches: Impact on flow and deposition. *Water Resources Research*, 50:3809–3825, 2014.
- Mendez, F. J. and Losada, I. J. Hydrodynamics induced by wind waves in a vegetation field. *Journal of Geophysical Research*, 104:18383–18396, 1999.
- Mendez, F. J. and Losada, I. J. An empirical model to estimate the propagation of random breaking and nonbreaking waves over vegetation fields. *Coastal Engineering*, 51:103–118, 2004.
- Miles, J. W. Damping of weakly nonlinear shallow-water waves. *Journal of Fluid Mechanics*, 76:251–257, 1976.

- Morison, J. R., O'Brien, M. P., Johnson, J. W., and Schaaf, S. A. The force exerted by surface waves on piles. *Petroleum Transactions*, 189:149–154, 1950.
- Ozeren, Y., Wren, D. G., and Wu, W. Experimental investigation of wave attenuation through model and live vegetation. *Journal of Waterway, Port, Coastal and Ocean Engineering*, 140:04014019, 2014.
- Quartel, S., Kroon, A., Augustinus, P., Santen, P. V., and Tri, N. H. Wave attenuation in coastal mangroves in the red river delta, vietnam. *Journal of Asian Earth Sciences*, 29:576–584, 2007.
- Stoesser, T., Salvador, G. P., Rodi, W., and Diplas, P. Large eddy simulation of turbulent flow through submerged vegetation. *Transport in Porous Media*, 78: 347–365, 2009.
- Stoesser, T., Kim, S. J., and Diplas, P. Turbulent flow through idealized emergent vegetation. *Journal of Hydraulic Engineering*, 136:1003–1017, 2010.
- Strusinska-Correia, A., Husrin, S., and Oumeraci, H. Tsunami damping by mangrove forest: a laboratory study using parameterized trees. *Natural Hazards*, 13:483–503, 2013.
- Sumer, B. M. and Fredsøe, J. *Hydrodynamics around cylindrical structures*. World Scientific, 2006.
- Tanaka, N., Sasaki, Y., Mowjood, M. I. M., Jinadasa, K. B. S. N., and Homchuen, S. Coastal vegetation structures and their functions in tsunami protection: experience of the recent indian ocean tsunami. *Landscape and Ecological Engineering*, 3:33–45, 2007.

- Tanino, Y. and Nepf, H. M. Lateral dispersion in random cylinder arrays at high Reynolds number. *Journal of Fluid Mechanics*, 600:339–371, 2008a.
- Tanino, Y. and Nepf, H. M. Laboratory investigation of mean drag in a random array of rigid, emergent cylinders. *Journal of Hydraulic Engineering*, 134:34–41, 2008b.
- Thuy, N. B., Tanimoto, K., Tanaka, N., Harada, K., and Iimura, K. Effect of open gap in coastal forest on tsunami run-up – investigations by experiment and numerical simulation. *Ocean Engineering*, 36:1258–1269, 2009.
- Truong, M. K., Whilden, K. A., Socolofsky, S. A., and Irish, J. L. Experimental study of wave dynamics in coastal wetlands. *Environmental Fluid Mechanics*, 15:851–880, 2015.
- Williams, A. N. Diffraction of long waves by rectangular pit. *Journal of Waterway, Port, Coastal and Ocean Engineering*, 116:459–469, 1990.
- Williams, A. N. and Vazquez, J. Wave interaction with a rectangular pit. *Journal of Offshore Mechanics and Arctic Engineering*, 113:193–198, 1991.
- Wu, J.-S. and Faeth, G. M. Sphere wakes at moderate Reynolds numbers in a turbulent environment. *AIAA Journal*, 32:535–541, 1994a.
- Wu, J.-S. and Faeth, G. M. Effect of ambient turbulence intensity on sphere wakes at intermediate Reynolds numbers. *AIAA Journal*, 33:171–173, 1994b.
- Wu, W., Ozeren, Y., Wren, D., Chen, Q., Zhang, G., Holland, M., Ding, Y., Kuiry, S. N., Zhang, M., Jadhav, R., Chatagnier, J., Chen, Y., and Gordji, L. Investigation of surge and wave reduction by vegetation. Technical Report SERRI Project 80037-1, U.S. Department of Homeland Security, 2011.

- Wu, W., Zhang, M., and Wren, D. Analysis of vegetation effect on waves using a vertical 2D RANS model. *Journal of Coastal Research*, 29:383–397, 2012.
- Yang, Y., Irish, J. L., and Socolofsky, S. A. Numerical investigation of wave-induced flow in mound-channel wetland systems. *Coastal Engineering*, 102:1–12, 2015.
- Yang, Y., Irish, J. L., and Weiss, R. Impact of patchy vegetation on tsunami dynamics. *Journal of Waterway, Port, Coastal, and Ocean Engineering*, 143:04017005, 2017.
- Yuksel-Ozan, A., Constantinescu, G., and Nepf, H. M. Free-surface gravity currents propagating in an open channel containing a porous layer at the free surface. *Journal of Fluid Mechanics*, 809:601–627, 2016.
- Zhang, M., Qiao, H., Xu, Y., Qiao, Y., and Yang, K. Numerical study of wave-current-vegetation interaction in coastal waters. *Environmental Fluid Mechanics*, 16:965–981, 2016.
- Zong, L. and Nepf, H. M. Vortex development behind a finite porous obstruction in a channel. *Journal of Fluid Mechanics*, 691:368–391, 2011.